EXPERIMENTAL STUDY ON THE TORSIONAL MECHANICS OF LAMINATED STRUCTURAL GLASS BEAMS

A PhD Thesis Presented by

KAL UHEIDA

Submitted to the School of Engineering and the Built Environment,

Edinburgh Napier University in partial fulfilment

of the requirements for the degree of

DOCTOR OF PHILOSOPHY

Submitted May 2022

TITLE OF THESIS: EXPERIMENTAL STUDY ON THE TORSIONAL MECHANICS OF LAMINATED STRUCTURAL GLASS BEAMS

A Thesis Presented

by

KAL UHEIDA

Candidate:

_____

Mr. Kalefa (Kal) Uheida

Under the Supervision of:

_____

Prof. Johnson Zhang, Director of Study

_____

Dr. Keng Goh. Research Supervisor

_____

Dr. John McDougall, Independent Panel Chair

_____

Prof. Peter Andras, Dean of School
School of Computing and School of
Engineering and the Built Environment

Declaration

I hereby declare that this Thesis and all the work contained within it were produced entirely by myself and contains no materials that have been accepted for the award of any other degree or diploma in any university. To the best of my knowledge, this Thesis contains no material previously published or written by another person, except where due acknowledgement to others has been made.

Signature: 

Mr. Kal Uheida

Dedication

This Thesis is dedicated to my father, Lotfi Uheida, who always believed I could achieve great things even when I did not believe it myself. He gave his full encouragement and support to me throughout this entire journey, from the first day I studied engineering to the end of this PhD, and in all other aspects of life. For this, I am forever thankful to him.

Acknowledgements

I would like to express my sincere gratitude and thanks to my supervision team. Firstly, as my Director of Study, Prof. Johnson Zhang has given an incredible amount of help, support, and guidance to me throughout the entirety of this Doctorate. From the countless long days, nights, and weekends he has dedicated to answering questions and providing his expert guidance on my research, to the many lab days he has dedicated his time to, and also to the many research projects he has involved me in, he has provided me with an invaluable learning experience and this PhD Thesis would have never been possible without his support. For that, I have the utmost gratitude. I would also like to express my sincere gratitude to my Research Supervisor Dr Keng Goh, who has provided invaluable insight, support, and guidance throughout the entirety of this Doctoral program.

I would also like to express my thanks to many of the technical staff at Edinburgh Napier University. Special thanks are due to Brian Black and Willie Laing, who have both helped out greatly at very short notice for fabricating and manufacturing vital components and items that allowed experiments and exhibitions to be delivered successfully. I would also like to express my thanks to the technicians at the Napier Institution for Sustainable Construction, with a special thanks to Stefan Lehneke for his help and support in the lab.

My thanks are also due to my colleague and fellow researcher, Dr. Ahmed Mohamed, who always made himself available to answer any questions I had about the PhD experience and was always happy to lend a helping hand. I would also like to extend my gratitude to the Undergraduate and Postgraduate Dissertation student groups for not only being bright and motivated students who improved my PhD experience, but also for their help and support in the lab which provided a mutual learning experience.

Finally, but certainly not least, I extend my utmost thanks and gratitude to my father, Lotfi, and my mother Fiona. The limitless, unwavering support I have received from them throughout this journey has been unfathomable, and I will be forever indebted to them.

Abstract

This thesis presents an experimental study on the torsional-mechanical behaviours of laminated structural glass beams. Glass structures are in increasing demand due to many favourable characteristics such as high compressive strength, flexibility, aesthetics, sustainability, and their positive effects on human mood and performance. However, monolithic glass is brittle in nature and fails instantaneously so laminated glass building elements are preferred, which have complex composite behaviours. An additional challenge is the lack of a finalised glass design code. This PhD study takes aim specifically at laminated glass beams and their torsional mechanics, which are crucial for supporting floor and roof plates, glass walls and other applications that enable fully transparent structures to be realised.

A concise concept for quantifying the torsional stiffness of laminated glass beam elements is introduced – the Equivalent-Sectional Shear Modulus (ESSM), which is directly measured from the torque and sectional-rotation correlation in non-destructive torsion experiments. This method is advantageous as it allows for the measurement of overall rotation to torque response of laminated glass beams compositely rather than their individual components, resultantly decreasing the uncertainties of commonly adopted analytical approximations. A tailor-made, non-contact displacement measurement system based on the principles of binocular stereo-vision was developed, tested, verified, and employed to the torsion test procedure to increase the accuracy of photogrammetric measurements to be acquired. This incorporates the use of dense displacement sample targets on the glass beam which are measured and extracted using basic machine vision techniques, providing flexible, accurate, and non-intrusive measurements.

Experimental torsion studies were performed on multiple samples of monolithic, two-layer, and three-layer polyvinyl butyral (PVB) and SentryGlas Plus (SGP) beams. The experimental setup, equipment, and procedures were continually improved and refined in a step-wise process throughout this work. The monolithic beams experimental ESSM results were validated against theoretical calculations from their elastic moduli relationship. Furthermore, the experimental ESSM results for two-layer and three-layer laminated beams were also compared with existing analytical solutions based on sandwich theory. Further experimental studies were also performed to evaluate the effects of ‘eccentric-torque’, where the effect of an eccentricated torsional load path on the overall torsional rigidity of the beam is studied, and on the effect of lengthened load-durations for SGP laminates. A variety of interesting and remarkable results were obtained regarding the composite torsional-mechanical behaviours of laminated structural glass beams and the optimisation of a first-of-its-kind glass beam torsion test approach. The results of this PhD thesis may help to support the further development of structural glass design codes and practices.

Table of Contents

List of Figures

List of Tables

1. Introduction

1.1 Background and Motivation

Glass has been manufactured for thousands of years in many forms and for many purposes due to its unique optical, physical, mechanical, and aesthetic properties. Glass is a unique material in the sense that it is transparent, chemically inert, environmentally friendly, strong, readily available and relatively cheap [1]. From its early uses in jewellery and hollow glass vessels, further glassmaking knowledge led to clearer glasses being produced in high enough quantities to be developed into windows during the Roman Empire. Due to the complexity of manufacture and installation process at this time, it was considered that only a truly prestigious property owner would have glass windows in their property [2, 3].

Advancements in structural engineering made larger window openings possible for all types of buildings. This in turn drove the demand for glass science to produce larger and better quality panes of glass [2]. Since the 19th century glass windows have been widely available in buildings and the home of the average person, providing an interface of transparent protection between inner and outer environments. In the modern era it is near impossible to find an occupied building where glass does not play a significant role. Glass additionally finds widespread use today in automotive and aeronautical industries, domestic appliances, the screens of electronic devices, nanotechnology applications such as fibre optics and in renewable energy applications such as solar panels and wind turbines [1].

Structural material use in buildings for frame elements has been largely dominated by steel since the industrial revolution. Its relative strength-to-weight properties, durability and recyclability allowed for large skyscrapers and other multi-storey buildings to be produced as it overtook cast iron as the dominant building frame material. This could be seen as the ‘steel revolution’ in the built environment. Initially, steel frames were thickly encased in concrete, with glass windows being of moderate size. As knowledge progressed, a shift toward fully steel-framed multi-storey structures took place. Glass, for most of this period, was still largely used in windows and within a

framed steel structure. Despite this, glass openings were now expanding in size to fit larger frames, resisting wind loads across a wider cross-sectional area and providing greater transparency in structures.

It is only over the past thirty or so years that glass has seen more widespread use in the building envelope. There has now been a noticeable shift in the view of glass in the built environment from purely architectural to being considered as a structural, load-bearing material. Innovative high strength glass has met with modern architectural desires to allow for primary structural members to be comprised partly or exclusively of glass. In modern buildings, structural glass members and components can perform almost every function that traditional construction materials such as steel, concrete, timber, or masonry can perform, with their own unique and appealing characteristics. Displayed in and are glass structures that showcase the use of glass as facades, beams, columns, and roof plates. It may be the case that a 'glass revolution' is just beginning, with a vast number of fully transparent and diverse glass structures set to appear in the coming decades. Despite this, constructing buildings that are larger and highly structurally demanding in glass exclusively remains a great challenge. Due to some of the mechanical behaviours of glass, it remains particularly challenging to apply glass frame elements, such as beams and columns to the structure. Overcoming this hurdle will require further progress and new knowledge in glass and glass composites from a structural engineering, materials science, and technological perspective.

Figure 1-1: Apple Store entrance, New York - (www.archilovers.com).

Figure 1-2: Entrance to Daman Building, Dubai - (www.malishevengineers.com).

Figure 1-3: Inland Steel Building, Chicago, constructed 1958 - (www.skyscrapercenter.com).

Figure 1-4: Flatiron Building, New York, constructed 1902 - (www.skyscrapercenter.com).

1.2 Structural Glass Beams

Structural glass beams are widely used in supporting floor and roof plates, glass walls and other applications due to many favourable characteristics inherent in the material such as high compressive strength, flexibility, aesthetics, and sustainability. With the growing demand for greater transparency in structures, they are required to maintain redundancy in a full load bearing manner as opposed to glass traditionally being limited to windows in buildings, only resisting wind loads. Glass is brittle in nature and fails instantaneously with no plastic region of failure, so monolithic glass beams pose risks as a structural member. Resultantly, most glass beams are of the laminated type – with two or more layers of glass bonded by viscoelastic interlayers. In the case of a shattered pane, fragments will adhere to the interlayer and maintain a level of redundancy post-failure. Understanding the behaviour of such composite structures is significantly different to monolithic members and poses new challenges in engineering design. Additionally, the absence of a finalised glass design code poses further uncertainty to the engineer and can result in overdesign to meet critical failure criteria.

The cross-section of a glass beam is normally thin and slender. One of the key design considerations is in the lateral torsional buckling (LTB) phenomena, which combines bending and shear deformations. Several researchers have focused studies on the LTB mode in glass beams, and analytical models have been proposed in the pre-normative glass design code. One of the key mechanical properties in modelling the structural behaviour of glass beams in lateral buckling failure is the estimation of the shear modulus, G, which is an important mechanical property when determining the recovery torque in the governing equation for lateral stability. Theoretically, for monolithic glass, the shear modulus can be determined in relation to two other elastic coefficients – the Young's Modulus, E, and the Poisson's Ratio, ν, – assuming a linear-elastic material response.

In a multi-ply laminated glass beam, modelling the composite effect is particularly challenging as the interlayer rigidity is many times lower than the glass layers. The assessment of this response is complicated by the viscoelastic, time and temperature dependent nature of the interlayer which differs greatly from glass itself. Several experimental methods have attempted to

physically determine the shear modulus in isotropic materials, such as tensile, compression, bending, ultrasonic and resonance techniques. Unfortunately, these have several limitations in recreating a similar stress scenario to the LTB mode in thin, slender glass beams. This results in discrepancies between experimental results and existing models which leads to overdesigning glass structures. Additionally, many of these tests are limited to the linear-elastic framework and homogeneous materials, therefore they are inapplicable to composites such as laminated glass beams.

The experimental method that induces the purest state of shear stress on a member is the torsion test. This creates a more optimal stress scenario to evaluate the torsional component of the LTB mode and thus the most ideal condition to determine the shear modulus. However, it is not as commonly used or well understood as other methods. A torsion test method exists for structural timber beams in the timber design code BS EN 408:2010. This has been studied and applied by researchers in the area of timber and timber-composite beams that are slender in nature with rectangular cross-sections. Shortcomings have also been identified with this method, particularly in the inability to obtain the required angular displacement data direct from the torsion machine. Traditional contact-based sensors such as inclinometers and linear variable differential transducers (LVDTs) have been applied to try to capture the torque-rotation relationship experimentally. However, these are also limited by their inability to measure in three-dimensions, limited in the precision of reading that can be acquired and are easily damaged during testing. In the case of structural glass and laminated glass beams, there is no evidence of a torsion test method to date.

1.3 Scope of the Research

1.3.1 Research Problems

In summary, the problems outlined above are as follows:

- Transparent glass structures are in great demand due to their aesthetics and sustainability. However, engineers are cautious when designing slender glass frame elements such as beams to act in a full load-bearing manner due to the brittle and elastic nature of glass, the increased complexity in analysing the mechanical behaviour of laminated glass, and lack of standardised design procedures.

- Structural glass beams like other slender beam elements are most commonly subject to failure by the LTB mode which is notoriously complex to model due to the combined bending and torsional displacements. This complexity further increases in laminated glass beams due to their composite nature.

- Experimental work in this area is required to enable existing models to be verified, improved, and for standardised test methods to be developed.

- The most accurate way to determine the shear modulus – a key elastic property in laminated structural glass beams under LTB which defines its torsional rigidity – is by torsion testing. However, there is no standardised torsion test method for laminated structural glass beams to date, nor any peer-reviewed experimental studies in this regard.

- Measuring the required angular displacements to determine the shear modulus cannot be obtained directly from the torsion machine, as a relative rotational change between two points on the beam is required. Existing sensory-based measurement devices are commonly used but also have several limitations.

1.3.2 Research Questions

Three primary research questions were posed for this work:

(1) How can the composite torsional stiffness of laminated structural glass beams be physically quantified to evaluate the efficacy of existing analytical models that are based on component properties?

(2) Can a non-destructive torsion test procedure for laminated glass beams be developed that enables the torsional behaviour to be studied across a substantial area of the beam and is applicable to Saint-Venants Torsion Theory?

(3) How can the required displacement data for the determination of torsional behaviours in laminated glass beam torsion experiments be extracted in a manner that is accurate and non-intrusive?

1.3.3 Research Methods

To attempt to resolve the problems and questions posed in this research, the following methodologies were undertaken:

(1) Develop a non-contact displacement measurement system based on the principles of binocular stereo-vision and digital photogrammetry.

(2) Develop a fully quantifiable experimental method to validate the measurement accuracy of the photogrammetric system for the specific application and for each individual experiment.

(3) Develop a tailor-made, non-destructive torsion test experimental approach for structural-sized laminated glass beams that considers their unique material properties.

(4) Develop a novel and verifiable approach to physically quantify the composite torsional stiffness of laminated structural glass beams.

(5) Determine the torsional stiffness (Shear Modulus) of laminated glass beams experimentally and compare the results to existing analytical models.

1.3.4 Assumptions

The following assumptions were made for the undertaking of this research:

- That the composition, material properties, specification of all test samples used, including interlayers, were as specified by the manufacturers/suppliers.

- There were no residual degrading effects of long-term loading or temperature present in any of the laminated glass beam test samples induced prior to receiving the samples. The temperature in the lab where they were stored throughout this research was checked by thermometer to be kept constant at 20º C, which was assumed to be correct.

- Experimental equipment such as cameras and the torsion machine were of the same specification as stated by the manufacturer and working correctly unless finding otherwise through trial experiments. In this case equipment would be replaced and any erroneous data would be discarded.

- Saint-Venants Torsion Theory for slender, rectangular cross-sectioned beam elements is valid and true.

- All the inbuilt operations, algorithms, and equations in the machine vision software HALCON that were used for calibration, image processing, and 3D coordinate extraction were as stated in the reference guides and manuals.

1.3.5 Limitations

The scope of limitations for this research are defined as follows:

- Experimental facilities did not include any form of heating chamber therefore the effect of high temperatures on laminated glass beam interlayers could not be studied during torsion experiments.

- Although an initial study on the effect of lengthened load durations on laminated glass beams was performed in Chapter 7 it was not possible to study significantly lengthened load durations. This is due to all experiments always requiring a researcher for image taking at intervals and would require many hours to over a day of attention.

- Due to budget and time constraints, it was not possible to acquire a vast set of experimental samples which could have given a broader insight into any variations present from sample to sample in laminated glass beams. To make up for lesser samples to some degree, the samples available were all tested several times each.

- As this research represents the first experimental torsion study on monolithic or laminated glass beams there is a clear absence of previous studies, codes, or procedures in this regard. This research therefore took some learnings from previous experimental torsion research and codes of practice for timber beams.

1.4 Organisation of Thesis

This thesis is divided into eight chapters, which are schematically presented in Figure 1-5.

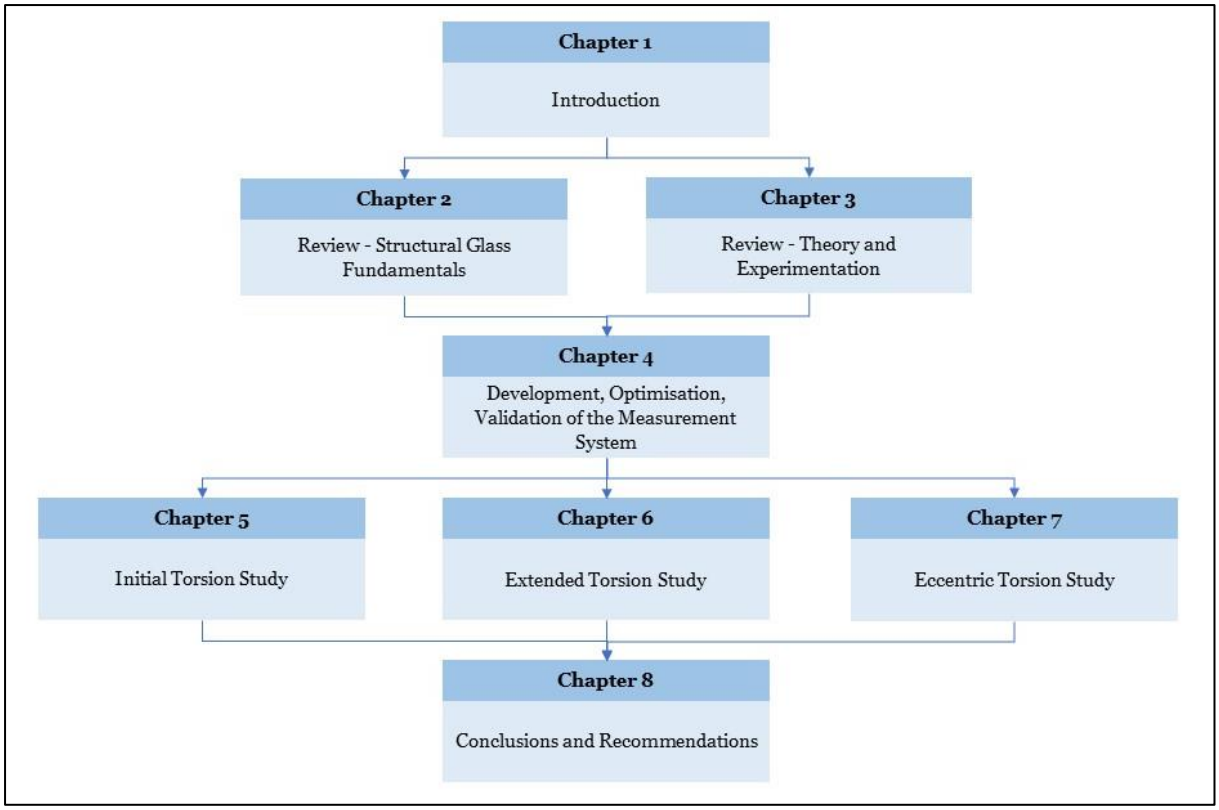

Figure 1-5: Organisation of the Thesis.

Chapter 2 introduces, in a non-exhaustive manner, the fundamental aspects of glass and structural glass. This chapter covers topics such as formation, production, physical properties, high-specification structural glass types and failure modes. While these were only basically covered, they intend to provide the information necessary to understand subsequent chapters.

Chapter 3 provides a more comprehensive review of literature that addresses the key topics and issues tackled in this research. This chapter begins by presenting the basic theories of linear and non-linear elasticity with relevance to glass structures. A detailed review of current experimental methods used to determine the relevant mechanical properties in glass and laminated glass elements is then presented, including the most important underpinning theories and analytical models behind these. The chapter also discusses the existing tools and methods for measuring stress-strain displacements in experiments – a necessity for determining many mechanical properties in structural members.

Chapter 4 presents the full development, optimisation, and verification of the binocular stereo-vision displacement measurement system that was employed in all subsequent experiments. Technical considerations and optimised setup are provided with reference to the required application. The methods and validation for calibrating the system using several metrics are presented. Additionally, a tailor-made experiment to prove measurement accuracy for the specific photogrammetric application is presented.

Chapter 5 presents the novel concept of the equivalent-sectional shear modulus (ESSM) method, which is used to quantify the torsional stiffness of two-layer PVB and SGP laminated structural glass beams through torsion experiments and digital photogrammetry. This chapter explains the setup and theory of the binocular-stereo photogrammetric system, including calibration and accuracy validation. Details of the materials and methods for the employed torsion test method are presented. The image and data processing in HALCON software including key algorithms and procedures are explained. Subsequently, the theory and torsional stiffness results of the ESSM method are presented and compared with calculated theoretical shear modulus values from existing models.

Continuing from the previous chapter, **Chapter 6** presents an extended torsion study by further applying the ESSM method to both additional two-layer, and three-layer laminated structural glass beams. This chapter employs the optimised photogrammetric system and validation methods described in **Chapter 4,** with several improvements to the experimental torsion approach employed in **Chapter 5,** such as enhanced equipment, precise methods of alignment for test samples and setup, and the introduction of inclinometer sensors for further comparison with the developed approach. A larger set of results are therefore presented in this chapter and subsequent conclusions are drawn.

Chapter 7 presents the first-of-its-kind eccentric torque experimental study on laminated structural glass beams. The term ‘eccentric torque’ in this study refers to the eccentric load path enforced in torsion experiments by clamping beam samples off their central plane. The use of laser-levelling and ruled markings on the clamping system detailed in **Chapter 6** are employed to

enforce the eccentric load path. Monolithic, two-, and three-layer laminated glass beams are experimentally studied under eccentric torsional load. The ESSM method was employed to determine the torsional stiffness of beam samples and compared to results from centrally loaded torsion experiments.

Chapter 8 summarises the work undertaken, the primary findings and the most significant conclusions. Finally, the key areas for further work are identified.

2. Structural Glass Fundamentals

This chapter introduces, in a non-exhaustive manner, the fundamental aspects of glass and structural glass. Topics such as formation, production, physical properties, high-specification structural glass types and failure modes are presented. While these are only basically covered, they intend to provide the information necessary to understand subsequent chapters.

2.1 Production

2.1.1 Natural Formation and History

Natural glass has existed for millions of years. It is formed when rocks firstly melt due to phenomena causing extremely high temperatures such as volcanic eruptions, lightning strikes, or meteorite impacts, then cool and solidify quickly enough for the liquid-like structure to freeze in a glassy state. This happens at a range of temperatures that depend on thermal history. Most natural glasses are obsidian – an igneous rock with a high silica content. This is said to have existed on earth for over 40 million years, demonstrating its resistance against devitrification and water corrosion. Natural glasses may form under three conditions [2];

- Magmatic formation, where silicate melt is expelled by volcanic activity and cools at a rate of 1°C per minute to 1°C per month.
- Metamorphic formation, where rapid ($\leq$ 1°C per second) heating and cooling of rocks and melts occur during impact, friction, or lightning strikes.
- Sedimentary formation, where accumulation of silica gel forms after drying over many years.

The earliest man-made objects using natural obsidian glass are documented back thousands of years, and this has carried through to modern times. Obsidian itself has been used for hunting tools such as blades and arrowheads, plates, and decorative objects. Examples can be observed in and . Most ancient man-made glasses have been discovered in Egyptian tombs, with non-transparent glass beads and other decorative objects thought to date back to 3500 BC. The first ancient glass workshop and factory were in use by 1500 BC and 1250 BC, respectively, with both situated in Egypt. The first glassmaking manual dates to around 650 BC [2, 3]. Glass foils were also produced around this time which may have been used for early windows.

The glassblowing method was invented by 50 BC in Syria, which enabled the glassmaker to control the thickness and shape of the glass and prevent thinning and rupture of uneven areas. Advancements in glassblowing first came in the form of blowing inside moulds allowing for greater variety of glass specimens. The first formation of flat glass came when long cylinders could be produced by this method, which were annealed at a relevant temperature, placed on a rock slab and flattened [2]. This method was used and improved over time until the 19th century and is still used today to produce coloured stained glass. The Romans were the first to develop clear glass in large enough quantities to be used in windows. Only highly prestigious property owners had these due to manufacture and installation being complex at this time.

The first British glass industry dates to around 680 AD in Northwest England. Lead glass was invented by George Ravenscroft in the 1670's and the British Plate Glass Company formed in 1773. The first American glass pressing machine was patented in 1825 [3]. Advancements in structural engineering proceeded to make larger window openings possible for all types of buildings, as prior to this, large windows were mostly found in cathedrals. This was a driving force for glass science to produce larger and better-quality panes of glass, where several methods and machine-based advancements automated the glassmaking process for both curved and flat glass panes over the 19th and 20th centuries.

Figure 2-1: Native American Indian arrowhead (www.icollector.com).

Figure 2-2: Globular jar of King Merneferre Aya (www.metmuseum.org).

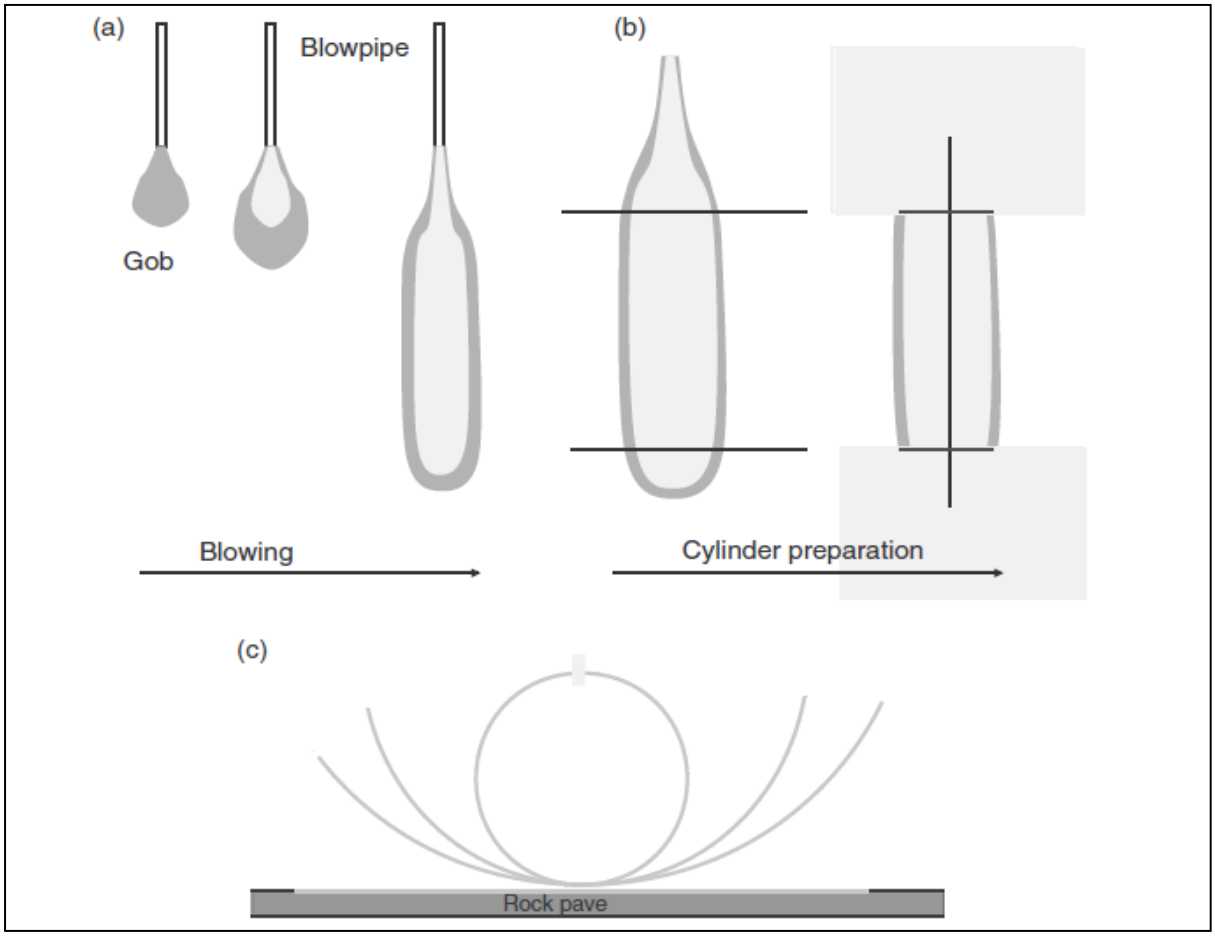

Figure 2-3: Glassblowing method; (a) blowing, (b) cutting and (c) flattening [2].

2.1.2 Flat Glass Production

The production of flat sheets of glass today is mostly performed using the float process, as developed by the Pilkington Brothers in 1959. This resulted from the need for a more cost-effective means to create flat glass for the automotive and architectural industries, as methods prior to this created glass with irregular surfaces that required a significant amount of post-processing for such applications [1, 4]. The float process came with significant advantages such as low cost, high availability and much improved optical and shape qualities [5, 6]. Combined with glass strengthening technologies and computer-based structural analysis methods, the float process has been a key driver in the use of glass in buildings and structural members. Around 90% of today's flat glass production worldwide is made using the float process [5, 6], and 80 - 85% of that is used in the construction industry [1].

In the float process, the chemical ingredients, which include silica sand, soda ash, limestone, and salt cake, are blended with cullet (recycled broken glass) and heated in a furnace to around 1500-1600°C to form molten glass. The molten glass is then fed onto the top of a molten tin bath. While there, controlled heating allows the glass to flow and form a flat ribbon of uniform thickness. At the end of the tin bath, the glass is slowly cooled and fed into the annealing lehr for further controlled gradual cooling. Changing the speed at which the glass ribbon moves into the annealing lehr varies the thickness of the flat glass sheets. To finish production, glass edges are trimmed to give a constant width to the emerging sheet, which is usually cut into jumbo sheets of 3 x 6m [1, 3]. This creates the type of glass commonly referred to as annealed glass. The annealing process induces an even stress distribution across the glass unit preventing any part of the glass coming under tension, where it is weaker in nature.

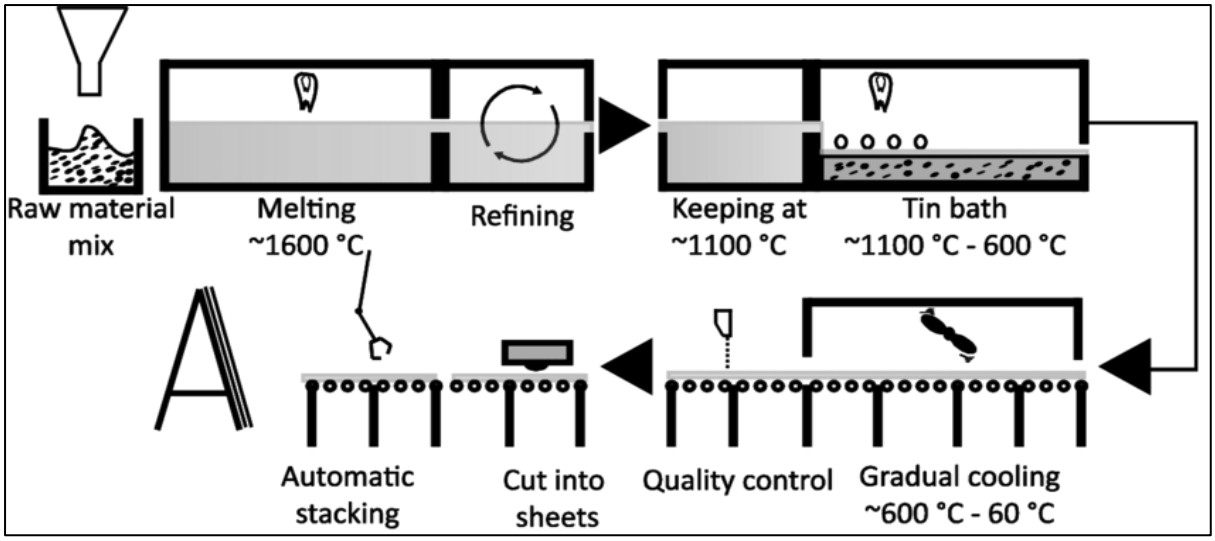

Figure 2-4: Float process [1].

Table 2-1: Stages of glass transition [2].

Temperature (°C)	State	Viscosity (Poiseuille – dPA s)
1500	Melting temperature	1-10
1040	Working point	10^3
720	Littleton softening point	$10^{6.6}$
540	Annealing point	10^{12}
530	Glass transition	$10^{12} – 10^{12.5}$
490	Strain point	$10^{13.5}$
20	Room temperature	10^{20}

2.2 Material Properties

2.2.1 Classification and Chemical Composition

Glass is generally described as a liquid that has cooled to a rigid condition without crystallising. It is not a super-cooled liquid, but an inorganic solid with an amorphous non-crystalline structure. Glass therefore refers to all non-crystalline solids showing a glass transition [2, 5, 6]. When studying engineering materials, a conventional method is to classify them into the following six classes, with members of each class having similar properties and forming processes [7]:

- Metals
- Polymers
- Elastomers
- Ceramics
- Glasses
- Hybrids

In terms of material classification based on their inherent properties, glass is similarly placed to ceramics [7] as several of their behaviours are similar. Like metals, glasses have high moduli. They are unique however as the non-crystalline structure suppresses plasticity, meaning they are hard, brittle, vulnerable to stress concentrations and do not yield thus have no plastic region of failure (Figure 2-6). Hybrids (or composites) are engineered elements that combine two or more materials to extract the beneficial properties of other material classes while mitigating some of their downsides. This description relates to sandwich structures and is relevant for laminated glass, which is described later in this chapter.

Structural glass is most commonly of the soda-lime silica type. This is the least expensive type of glass, whilst having high workability and chemical stability. Great improvements in quality were achieved by changes to the raw materials over time, until synthetic materials could be produced [4]. For example, Saint Gobain's addition of up to 6% of lime increased moisture resistance, and Schott's addition of a small percentage of alumina improved chemical and devitrification resistance [2]. The fabrication and automated manufacture methods are highly efficient therefore it is easily produced in high quantities and to very high quality. Another common type of glass is borosilicate, which includes boron-oxide in its fabrication. The boron-oxide addition provides high resistance to thermal shock and a lower coefficient of thermal expansion compared to common soda-lime silica glasses. Borosilicate glass is more difficult and costly to

manufacture than soda-lime silica glass, so it is reserved for some special structural applications such as fire and heat-resistant glazing. Further uses include optical and curved glasses, aircraft exterior lenses, chemical laboratory glassware and household cookware. The chemical constituents of soda-lime silica and borosilicate glasses are presented in Table 2-2 for comparison.

Table 2-2: Magnitude of the proportions by mass of the constituents of soda-lime silica and borosilicate glass (BS EN 572-1:2004, BS EN 1748-1-1:2004).

Constituent		**Soda-lime silica glass**	**Borosilicate glass**
Silica sand	SiO_2	69 – 74%	70 – 87%
Lime (calcium oxide)	CaO	5 – 14%	–
Soda	Na_2O	10 – 16%	0 – 8%
Boron-oxide	B_2O_3	–	7 – 15%
Potassium oxide	K_20	–	0 – 8%
Magnesia	MgO	0 – 6%	–
Alumina	Al_2O_3	0 – 3%	0 – 8%
others		0 – 5%	0 – 8%

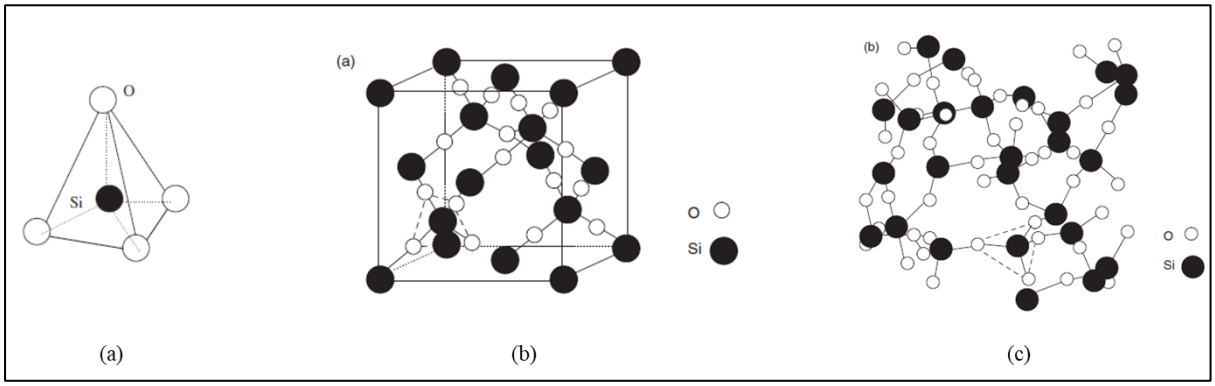

Figure 2-5: Si elemental tetrahedron (a), SiO_2 crystal structure (b), SiO_2 glassy structure (c) [2].

Glass is also unique in its chemical bonding structure. The glass structure is out of equilibrium as it is obtained when a liquid is cooled in a manner that when passing melting temperature, freezing happens instead of crystallisation. The final temperature is so low that the molecules or atoms move too slowly to rearrange into a stable crystalline structure [2]. In silica glass the silicon (Si) bonds to four different oxygen atoms, forming the SiO_2 tetrahedral structure

(Figure 2-5). Differences in glass chemical composition play a significant role in the viscosity, melting temperature and coefficient of thermal expansion.

2.2.2 Physical Properties and Behaviour

Some of the relevant physical properties and characteristics of soda-lime silica glass are presented in Table 2-3. Glass is one of the few solid materials that transmits visible light. The high transparency due to optical properties have made glass a highly sought-after structural material by architects and sustainable building designers. This brings benefits to the occupied structure extending further than aesthetics, such as passive solar light and heat gain - the same principle as the 'greenhouse effect'. The average refractive index n measures a ray of light as it travels from one medium to another, is determined by the ratio between the speed of light in a vacuum and the lower velocity of light as it travels through the glass material. On average for soda lime silica glass n = 1.5 which results in roughly 4% reflection of visual light per surface, giving a total of 8% per pane [5, 6]. This is determined by the ratio between the speed of light in a vacuum and the lower velocity of light as it travels through the glass material. These properties can be modified and improved as required by modifying the glass thickness, proportion of chemical constituents and the type of coating used.

Table 2-3: Physical properties and characteristics of basic soda-lime silica glass (BS EN 572-1:2004).

Characteristic	Symbol	Unit and numerical value
Density (at 18 °C)	ρ	2500 kg/m^3
Hardness (Knoop)	$HK_{0,1/20}$	6 GPa
Young's modulus	E	70,000 MPa
Poisson's ratio	ν	0.2-0.24
Coefficient of thermal expansion	α	9 10^{-6} K^{-1}
Specific thermal capacity	C_p	720 J kg^{-1} K^{-1}
Thermal conductivity	λ	1 W m^{-1} K^{-1}
Average refractive index	n	1.5
Emissivity	ε	0.837

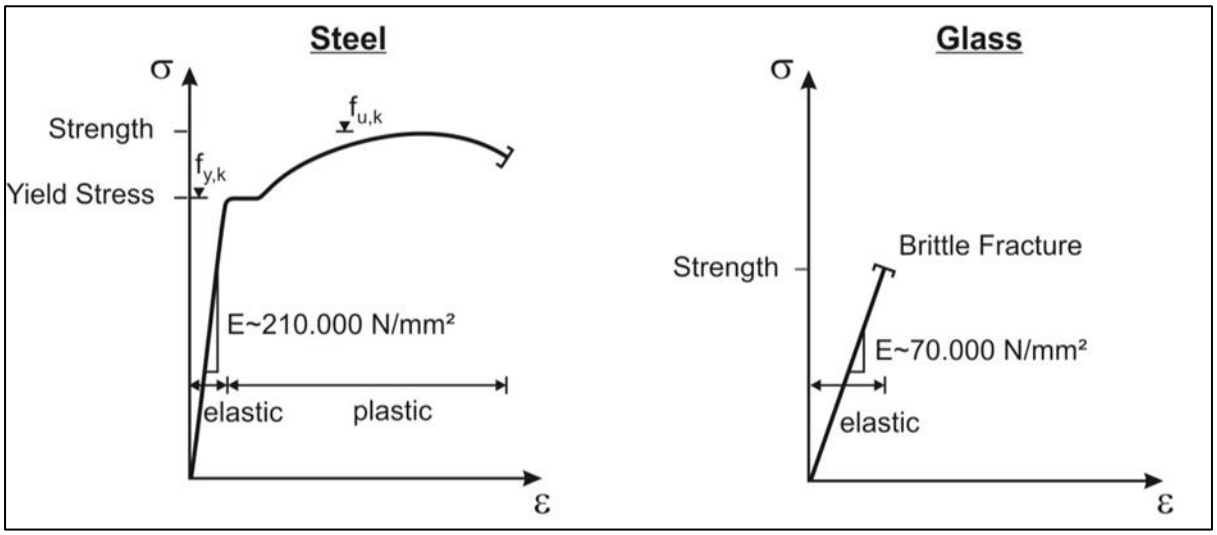

Figure 2-6: Stress-strain behaviour of glass vs steel [8].

As per Orowans rupture criterion, soda-lime silica glasses have extremely high theoretical strength (up to 21 *GPa*), when they are examined simply from the atomic bonding [9]:

$$\sigma_{th} = \sqrt{\frac{E\zeta}{r_0}}, \tag{2.1}$$

where σ_{th} is the theoretical cleavage strength, E is the Young's Modulus (70 *GPa*), ζ is the surface energy (0.4 - 1 $J\,m^{-2}$) and r_0 is the interatomic spacing (0.15 *nm*). The practical strength however is significantly lower than the theoretical strength. Glass is heavily affected by microscopic factors such as surface defects, stress concentrations and its own structure, as well as macroscopic factors such as panel size, load rate and surface condition, all of which lower the practical strength. Experiments were carried out in accordance with BS EN 1288-2 on 740 identical 6mm annealed glass samples at nine European factories [3]. The breakage stress was on average found to be roughly 0.5% of the theoretical strength. The results also revealed that the coefficient of variation of strength is around 25% higher than that of more common structural materials such as steel or concrete.

The high variance and unpredictability of glass breakage stress is primarily due to the propagation of surface cracks due to stress concentrations. The earliest study on stresses around elliptical holes was performed by C.E. Inglis [10], where he derived a generally applicable linear-elastic solution to determine these. The pioneering work of A. A Griffith [11] resulted from a limitation in Inglis method – in the case of a perfectly sharp crack, stresses approach infinity at the crack tip meaning materials would in theory have near zero strength even against very small loads. Griffith postulated that low strengths were related to pre-existing defects which harboured stress concentrations. He performed the first energy-based analysis of glass fracture in 1920 founding the field of fracture mechanics. Many other materials exhibit some inherent resistance against crack propagation through grain or fibre interactions, and crack tip shielding may occur by phase transformation or micro-cracking. Glass, however, does not exhibit these behaviours.

With the presence of cracks and surface flaws on the glass surface there are several other factors that can exacerbate the issue. The sample size of glass factors into the practical strength, as in larger samples there is a higher chance of surface defects being present. It only requires tensile stress to reach a critical value at one crack tip to cause full rupture of the entire sample. Strength in glass is also affected by the load rate – with longer load durations incurring greater loss of strength as surface flaws grow with time when loaded [11]. This can be explained by increased moisture levels causing stress corrosion, as water vapour forms alkali solutions which attack the silica network. Basically, water vapour initiates corrosion at crack tips, then the crack tips sharpen leading to greater stress concentrations and thus greater chance of failure. The more time spent under tensile stress, the more time available for stress corrosion to occur. The compressive strength of glass is significantly greater than in tension, and compressive stress does not result in crack propagation or failure. Glass structural members are mostly thin and slender in nature and fail due to buckling (e.g., the lateral-torsional buckling mode explained in Chapter 3), where tensile stresses develop, and the critical tensile load is reached much faster than the critical compressive load. Another factor that may reduce the strength of glass is the presence of ceramic inks in printed

glasses, which are weaker than unprinted glasses. This effect propagates if there are more than one ink on top of each other.

These conditions pose challenges in the fabrication, delivery, handling, and erection of structural glass members, as care must be taken to prevent any edge and surface damage that may weaken the glass. The means of connecting glass members is also a core design component, as engineers cannot ignore stress concentrations unlike when designing with steel. Point fixings are widely applied in glass structures such as façade and roof panels, by means of drilled holes, clamping, embedded connections or adhesive connections. In clamped systems, stress concentrations are of concern as a local load is being applied. Bolt holes expectedly serve as structural weak points. Thermal pre-stressing is also an issue at bore hole locations, the degree to which depends on the level of pre-stress and the hole shape [8]. Point fixings are commonly made of stainless steel, and all direct steel-to-glass contact must be avoided. Protection to the glass surface from points of contact can be achieved to a certain degree through rubber, plastic, or aluminium bushes. Adhesive bonding is an advantageous alternative method to holed connections, as these limit damage to the glass and stress concentrations from drilling. The load is also spread over a wider surface area, reducing localised stresses. There is still a hesitancy in use however, as less information on the long-term performance and performance under different environmental conditions of adhesive connections is available. Several studies [12-16] have begun to address this, however. A modern innovative solution involving embedded systems within laminated glass beam and fin interlayers brings many improvements to glass connectivity. Current systems incorporate metallic fittings into laminated glass, improving the distribution of applied loading between connected glass components and the laminate, which increases load bearing capacity and reduces the thickness of glass required. At present, many of these solutions are highly specialised, patent protected and come with high cost. Again, however, researchers are actively studying this area [17-20].

Another important physical characteristic of glass is its high flexibility. This may be advantageous in some ways; however, it is also something that must be carefully considered in a

structural context. Although glass can elastically deform to a great degree without any permanent change of shape, there are acceptable limits of deflection that structural glass members must adhere to. A main reason for this is fear of the occupant – the average person does not take well to the idea they are in a structure that visibly deforms. The pre-normative glass design document [8] and existing glass design standards have limits for several scenarios of glass, mostly relating to how they are supported. Some of these are presented in Table 2-4.

Table 2-4: Design limits for deflection of structural glass by code.

Document	Deflection limit	Condition
BS 6262	L/125 (single), L/175 (insulated)	Allowable deflections of edges for 4 edge full supported glass
BS 5516	Single, (S^2*1000)/180 or 50mm (less of)	2 edge supported glass, where S=span (m) between supports
BS 5516	IGU, (S^2*1000)/540 or 20mm (less of)	2 edge supported glass, where S=span (m) between supports
ASTM E-1300-04	19mm	Deflection of supported edges less than L/175, L=length
AS1288-94	L/60	Deflection of unframed toughened glass, L=length

Figure 2-7: Glass point-fixing with modern adhesive [13].

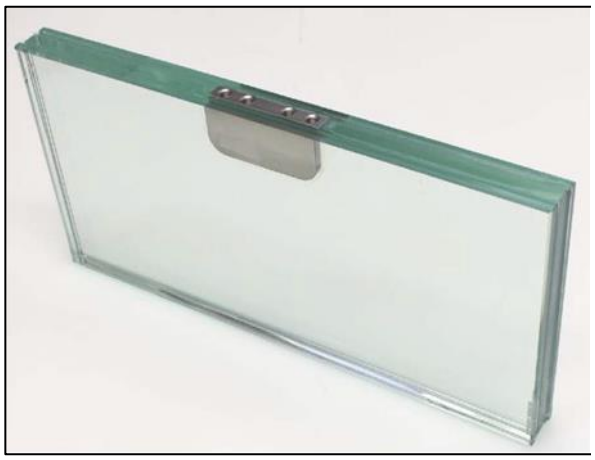

Figure 2-8: Embedded laminated connection [18].

As previously noted, annealed glass is entirely elastic in nature, with no plastic region of failure observed under applied stress before full rupture of the member. This means it can retain all its properties when loading subsides, so long as the glass is not fractured. However, this poses a significant issue in monolithic annealed glass structural members. Firstly, from their single-layered nature they will fracture instantaneously without any warning or post-failure redundancy - a vital characteristic when avoiding catastrophic failure in structures by repairing a visibly damaged member. Secondly, in the case of annealed glass this fracture occurs in the form of large, sharp shards, posing an additional danger in occupied structures (see Figure 2-9). This has traditionally made the engineer hesitant and overly cautious when designing glass structures. For this reason, monolithic annealed glass members are avoided in glass structures. Thankfully, innovations in glass processing have yielded high-strength structural glass types with properties in this regard.

2.3 Glass Processing and Strengthening

2.3.1 Popular Processing Methods

Glass is a highly workable material. After the main fabrication of flat glass takes place there are many secondary processing methods available that can modify and refine the glass unit for desired applications and properties. Some of the most popular methods and glass types are as follows:

- Edge cutting and finishing to remove edge damage and produce the desired size and shape of panels.
- Curving for applications such as curved glass structures.
- Drilling for connective holes.
- Coatings to modify glass properties such as transparency, heat and light transmission, and others.
- Surface modification for decoration, shading/tinting, privacy.

- Heat soaking to reduce the risk of nickel-sulphide failure (explained further in section 2.3.3).

- Thermal and chemical treatment to improve the strength and breakage characteristics, also known toughening or tempering (explained further in sections 2.3.2, 2.3.3).

- Lamination to produce composite glass members with enhanced properties (explained further in section 2.3.4).

- Insulating Glass Units (IGU's) – a multi-pane window with an internal gap filled with a noble gas, which can be configured to modify heat loss, solar gain and acoustic performance.

The methods most relevant to this research are described in more detail in subsequent sections. One glass type that is not covered in subsequent sections is chemically toughened glass. To briefly describe this method, annealed glass is dipped into an electrolysis bath which causes an exchange of sodium ions on the glass surface to potassium ions. This allows less deformation than thermal toughening methods and thinner sheets may be produced. The downsides are that the resultant panes are less robust, and the method is significantly more expensive than the methods covered. Another glass type not covered is wired glass, where embedded wires aim to act as reinforcements. These may provide some improved post-failure redundancy to the glass unit, but they also act as stress concentrations and promote crack growth.

2.3.2 Heat-Strengthened Glass

Heat-strengthened soda lime silica glass, also referred to as partially toughened or semi-tempered, is glass within which a permanent surface compressive stress, additionally to the basic mechanical strength, has been induced by a controlled heating and cooling process in order to give it increased resistance to mechanical and thermal stress and prescribed fracture characteristics [21, 22]. Basic annealed glass is heated to approximately 620 °C, then reheated to the same temperature and

quenched by jets of cooled air to cool and solidify the surface. As the interior cools it attempts to shrink applying tensile stress within, and in response increased compressive stress is induced on the surfaces, ranging from 30 N/mm^2 to 50N/mm^2 [8]. As the interior of glass does not contain flaws, it is safe to be subjected to this increase in tensile stresses. By the nature of heat-strengthened glass, it is not possible to obtain a glass pane as flat as with basic annealed glass. It is also not recommended to perform any cutting, drilling, edge working or surface finishing after the heat-strengthening process as the risk of breakage is increased and glass may be immediately destroyed [21, 22]. In the event of breakage, heat-strengthened soda lime silica glass fractures in a similar manner to annealed glass, therefore the same safety issues arise in structures using monolithic members. Heat-strengthened glass is however less susceptible to nickel-sulphide failure than toughened glass, and therefore it is unnecessary to perform heat soaking (section 2.3.3).

2.3.3 Toughened Glass

Toughened soda-lime silica glass may also be referred to as thermally toughened, tempered or fully tempered glass and also termed as thermally-toughened safety glass [3, 23]. For convenience, the term toughened glass will be used herein. The process, as described in BS EN 12150-1, is mostly the same as that of heat-strengthened glass. The main difference between toughened and heat-strengthened glass is that toughened glass is cooled more rapidly. This induces the same effect of cooling and solidifying the glass interior which causes it to shrink creating a tensile layer, causing the glass surface to be compressed and thus less likely to failure in tension. The induced stress profiles of heat strengthened, and toughened glass are displayed in Figure 2-10. This is more profound in toughened glass than heat-strengthened glass, however. In the UK and Europe surface compressive stresses generally range from 80 N/mm^2 and 150 N/mm^2 [3, 8], with the minimum requirement being at least 75 N/mm^2. The minimum requirement in the United States of America per ASTM C1048-18 is at least 69 N/mm^2 [24]. The characteristic bending strengths of basic annealed, heat-strengthened, and toughened glasses are presented in Table 2-5.

The glass toughening process may be done by either of three processes:

- The horizontal process, where glass is supported by horizontal rollers and transported through the toughening furnace
- The vertical process, where the glass is suspended by tongs
- The air cushion process in which the glass is supported by an air cushion with or without additional rollers.

The horizontal process is the most common method in current times, where previously the vertical process was used. Contact between the glass and horizontal rollers used in the toughening process can cause roller wave distortion to the glass pane [23], meaning that less 'flatness' in the final unit is achieved. BS EN 12150 also describes methods to measure these distortions.

The increased strength in bending of toughened glass is an obvious benefit. Arguably an even greater benefit is found in the fracture characteristics, which are directly related to the amount of surface compression induced by the thermal toughening process. In the case of failure, toughened glass fractures into numerous small pieces with blunt edges. This is due to a greater release of thermally induced stresses causing the fatal crack to progress rapidly, which bifurcates and causes complete and virtually instantaneous fragmentation. Provided any applied surface tensile stresses do not exceed the induced residual compressive stress, there will be no crack growth and thus no failure. Fragmentation tests to BS EN 12150-1 standard can determine whether the glass breaks in the described manner, and the amount of residual surface compressive stress present. These tests are impact based using a pointed steel tool which impacts an undrilled, holed or notched toughened glass pane, which is laid flat and unrestrained on a table, until breakage occurs [23]. Assessment of fragmentation is then performed where a minimum count, minimum size and shape of glass fragments must be met, and this can be used to estimate the surface compressive stress. A more precise approach for design purposes that is also used at the quality control stage is differential stress refractometry [3, 25] (DSR), which measures the twist of polarised light from the

thin surface of glass from which the surface stress can be determined. The fracture characteristics of toughened glass translate to enhanced safety in occupied structures as opposed to the breakage mode of annealed and heat-strengthened glasses. Measuring the residual surface compressive stress in toughened glass before structural application is crucially important to prevent failure due to variations between assumedly alike glass members.

One concern of toughened glass that is negligible in basic annealed and heat-strengthened glasses is the effect of inclusions and impurities, most notably nickel sulphide. All glass can contain these impurities; however, nickel sulphide inclusions expand in size when heated over a prolonged period and may cause instantaneous fracture. It may be difficult to identify the cause of instantaneous fracture as being from nickel sulphide inclusions [26]. When fracture occurs through this mechanism it does so in large clumps, however upon impact with the ground these will fragment as toughened glass usually does. This is still relatively uncommon in toughened glass, however in certain applications such as in primary structural members or experimental settings where results reliability is vital it can be of relevance.

A treatment known as heat-soaking can be applied to significantly reduce the risk of nickel-sulphide failure. The heat-soaking process prematurely subjects the nickel sulphide inclusions to expansion. If the inclusions are great enough to cause failure at any time, they are most likely to fail at this stage, rather than failing when installed in a structure or during experimentation [3]. A risk analysis may be used to decide if heat-soaking is required for any individual project.

Table 2-5: Characteristic bending strengths of main glass types

Glass type	**Characteristic bending strength (N/mm^2)**
Annealed	45
Heat-strengthened	70
Toughened	120

Figure 2-9: Fracture of main glass types: annealed (left), tempered (centre), laminate (right) (www.brennancorp.com).

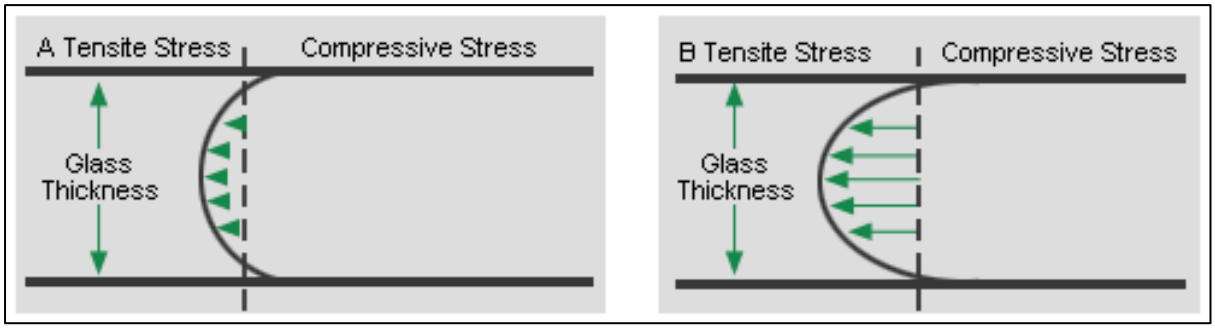

Figure 2-10: Induced stress profiles of heat strengthened glass (left) and toughened glass (right) (www.qdneoglass.com).

2.3.4 Laminated Glass

As discussed, engineers must achieve safety in glass structures to support the demand for highly transparent buildings. The instantaneous failure mechanism of annealed and toughened glass in monolithic form means these members are insufficient alone to provide the required redundancy. For this reason, the use of laminated glass is greatly preferred in load-bearing applications.

Laminating is the process in which two or more panes of glass are bonded by means of a viscoelastic interlayer (). This is beneficial in structures as in the case of breakage the interlayer serves to retain glass fragments, offering enhanced residual redundancy post failure and reducing the risk of injury due to falling glass, cutting or piercing [7]. In the case of framed laminated glass panels, however, there is a chance the broken panel may fall from the frame when mounted

horizontally if all glass panes are of the toughened type. As the interlayer is viscoelastic in nature it has both viscous and elastic characteristics. Shear flow and strain are resisted linearly when stress is applied (viscous), while time-dependent strain is exhibited when the interlayer is stretched, then returns to its original shape when loading subsides (elastic). The bonded glass panes making up the laminated structure can be either basic annealed or of a toughened type, or a combination of both depending on the application.

Understanding the behaviour of such composite glass-based structures is significantly different to monolithic members due to the high degree of variance in behaviour between the interlayer material and glass. There are seven established interlayer materials that are being used in laminated glass at present, split by common lamination methods, sheet and resin:

Sheet laminates

- Poly vinyl butyral (PVB), including modern variants like Saflex DG41 produced from plasticised PVB
- Ethyl vinyl acetate (EVA)
- Polyester (PET) when in a PVB-PET-PVB sandwich
- Ionoplast: most notably DuPont's SentryGlas (SG) / SentryGlas Plus (SGP)

Resin laminates

- Thermoplastic polyurethane (TPU)
- Other resins such as acrylic

Sheet laminating is performed by first assembling sheets of glass with an extruded interlayer between them, effectively creating a 'sandwich structure'. This sandwich is then passed through an oven heated to approximately 70 °C between a set of rollers that remove any excess air and bond the layers. The laminate is then heated in an autoclave to approximately 140 °C under a pressure of around 800 kN/m^2 in a vacuum bag [3]. Resin laminating is performed by bringing together glass sheets, which are set at a distance apart by double sided tape around the edges, then pouring the viscous resin between them. When all excess air has dissipated, the open edge is sealed, and the laminate unit is stored horizontally to cure. The curing process is done by means of chemical reaction or ultraviolet (UV) light. Laminated glass in structural applications today commonly use PVB or Ionoplast interlayers (SG/SGP) which are of polymer and ionomer type respectively. The interlayer thickness of these generally ranges from 0.38 mm to 6 mm, and usually comes in multiples of 0.38 mm [3]. Intumescent resin interlayers are noteworthy for fire protection applications, as in extreme heat these will turn to foam resisting the passage of fire and heat [27].

The elastic properties and therefore the shear moduli of these types of materials are affected by time-under-load and temperature, where their rigidity is reduced under higher temperatures and longer load durations. Additionally, the elastic properties of PVB and Ionoplast interlayers differ significantly to that of glass and from each other, which adds to the complexity of predicting laminated glass behaviours. PVB is effective at internally absorbing shear forces under short-term loading, however it is a soft polymer and will creep under long-term loads. This results in PVB laminates acting without much composite action, with loads being shared in proportion to their relative stiffness. The Ionomer based interlayers are significantly more resistant to creep due to both time and temperature effects. They begin with an initially higher stiffness than PVB, then proceed to retain this to a greater degree under higher temperatures and longer load-durations. The SG and SGP ionomer interlayers have shown to considerably have the greatest mechanical performance in glass laminates in [28, 29]. In an experimental setting PVB laminated glass beams have also shown that local delamination in the tensile zone near the crack origin is possible post-failure [28]. In some structural applications where risk to the occupant is low, generally, the PVB

interlayer can be sufficient as the main function of the interlayer is to maintain the glasses position and strength in the event of a pane rupturing, which PVB does albeit to a lesser degree. It is a very rare case for all panes in a laminate to break. Impact testing was performed on both PVB and SGP 2-layer laminates constrained in the form of a balustrade where both panes fracture show the SGP laminate maintains full integrity under heavy impact while PVB does not [30].

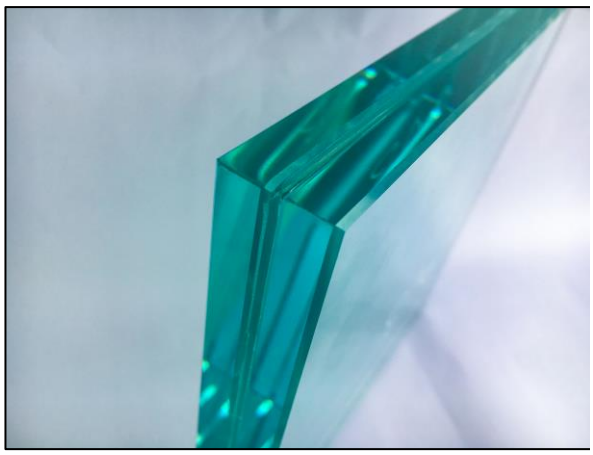

Figure 2-11: Toughened laminated glass (www.direct-glass.co.uk).

Figure 2-12: Fractured but not perforated laminated glass after hard body drop test [8].

3. Theory and Experimentation

This chapter provides a review of the current experimental approaches and their underpinning theories relevant to structural glass, and with a focus on glass beams. The basic theories of linear and non-linear elasticity are covered to provide background knowledge that can help understand the subsequent experimental and analytical approaches. The chapter also discusses the existing tools and methods for measuring stress-strain displacements in such experiments.

3.1 Linear and Non-Linear Elasticity of Glass

Glass is considered a homogeneous and isotropic material, therefore under small stress-strain deformations it will behave in a linearly elastic manner. Despite glass being considered an entirely elastic material it can exhibit plasticity under extreme compression and sharp contact, although in a structural context this is generally not a consideration. Various sizes and shapes of glass members, such as thin and slender beams, may endure larger deflections and combined deformation modes under applied loading and behave in a non-linear manner. In addition, the viscoelastic interlayer in glass laminates behaves very differently to that of the glass layers and adds to the non-linearity of these structures. An explanation of basic stress-strain theory, followed by linear and non-linear theories relevant to glass structures are first presented in coming sub-sections. Subsequently, the available experimental approaches for determining key elastic moduli in accordance with these theories are reviewed.

3.1.1 Elementary Stress-Strain Theory

The material response for linearly elastic behaviour can most basically be described by elementary stress-strain theory on an axially loaded straight tensile specimen [31] (Figure 3-1), such as a bar or rod. The stress measured in N-m^2 is defined as [31, 32]:

$$\sigma = \frac{F}{S}. \tag{3.1}$$

With F being the applied load on the cross-section S. In the tensile example, the specimen will extend under stress. The strain (or elongation) ε is a dimensionless measure and is defined by the difference between the change in length L of the specimen and the original length [31, 32]:

$$\varepsilon = \frac{\Delta L}{L}. \tag{3.2}$$

In a three-dimensional member three components of stress and strain are possible. This can be most basically described in a cubic shape (), where one surface x forms an orthonormal basis with y and z. When load F is applied to its surface area S, these components become [31, 32]:

$$F = F_x x + F_y y + F_z z. \tag{3.3}$$

And the three corresponding stress components are [31, 32]:

$$\sigma_{xx} = \frac{F_x}{S};\ \sigma_{xy} = \frac{F_y}{S};\ \sigma_{xz} = \frac{F_z}{S}. \tag{3.4}$$

With the other surfaces, their normal vectors y and z (the other surfaces have normal vectors -x, -y, -z), six other stress components can define the stress tensor [31, 32]:

$$\sigma = \begin{bmatrix} \sigma_{xx} & \sigma_{xy} & \sigma_{xz} \\ \sigma_{yx} & \sigma_{yy} & \sigma_{yz} \\ \sigma_{zx} & \sigma_{zy} & \sigma_{zz} \end{bmatrix}_{x,y,z} \tag{3.5}$$

The equilibrium of the moment of forces inducing the stress tensor is directly proportionate to the strain tensor as per Cauchy's Second Law; $\sigma_{ij}=\sigma_{ji}$. In a tensile or compressive test only σ_{xx}, σ_{yy} or σ_{zz} is not equal to zero. When only σ_{ij} for $i \neq j$ is not equal to zero this corresponds to pure shear, such as in a torsion test. Under stress, the surface with x as its normal vector can be subject to movement in x direction, with displacement as u_x, u_y, or u_z. Under the mode of small strain, the strain tensor is defined as [31, 32]:

$$\varepsilon = \begin{bmatrix} \varepsilon_{xx} & \varepsilon_{xy} & \varepsilon_{xz} \\ \varepsilon_{yx} & \varepsilon_{yy} & \varepsilon_{yz} \\ \varepsilon_{zx} & \varepsilon_{zy} & \varepsilon_{zz} \end{bmatrix}_{x,y,z} \tag{3.6}$$

Where [31, 32]:

$$\begin{aligned} \varepsilon_{ij} = \varepsilon_{ji} &= \frac{1}{2}\left(\frac{\mathrm{d}u_i}{\mathrm{d}x_j} + \frac{\mathrm{d}u_j}{\mathrm{d}x_i} \right) \rightarrow \varepsilon_{xy} \\ &= \varepsilon_{yx} = \frac{1}{2}\left(\frac{\mathrm{d}u_x}{\mathrm{d}y} + \frac{\mathrm{d}u_y}{\mathrm{d}x} \right). \end{aligned} \tag{3.7}$$

In the example of a straight member under tension, $\varepsilon_{xx} = du_x / dx$. The displacement is a linear function of x, with $u_x(x=0): \varepsilon_{xx} = u_x(L)/L = \dfrac{\Delta L}{L}$.

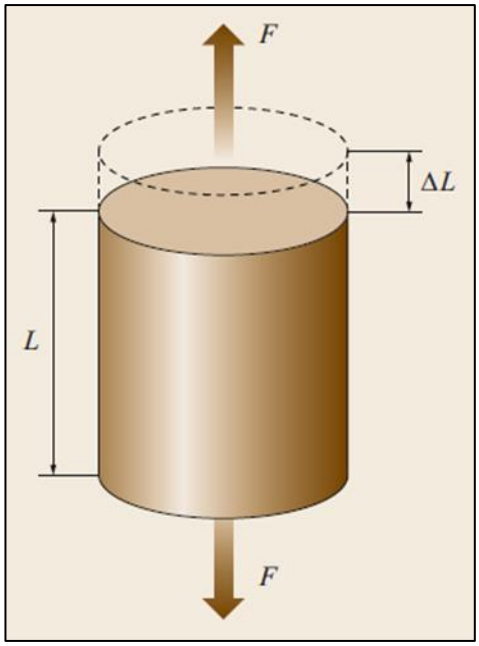

Figure 3-1: Tensile specimen [32].

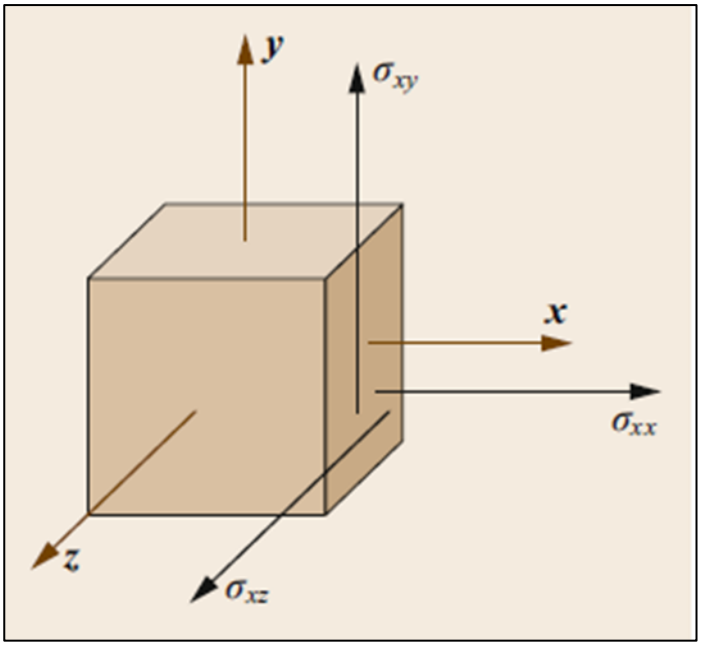

Figure 3-2: Three-dimensional cubic specimen [32].

3.1.2 Linear Elasticity of Glass

Glass behaves in a linearly elastic manner when only small stresses are applied, and small displacements are observed. Structural engineers are also more familiar with design and analysis to small deflection theory [8]. To properly explain the elasticity of glass, it is important to describe the elastic moduli. Six elastic moduli for glass and alike solid materials exist: the Young's Modulus (E), the Poisson's Ratio (ν), the Shear Modulus (G), the Bulk Modulus (K), Lamè's First Parameter (λ) and the P-wave Modulus (M).

The Young's Modulus, otherwise known as the Modulus of Elasticity, is the constant of proportionality from the stress-strain relationship, where the stress is directly proportionate to the strain. The Poisson's Ratio is a dimensionless measure resulting from the lateral strain occurring in the direction of loading in a member. The value of Poisson's Ratio is the negative of the ratio of transverse strain to axial strain. The Shear Modulus, which denotes rigidity, is a measure of the elastic shear stiffness of a material and is defined as the ratio of shear stress to shear strain. The Bulk Modulus measures the materials resistance to compression, defined by the infinitesimal

pressure increase to the resulting volume decrease. Lamè's First Parameter constitutes a parametrisation of the elastic moduli and is related to the Bulk Modulus and Shear Modulus (which is Lamè's Second Parameter). The P-wave Modulus describes seismic body pressure waves in a material by the ratio of axial stress to axial strain in a uniaxial state and occurs when expansion in a transverse direction is prevented by the inertia of neighbouring material [31].

The first three elastic moduli described - the Young's Modulus, Poisson's Ratio and Shear Modulus, best describe all the required elastic material responses for glass and laminated glass members in a structural context. When any two of these three moduli are known, the third can be determined.

In the linear-elastic case, the relationship between the stress and strain tensors are [31, 32]:

$$\varepsilon = \frac{1+\nu}{E}\sigma - \frac{\nu}{E} tr(\sigma)\mathbf{I} \tag{3.8}$$

where $tr(\sigma) = \sigma_{xx} + \sigma_{yy} + \sigma_{zz}$ and $\mathbf{I}$ is the identity tensor with its diagonal terms equal to one and all other terms equal to zero. According to Hooke's law [33], for a member in pure tension in x direction [31, 32]:

$$\sigma_{xx} = E\varepsilon_{xx}; \quad \varepsilon_{yy} = \varepsilon_{zz} = -\nu\varepsilon_{xx} \tag{3.9}$$

where all other strain components are zero. When a member is subjected to pure shear within the linear-elastic range; $\sigma_{xy} = \sigma_{yx} \neq 0$ with all other stress components equal to zero and $u_x = 0$, the shear stress is [31, 32]:

$$\sigma_{xy} = \frac{E}{1+\nu}\varepsilon_{xy} = \frac{E}{2(1+\nu)}\frac{\mathrm{d}u_y}{\mathrm{d}x}. \tag{3.10}$$

This shear stress results in a shear distortion angle γ, which under the linear-elastic framework is [31, 32]:

$$\tan\gamma \approx \lambda = \frac{\mathrm{d}u_y}{\mathrm{d}x}. \tag{3.11}$$

Once the Young's Modulus and Poisson's Ratio have been determined through a form of test, the Shear Modulus can be established from the following relationship [31, 32]:

$$G = \frac{E}{2(1+\nu)} \tag{3.12}$$

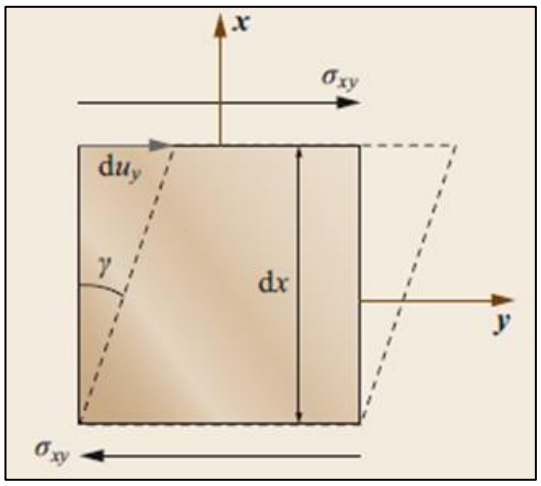

Figure 3-3: Shear stress and induced distortion angle [32].

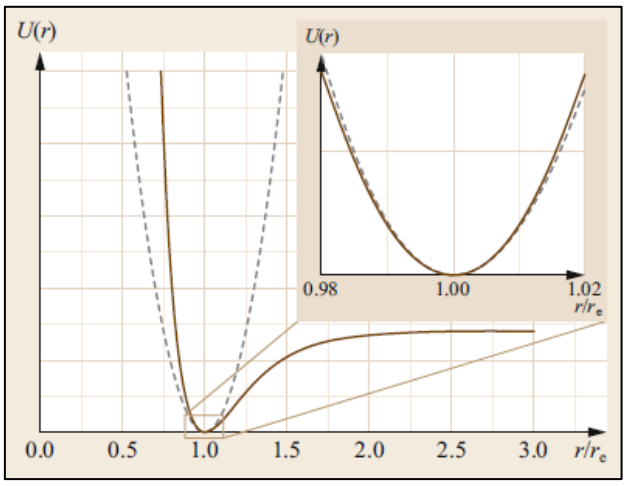

Figure 3-4: Interatomic Morse Potential (solid line) approximated around equilibrium position using Taylor Series (dashed line) [32].

3.1.3 Non-Linear Elasticity of Glass

Glass may also be subject to larger and combined deformations in a structural context due to its elastic properties, the slender nature of many structural glass members and the loading conditions. By evaluating the interatomic potential, as proposed by Morse [34] (Figure 3-4), an understanding of whether the stress-strain relationship is linear or non-linear can be gained [31, 32]:

$$U(r) = U_0(1-\exp[-a(r-r_e)])^2, \tag{3.13}$$

where U_0 is the energy dissociation, r is the interatomic distance, and r_e is the interatomic distance at rest (no applied load). Now U can be approximated around r_e using the second order Taylor Series [31, 32]:

$$U(r) = U_0 a^2 (r - r_e)^2. \tag{3.14}$$

The load F required to expand the interatomic distance is derived from $U(F = -\mathrm{d}U / \mathrm{d}r)$ and is a linear function of r, and only around r_e . Hooke's Law is only valid when the member undergoes a strain small enough to satisfy $((r - r_e) / r_e \ll 1.0)$. As glass can elastically deform to a large degree it inevitably undergoes situations of larger strain, exhibiting non-linear elasticity. This can be most basically described by 'true strain' in a straight bar, for example, with an actual length L which under tension undergoes an elongation $\mathrm{d}L$. The corresponding strain increment is [31, 32]:

$$d\varepsilon = \frac{\mathrm{d}L}{L}. \tag{3.15}$$

Then the true strain is given by [31, 32]:

$$\varepsilon \int_{L_0}^{L} d\varepsilon = \int_{L_0}^{L} \frac{dL}{L} = \ln\left(\frac{L}{L_0}\right), \tag{3.16}$$

With L_0 being the initial length of the bar at zero stress. Then the relationship between tensile stress and true strain in glass as proposed by Gupta and Kurkjian [35] is:

$$\sigma(\varepsilon) = E_0\varepsilon + \frac{E_1}{2}\varepsilon^2 + \frac{E_2}{6}\varepsilon^3 \tag{3.17}$$

Where E_0 is the conventional Young's Modulus, E_1 is the third-order Young's Modulus and E_2 is the fourth-order Young's Modulus. For soda-lime silica glass at room temperature, E_1 = 772 GPa and E_2 = -11 084 GPa [32]. In the non-linear framework according to (3.17) and the values of E_0, E_1, E_2, the curve of stress-true strain of soda-lime silica glass deviates from Hooke's Law by 1% and when the strain reaches 0.184% and the stress reaches 131 MPa. Shown in (Figure 3-4) is

the Young's Modulus decreasing as stress increases from the interatomic potential. In soda-lime silica glass however this is not the case as can be seen from the aforementioned *E* values. This is due to this glass type having a large free volume causing more irregular deformation modes under these conditions, as per Mallinder and Proctors observation [36].

3.2 Experimentation for Elastic Properties and Shear Modulus

3.2.1 Tensile Test

As discussed in (3.1.2), the determination of any two moduli from the Young's Modulus, Poisson's Ratio and Shear Modulus in theory allows the determination of the third. The tensile test method would appear to be a logical approach in this regard, as this experimentally applies Hooke's Law in equation (3.9) allowing measurement of E and ν, which can then be used to deduce the Shear Modulus *G* from the relationship in equation (3.12). To perform the tensile test, a sample with standardised geometry to fit tensile specimen profile [37, 38] (long, thin, slender, and can have round or rectangular cross-sections) is fixed to a universal tensile testing rig and subjected to quasi-static uniaxial load, which increases in magnitude until failure. The elongation is recorded as a function of tensile force. Several other parameters can be evaluated due to the destructive nature of these tests, as presented in Table 3-1.

The tensile test method is commonly applied to evaluate the strength and ductility of materials under uniaxial tensile stress [37]. Tensile testing is a well-established and popular method used for many materials; for example metallic materials [37, 38] including weld and connection strengths [39-42], rubbers and elastomers [43], carbon and graphite materials [44], plastics and hybrid polymer composites [45-49], and is also used to evaluate the strength of adhesive connections [50]. The tensile test method has several limitations for glass, however. This is not only for glass as a material in general, but also related to the common shape, size, and composite nature of structural and laminated glass members under their relevant loading scenarios. Codified approaches to tensile testing and experimental studies conducted by researchers are therefore

generally only applied to metallic-glass composites [51-53] and glass fibre-reinforced plastics [54, 55], which are less brittle in nature to pure glass, and to study the strength of glass adhesive connections [20].

In tensile tests, large stresses and strains must be applied to induce a large elongation of the specimen to achieve a low uncertainty measurement. Glass test samples are at high vulnerability under tension to surface flaws, so great care must be taken in sample preparation to ensure near-perfectly smooth surfaces to avoid failure even at low stresses. Additionally, the size of samples is greatly limited to only small samples in general. Practically, only linear and homogeneous stresses and strains can be studied through tensile testing. These factors neglect the non-linear deformation modes that many thin and slender glass members are subjected to, such as beams and fins subject to lateral-torsional buckling. Another key drawback of the tensile test is that they are destructive tests by nature [56], due to such large stresses being required to reach a high degree of certainty in measurement for the elastic moduli. As glass is entirely elastic in nature and the elastic moduli can be obtained without taking the sample to failure it is beneficial to reuse each sample for multiple tests, therefore alternative non-destructive test methods are preferred.

3.2.2 Compression Test

An alternative uniaxial stress test that can be applied is the compression test. Compression testing also has several codified approaches for different engineering materials and studies conducted by researchers [54, 57-60]. To perform the compression test, a rounded material sample is usually used, which is considerably thicker than a tensile sample ($diameter \geq 2 \cdot height$) [59]. This geometry is to avoid buckling under compression which occurs to slender members. The specimen is clamped between two pressure plates and compressively loaded under increasing force until failure. Compression testing can determine the same characteristic values as tensile testing, but naturally with stresses and strains occurring in the opposite direction (Table 3-1).

Table 3-1: Comparison of tensile and compression tests.

Parameter	Tensile Test	Compression Test
Nominal stress	Tensile stress σ	Compressive stress σ_c
Relative change in length	Strain ε	Compression εc
Flow limit	Yield strength σ_y	Compressive yield strength σ_{cy}
Alternative limits	0.2% offset yield strength $\sigma_{y\,0.2}$	0.2% compressive offset yield strength $\sigma_{cy\,0.2}$
Failure parameter	Tensile strength σ_u	Compressive strength σ_{cu}
Relative permanent change in length	Fracture strain A (elongation at fracture)	Fracture compression A_c (compression at fracture)
Relative permanent cross-sectional change	Reduction in area Z	Increase in area ψ

Compression tests are also not the most effective means to determine the elastic moduli of glass. The geometry of samples must be carefully considered. In long samples, buckling is an issue, which is why it is recommended for the samples diameter to be greater-or-equal-than twice its height [59]. In short samples barrelling occurs, where the sample forms conical stress zones that result in a bulging expansion toward the middle region. The outer face of the sample is then stretched due to this expansion inducing tensile stress which can cause premature fracture, especially where surface flaws are present. In glass and brittle materials, these conical stress regions form wedges into the surrounding material creating shear stresses, which reach their peak at 45° to the direction of compressive stress and therefore fracture in this direction. This effect complicates test results and should be minimised [59]. Like tensile tests, compression tests are also destructive in nature and therefore are not optimal for determining elastic and shear properties in glass, and particularly structural glass members.

Figure 3-5: ASTM E8 metal tensile testing machine (www.admet.com).

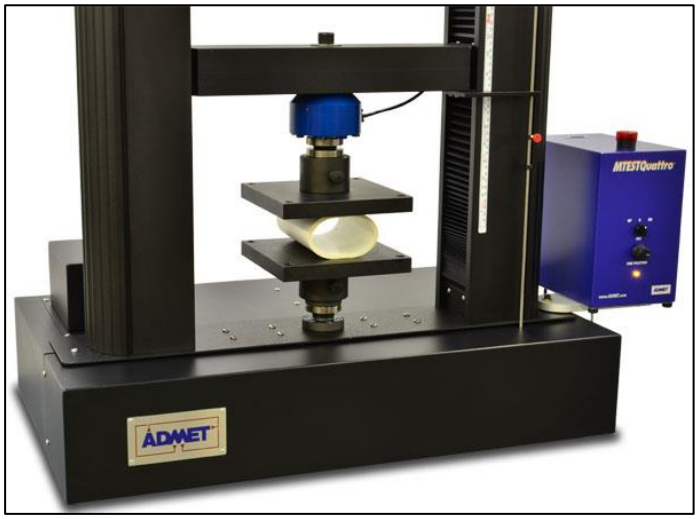

Figure 3-6: Compression testing machine applied to plastic pipe (www.admet.com).

3.2.3 Three-Point Beam Bending Test

The three-point bending test is a mechanical technique occasionally applied to measure the elastic behaviour of structural glass beams [61, 62]. In the ASTM standard [63] this is only applied in glass to viscosity and annealing point, however, and is less common for structural purposes. This method is performed by supporting a glass beam by two solid cylinders at its underside, with distance L between each other. A third cylinder is situated at the topside of the beam, and at the exact centre between the other two cylinders. A load F is applied through the central cylinder to

induce deflection *f* in the middle of the beam. The relationship between *f* and *F* is then deduced as [32]:

$$f = \frac{FL^3}{48EI_G}. \tag{3.18}$$

Where I_G is the second moment of area $(bh^3/12)$ when the beam has a rectangular cross-section with of height *h* and thickness *b*. The three-point beam bending test conforms with Euler-Bernoulli Beam Theory [64], therefore the beam length *L* must be $\geq$ ten times larger than the height and thickness.

One benefit of this to tensile or compression tests is that in samples with similar thin and slender geometry much larger displacements can be reached for an equivalent amount of stress. As mentioned, the geometry of the beam must be thin and slender, but the length must also not be so great that the deflection of the sample due to its own weight becomes negligible. The uncertainty in determining the Young's Modulus *E* is another limitation to the three-point beam bending method, as a large deflection must be achieved to obtain a low uncertainty measurement in this regard, therefore any surface flaws collected in the test sample can lead to premature fracture. Finally, and perhaps the most limiting factor in this method is that it is only able to determine the Young's Modulus. This is not comprehensive enough as a test for structural glass members, as other critical elastic moduli such as the Shear Modulus - which describes the rigidity of each structural member - cannot be determined.

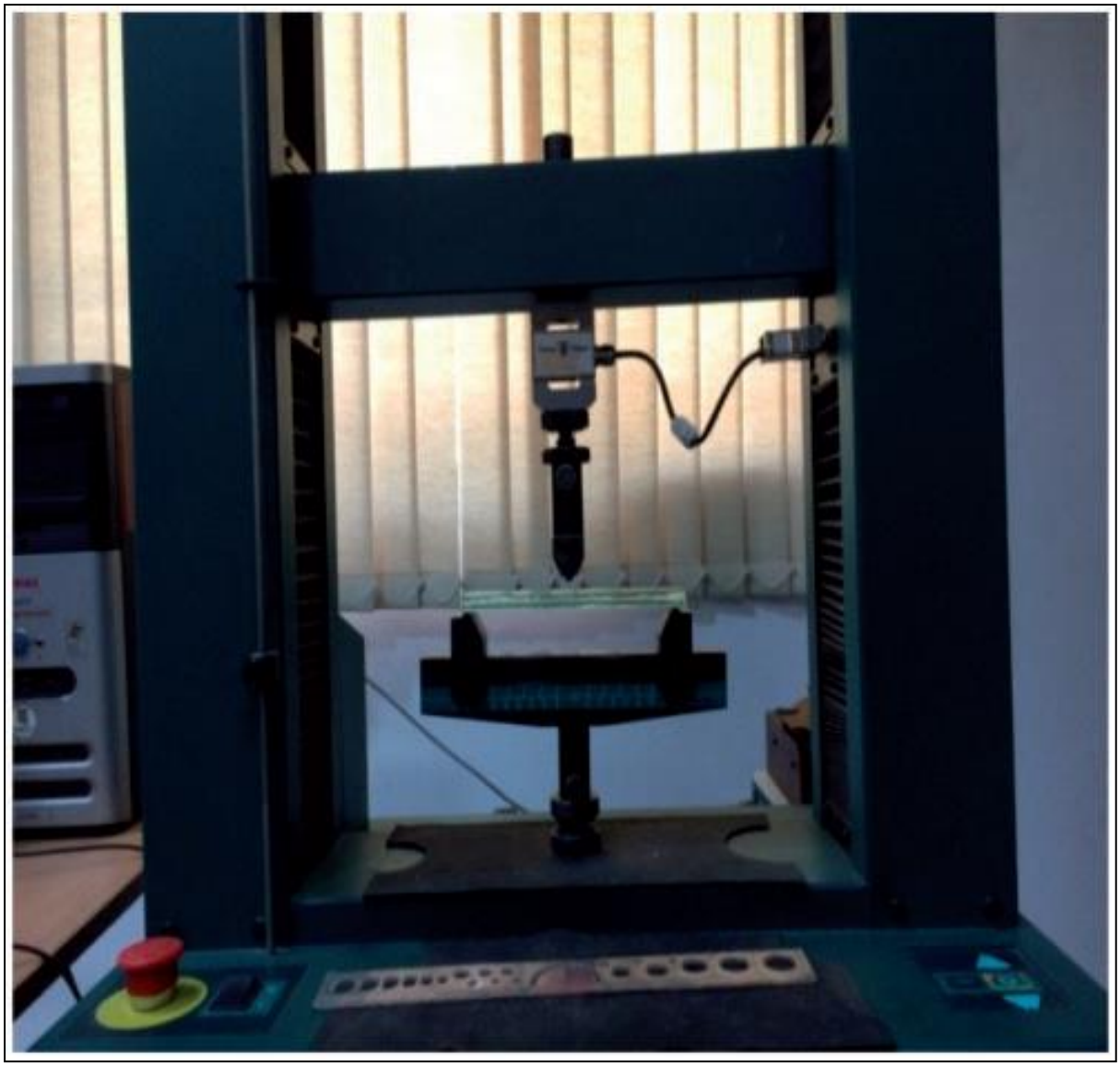

Figure 3-7: Three-point bending test on laminated glass sample [62].

3.2.4 Ultrasonic Measurement Test

Some alternative methods to basic mechanical testing have also been developed and applied to glass to obtain elastic moduli. A category of interest regarding these methods involves ultrasonic measurement techniques. As the strain tensor is derived only from displacement, and the stress tensor only from applied load, the load-displacement relationship can be derived under the assumption of linear-elastic theory irrespective of the mechanical loading and sample geometry. Ultrasonic testing involves the transmission of high frequency sound waves through a material

sample which interacts with its properties, reflecting or attenuating it. Sound velocities are usually measured using a pulse-echo technique or similar through-transmission technique and can be referred to as ultrasonic spectroscopy or echography [65, 66]. A pulse is produced at the surface of the sample using a piezoelectric transducer, typically at frequencies larger than a MHz. The pulse propagates through the sample to reach the opposite surface, parallel to the first surface, is partially reflected and goes back to the transducer, acting also as a receiver. By measuring the transit time of the pulse, thanks to the piezoelectric transducer, if the thickness is known the velocity is deduced. By using two separate transducers the longitudinal and shear waves can be measured.

By converting the load into its associated elastic displacement, Newtons second law becomes, when the displacement field is $\boldsymbol{u}(x,y,z,t) = u_x(x,t)\boldsymbol{x}$, and when gravity is neglected, as per the Navier-Lamé equation [32]:

$$(\lambda + 2G)\frac{\partial^2 u_x}{\partial x^2} = \rho\frac{\partial^2 u_x}{\partial t^2}, \tag{3.19}$$

Where $\lambda = \frac{E\nu}{(1-\nu-2\nu^2)}$. $(\lambda + 2G)$ is also known as the longitudinal modulus C_L. For a standing longitudinal wave [32]:

$$u_x(x,t) = A\cos\left(\frac{\omega}{\upsilon_L}x\right)\cos(\omega t), \tag{3.20}$$

where A is the maximum amplitude of displacement, ω is the pulsation of the wave, and υ_L is the velocity of the longitudinal wave form. Equation (3.19) gives [32]:

$$C_L = \rho\upsilon_L^2. \tag{3.21}$$

As per Newtons second law, the velocity always depends on the density which must be determined. Considering a standing transverse wave [32]:

$$u_y(x,t) = A\cos\left(\frac{\omega}{\upsilon_T}x\right)\cos(\omega t). \tag{3.22}$$

The corresponding Navier-Lamé equation gives [32]:

$$G\frac{\partial^2 u_y}{\partial t^2} = \rho\frac{\partial^2 u_y}{\partial t^2} \rightarrow G = \rho{\upsilon_T}^2, \tag{3.23}$$

where υ_T is the velocity of the transverse wave form. By measuring the longitudinal and transverse velocities two elastic moduli of C_L and G can be obtained, satisfying the requirement to make any other elastic moduli obtainable. The Young's Modulus can be derived from the ultrasonic measurement method by [32]:

$$E = \rho\frac{3{\upsilon_L}^2 - 4{\upsilon_T}^2}{\left(\frac{\upsilon_L}{\upsilon_T}\right)^2 - 1}. \tag{3.24}$$

Ultrasonic measurements are a non-destructive test method and therefore have this advantage over some mechanical tests for glass. Small samples are generally used – they are only required to be greater than the wavelength to propagate through the sample properly, which is short in correspondence with the short ultrasonic pulses used. All elastic moduli of glass can also be determined in theory using the ultrasonic measurement method for monolithic glass.

Ultrasonic measurements still have several limitations, however, when determining the key elastic and shear properties accurately in the context of structural glass members. At the wavelength scale, this method does not work when there is any non-homogeneity present, even slightly [32]. This rules out measuring the elastic and shear properties of monolithic glass with any internal defects (bubbles, crystals etc), unless only surface waves (Rayleigh waves) [67] are induced and measured by a piezoelectric transducer known as acoustic microscopy. Even in this case, laminated glass structures cannot be studied using this method. An additional limitation is that only miniscule

stresses can be produced, therefore the elastic and shear properties under non-linearly elastic behaviour as is common in glass structural members cannot be obtained.

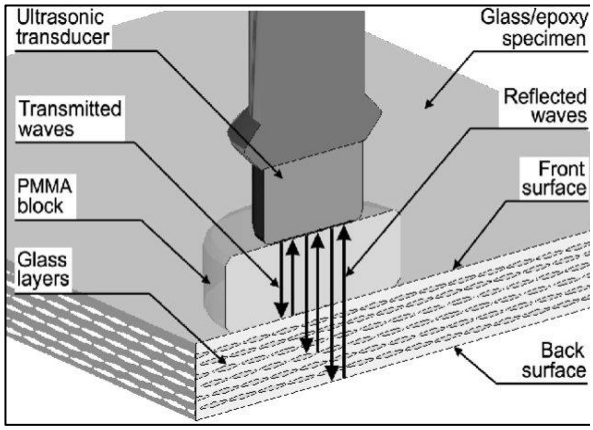

Figure 3-8: Ultrasonic testing pulse-echo technique [68].

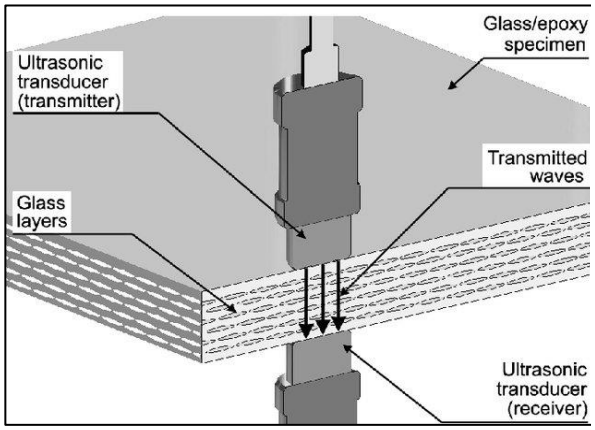

Figure 3-9: Through-transmission technique [68].

3.2.5 Resonance Test

Another non-mechanical test method that can be used to determine elastic and shear properties in glass is the resonance test. The resonance test method has been adopted in ASTM C623-92 [69] to determine the Young's Modulus, Shear Modulus and Poisson's Ratio in glasses and ceramics. This method uses an induced 'ringing' into the test sample causing vibrational frequencies, where the note produced is dependent on the sample geometry and physical properties such as the elastic moduli. In the case of a glass beam, three types of vibrational frequency can be measured in the beam: elongation, torsion and bending. In this codified approach, the Young's Modulus is measured from the bending mode of vibration, and the Shear Modulus is measured from the torsional mode. These are then used to compute the Poisson's Ratio giving these three key elastic moduli.

The induced vibration in the sample does not need to be great to disrupt its state of equilibrium and create extractable strains. This is generally performed using what is referred to as the Impulse Excitation Method [70], where a pneumatic gun fires a lightweight projectile at low speed into the glass sample. The 'ringing' sound is recorded by a sensitive microphone close to the

sample. A fast Fourier transform is used to extract the elongation, bending and torsional frequencies for calculation of their related elastic moduli.

Where the beam is free with no limited displacement at any point, the natural vibrational frequency for elongation in longitudinal direction is given by [32]:

$$f_i = \frac{i}{2L}\sqrt{\frac{E}{\rho}}, \qquad i \in \{1,2,3,....\}, \tag{3.25}$$

where *L* is the beam length, $i=1$ is the first mode, $i=2$ is the second. For the torsional vibration, the frequency is given by [32]:

$$f_i = \frac{i}{2L}\sqrt{\frac{G}{\rho}}, \qquad i \in \{1,2,3,...\}, \tag{3.26}$$

and finally, the bending vibrational frequency according to Euler-Bernoulli beam theory is given by [32]:

$$f_i = \frac{k_i^{\,2}}{2\pi}\sqrt{\frac{EI_G}{\rho S L^4}}, \qquad i \in \{1,2,3,...\}, \tag{3.27}$$

where *S* is the cross-sectional area of the beam face (*b*h*) and I_G is the second moment of area of the beam. k_i are values depending on the mode *i* which cannot be calculated analytically for a free beam (k_i is the $i-th$ solution of $\cos(x)\cosh(x)=1$), but have numerical values for the first four modes ($k_1 = 4.73004,\ k_2 = 7.8532,\ k_3 = 10.9956,\ k_4 = 14.1372$) [32].

The resonance method has flexibility with the geometry of samples, where rectangular beams, cylinders or disk-shaped samples can be used. In cylinders however it is difficult to induce torsional vibrations [32]. With relevance to rectangular beams as is present in glass structures, using equations (3.26) and (3.27) as per ASTM E1875-13 [71]:

$$E = 0.946415\frac{\rho f_1^{\,2} L^4}{h^2} T'_1 \tag{3.28}$$

$$G = 4\rho f_1^2 L^2 B, \tag{3.29}$$

where f_1 is the frequency of the first mode of bending vibrations (3.28) and torsional vibrations (3.29), and $T_1^{'}$ and B and are both correction factors that correspond to the sample geometry. The correction factor *B* for the determination of Shear Modulus is calculated, based on the sample geometry, by the following as per ASTM E1875-13 [71]:

$$B = \frac{\frac{b}{h} + \frac{h}{b}}{4\left(\frac{h}{b}\right) - 2.52\left(\frac{h}{b}\right)^2 + 0.21\left(\frac{h}{b}\right)^6}. \tag{3.30}$$

Differences in testing between flexural and torsional modes come in the mode of hanging the plate, the way it is struck and positioning of the accelerometer. For flexure the plate is hung on flexure node lines (Figure 3-10), accelerometer is placed centrally on its transverse axis and towards the edge and is struck lightly and elastically towards the opposite end of the accelerometer. For torsion (Figure 3-11) the plate is hung at midpoint of its length and width, accelerometer placed at 0.224*L* from one end and near the edge which is a nodal point of flexural vibration avoiding detection of a flexural mode, and it is struck diagonally [72].

In the context of basic material testing, the resonance method appears to be reasonable candidate for determining the elastic moduli E, G, ν in glass experimentally. Researchers have also recently applied the resonance method to laminated composite plates to measure these moduli [72, 73]. Like ultrasonic measurement methods the resonance test is also non-destructive in nature, which is advantageous, and is also applicable to various sample geometries (in small sizes). However, also like ultrasonic methods, only very small stresses can be applied which limits this to the linear-elastic framework, preventing proper analysis of these moduli under non-linear modes that slender glass beams are subjected to. This method also does not have any codified approaches for laminated glass, although there is a small amount of published research studying this in other composite materials [72, 73]. The main drawback appears to be the accountability of size- and

shape- effects in structural glass beams and recreating realistic stress scenarios for structural applications.

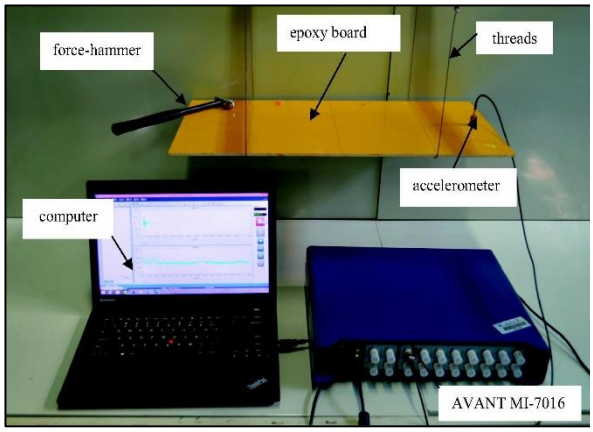

Figure 3-10: Experimental test setup of impulse excitation technique in flexural mode by Song *et al* [72].

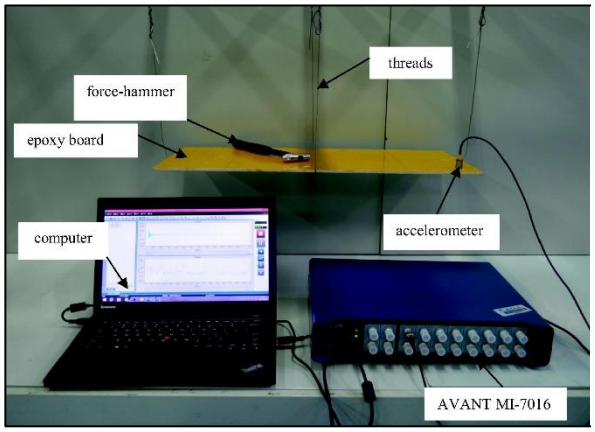

Figure 3-11: Experimental test setup of impulse excitation technique in torsional mode by Song *et al* [72].

3.2.6 Four-Point Beam Bending Test

Due to the high slenderness ratio of structural glass elements, one of the most important design considerations is in the lateral torsional buckling (LTB) phenomena. The four-point beam bending test is a method that induces this deformation mode, and thus has been a primary focus of research in the structural assessment of glass beams in recent years. Although no finalised testing standard for this method exists yet for glass, analytical models are presented in the pre-normative glass design code [8], and several studies have been conducted to assess the lateral-torsional bucking (LTB) failure mode in this regard [74-86].

In the LTB mode the glass beam is bent about the axis of largest flexural rigidity and may therefore buckle at a critical load value. The cross-section of a glass beam is thin, slender, and rectangular (Figure 3-14), so LTB design and analysis is crucial in beams without lateral restraints. The deformation of the beam in this mode can be described as a shape that is slightly deflected and twisted from the equilibrium, or in other words a combination of bending and torsion occur.

The methods of experimentation for four-point beam bending have some variants between researchers who wish to focus on specific effects alongside the LTB mode, such as time and temperature dependent behaviour, however the mechanical principle remains the same. The experimental procedure presented by Pesek and Melcher [83] can be referred to for a general understanding of this. The glass beam specimen is placed in a steel frame comprised of a girder and two columns. The loading force is generated by an electrically operated hydraulic press. Fork supports are situated at each end of the beam in the form of steel coulters, which are each equipped with a gusset plate containing a pin hole. A commonality in all mechanical experimentation on glass elements is that direct steel-to-glass contact must be avoided – in this case timber pads are applied. The beam is loaded by two concentrated loads situated symmetrically to the midspan at about one third distance, inducing four points of bending (Figure 3-12). Loading force is applied by one hydraulic press and is introduced by the balance arm and loading frames into two points. The test specimen sits on supporting blocks throughout the test. The measurements of loading force, vertical deflection and horizontal (lateral) deflections are taken by a force transducer and wire sensors respectively. This test is again generally destructive in nature and the author notes that all specimens were destroyed by brittle fracture.

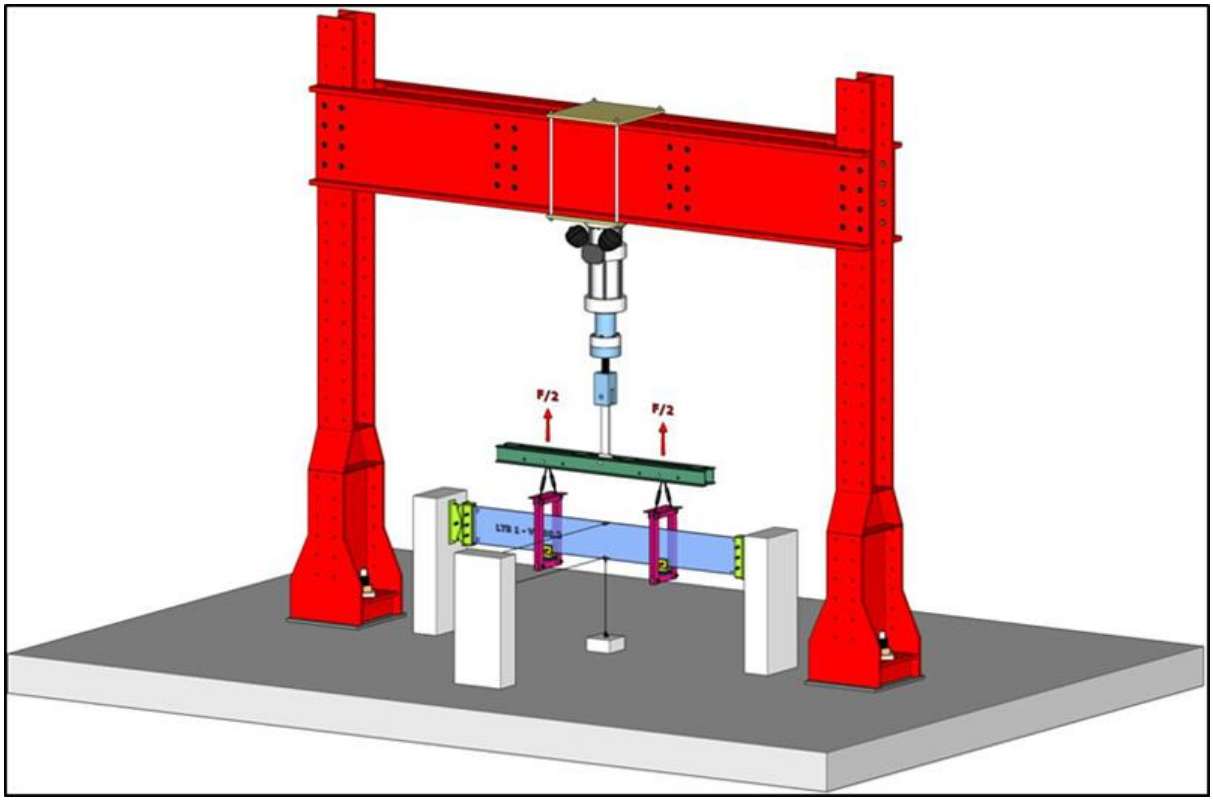

Figure 3-12: Four-point bending test setup by Pesek & Melcher [83].

In the pre-normative glass design code for monolithic sections, the elastic critical buckling moment M_{cr} for different loading scenarios, without further analytical derivations that may be based on equilibrium or energy approaches, are determined by [8]:

$$M_{cr} = \frac{\pi}{\ell}\sqrt{E \cdot I_z \cdot G \cdot I_t} \tag{3.31}$$

$$M_{cr} = \frac{1}{c_1} \cdot N_{ki}\left(\frac{1}{2}\frac{c_2}{c_1} \cdot z_p^M + \sqrt{\left(\frac{1}{2}\frac{c_2}{c_1} \cdot z_p^M\right)^2 + \frac{G \cdot I_t}{E \cdot I_z} \cdot \left(\frac{\ell}{\pi}\right)^2}\right) \tag{3.32}$$

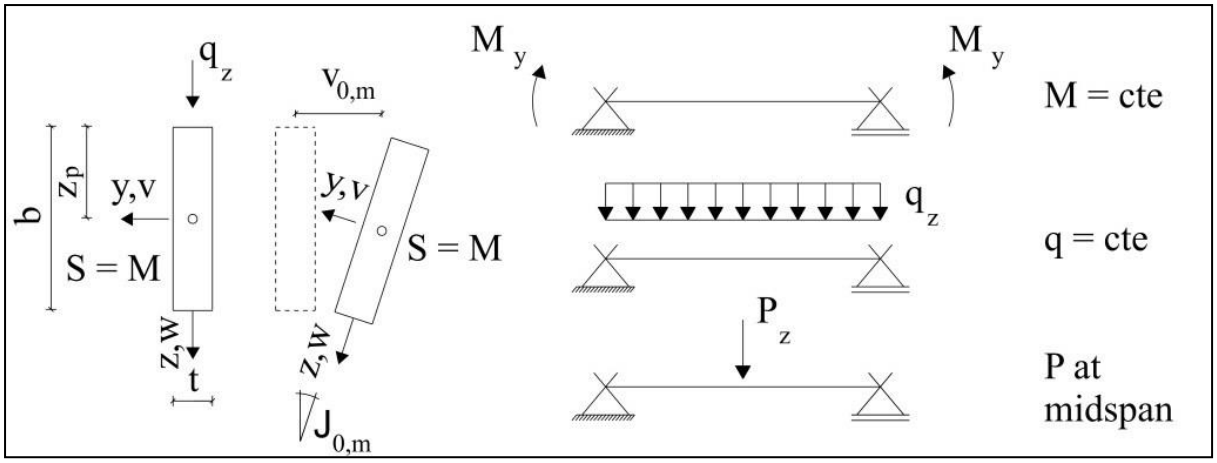

Figure 3-13: Loading scenarios for the LTB of monolithic glass beam sections [8].

where (3.31) describes the moments resulting from loading scenario $M_y = cte$, and (3.32) describes the moments resulting from loading scenarios $q_z = cte$ and P_z at midspan (Figure 3-13). The second moment of area about their respective axes are I_t and I_z.

For glass beams fully restrained along one edge of their length, appendix C of Australian code AS 1288 recommends [3, 87]:

$$M_{cr} = \frac{\left(\pi / L_{ay}\right)^2 \cdot \left(E \cdot I\right)_y \left[d^2/12 + y_0^2\right] + \left(G \cdot J\right)}{\left(2 \cdot y_0 + y_h\right)} \tag{3.33}$$

where L_{ay} is the distance between points of effective rigid rotational restraint, $(E \cdot I)_y$ is the effective rigidity for bending about the minor axis, $G \cdot J$ is the effective torsional rigidity, y_h is the location from the neutral axis of the loading point, which is sensitive in terms of direction of the applied load, and y_0 is the distance of restraint to the neutral axis of the loading element, which is also sensitive in terms of direction of applied load. For beams with intermediate restraints [3, 87]:

$$M_{cr} = \left(g_1 / L_{ay}\right)\left[\left(E \cdot I\right)_y \left(G \cdot J\right)\right]^{1/2} \tag{3.34}$$

where g_1 is the coefficient of slenderness and $(E \cdot I)_y$ is the stiffness of the beam in the minor axis. Finally for unrestrained beams, the code gives [3, 87]:

$$M_{cr} = \left(\frac{g_2}{L_{ay}}\right) \cdot \left[(E \cdot I)_y (G \cdot J)\right]^{1/2} \cdot \left[1 - g_3 \left(\frac{y_h}{L_{ay}}\right) \left[(E \cdot I)_y / (G \cdot J)\right]^{1/2}\right] \tag{3.35}$$

where g_2 and g_3 are slenderness factors based on the form of applied load and support conditions of the beam.

Further non-linear analysis is then required to determine non-linear behaviours such as flexural buckling. In monolithic sections an effective imperfection of $e_0 = L/400$ is noted in the pre-normative glass design code [8]. The consequent non-linear analysis can be performed by second order calculation or by buckling curves. The latter is the more popular and less time-consuming method and has been studied by several researchers in monolithic glass beams [75, 81, 82]. In this approach, by [8]:

$$\bar{\lambda}_{LT} = \sqrt{\frac{M_{cr}}{M_{el}}} \text{ where } M_{el} = \frac{t \cdot h^2}{b} \cdot f_t, M_{cr} \tag{3.36}$$

the verification format for LTB of monolithic glass beam sections becomes [8]:

$$\frac{M_{Ed}}{\chi(\bar{\lambda}_{LT}) \cdot M_{el,d}} \leq 1.0 \tag{3.37}$$

As most structural glass beams are of the laminated type, evaluating the LTB mode in these is a significantly more complex procedure, as considerations must be made for the sandwich effect, non-linear behaviours, as well as the temperature and time-dependent effects of viscoelastic interlayers. Therefore, laminated glass beams undergo both geometrically non-linear behaviour under the LTB mode, and materially non-linear behaviour due to the interlayer. Most of the theoretical non-linear analyses are conducted numerically, through finite element analysis.

Experimentally, several researchers have focused on the LTB mode in in laminated glass beams [76, 77, 81-84, 86] to build upon existing analytical and numerical information.

Initial approaches have considered a laminated glass beam as the sum of individual monolithic sections, ignoring the composite action of the interlayer. These traditional approaches are overly cautious and not economical, however, determining that critical load scenarios resulting in LTB failure are reached in a short period of time. Therefore, composite action must be studied to provide the most efficient design solutions.

Many of the recently developed analytical and numerical solutions build upon the approaches by Newmark [88], followed by Wölfel [89] and Bennison [90]. Newmark originally presented a simple analytical procedure which modelled a composite structure made of two beams with elastic interaction. This was originally developed for a steel-composite concrete bridge deck bonded by shear connectors. The model assumed that the shear connection is continuous, the permitted amount of slip is proportionate to the transmitted load, there is linear strain distribution in the slab, and the slab and beam will deflect at equal magnitude at all points along its length. The Wölfel-Bennison model for composite sandwich structures which provides a method to calculate the "effective thickness" of a monolithic beam with equivalent properties to a laminated glass beam is described by Galuppi and Royer-Carfagni [80]. The model was developed with focus on what would in effect be a two-layer laminated beam, as the two external layers are assumed to have high axial stiffness but negligible bending stiffness. The authors also express the difficulty in finding the original work by Wölfel in the literature, as it is rarely cited, and is written in German. This has also been verified by a search from the author herein. Work by Bennison is, however, available [90]. This analytical approach has since been built upon and expanded by Galuppi and Royer-Carfagni [78-80].

The pre-normative glass design code presents a model of calculative design for the LTB behaviour of laminated glass beams that allows for consideration of the time and temperature dependent stiffness of the interlayer. The approach also considers the warping effects of lamination influence. As the mode of LTB is a combination of lateral bending and torsional deformations,

these are both modelled individually for the moments resulting from each of the loading conditions $M_y = cte$, $q_z = cte$, and P_z at midspan. For the lateral deformations [8]:

$$v(x)^{Th.II} = \frac{\frac{G \cdot I_t}{E \cdot I_z} \cdot M_y \cdot \vartheta_0 + \frac{M_y^2}{E \cdot I_z} \cdot v_o}{G \cdot I_t \cdot \left(\frac{\pi}{\ell}\right)^2 - \frac{M_y^2}{E \cdot I_z}} \cdot \sin\left(\frac{\pi}{\ell} x\right) \tag{3.38}$$

$$v(x)^{Th.II} = \frac{c_1 \cdot \frac{G \cdot I_t}{E \cdot I_z} \cdot M_y \cdot \vartheta_0 + c_1^2 \frac{M_y^2}{E \cdot I_z} v_0}{G \cdot I_t \cdot \left(\frac{\pi}{\ell}\right)^2 - \frac{c_1^2 \cdot M_y^2}{E \cdot I_z} + c_2 \cdot M_y \cdot z_p \cdot \left(\frac{\pi}{\ell}\right)^2} \cdot \sin\left(\frac{\pi}{\ell} x\right) \tag{3.39}$$

where (3.38) describes the moments resulting from loading scenario $M_y = cte$, and (3.39) describes the moments resulting from loading scenarios $q_z = cte$ and P_z at mid span. For the non-linear rotations resulting in torsional deformation [8]:

$$\vartheta(x)^{Th.II} = \frac{\frac{M_y^2}{E \cdot I_z} \cdot \vartheta_0 + \left(\frac{\pi}{\ell}\right)^2 \cdot M_y \cdot v_0}{G \cdot I_t \cdot \left(\frac{\pi}{\ell}\right)^2 - \frac{M_y^2}{E \cdot I_z}} \cdot \sin\left(\frac{\pi}{\ell} x\right) \tag{3.40}$$

$$\vartheta(x)^{Th.II} = \frac{\vartheta_0 \left(\frac{c_1^2 \cdot M_y^2}{E \cdot I_z} - c_2 \cdot \left(\frac{\pi}{\ell}\right)^2 \cdot M_y \cdot z_p\right) + c_1 \cdot \left(\frac{\pi}{\ell}\right)^2 \cdot M_y \cdot v_0}{G \cdot I_t \cdot \left(\frac{\pi}{\ell}\right)^2 - \frac{c_1^2 \cdot M_y^2}{E \cdot I_z} + c_2 \cdot M_y \cdot z_p \cdot \left(\frac{\pi}{\ell}\right)^2} \cdot \sin\left(\frac{\pi}{\ell} x\right) \tag{3.41}$$

Table 3-2: Coefficients c_1 and c_2 [8].

	c_1	c_2
$q_z = cte$	$\frac{2}{3} + \frac{2}{\pi^2} = 0.8693$	$\frac{8}{\pi^2} = 0.8106$
P_z at midspan	$\frac{2}{\pi^2} + \frac{1}{2} = 0.7026$	$\frac{8}{\pi^2} = 0.8106$

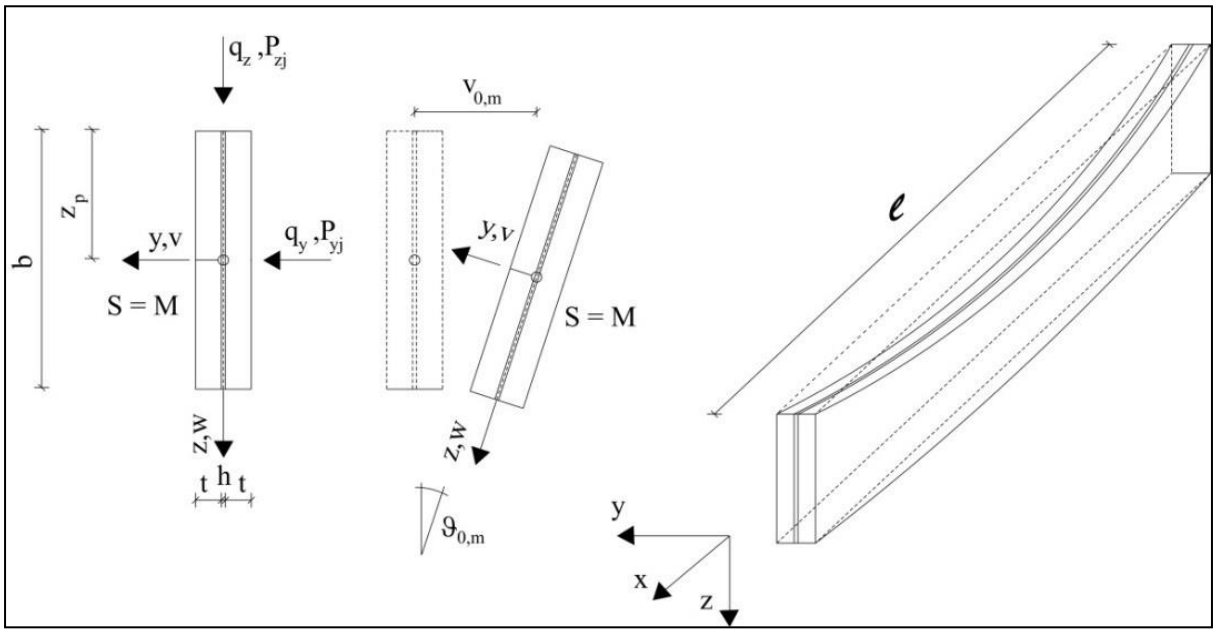

Figure 3-14: LTB of laminated glass beams: denominations and imperfection approach [8].

Where (3.40) describes the moments resulting from loading scenario $M_y = cte$, and (3.41) describes the moments resulting from loading scenarios $q_z = cte$ and P_z at midspan. Coefficients c_1 and c_2 are defined, as per their relevant loading scenarios, above in (Table 3-2). $G \cdot I_t$ is the torsional stiffness and $E \cdot I_z$ is the bending stiffness about the weak axis.

Both the torsional and bending stiffness are greatly influenced by the shear stiffness of the interlayer G_F, which is greatly dependent on time and temperature influence. These effects can be determined experimentally through relaxation tests, where the room temperature and load duration can be measured and adjusted as the variables [84]. In order to evaluate temperature effects, tests are generally performed in a climate chamber [84]. Where structural-sized laminated glass beams are used in the four-point bending test, this is beneficial to previous methods mentioned as not only does it replicate the size and shape effects of real beams, but also the composite action between glass and interlayer can be studied.

The influence of the shear modulus of the interlayer shear modulus G_F on stiffness and stress can be determined using 'extended bending and torsion theory' [8], which considers displacements in the shear gap due to warping deformations, which can occur by 'step-like' warping ω_δ and ω_φ, and rigid body warping due to normal forces ω_N, ω_B due to bending and ω_T due to torsion (,). By solving the differential equations of the extended bending and torsion theory the equivalent geometric stiffness is obtained by [8]:

$$I_t^{eq} = \frac{1}{\left(\frac{1}{S_{11}} + \frac{S_{12}^2}{S_{11}^2} \frac{1}{\tilde{T}_{22}} \right)}, \tag{3.42}$$

where coefficients S_{ik} and the function $\tilde{T}_{22}$ are shown in (Table 3-3). Furthermore, for the other loading scenarios [8]:

$$EI_z^{eq} = \frac{1}{v_B\left(\ell/2\right)} \cdot \frac{5}{384} \cdot L^4 \cdot q_y \tag{3.43}$$

for $q = const$, and for a single load P at midspan [8]:

$$EI_z^{eq} = \frac{1}{v_B\left(\ell/2\right)} \cdot \frac{1}{48} \cdot L^3 \cdot P_y. \tag{3.44}$$

The solutions for $v_B\left(L/2\right)$, and the calculation of stresses σ_{xx} that originate from lateral deformation v and rotational deformation ϑ are presented in (Table 3-4). The calculative procedures were verified by pilot experiments on PVB laminated glass beams [8].

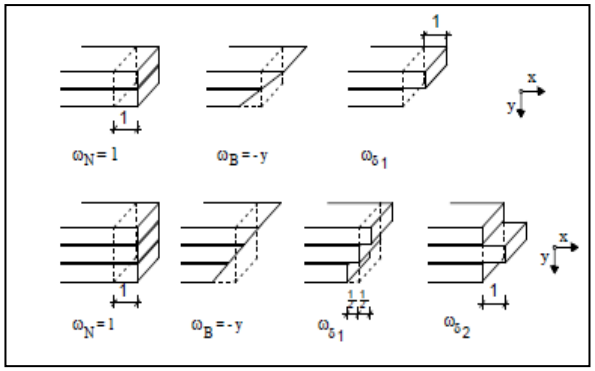

Figure 3-15: Rigid body warping with additional step-like warping deformations ω_N and ω_δ for bending [8].

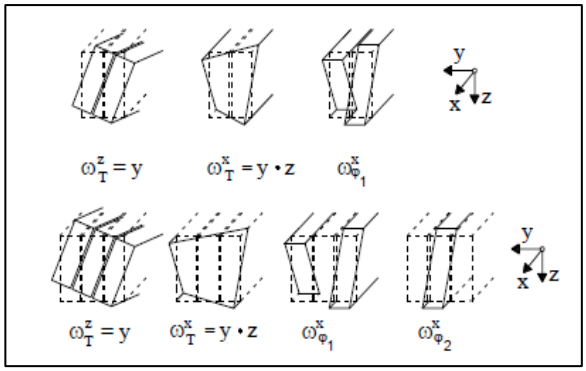

Figure 3-16: Rigid body warping ω_T^z and ω_T^x, and additional warping deformation ω_φ for torsion [8].

Table 3-3: Coefficients S_{ik} and function $\tilde{T}_{22}$ for torsion [8].

	Laminated glass with 2 layers	Laminated glass with 3 layers
S_{11}	$\frac{8}{3}\cdot b\cdot\left[-\left(\frac{1}{2}h\right)^3+\left(t+\frac{1}{2}h\right)^3\right]$	$\frac{8}{3}\cdot b\cdot\left[-\left(\frac{1}{2}t+h\right)^3+\left(\frac{3}{2}t+h\right)^3+\left(\frac{1}{2}t\right)^3\right]$
S_{22}	$\frac{1}{2}\cdot b\cdot t$	$2\cdot b\cdot t$
S_{12}	$b\cdot\left[\left(\frac{1}{2}h\right)^2-\left(t-\frac{1}{2}h\right)^2\right]$	$2\cdot b\cdot\left[\left(\frac{1}{2}t+h\right)^2-\left(\frac{3}{2}t+h\right)^2\right]$
$S_{\varphi,22}$	$\frac{1}{12}\frac{b^3}{h}$	$\frac{1}{6}\frac{b^3}{h}$
$\tilde{T}_{22}$	$-\frac{S_{12}^2}{S_{11}}+S_{22}+\frac{G_F}{G}S_{\varphi,22}$	

Table 3-4: Solutions $v_B(\ell/2)$ for bending [8].

	Laminated glass with 2 layers	Laminated glass with 3 layers
B_{11}	$2\cdot b\cdot t$	$3\cdot b\cdot t$
B_{22}	$\frac{2}{3}b\cdot\left[\left(t+\frac{1}{2}h\right)^3-\left(\frac{1}{2}h\right)^3\right]$	$\frac{2}{3}\cdot b\cdot\left[-\left(\frac{1}{2}t+h\right)^3+\left(\frac{3}{2}t+h\right)^3+\left(\frac{1}{2}t\right)^3\right]$
B_{33}	$t\cdot b$	$\frac{1}{2}\cdot b\cdot t$
B_{13}	$t\cdot b$	0
B_{23}	$\frac{1}{2}\cdot b\cdot\left[t^2+h\cdot t\right]$	$\frac{1}{2}\cdot b\cdot\left[-\left(\frac{3}{2}t+h\right)^2+\left(\frac{1}{2}t+h\right)^2\right]$
$\tilde{B}_{33}$	$-\frac{B_{13}^2}{B_{11}}-\frac{B_{23}^2}{B_{22}}+B_{33}$	$-\frac{B_{23}^2}{B_{22}}+B_{33}$
$S_{\delta,33}$	$\frac{b}{h}$	$\frac{b}{2\cdot h}$
$\tilde{v}_B(\ell/2)$	$\frac{5\cdot q_y\cdot\ell^4}{384\cdot E\cdot B_{22}}$	$\frac{P_y\cdot\ell^3}{48\cdot E\cdot B_{22}}$ (P at midspan)
ξ_3	$\frac{G_F\cdot\tilde{S}_{\delta,33}\cdot\ell^2}{E\cdot\tilde{B}_{33}}$	
$\Phi_{M,3}$	$\frac{8}{\xi_3}\left(1-\frac{1}{\cosh\left(\frac{\sqrt{\xi_3}}{2}\right)}\right)$	$\frac{2\cdot\tanh\left(\frac{1}{2}\sqrt{\xi_3}\right)}{\sqrt{\xi_3}}$ (P at midspan)
$\Phi_{V,3}$	$\frac{B_{22}}{\tilde{B}_{33}}\cdot\frac{48}{5\cdot\xi_3}\left(1-\Phi_{M,3}\right)$	$\frac{B_{22}}{\tilde{B}_{33}}\cdot\frac{48}{5\cdot\xi_3}\left(1-\Phi_{M,3}\right)$ (P at midspan)
$\tilde{v}_{\delta 1}(\ell/2)$	$-\frac{B_{32}}{B_{22}}\cdot\Phi_{V,3}\cdot\tilde{v}_B(\ell/2)$	
$v_B(\ell/2)$	$\tilde{v}_B-\frac{B_{32}}{B_{22}}\cdot\tilde{v}_{\delta 1}$	
$M_{\omega_B}(\ell/2)$	$\frac{q_y\cdot\ell^2}{8}$ ($q=$ const.)	$\frac{P_y\cdot\ell}{4}$ (P at midspan)

$\tilde{\omega}_{\delta 1}$	$-\frac{B_{31}}{B_{11}}-\frac{B_{32}}{B_{22}}\cdot y+\omega_{\delta 1}$ with $\omega_{\delta 1}=\begin{cases}1 \ for -\left(t+\frac{1}{2}h\right)<y<\frac{1}{2}h\\ 0 \ for \ \frac{1}{2}h<y<t+\frac{1}{2}h\end{cases}$	$\frac{B_{23}}{B_{22}}y+\omega_{\delta 1}$ with $\omega_{\delta 1}=\begin{cases}-1/2 \ for \ -\left(\frac{3}{2}t+h\right)<y<-\left(\frac{1}{2}t+h\right)\\ 0 \quad for \ -\frac{1}{2}t<y<\frac{1}{2}t\\ 1/2 \ for \ \frac{1}{2}t+h<y<\frac{3}{2}t+h\end{cases}$
σ_{xx}	$M_{\omega_B}\left(-\frac{\tilde{\omega}_B}{B_{22}}-\frac{\tilde{r}_3\cdot\Phi_{M,3}}{\tilde{B}_{33}}\cdot\tilde{\omega}_{\delta 1}\right)$	

The four-point bending test has several benefits to previously discussed experimental methods. It induces the failure mode of LTB in the glass beam specimen which represents perhaps the most crucial failure mode to be studied in glass beams situated in physical glass structures. The four-point bending test is also applicable to laminated glass beams as the important elastic moduli are attainable and can be applied to existing models developed by researchers, and those presented in the pre-normative glass design code. It does still have the drawback of generally being destructive in nature, however.

The greatest perceived drawback of this method may be in the estimation and modelling of the shear modulus. As the LTB mode induces a combination of bending and torsional deformations in a non-linear nature, determination of the recovery torque in this method will theoretically be inaccurate. In other words, the torsional recovery moment required to bring the beam back into equilibrium is extremely unlikely to be directly relatable to its initial mode of torque due to this combined effect, as well as the large deformations induced. For example, Belis et al [76] were able to measure the lateral imperfection shape, but information on torsional imperfections is completely lacking – a sentiment also echoed in the later study by Sonck, Belis [85]. In addition, the viscoelastic nature of the interlayer in laminated glass beams adds increased difficulty in accurately modelling composite shear modulus in these elements.

3.2.7 Torsion Test

As the shear modulus of glass and laminated structural glass beams may not be accurately determined by four-point beam bending and from the LTB mode, an alternative approach to isolate a pure shear deformation may be considered. The approach should consider the size and shape of structural glass beam elements to recreate a similar stress scenario to the LTB mode, so this excludes many small-scale tests. The most viable approach to solve this problem may therefore be structural-sized torsion testing. This creates a more comparable torsional stress scenario to four-point beam bending tests while inducing a state of 'pure shear' in the beam, which is the most ideal condition to determine the shear modulus.

Unfortunately, aside from a panel torsion test method which focuses on time- and temperature-effects on the interlayer in the pre-normative glass design code, there have been no published experimental torsion studies on structural-sized monolithic or laminated glass beams to date. Inspiration can be taken, however, from the existing structural timber design code BS EN 408:2010+A1:2012 [91], and several studies that have been conducted by researchers on narrow rectangular structural timber beam elements [92-101].

To perform the torsion test to obtain the shear modulus as per the timber code [91], the beam specimen must be of rectangular cross-section and have a testing length (Figure 3-17) of at least 19 times the largest cross-sectional dimension. The test specimen is clamped at supports spaced more than sixteen times the cross-sectional dimension and subjected to torsional force along the longitudinal axis by a relative rotation of the supports. The test specimen is mounted in a manner that minimises the bending deflection caused by self-weight. The centres of each end support are aligned so that clamping the test specimen does not cause any deformation that may influence torsion results. The torque may be applied at one or both supports, provided there is a relative rotation. The free testing length l_1 is defined as being the space between two points (1 and 2) on the beam specimen. The distance between supports and cross-sections l_2 must be between 2 and 3 times the thickness. These points must have some form of stress-strain displacement

measuring gauge or device to measure the rotation at both ends (popular devices are presented in section 3.3).

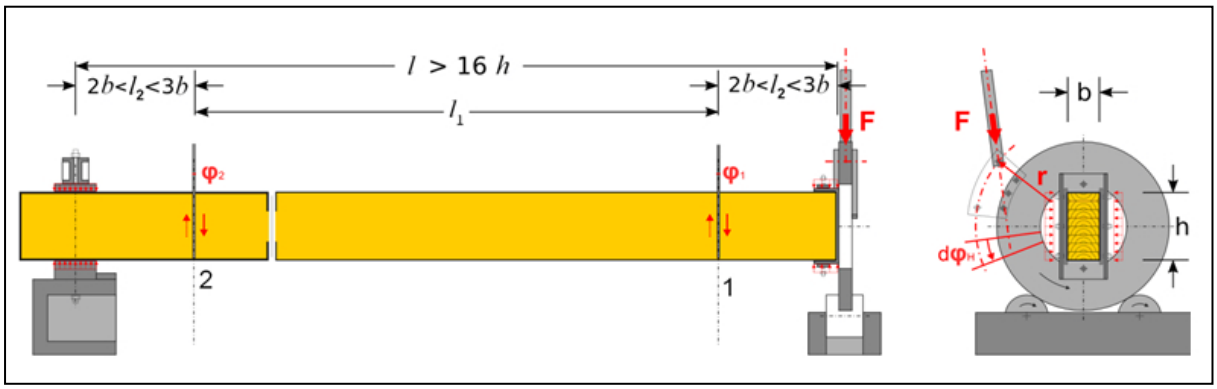

Figure 3-17: Example of timber beam torsion test setup with requirements of specific locations for gauges [91].

The timber code subsequently presents design equations to determine the shear modulus tailored to the timber material. These design principles and equations are based upon Saint-Venant's semi-inverse method to treat torsional problems in non-circular cross-sectioned elements. Saint-Venant's torsion theory can be applied directly to narrow rectangular cross-sectioned elements, thus in theory it is highly applicable to determine the shear modulus structural glass beams.

The simplest cases of torsion are present in circular cross-sectioned elements. The underpinning theories behind these are well documented in several material mechanics textbooks, such as that of Boresi and Schmidt [31], so will not be discussed explicitly herein. In other torsion members with more complicated cross-sections with narrow rectangular components, it is difficult to achieve exact solutions for the elastic membrane behaviour. In cases like this, such as basic rectangular, thin walled or open box cross-sections, Prandtl's Elastic Membrane (Soap-Film) Analogy provides approximate solutions [31]. Again, all these theories will not be exhaustively listed here to keep this section more concise, but relevant notes are included in the analytical model

narrow rectangular sections herein, and are fully explained in fundamental material mechanics literature [31].

The case of a bar subjected to torsion with narrow rectangular cross-sectional properties, with width = $2h$ and depth = $2b$, where $b \gg h$, is displayed in (). The membrane deflection is assumed to be approximately independent of x and parabolic with respect to y, resulting in the displacement equation [31]:

$$z = z_0 \left[1 - \left(\frac{y}{h} \right)^2 \right] \tag{3.45}$$

where z_0 is the maximum deflection of the membrane based on Prandtl's analogy, and the above equation (3.45), which is an approximate solution of membrane displacement, satisfies the condition $z = 0$ on boundaries $y = \pm h$. Furthermore, by equation (3.45) the following relationship is present [31]:

$$\frac{\partial^2 z}{\partial x^2} + \frac{\partial^2 z}{\partial y^2} = -\frac{2z_0}{h^2}. \tag{3.46}$$

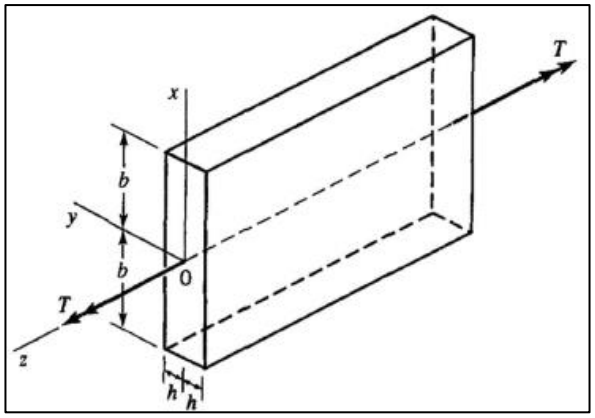

Figure 3-18: Narrow rectangular torsion member [31].

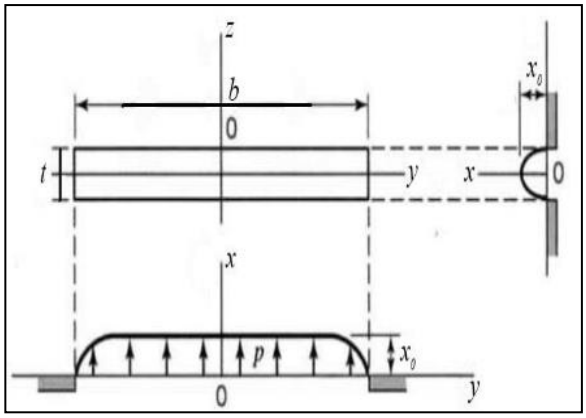

Figure 3-19: Membrane for narrow rectangular cross section [31].

Based upon (3.46), and due to the summation of vertical forces and analogous quantities for membrane equilibrium (Prandtl's analogy), equation (3.45) becomes [31]:

$$\phi = G\theta h^2 \left[1 - \left(\frac{y}{h} \right)^2 \right] \tag{3.47}$$

and resultantly Prandtl's stress constants yield [31]:

$$\sigma_{zx} = \frac{\partial \phi}{\partial y} = -2G\theta y, \quad \sigma_{zy} = -\frac{\partial \phi}{\partial x} = 0 \tag{3.48}$$

also, the maximum value of σ_{zx} is [31]:

$$\tau_{\max} = 2G\theta h, \quad \text{for } y \approx \pm h \tag{3.49}$$

now from the torsional relationship ($T = 2\iint \phi dx\, dy$) and equation (3.47) the following relationship is yielded [31]:

$$T = 2\int_{-b}^{b}\int_{-h}^{h} \phi dx\, dy = \frac{1}{3} G\theta (2b)(2h)^3 = GJ\theta \tag{3.50}$$

where [31]:

$$J = \frac{1}{3}(2b)(2h)^3 \tag{3.51}$$

where J is the torsional constant and GJ is the torsional rigidity. The torsional constant here is small in comparison to the polar moment of inertia $J_0 = \left[(2b)(2h)^3 + (2h)(2b)^3 \right] / 12$, and the solution is an approximate one. Finally from equations (3.49) and (3.50) the following relationships are obtained [31]:

$$\tau_{\max} = \frac{3T}{(2b)(2h)^2} = \frac{2Th}{J}, \tag{3.52}$$

$$\theta = \frac{3T}{G(2b)(2h)^3} = \frac{T}{GJ}. \tag{3.53}$$

Structural-sized torsion testing and calculation based on Saint-Venant's torsion theory can theoretically provide the most accurate description of torsional rigidity with a highly comparable stress scenario to the mode of LTB in slender rectangular cross-sectioned glass and laminated structural glass beams. As has been highlighted in experimental torsion studies on timber beams, particularly by Zhang, Mohamed, Gharavi, Uheida and their co-authors [92, 98, 99, 102, 103], one of the main difficulties inherent in the torsion test method is how rotational displacements are measured. As the relative rotation from two locations on the beam is required for angular measurement, it is not sufficient alone to take the rotational data at the end support outputted by the torsion machine. In the final section of this chapter, an overview of displacement measuring tools and procedures are presented.

3.3 Displacement Measuring Techniques

3.3.1 Traditional Measurement Devices

The techniques and devices used to measure the stress-strain displacements in experiments are also a critical consideration, as this data must be accurately extracted to calculate mechanical properties. While in large scale global positional change measurements the global positioning system (GPS) is used, the relative displacement between two positions on a test specimen, or for structural health monitoring in civil infrastructure has traditionally required some form of contact-based sensory equipment.

Typically, in these cases, linear variable differential transformers (LVDTs) are used to measure the relative displacement between two or more points of interest on a test or physical specimen. The LVDT is an electromechanical sensor that converts linear mechanical motion into a variable electric current, voltage or signal, and the reverse [104]. To measure displacement, an LVDT displacement transducer, normally in the form of a hollow metallic cylinder which has a

shaft that moves linearly along its longitudinal axis, is placed at two or more points of contact on the specimen. Movement of the test specimen in turn displaces the shaft within the displacement transducer, and the motion is electrically measured at each point as the distance in mm the specimen has travelled at that point.

LVDTs have previously been attractive for measuring displacements [105-107] due to a few attributes. As there is no mechanical contact between sensing elements, no distortion of readings occurs due to frictional forces and no fatigue occurs to mechanical connections. Unfortunately, LVDTs also come with several limitations when it comes to mechanical stress-strain displacement measurements. LVDT displacement transducers are limited to measure in only one direction, making accurate displacements in 3D, such as rotational displacements unobtainable. Additionally, the LVDT sensors operating range is limited by the size of the sensor itself, as the system requires that the core remains within its internal coils. Finally, this measurement method is contact based, so there is a likelihood that the equipment may be moved or damaged during structural testing.

Extensometers (or strain gauges) are also commonly used to measure variations in the length of a test specimen and is commonly used in tensile testing [108, 109]. Whilst these were originally designed as contact based, these have evolved into non-contact-based extensometers which are laser and video based. These optical devices are more accurate than their contact-based counterparts and require calibration to operate correctly, however are also limited to measure in one direction.

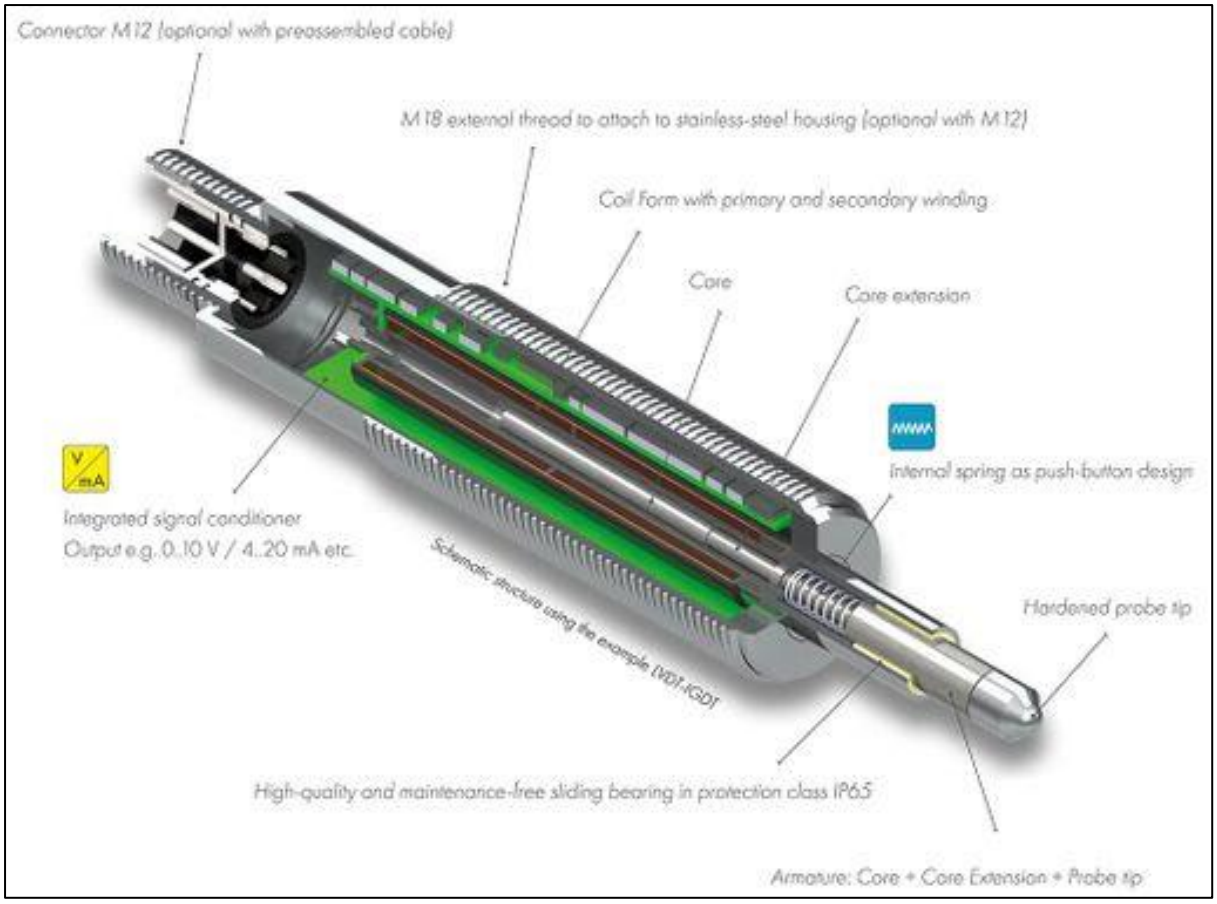

Figure 3-20: Anatomy of LVDT linear displacement transducer (www.hoffmann-krippner.com).

Figure 3-21: Dual axis inclinometer (www.leveldevelopments.com).

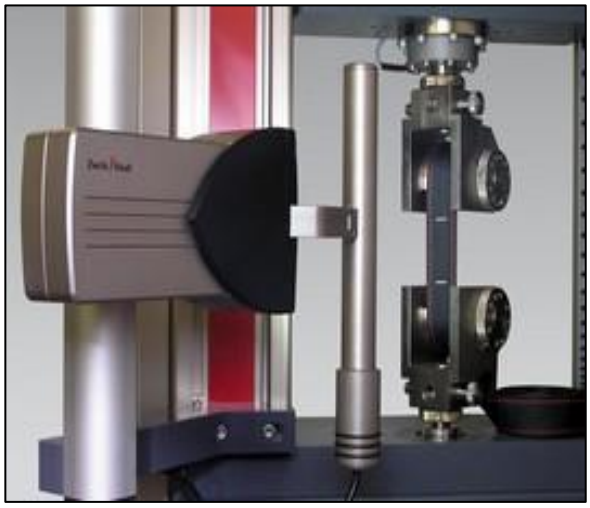

Figure 3-22: Zwick video extensometer (www.news.thomasnet.com).

A further improvement to one-dimensional displacement measuring instruments may be the inclinometer. The inclinometer is a contact-based attachable sensor that measures tilt angles of an object with respect to the direction of gravity. The inclinometer improves upon previous methods as it is possible to measure in two axes rather than one to obtain slope information in the case of dual axis inclinometers (). The inclinometer still has several limitations, however. The inclinometer is limited to one unit per point of inspection, which can be quite large if one wants to capture multiple points of interest across a small area. The accuracy of the inclinometer is also limited by the size of the sensor, where the reading is taken as an average of the sensors cross-sectional area. As these are again contact based wired devices, attachment to the test specimens' surface can be problematic, as can the risk of damage and movement during testing.

3.3.2 Photogrammetry and Stereo-Vision

Due to the limitations of traditional displacement measurement methods which are generally contact based, alternative non-contact based optical techniques that have been applied across many other fields and measurement applications have become increasingly explored for mechanical displacement measurement. The most relevant include digital photogrammetric and stereo-vision approaches. The term 'photogrammetry' has been around since the 19th century and appeared at a very similar time to photography itself with the idea being proposed for topographic mapping [110]. Photogrammetry can be described as the science and technology of obtaining reliable information about physical objects and the environment through the process of recording, measuring, and interpreting photographic images and patterns of electromagnetic radiant imagery and other phenomena [111].

In its earliest form, photogrammetry used purely analogue, optical-mechanical techniques. Today photogrammetry incorporates analytical techniques with sophisticated, yet simple and efficient computer aided methods and is used in many fields, such as architecture, engineering, manufacturing, quality control, police investigation, cultural heritage, geology and in the film

industry. Modern innovations in computerised vision have greatly improved efficiency and accuracy in one of its key sectors, manufacturing, where it is used for the guidance of robots such as pick and place machines, quality inspection, and traceability of products [112].

Photogrammetry can be categorised into two types – aerial (with camera in the air) and terrestrial (camera handheld or fixed to a tripod) [111]. 'Close-range photogrammetry', also referred to as machine vision or computer vision, is one of the most useful applications of photogrammetry in civil and mechanical engineering as it allows for the extraction of precise 3D measurements from 2D images, which can be performed at a much closer distance and smaller scale than traditional methods. The earliest introduction of this technique to experimentally measure mechanical stress/strain deformations in structures was in 1982 by Peters and Ranson [113], refined in the following year [114], and further explored in Civil and Structural Engineering applications by Hampel and Maas [115, 116]. Furthermore, photogrammetric approaches applied to measure experimental stress-strain displacements in structural timber have been studied by researchers at the authors' institution [92, 93, 98, 99, 102, 103, 117-123].

Photogrammetry encompasses the principle of stereo-vision. While highly accurate measurements can be taken from a calibrated single camera image by determining its exterior orientation with respect to a plane, then converting these to world coordinates by intersecting optical rays [124], only 2D measurements are possible through this method. In the case of taking 3D measurements, the principle of binocular stereo-vision can be employed. The binocular stereo-vision system simulates the visual system of humans and most animals, where two eyes, left and right, which are simulated by two interconnected cameras, both focus on a third conjugate point from which depth perception is generated. In the form of digital binocular stereo-vision systems, disparity, distance, and 3D coordinates of any desired point of interest in the visual area can be computed by triangulation [124]. To achieve true 3D stereo reconstruction of a scene therefore, at least two images taken simultaneously of the same scene are essential to perform triangulation.

Before it is possible to reconstruct 3D measurements in a world coordinate system for measuring applications, the system of interconnected cameras must also be calibrated to determine

their relative pose in the world and to correct any lens distortions. To perform a binocular stereo calibration, an object with known dimensional properties and recognisable features must be placed visibly and captured in the images of both cameras. The more pairs of images taken of the calibration plate, the greater the calibration accuracy is likely to be [125]. By translating recognisable points from the calibration plate in multiple image pairs into world coordinates and computing their spatial relationship to the world position and orientation (pose) of the cameras and back, an exact world spatial pose of both cameras can be determined and thus the 3D coordinates of any other point of interest in the image plane can be determined.

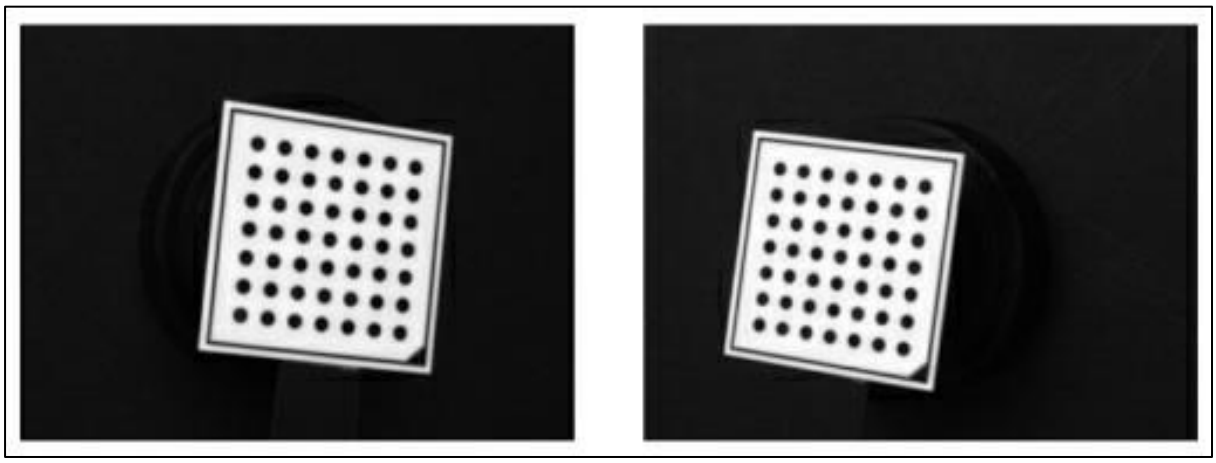

Figure 3-23: Stereo image pair from a set of calibration images of a calibration plate [124].

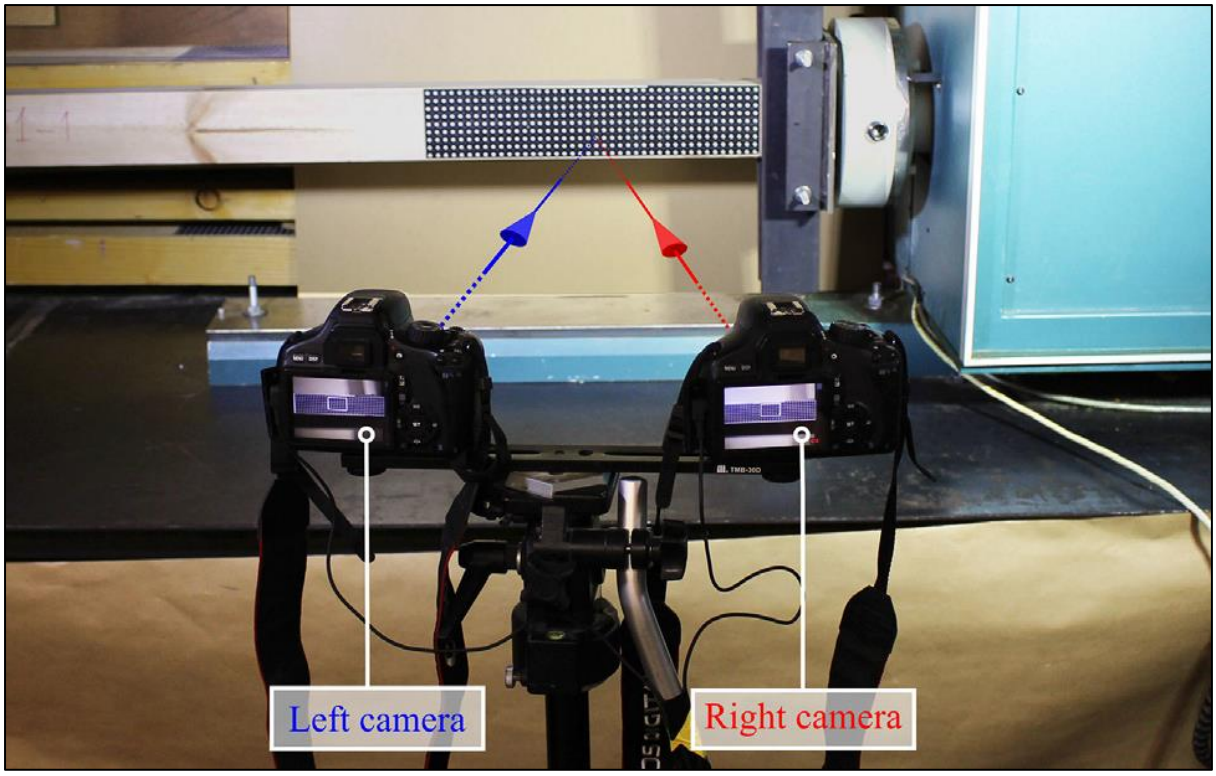

Figure 3-24: A binocular stereo-vision setup with target-based points of interest [102]

3.4 Summary and Conclusions

- An in-depth review of the technical literature relating to the experimentation and theoretical modelling of structural glass and laminated glass beams was undertaken, including the techniques available for obtaining relevant displacement information from such experiments.

- Experimentation for glass' key elastic properties must consider that, despite glass being fundamentally a homogeneous, isotropic, linearly-elastic material, slender glass members such as beams can deform greatly under structural loading causing non-linear behaviours that complicate the work of the engineer.

- Viscoelastic interlayer materials used in laminated glass have significantly different properties and behaviours to glass itself, particularly relating to time- and temperature-

dependent behaviour, making the composite action of these structures particularly complex to model.

- Due to these complexities, solid experimental work is required to build and improve existing theoretical models.

- Through evaluation of existing experimental methods several limitations were identified relating to the composite nature of laminated glass, and the unpredictable non-linear deformation modes of slender glass beam elements. Profound challenges were discovered under the highly relevant lateral-torsional buckling (LTB) mode and accurately acquiring the shear modulus in this regard.

- The torsion test is theoretically the most accurate means to determine the shear modulus and has been proven in practice for other structural-sized beam elements such as timber. However, no evidence was found of a torsion test method for glass beams nor evidence of experimental torsion peer-reviewed studies.

- A further challenge in determining key mechanical properties in experimentation is the means of accurately measuring displacements. Traditional contact-based sensors can be problematic, however non-contact-based methods such as photogrammetry offer an accurate and adaptable alternative that could be explored for glass beam experimentation.

4. Development, Optimisation and Validation of the Measurement System

This chapter presents the full development, optimisation and validation of the photogrammetric measurement system and approach. The equipment, setup and software are described with important factors for optimisation. Full stereo-camera calibration is performed and verified for its accuracy. Additionally, to further validate measurement accuracy for the specific application required, a tailor-made accuracy experiment was developed and performed.

4.1 Binocular Stereo-Vision System

4.1.1 Camera Setup

The principles of binocular stereo-vision can be applied using many different methods and equipment types depending on the application, so long as the primary components – two interconnected cameras situated in a fixed position and their lenses – are present. In present times the setup can be made cost-effective due to the availability of affordable, modern, high-specification cameras, without the need for high-speed cameras which are used in other machine vision applications.

For the primary components of the stereo-vision system, two Canon EOS 7D digital single-lens reflect (DSLR) cameras with 50 mm Canon EF f/1.8 II fixed focal lenses were selected. It is vital that both cameras are fixed in place securely, as any slight movement to their position post-calibration will invalidate all prior coordinate data. A robust steel-based tripod was used as the stand for the cameras. In combination with this, an adjustable aluminium-alloy horizontal extension arm was used to position the cameras apart from each other, left and right of the tripod respectively. A wider distance between left and right cameras can preferentially affect the accuracy of calibration and 3D coordinate generation. Despite a larger distance generally leading to more accurate

triangulation [124, 125], the cameras' field of view must also be large enough for the area of interest to be fully visible. The cameras were spaced approximately 550 mm apart and approximately 2.8 m from the central longitudinal plane of the torsion machine. Additionally, the rotation around the optical axis should be similar between the two cameras to give accurate calibration [124, 125], so this was accounted for in their positioning.

Both cameras were linked using splitter, wires, and shutter to enable simultaneous images to be taken, which are all required at the same moment for 3D scene reconstruction. All wiring was hazard taped to the ground and taped to the tripod to reduce risk of accident during testing, which could move and invalidate the stereo-camera system once calibrated.

Figure 4-1: Stereo-camera system.

4.1.2 Illumination

When preparing a photogrammetric setup, points of interest must be clearly visible in images to be identified in machine vision software. An effective method of illumination is therefore required to make the important features visible on the test specimen - namely the photogrammetric targets - and to suppress undesired features. Consideration must therefore be given to how light interacts with the object under testing. As glass is a highly reflective material, minimisation of glare must be achieved to make points of interest easily readable by HALCON software.

Two Softbox lights with 800 W compact fluorescent lamps (CFLs) and reflective covers were set up to illuminate the test area by transmitting continuous smoothed light streams. Further considerations for illumination were required when the glass beams were torsion tested in latter chapters, as level of reflectivity may still be observed. These included setting both Softbox lights at a shallow angle to the test specimen (post installation) and checking via the cameras that glare is not present. Any ceiling lights should be turned off or covered during the test as glare may occur from these when the test specimen is rotated. A further implementation was to fit polarising lens filters to the cameras, as this smooths light from any unexpected reflection and increases the likelihood of all photogrammetric targets being identified by the machine vision software.

4.1.3 Machine Vision Software

There are several machine vision software solutions available currently. Some of which focus on specific applications and are rigid in this nature, whereas others have built in programmability. For dynamic 3D displacement measuring tasks it is preferable to have the ability to customise algorithms through a programming environment, whilst also having a highly functional library of built-in operators suited to machine vision tasks, reducing the time and complexity of developing these applications. HALCON software by MVTec contains an extensive library of functional operators for machine vision tasks, including camera calibration and shape/pattern recognition,

whilst also enabling programmability through the HDevelop integrated development environment (IDE). Therefore, HALCON was selected for all the image processing tasks in this study.

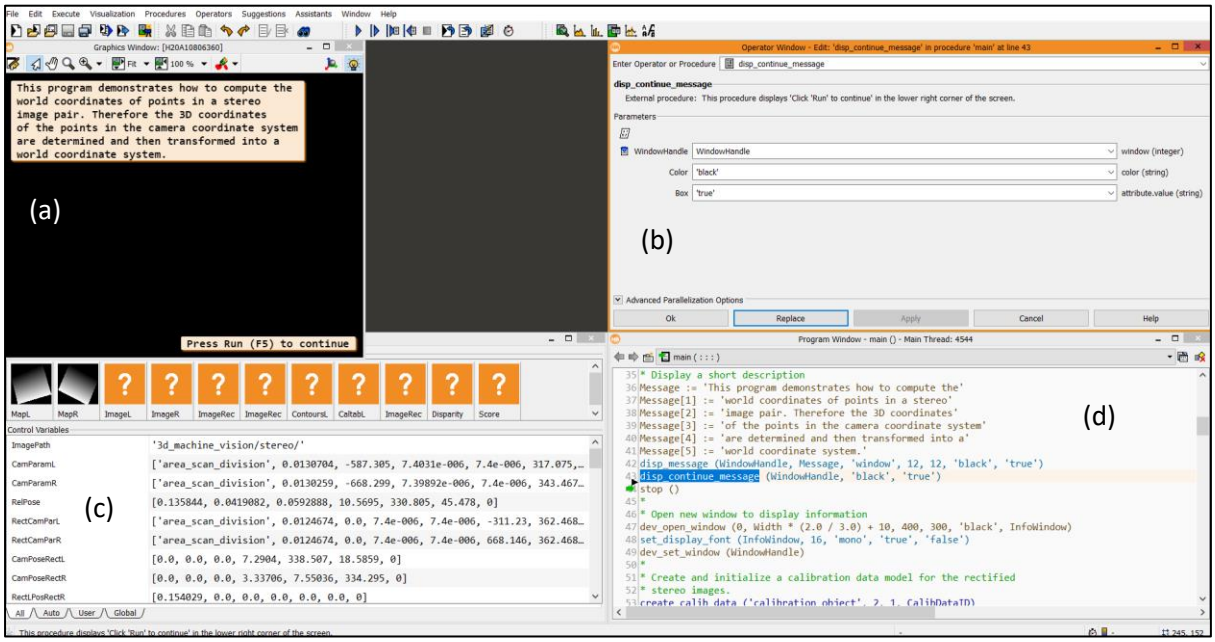

Figure 4-2: HALCON software interface; (a) visualisation window, (b) operation descriptor, (c) control variables, (d) programming environment.

4.1.4 Stereo-Vision Principle

Disparity, distance, and 3D coordinates of an object in view are computed in a means similar to the human and animal visual system. Two interconnected cameras simulate two eyes focusing on the same object, which capture simultaneous pairs of images from different positions and orientations.

The camera coordinate systems (CCS) of left and right cameras are depicted in figure x which are situated at the optical centres of the lenses. The focal length, *f*, is the distance between the CCS and the image coordinate system (ICS) which is situated at the image sensor within the camera. The world coordinate system (WCS) is set as the left camera CCS for convenience.

The spatial relationship between the WCS and right camera CCS is obtained by [126]:

$$\begin{bmatrix} x_r \\ y_r \\ z_r \end{bmatrix} = M \begin{bmatrix} x \\ y \\ z \\ 1 \end{bmatrix} = \begin{bmatrix} r_{11} & r_{12} & r_{13} & t_x \\ r_{21} & r_{22} & r_{23} & t_y \\ r_{31} & r_{32} & r_{33} & t_z \end{bmatrix} \begin{bmatrix} x \\ y \\ z \\ 1 \end{bmatrix} \tag{4.1}$$

where $M = [R \mid T], [R]$ denotes the rotation matrix, and $[T]$ is the translation vector for the transformation between the WCS and right camera CCS. The rotation matrix and translation vector are [126]:

$$R = \begin{bmatrix} r_{11} & r_{12} & r_{13} \\ r_{21} & r_{22} & r_{23} \\ r_{31} & r_{32} & r_{33} \end{bmatrix}, \; T = \begin{bmatrix} t_x \\ t_y \\ t_z \end{bmatrix} \tag{4.2}$$

Then the following expressions can be made according to pinhole imaging theory [126]:

$$S_l \begin{bmatrix} X_l \\ Y_l \\ 1 \end{bmatrix} = \begin{bmatrix} f_l & 0 & 0 \\ 0 & f_l & 0 \\ 0 & 0 & 1 \end{bmatrix} \begin{bmatrix} x \\ y \\ z \end{bmatrix}, \quad S_r \begin{bmatrix} X_r \\ Y_r \\ 1 \end{bmatrix} = \begin{bmatrix} f_r & 0 & 0 \\ 0 & f_r & 0 \\ 0 & 0 & 1 \end{bmatrix} \begin{bmatrix} x_r \\ y_r \\ z_r \end{bmatrix} \tag{4.3}$$

The corresponding coordinates in left and right images for the spatial point in the WCS are then obtained as [126]:

$$\rho \begin{bmatrix} X_r \\ Y_r \\ 1 \end{bmatrix} = \begin{bmatrix} f_r r_{11} & f_r r_{12} & f_r r_{13} & f_r t_x \\ f_r r_{21} & f_r r_{22} & f_r r_{23} & f_r t_y \\ r_{31} & r_{32} & r_{33} & t_z \end{bmatrix} \begin{bmatrix} x \\ y \\ z \\ 1 \end{bmatrix} \tag{4.4}$$

The 3D coordinate of the object can then be determined as [126]:

$$
\begin{aligned}
x &= z\frac{X_l}{f_l} \\
y &= z\frac{Y_l}{f_l} \\
z &= \frac{f_l(f_r t_x - X_r t_z)}{X_r\left(r_{31}X_l + r_{32}Y_l + r_{33}f_l\right) - f_l\left(r_{11}X_l + r_{12}Y_l + r_{13}f_l\right)} \\
&= \frac{f_l\left(f_r t_y - Y_r t_z\right)}{Y_r\left(r_{31}X_l + r_{32}Y_l + r_{33}f_l\right) - f_l\left(r_{21}X_l + r_{22}Y_l + r_{23}f_l\right)}
\end{aligned}
\tag{4.5}
$$

Once both the focal length of the left and right cameras, f_l and f_r, and the coordinates of the spatial point in left and right images are known, then 3D coordinates of that point in WCS can be computed. To determine the rotation matrix and translation vector calibration of the stereo camera system is required.

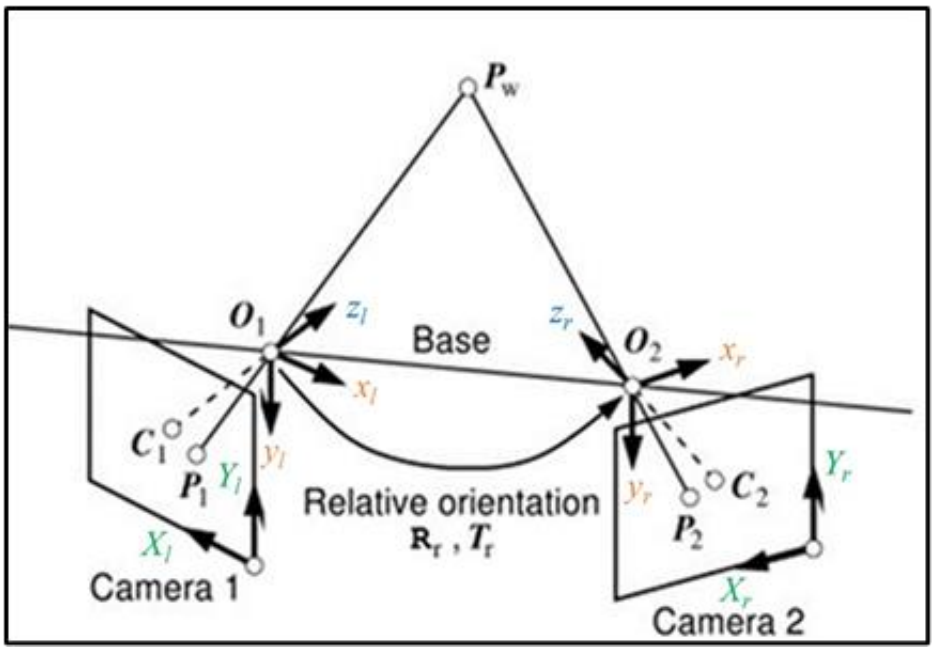

Figure 4-3: Binocular stereo geometry principle [124] (C_1, C_2 = principle points, O_1, O_2 = projection centres, R_r = rotation matrix, T_r = translation vector, P_1, P_2 = a point in each image, P_w = object point of interest).

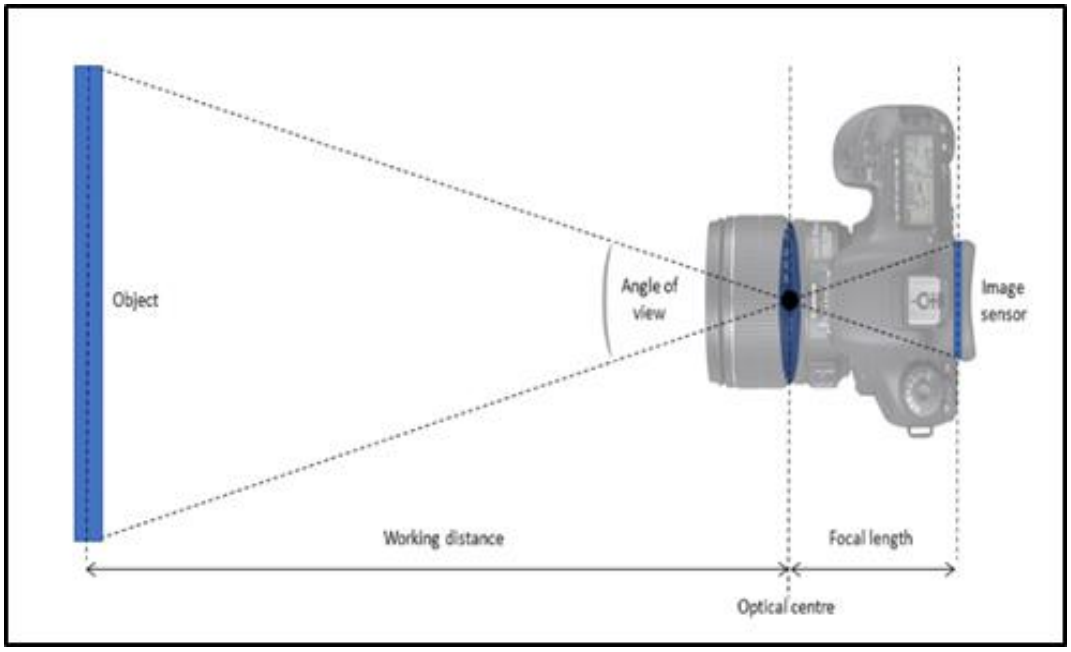

Figure 4-4: Camera and lens relationship.

4.2 Calibration

4.2.1 Calibration Equipment

Calibration of stereo camera systems require multiple image pairs in different positions and orientations (poses) to be taken of a patterned calibration object with known properties. A custom calibration object may be used with manually created descriptive data; however, the likelihood of error and inaccuracy is greatly increased. Resultantly, a standard 160 x 120 mm calibration plate (a) with its corresponding data file provided by MVTec were used in this study. The target area of the calibration plate contains multiple small circular target marks, which are an optimal shape to pinpoint and extract centre points using machine vision software.

A means to position the calibration plate for each pair of images must also be considered. It may be sufficient in some cases for the plate to be handheld by a second person in different poses for each image, so long as no part of the target area is obstructed. This is not optimal, however, as movement may occur from human error causing blurred imaging. It can also be problematic to achieve a wide range of poses covering the full area of interest using only a backboard. To optimise this, a tailor-made calibration plate holder was designed and fabricated for this study. The holder

was designed to be adjustable in 6 height increments that cover up to the top edge of the test specimen and allow for 360° rotation of the calibration plate to achieve a wide range of poses. The main base and column were fabricated in steel for strength and stability. A holding unit to secure the calibration plate in place was fabricated in PVC plastic, with slots at the top and bottom to allow for the calibration plate to be slotted into place. An l-shaped fitment was also included in this unit to secure the plate in place for rotated poses. The holding unit connects to the steel column from its rear by a single M8 plastic star head screw at the desired height (d), which can be easily loosened by hand between calibration images to alter the pose.

Figure 4-5a: HALCON calibration plate.

Figure 4-6b: Calibration plate holder

Figure 4-7c: Installed calibration unit.

Figure 4-8d: Adjustable heights from rear.

4.2.2 Calibration Method

To obtain the world coordinates of a point in a stereo-image pair to perform accurate measurements, the system must first be calibrated. The purpose of calibration is to determine the internal and external camera parameters and correct lens distortions (Figure 4-9). The internal parameters describe the internal geometry and optical characteristics of the camera, such as focus, lens distortion coefficient (which is determined by the lens properties and combined with the pinhole model), and the distance between cells in the sensor. The external, or pose parameters, describe the position and orientation of the cameras relative to a world coordinate system and are therefore essential to apply triangulation-based 3D scene reconstruction.

To perform the most accurate binocular calibration for 3D scene reconstruction, multiple image pairs of the calibration plate must be taken in various poses. Machine vision documentation and published work recommend that around 10 stereo image pairs are taken for calibration [124, 125, 127]. This assumes that the circular calibration marks in all 10 images are perfectly read by the

machine vision program without any issues. A further consideration to perform the most accurate calibration is that the calibration marks must be captured covering the entire area of interest from which measurements will be taken in subsequent experiments. Rotation and tilt should also be applied to the calibration plate amongst the image set to calibrate for experimental rotations. It is for this reason that, in the case of larger measurement areas of interest, a greater number of images was be taken to achieve full positional and rotational coverage.

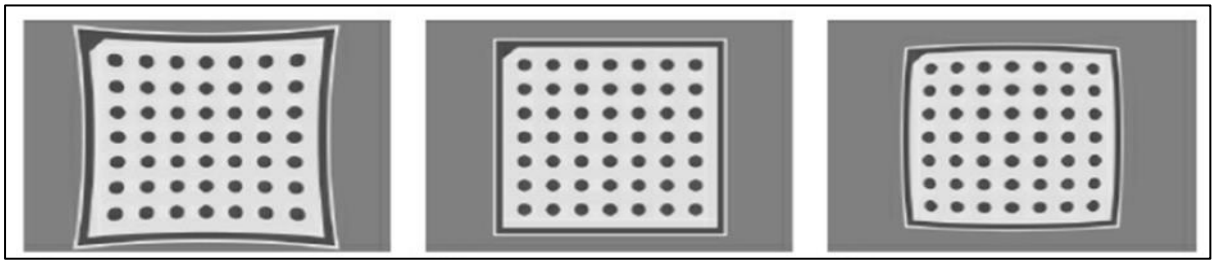

Figure 4-9: Lens distortion effects; (a) pincushion distortion, (b) no distortion, (c) barrel distortion [124].

The first step of calibration in this study involved field-of-view alignment with the cameras and measurement area. The calibration plate was set inside the plate holder and the height was adjusted to mid-level. The plate was then positioned in the centre of the measurement area using with the aid of alignment markings and both stereo cameras' field of view was adjusted so that the plate was in their centre, and the external boundaries of the measurement area were also visible. The calibration plate was then moved to the left boundary of the measurement area, to alternate through user defined poses from left to right.

The next stage of calibration involved taking pairs of stereo images. This is most efficiently performed with two people, one to control the cameras and one to adjust the calibration plates' pose. Two calibrations were performed in this study. Totals of 45 and 65 calibration images were taken per each calibration run covering the entire measurement area. These included varying longitudinal positions, 3 height levels, front facing, left/right tilted, left/right diagonal rotation, and forward and backward leaning positions for the 65-image set. Some examples of calibration image pairs are displayed in Figure 4-10. This larger set of calibration images overcompensates for cases

where there is an issue in reading the calibration plate in some images in machine vision software, whilst still being efficient time-wise due to use of the calibration plate holder.

Figure 4-10: Calibration images taken in various poses – left camera images taken from 50 cm horizontally apart from right camera images.

4.3 Micrometre Accuracy Experiment

4.3.1 Equipment

Once calibrated, the measuring accuracy of the stereo-vision system should be evaluated and verified for its use in the specific displacement measuring application. A simple but effective tailor-made accuracy experiment was therefore employed to determine and compare the accuracy of the calibrated system against an existing, trusted device with high measuring accuracy – the digital micrometre.

A DML 75 – 100 mm digital micrometre with external gauge and a measurement accuracy of $\pm$ 0.003 mm was used in this experiment. First two, then four circular target points were fixed to the micrometre apart from each other longitudinally. To achieve the greatest reproducibility, if proven to be accurate, these targets were to be identical in size, shape, and colour to those that would be set to glass beam samples in subsequent tests. The targets were again plotted to adhesive labels, cut, and stuck to squares of PVC plastic for firm backing to prevent any distortion. The first two targets were fixed to the stationery end at the left of the micrometre, while the second two were fixed to the spindle which moves laterally as it is rotated by the user, incurring change in distance. The difference in positioning of the targets is displayed in Figure 4-13, where the additional two targets for the second experiment were placed in central alignment with the micrometre spindles measurement plane. This was to study whether there would be any loss in accuracy of the test from the first two targets not being placed on the central measurement plane. Targets were fixed to the micrometre using a hot glue gun. A universal swivel clamp with magnetic base – which locks to the steel test bench – was used to hold the micrometre in place securely for the experimental process.

Figure 4-11: Micrometre and swivel-clamp.

4.3.2 Experimental Method

Two micrometre accuracy experiments were performed: one per each calibration and target setup. To set up the experiment, the micrometre was first clamped within the swivel clamp. Using the spindle, the micrometre was rotated to as close to the far end as possible with the target being forward facing. The moving target(s) on the spindle was aligned to be forward facing to correspond with the static target by using a laser level along the target's longitudinal planes (Figure 4-12), as this alignment provides the best correspondence with micrometre gauge readings. Once aligned, the gauge was set to zero to begin the experimental process.

The micrometre was fixed to the test bench at the end-left boundary of the target area, and along the longitudinal measurement plane for best reproducibility to the forthcoming torsion test. With the gauge set to zero mm, the first reference stereo image pair was taken of the micrometre at this location. Subsequently, whilst keeping the micrometre distance to zero mm, the micrometre

and swivel clamp were moved further along the longitudinal test plane, secured in place and another image pair was taken. This process was repeated for 5 locations along the test plane in total resulting in 5 reference image pairs.

The micrometre was then returned to the first location and the distance was changed to create the first measurement interval. Image pairs were then captured at this location and in 5 different poses, alternating through from left-facing to right-facing (Figure 4-14). The distance was then changed by rotating the spindle to set the next measurement interval and the micrometre was moved further along the test plane to the next interval. Another five stereo image pairs were taken in different poses, left-facing to right-facing in the same manner as previous. This process was repeated for 5 measurement intervals at 4 locations and for 5 poses each, resulting in a total of 105 micrometre stereo image pairs for each test including the reference images.

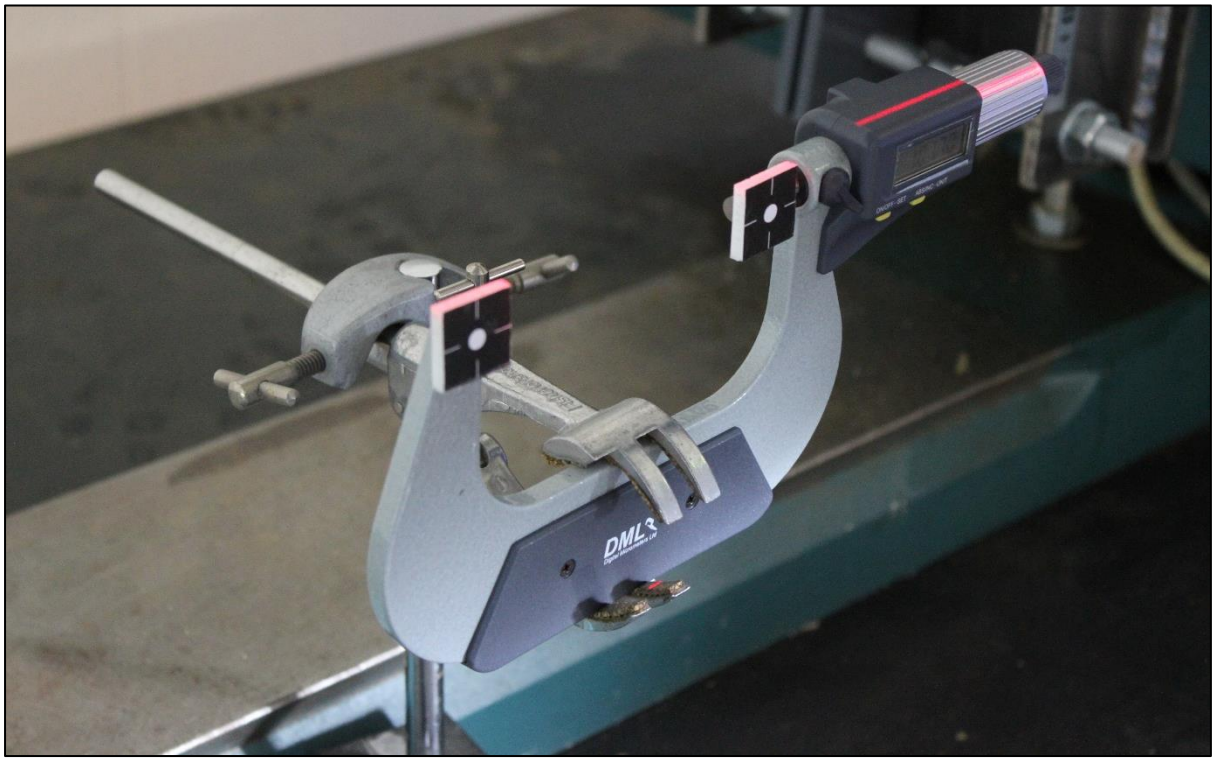

Figure 4-12: Micrometre target alignment using laser level.

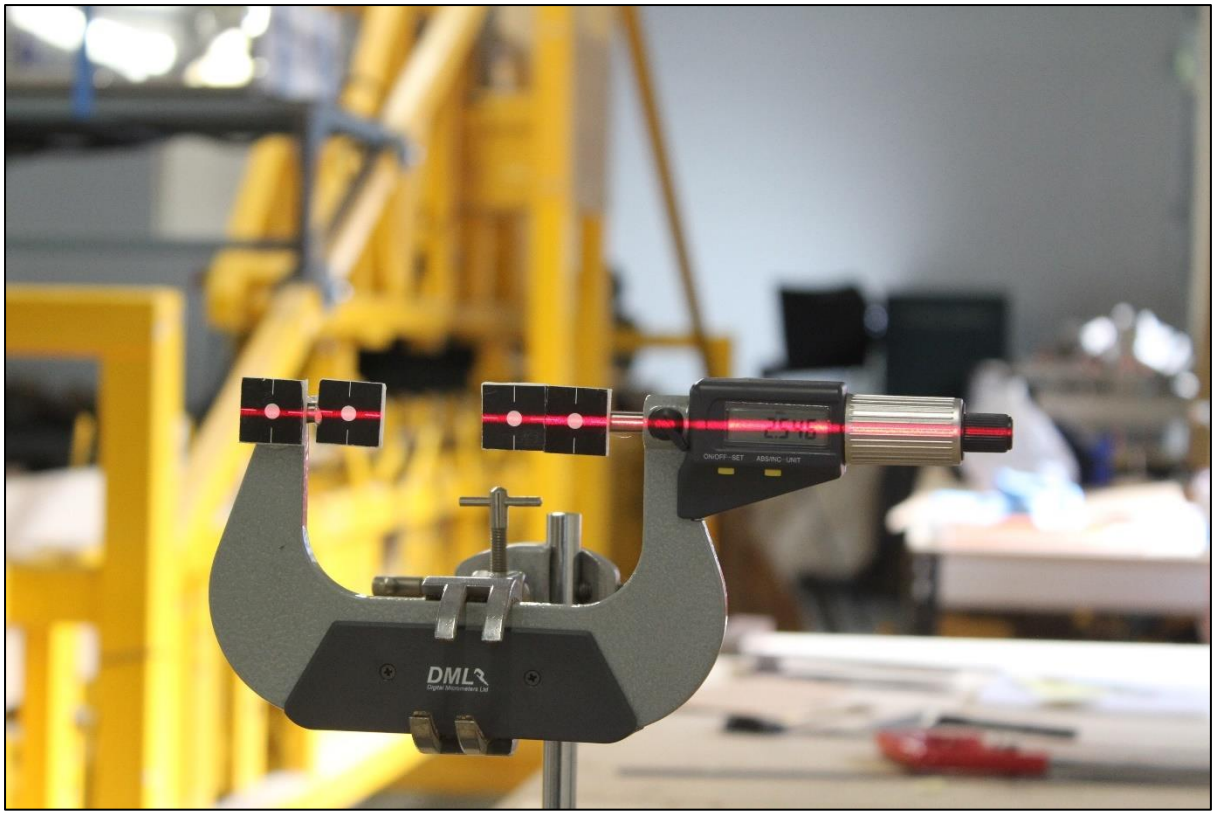

Figure 4-13: Four-point micrometre setup.

Figure 4-14: Micrometre pose cycles, left-facing to right-facing - left camera images taken from 50 cm horizontally apart from right camera images.

4.4 Results and Discussion

4.4.1 Calibration

Calibration of the stereo-camera system was performed using HALCON machine vision software with a tailor-made algorithmic procedure within the HDevelop programming environment. A summary of the processes and operations involved is displayed in Figure 4-16. The starting calibration data model was generated using internal camera parameters for the sensor and lens of the specific camera model used, and from the calibration plate descriptive file. Approximate values from the camera and lens manufacturer data are set for the starting calibration model for the focal length of the lens and sensors cell size. These values are then precisely computed by the calibration itself. The rotation angles and translation vectors were determined by location the calibration plate in each image pair, then performing a least squares solution in the software.

The following optimisation problem for multi-image calibration must be solved to calibrate the stereo system [124]:

$$d(\theta) = \sum_{l=1}^{2} \sum_{k=1}^{n_0} \sum_{j=1}^{n_m} \upsilon_{j,k,l} \, \| \boldsymbol{\pi}_r \left(\boldsymbol{m}_{j,k,l}, \boldsymbol{\theta}_{r,l} \right) - \boldsymbol{\pi}_i \left(\boldsymbol{M}_j, \boldsymbol{\theta}_{i,l} \right) \|^2 \rightarrow \min . \tag{4.6}$$

where n_m is the number of calibration marks. n_0 is the total images used for calibration. $\boldsymbol{M}_j$ denotes the positions of the calibration marks, $\boldsymbol{m}_{j,k,l}$ denotes the projection of the centres of the marks in the first set of calibration images and $\boldsymbol{m}_{j,k,2}$ denotes the second set. The vector $\boldsymbol{\theta}$ denotes the camera parameters including the interior orientations of the first and second cameras, the exterior rotations of n_0 calibration targets in the second image. $\boldsymbol{\pi}_i$ denotes the projection of a calibration mark into the image coordinate system (ICS), $\theta_{i,l}$ are the subset of camera parameters that influence this projection for the left camera, $\boldsymbol{\pi}_r$ denotes the rectification of an image point into the image plane coordinate system, $\boldsymbol{\theta}_{r,l}$ are the subset of camera parameters that influence this rectification for left camera, and $\upsilon_{j,k,l}$ is a variable that is 1 if the calibration mark $\boldsymbol{M}_j$ is visible in image $\boldsymbol{k}$ of left camera, otherwise it will be zero.

The success of the calibration was evaluated in a few of ways. Firstly, if the calibration plates marks were identified in all the images by the HALCON program, this indicates that the stereo-cameras focus, position relative to the test area, and the lighting setup were optimal for photogrammetric application. Operations to visualise the calibration marks in green colour if identified were included in the HALCON program (Figure 4-15). Secondly, the calibration error is computed and checked against acceptable values. This error corresponds to the average distance in pixels between the back-projected calibration marks and their extracted coordinates. An error of up to 0.1 pixels indicates a successful calibration [125]. Additionally, a pair of stereo-images were rectified to a common plane once the internal and external camera parameters were computed. Further details on the expressions of rectification are presented in Chapter 5. The calibration algorithm assumes that the 1st camera is the left camera, and the 2nd camera is right of the 1st camera. If images have been used in reverse order, they will appear upside down when the rectification is performed. If the calibration was successful, the row coordinates of the conjugate points will match, and by displaying the images they should visibly align. The origin of the WCS, which is required for accurate 3D measurements, is equal to the left camera coordinate system.

The calibration was successfully performed for both tests and returned all the required internal and external camera parameters, which are presented in Table 4-1 to 4-4. The calibration plate marks were identified successfully in the entire 45 and 65 pairs of images, respectively, by the calibration program, which was confirmed by visualising the entire process. Once the calibration was computed, the error in pixels was returned (Figure 4-18). The error returned was 0.042253 pixels from the first 45 image calibration, indicating a highly effective and accurate calibration. The error returned from the second 65 image calibration was 0.0314675 pixels, indicating another highly accurate calibration. Additionally, a pair of stereo-images were rectified to a common plane post calibration as described. The image pairs were successfully rectified after both calibrations. An example is displayed in Figure 4-18. Once calibrated, the stereo-camera system was not moved or touched at all prior to conducting further experiments, otherwise any subsequent results would be invalidated, and re-calibration would be needed.

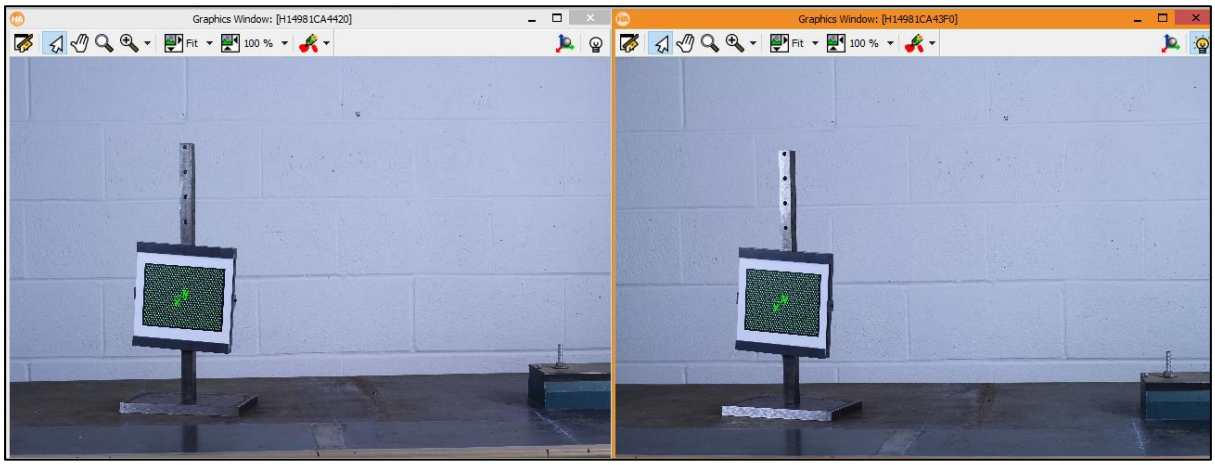

Figure 4-15: Calibration plate marks identified in HALCON.

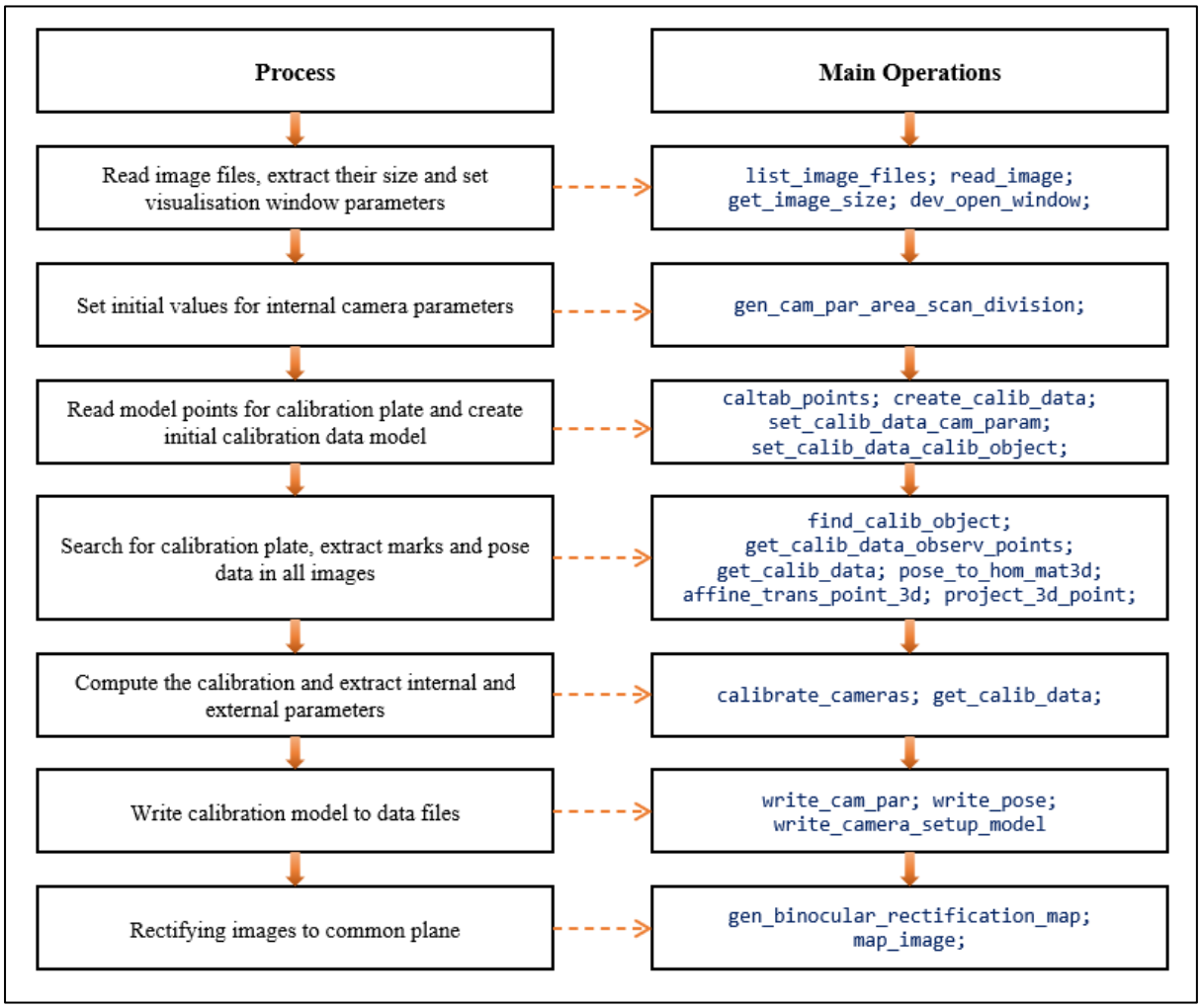

Figure 4-16: Calibration process and main operations in HDevelop.

Table 4-1: Internal camera parameters of stereo-camera system (first calibration).

Camera Parameter	Description	Unit	1st (Left) Camera	2nd (Right) Camera
Focus	Focal length of lens	m	0.0521705	0.0519504
Kappa	Radial distortion coefficient	m^{-2}	-33.0869	-36.7509
S_x	Width of a cell on CCD-chip	m	$4.3e^{-006}$	$4.3e^{-006}$
S_y	Height of a cell on CCD-chip	m	$4.3e^{-006}$	$4.3e^{-006}$
C_x	x coordinate of image centre	Pixels	2595.78	2597.2
C_y	y coordinate of image centre	Pixels	1727.59	1742.61
Image width	Width of images	Pixels	5184	5184
Image height	Height of images	Pixels	3456	3456

Table 4-2: 3D pose (rotation and translation) parameters (first calibration).

Translation vector (x y z [m])	x	0.467049
	y	0.00352011
	z	0.0628901
Rotation angle [deg]	Rot(x)	0.223836
	Rot(y)	350.768
	Rot(z)	0.0847393

Table 4-3: Internal camera parameters of stereo-camera system (second calibration).

Camera Parameter	Description	Unit	1st (Left) Camera	2nd (Right) Camera
Focus	Focal length of lens	m	0.0521711	0.052057
Kappa	Radial distortion coefficient	m^{-2}	-34.48	-36.6443
S_x	Width of a cell on CCD-chip	m	$4.3e^{-006}$	$4.3e^{-006}$
S_y	Height of a cell on CCD-chip	m	$4.3e^{-006}$	$4.3e^{-006}$
C_x	x coordinate of image centre	Pixels	2599.16	2578.53
C_y	y coordinate of image centre	Pixels	1729.43	1756.81
Image width	Width of images	Pixels	5184	5184
Image height	Height of images	Pixels	3456	3456

Table 4-4: 3D pose (rotation and translation) parameters (second calibration).

Translation vector (x y z [m])	x	0.459753
	y	-0.00185887
	z	0.0666333
Rotation angle [deg]	Rot(x)	359.41
	Rot(y)	351.515
	Rot(z)	359.402

Figure 4-17: Completed calibration with error in pixels returned.

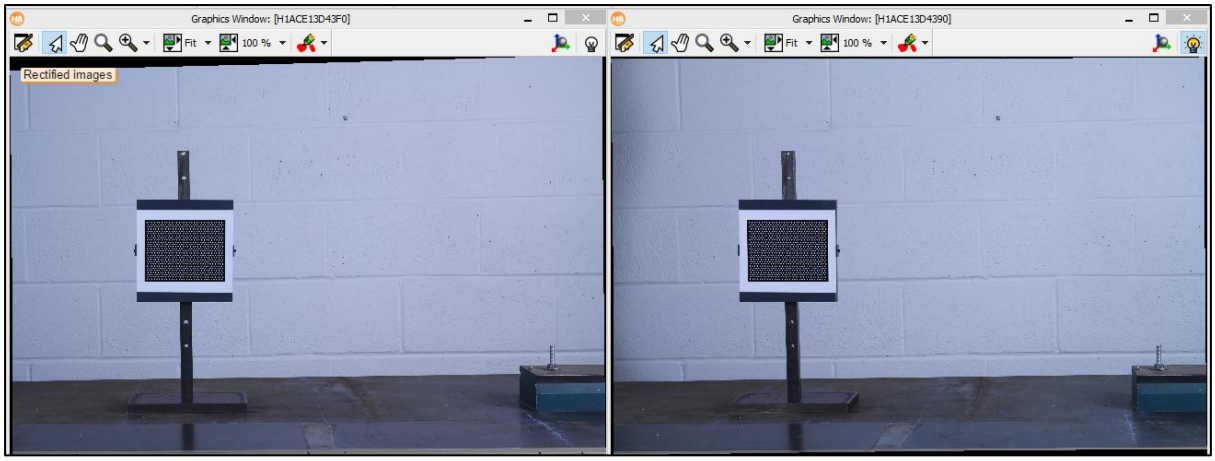

Figure 4-18: Rectified image pair.

4.4.2 Micrometre Accuracy Experiment

Despite calibration of the stereo-camera system being successful, further verification tests were also performed in the form of the developed micrometre accuracy experiment. The purpose of this experiment was to quantify the actual accuracy range for this specific target-based photogrammetric measurement application. Performing this additional layer of validation also ensures that there are no inaccuracies present with the inbuilt operators within the machine vision software.

The micrometre accuracy experiment worked by first setting the photogrammetric targets on the micrometre at a set distance apart and setting the micrometre gauge to zero, which became the reference interval. A stereo image was taken at the reference interval in 5 poses, and the 3D coordinates of the targets were computed using another tailor-made program compiled in HDevelop. Any change in lateral distance to the 'free' target then corresponded to the distance displayed on the micrometre gauge. Therefore, once the reference interval was established, it was possible to calculate the relative change in distance between the targets and compare this result with the micrometre gauge reading.

Recognition and coordinate extraction was performed in HALCON using a tailor-made program. First, the grey value of the images was segmented using a global threshold algorithm based on the pixels grey colour value. The threshold operation selects all points in the region of

interest (ROI) R, which is the part, or all the image selected for processing that lie within a specified range of grey values *g* and outputs these into a new region S. This is defined by [124]:

$$S = \left\{ (r,c)^T \in R \mid g_{\min} \le f_{r,c} \le g_{\max} \right\} \tag{4.7}$$

Where r and c are the row and column numbers of a pixel in region R. The default values of $g_{\min}$ and $g_{\max}$ were sufficient to segment the targets in the images assessed for this study. As the previous segmentation algorithm returns one region for the result, the individual components of the region separated by grey value, which are the targets, must be computed as connected components by defining pixels with commonalities.

Some further filtering algorithms were then applied to remove unwanted features from the image, based on the characteristics of target size and shape. The area a is the simplest region to be filtered and is defined as [124]:

$$a = \mid R \mid = \sum_{(r,c)^T \in R} 1 = \sum_{i=1}^{n} \left(ce_i - cs_i + 1 \right) \tag{4.8}$$

where cs_i and ce_i are the start and end pixel's column number of the i_{th} run of a region extracted. Therefore, the area a is simply the number of point's $\mid R \mid$ in the region. Additionally, the circular shape of the targets was computed using the circularity algorithm [125]:

$$C' = \frac{F}{\left(\pi \max^2 \right)}, \qquad C = \min\left(1, C'\right) \tag{4.9}$$

Where the shape factor C of a perfect circle is 1.0, F is the area of the region and 'max' is the maximum distance from the centre to all contour pixels. Then the centre point of each target was calculated as the mean value of the line or column coordinates respectively of all pixels in the region, which is the area of each target. The targets were also sorted chronologically into tuples in order of top-to-bottom, left-to-right.

The results from the 105 micrometre data intervals from both tests have been summarised in Table 4-5 and Table 4-6. Aside from the reference interval, which was taken in 5 poses, the other intervals were each captured in 25 poses (5 orientations at 4 positions along the test plane). The distance between photogrammetric targets at each position were calculated from their extracted world coordinate data using the following standard equation of 3D geometry:

$$\text{Distance} = \sqrt{\left(X_1 - X_2\right)^2 + \left(Y_1 - Y_2\right)^2 + \left(Z_1 - Z_2\right)^2} \tag{4.10}$$

where X_1, Y_1, Z_1 and X_2, Y_2, Z_2 are the world coordinates of the two extracted target points. Then the relative displacement between targets was calculated as the difference between the calculated distances between each interval and the reference interval. The error percentage between the stereo-vision system and the micrometre dial reading was then calculated by the following standard equation:

$$Error\% = \frac{D_{stereo} - D_{mic}}{D_{mic}} \cdot 100 \tag{4.11}$$

where D_{stereo} is the distance measured by the stereo-vision system and D_{mic} is the distance measured by the micrometre dial.

Table 4-5: Two-target micrometre accuracy test results.

Interval	Dial Reading (mm)	Photogrammetric Distance (Avg) (mm)	Distance Between Target and Zero (mm)	Avg Error (%)
Reference	0.00	86.674	-	-
1	5.728	92.419	5.745	0.382
2	10.17	96.875	10.201	0.461
3	13.981	100.656	13.982	0.549
4	4.457	91.100	4.426	0.695

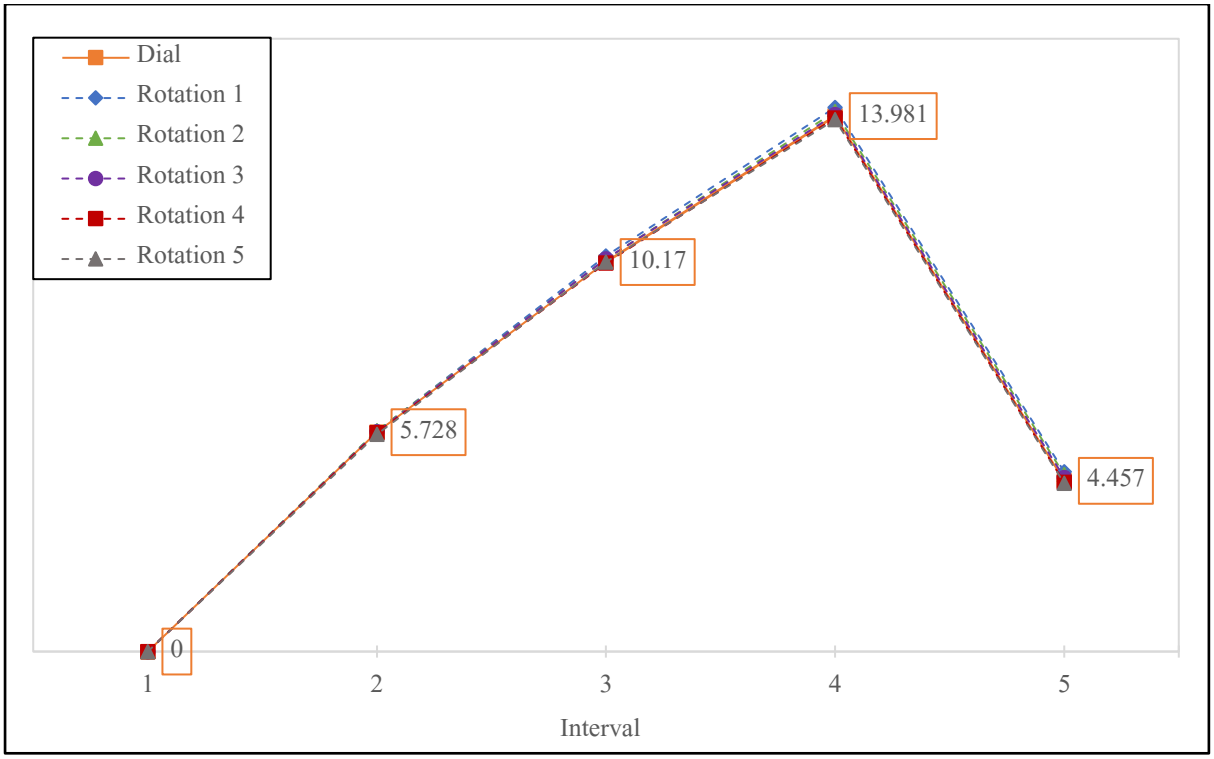

Figure 4-19: Two-target micrometre correlation between dial reading and photogrammetric targets.

Table 4-6: Four-target micrometre accuracy test results.

Interval	Dial Reading (mm)	Ext. Target Dist. (Avg) (mm)	Int. Target Dist. (Avg) (mm)	Dist. Target-Zero Ext. (mm)	Dist. Target-Zero Int. (mm)	Avg Error Ext. (%)	Avg Error Int. (%)
Reference	0.00	49.496	91.777	-	-	-	-
1	2.546	52.025	94.341	2.527	2.561	0.729	0.619
2	5.089	54.574	96.880	5.078	5.103	0.269	0.335
3	7.626	57.107	99.411	7.611	7.634	0.228	0.113
4	2.548	52.039	94.339	2.543	2.562	0.411	0.715

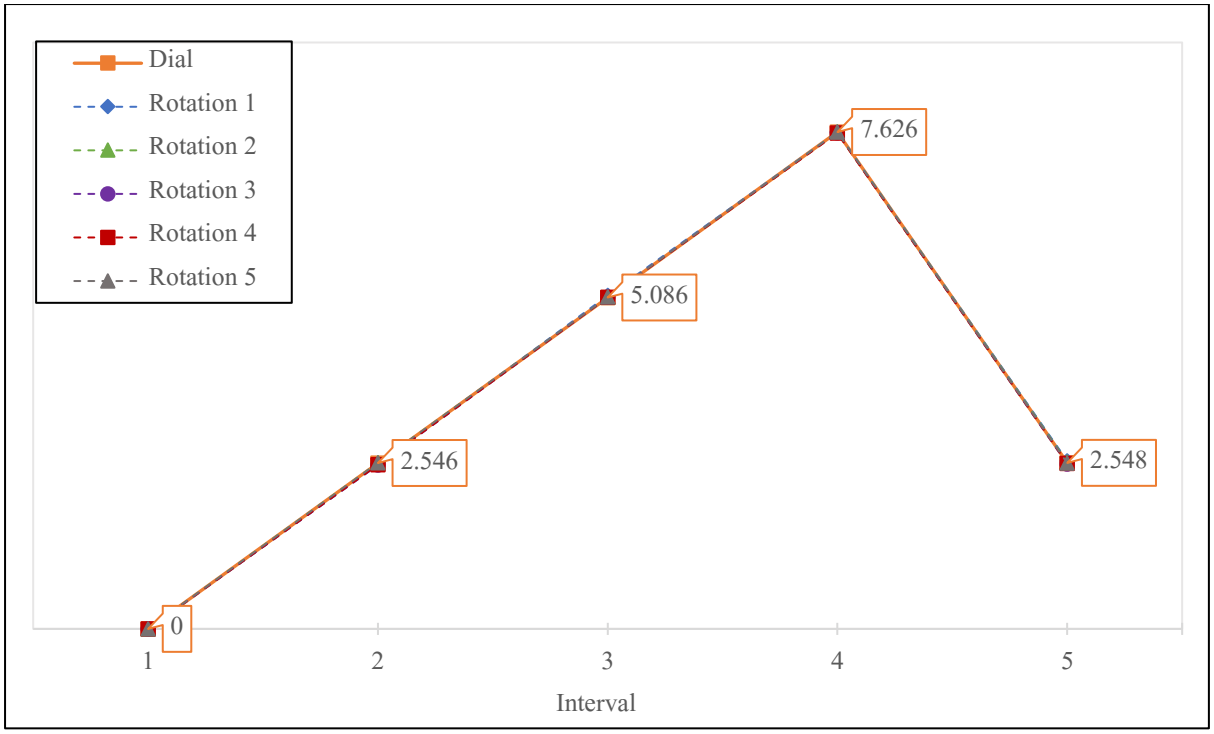

Figure 4-20: Four-target (internal) micrometre correlation between dial reading and photogrammetric targets.

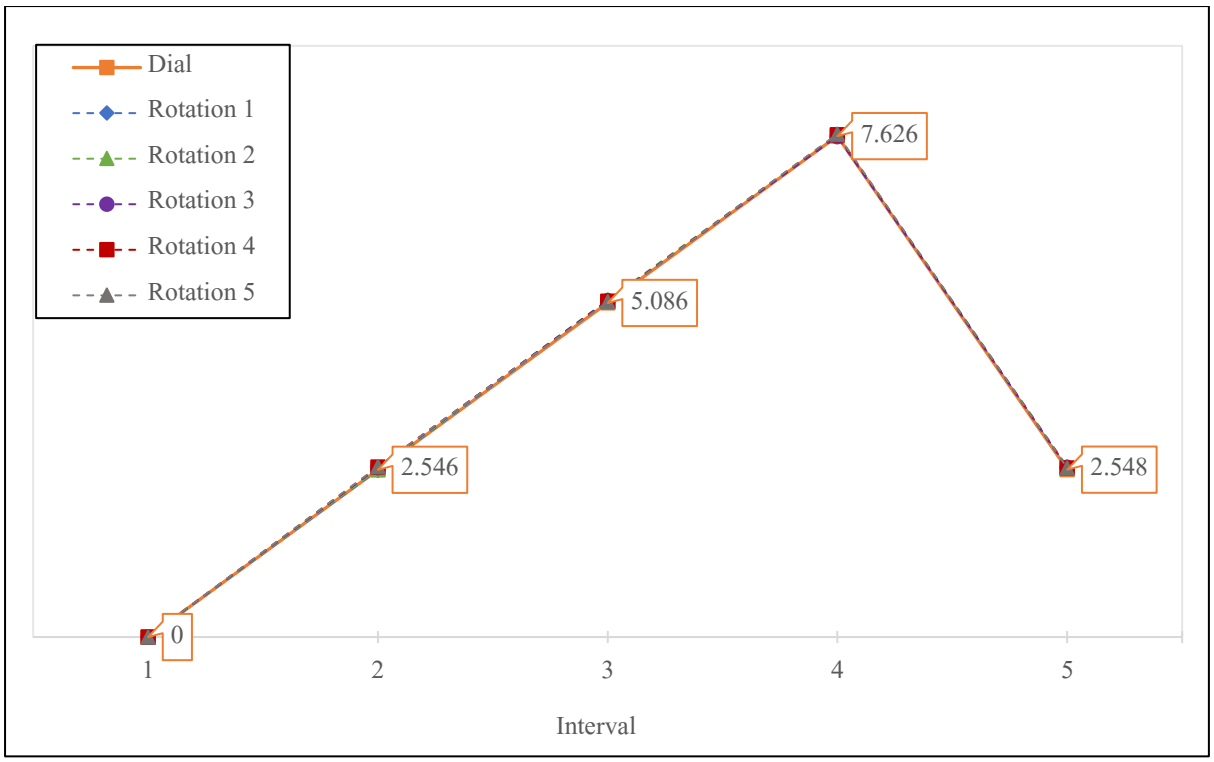

Figure 4-21: Four-target (external) micrometre correlation between dial reading and photogrammetric targets.

In the two-target micrometre test, out of 105 data points, 7 anomalies with unusual readings were removed from the results, which may have occurred due to an error with positioning the micrometre with excess rotation, or with image taking or lighting at that point. The micrometre spindle distance was not changed within the intervals as confirmed by dial readings reinforcing that these were likely anomalies. In the four-target micrometre test, only 1 anomaly with unusual reading was present and removed from the results. When working at such ranges of high precision as with the micrometre and target-based photogrammetric approach, the aim was to consistently achieve measurements with less than 1% error compared with micrometre gauge readings. By observing the results from both experiments, this was successfully achieved across all intervals, so confidence can be had in the measurement accuracy of the calibrated stereo-vision system and target setup.

4.5 Summary and Conclusions

- The development, optimisation, and measurement accuracy verification of a non-contact, tailor-made displacement measurement system was undertaken in this study based on binocular stereo-vision principles, for the purpose of measuring torsional displacements in structural glass beams experimentally.

- A cost-effective experimental setup with readily available equipment was utilised for the photogrammetric system, in combination with HALCON machine vision software to perform calibrated displacement measurement tasks.

- Two separate calibrations were performed for measuring tasks using a standard HALCON calibration object, which were accuracy-verified by confirming the pixel error to be well below 0.1, the calibration object being identified in all image pairs, and by correctly rectifying images to a common plane.

- A tailor-made micrometre accuracy experiment was setup and performed for both calibrations, with setups encompassing two- and four-targets attached to a digital micrometre for non-contact displacement measurement evaluation.

- In both cases, the measurement accuracy of the calibrated photogrammetric system proved to be extremely high for target-based applications, with both experimental results being below 1% measurement error across all intervals. There was also no significant difference in errors between the two- and four- target measurements proving its efficacy for measuring *z*-axis displacements (depth).

- It was concluded that the employed equipment, setup, and calibration procedures were accurate, reliable, and effective for target-based displacement measurement tasks, and could therefore be applied as an alternative, non-contact measurement solution for glass beam experimentation.

5. Initial Torsion Study – Introducing the Equivalent-Sectional Shear Modulus

This chapter presents a concise concept for quantifying the torsional shear stiffness of laminated structural glass beams experimentally, termed the 'equivalent-sectional shear modulus (ESSM)'. Torsion experiments were performed on monolithic, and 2-layer PVB and SGP laminated glass beams. Displacements were measured using the developed photogrammetric approach with a specialised formation of targets. The ESSM method was validated for the monolithic beam against the known shear modulus of glass. The ESSM method was then compared against two existing analytical models for PVB and SGP beams.

This chapter relates to the authors peer-reviewed publication:

Uheida, K. et al. *Determining equivalent-sectional shear modulus in torsion tests for laminated glass beams using photogrammetry method*. Composite Structures, 2021. 276, 114572.

https://doi.org/10.1016/j.compstruct.2021.114572

5.1 Samples and Equipment

5.1.1 Test Specimens

The experimental procedure was designed to perform structural-sized, non-destructive torsion tests on monolithic, PVB and SGP laminated glass beams to evaluate the shear modulus, or the ESSM in these types of beams. To accurately measure the deformation in torqued beam samples, a close-range non-contact photogrammetry method was employed and evaluated in terms of its measuring accuracy. The three different structural glass beam types examined (Table 5-1) were 2.4 m long with a length-to-height ratio of 10:1. All beams were (thermally) toughened and have been heat-

soaked post manufacture to reduce the risk of nickel-sulphide failure during testing [26]. Two pairs of beech wood inserts were used to cushion the glass-steel clamp contacts at both ends of the glass beam (Figure 5-1). The first sample, MONO1, is a monolithic beam of 10mm width (b). The second sample, 2PVB1, is a two-ply laminated beam with a polyvinyl butyral (PVB) interlayer. The third sample, 2SGP1, is a two-ply laminated beam with a SentryGlasPlus (SGP) interlayer. Glass plies for laminate samples are 10mm each with 1.52mm interlayers. Table 5-2 lists some of the relevant listed material properties for soda-lime silica glass for convenience.

Table 5-1: Test samples (* = toughened, ** = heat-soaked).

ABBREV	Length (mm)	Height (mm)	Thickness (mm)	Glass Type	No. Glass Plys	Composition (mm)
MONO1	2400	240	10	T*, HS**	1	10
2PVB1	2400	240	21.52	T*, HS**	2	10 | 1.52 | 10
2SGP1	2400	240	21.52	T*, HS**	2	10 | 1.52 | 10

Table 5-2: Material properties of soda-lime silica glass (* bending strength from basic annealed to thermally-toughened) [3, 8, 128].

Material Property	Value
Characteristic bending strength* $f_{g;k}$	45 N/mm^2 to 120 N/mm^2
Density ρ	2500 kg/m^3
Young's modulus E	70,000 N/mm^2
Shear modulus G	28,700 N/mm^2
Poisson's ratio μ	0.23 [128]

Figure 5-1: Clamp and inserts.

5.1.2 Target Marking

All beam samples were set up with small 5 mm diameter circular targets as it is simple to accurately extract the centre points of circles. These have been arranged into columns at even distance apart (Figure 5-2), and act as points of interest for displacement measurement. To maximise the visibility and readability of targets when extracting the data, a contrasting grey colour value between targets and background was used. White targets on a black background were plotted to strips of adhesive label and stuck to the beam face parallel to each other, with 70 mm horizontal spacing and 15 mm vertical spacing between each target. Additionally, thin reticules are plotted between targets to aid in the target recognition process. Considering that the adhesive paper may not deform at the same pattern or rate with the glass surface, the paper connecting two adjacent target points in a column line were cut through with a sharp-blade knife to make sure there were separated to avoid the interference of each other during the test. There will usually be a small variation in the spacing between columns from human error due to cutting, measuring, and placing. However, the exact measurements are calculated from the images taken in the calibrated binocular stereo-vision

system, therefore in a properly calibrated system the real location of each target will be accurate and reliable.

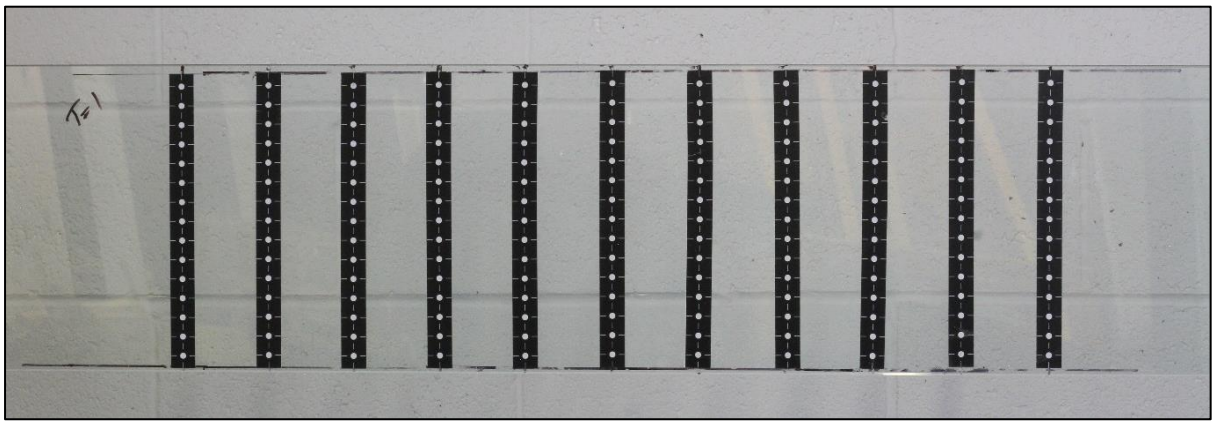

Figure 5-2: Beam target setup.

5.1.3 Torsion Machine

The torsion testing machine manufactured by Tinius Olsen outputs roughly 1 kN-m of pure torsional force (Figure 5-3). It is comprised of one fixed end and one free end allowing for rotation. The rig is fixed to a 5.6 m long heavy steel bench, which allows for adjustments in length at the fixed end. Chuck jaws are situated at each end with open hexagonal connection points from which clamps can be fixated. The clamps and clamp inserts were custom designed for these experiments for the required size of test samples and were manufactured at the Edinburgh Napier University fabrication and welding laboratories. The clamps were fabricated in steel for strength and stability, whilst a combination of hard beech wood and plastic were used for the inserts to prevent any surface damage from direct steel-to-glass contact. A control PC with Test Navigator software is linked to the torsion machines sensory system to provide the outputs of angle of twist (°) at the machines rotating end, and torsional force in kN-m.

5.1.4 Illumination

The goal of illumination is to make important features of the specimen visible and to suppress undesired features, so that they can later be processed in the machine vision software. To do so, consideration must be given to how light interacts with the object [30]. When working with glass samples, glare from lighting is an important consideration and must be limited as much as possible as this can interfere with the visibility when inspecting points of interest. Setting optimal lighting conditions is therefore of high importance for test images. As standard lights or lamps will reflect to a high degree, a soft box lighting kit was set up to illuminate the test area without causing excessive glare. Additionally, a polarising lens filter was fitted to each camera as there can still be some moderate glare on the test samples causing some difficulty in inspecting points of interest, even with the soft box lights. Furthermore, the direction from which specimens are illuminated must be considered in the setup, as this will continually alter as the specimen rotates under torsion.

5.2 Binocular Stereo-Vision System

5.2.1 Components

The primary components of the setup are the cameras and their lenses. In this case due to the low data processing load from the images an inexpensive setup can be comfortably used. Two linked Canon EOS 70D cameras with 50 mm Canon EF f/1.8 II fixed focal lenses were used, with the two-camera setup defining the system as ‘binocular’ stereo. Cameras were fixed to the left and right of a tripod and linked using a splitter and shutter. A third camera and tripod were set up and additionally linked to the system to acquire data images from the Test Navigator software on the control PC’s monitor. This allows the torsion machine data (end rotation, torsional force) to be matched with each stereo image pair.

5.2.2 Pinhole Model

The reconstruction of a 3D scene from 2D images that is taken by cameras with optical lenses is mathematically described by the pinhole model [124], which is based on perspective projection. The camera lens is represented by its optical centre, which corresponds to a point between the 3D scene and 2D image plane and the optical axis which is perpendicular to the plane defined by the lens and passes through the optical centre. The image, camera, and world coordinate systems (*ICS*; *CCS*; *WCS*) are presented in Figure 5-4. The camera coordinate system at the lens is at distance of the focal length *f* to the image coordinate system at the image plane, which is at the sensor. The world coordinate system is set to match the camera coordinate system of the left camera, which makes it possible to determine the spatial position of the right camera in relation to the left. Lens distortions (Figure 4-9) can cause the 3D world point *P* not to lie on a straight line through the projection centre, which are fixed by calibration.

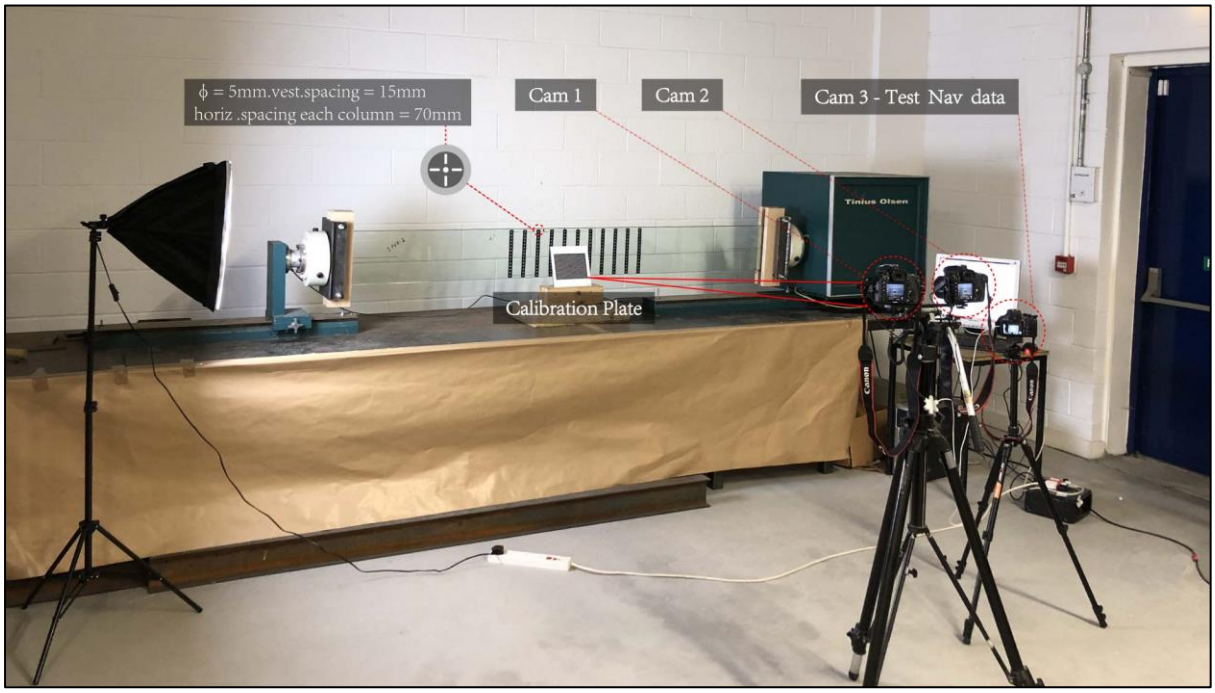

Figure 5-3: Test setup.

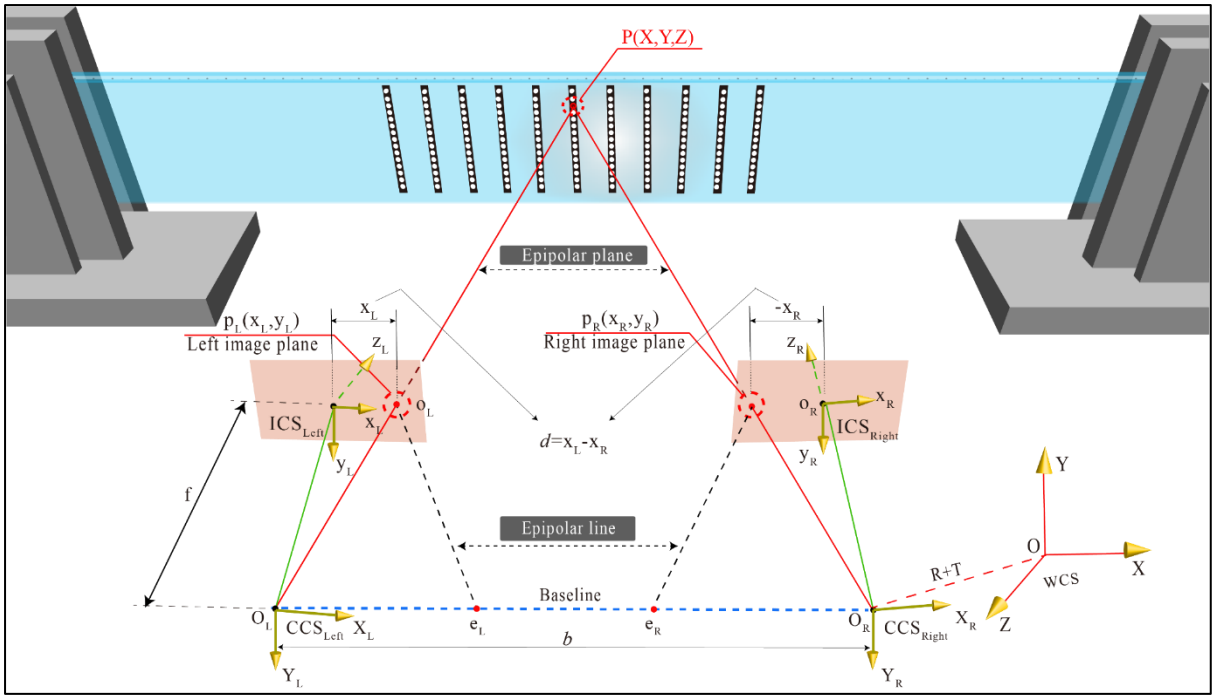

Figure 5-4: Binocular stereo-vision principle depicting a beam target as object point P .

5.2.3 Calibration

To calibrate the stereo-vision system, the location of 3D points in the world coordinate system must be known and related to their image projection. The calibration in this work was performed by taking multiple image pairs of a highly-accurate, 160 x 120 mm ceramic planar calibration plate supplied by MvTec with exactly known dimension and grey colour properties. Several poses were used to acquire an accurate calibration. A data file with full dimensional properties corresponding to the calibration plate was read within the machine vision software HALCON. To locate the calibration plate within the program the entire rectangular target area must be visible in both images per stereo image pair. In the 3D setup of the binocular stereo-vision system, Object point P is any point on the calibration plate during the calibration process.

Once the calibration process is complete, the setup must not be moved otherwise coordinate data for targets are not relatable to the calibrated system and will thus be invalidated. For the calibration method in this study, images of the calibration plate were taken in six different orientations at six different positions around the target area of the beam (36 stereo-image pair's

total), as although around 10 poses are usually sufficient for accurate calibration, the authors used a larger number of poses to overcompensate for any cases where some images may be unreadable. It should be noted that the study in this chapter was performed prior to the calibration plate holder from Chapter 4 being fabricated, therefore the calibration plate was positioned using wooden blocks at this time. A calibration image pair with the plate at a left-tilted pose is displayed in Figure 5-5.

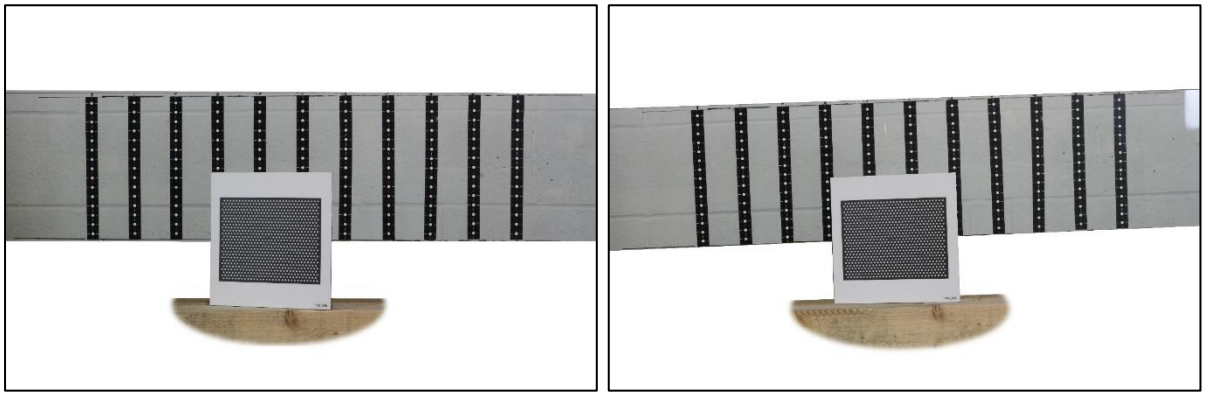

Figure 5-5: Calibration image pair taken by left and right cameras, respectively.

5.2.4 Stereo Reconstruction

3D scene reconstruction can be performed once the camera and pose parameters have been determined through calibration. Before reconstruction the stereo-image pairs must be rectified, meaning that the conjugate points are projected to one common plane which corresponds in parallel to the baseline in Figure 5-4. This can be viewed as acquiring stereo-image pairs with a virtual camera system where optical centres and focal lengths are the same as in the real system, however the orientation of the cameras are rotated so they are looking parallel and with collinear x-axes so both image planes are in correspondence.

Firstly, the spatial and positional relationship between both cameras in the binocular-stereo system can be expressed through the following rigid transformation [124]:

$$Pc_{left} = R_r Pc_{right} + T_r \tag{5.1}$$

Where Pc_{left} is the coordinate of the left camera. Pc_{right} is the coordinate of the right camera. Rr is the rotation matrix and T_r is the translation vector. Then the reconstruction of 3D points is determined from the epipolar geometry as depicted in Figure 5-4. Corresponding points P_L and P_R are projects of world point P, epipoles e_L and e_R also intersect with the image plane to form epipolar lines of intersection, and optical centres O_L and O_R have their lines of sight projected to form the epipolar plane. Then the known epipolar geometry allows corresponding features to be reduced to one dimension. The rectification of image pairs to the common epipolar geometry is then expressed by [125]:

$$X_L = f\frac{X}{Z} \tag{5.2}$$

$$X_R = f\frac{X-b}{Z} \tag{5.3}$$

$$Z = \frac{b\,f}{\left(X_L - X_R\right)} = \frac{b\,f}{d} \tag{5.4}$$

where f is the focal length, d is the disparity between the two image locations of the conjugate points and b is the baseline as displayed in Figure 5-4.

5.2.5 Target Recognition and Coordinate Extraction in HALCON

The processing and extraction of data for these experiments were performed using MVTec's HALCON software and the in-built development tool HDevelop, which includes an integrated database of operators for many machine-vision functions and therefore tailor-made algorithms can be developed in a time-effective manner. Figure 5-6 shows the procedures and main operations performed in HALCON to process and extract stereo-images and their relevant data.

The calibration data model was first created and set based on the calibration that was just performed, by reading the internal and external camera parameters from the data files generated.

The circular targets that were set to the test specimens were first recognised using machine vision techniques based on specific features such as shape, size, and colour (grey) value as shown in Figure 5-7, using the same procedures as the previous chapter (4.3.2). The grey value range used was from $g_{\min}$ = 128 to $g_{\max}$ = 255, and this was sufficient to segment and identify all targets. In cases where recognition is more difficult this can be modified by checking the grey value histogram for each image in the software. In cases where there are large random fluctuations in the grey value histogram a smoothing filter operation can be applied. As the previous segmentation algorithm returns one region for the result, the individual components of the region separated by grey value, which are the targets, must be computed as connected components by defining pixels with commonalities. The area of each circular target was filtered and computed, and the circular shape of the targets was computed using the circular algorithm as applied in the previous chapter.

Centre point coordinates of each target were computed and extracted by the program. The x, y and z coordinates were computed from the image coordinates of the respective conjugate points from each stereo image pair to determine the 3D position of targets, and returns these in the CCS, which is that of the first (left) camera. The resulting pose was then converted into a homogeneous transformation matrix, then inverted to represent the transformation from the rectified CCS into the WCS. Finally, the 3D coordinates were transformed in this regard.

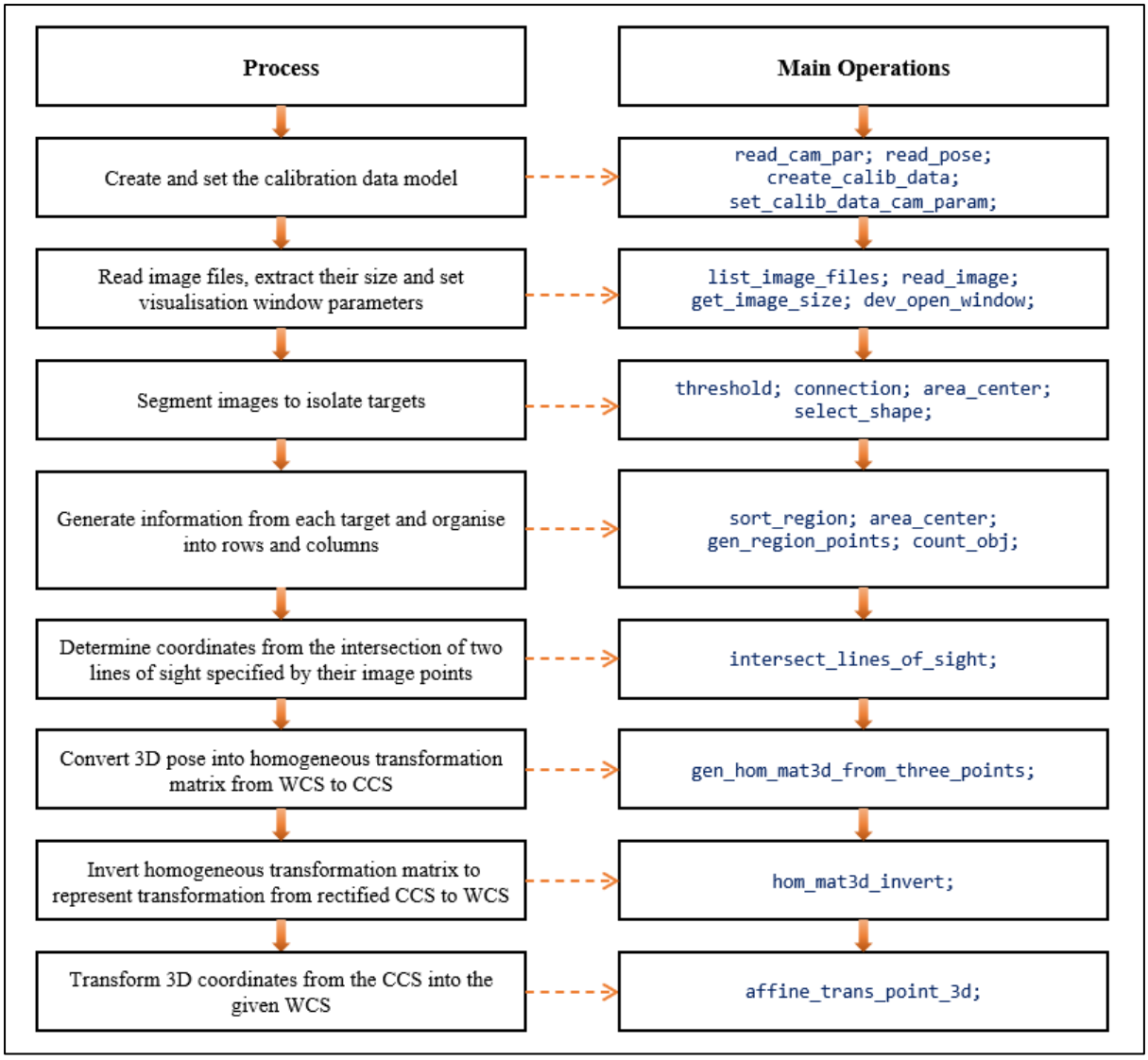

Figure 5-6: Target processing in HALCON.

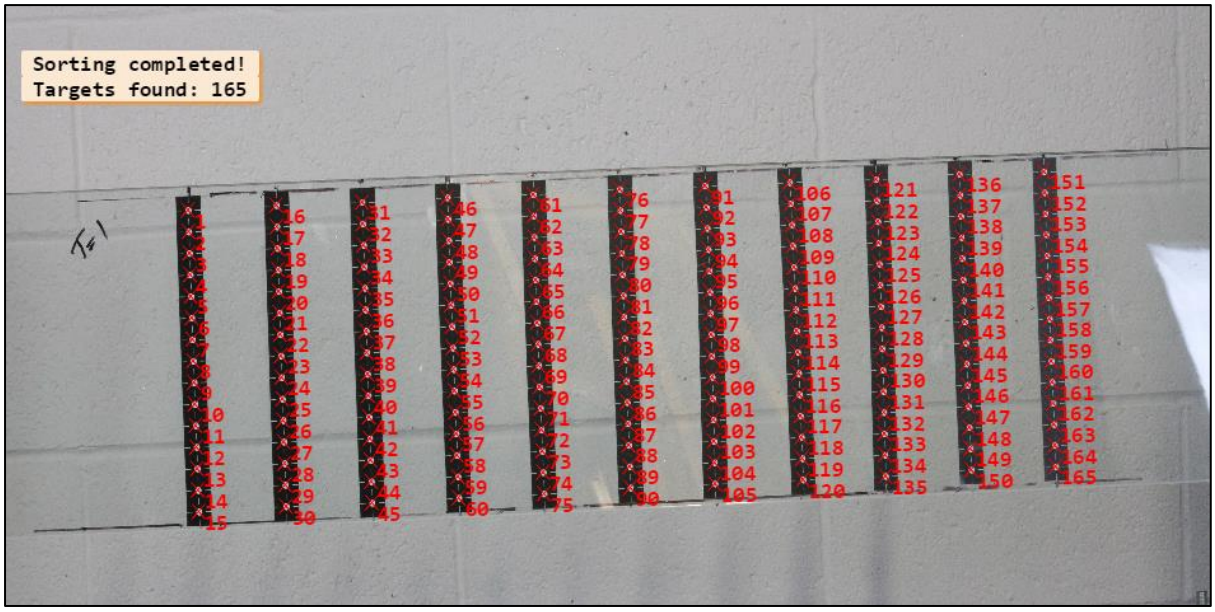

Figure 5-7: Extracted targets and centres in HALCON.

5.3 Experimental Procedure

5.3.1 Accuracy Experiment

To validate the measuring accuracy of a calibrated stereo-vision system the measurement uncertainty can be evaluated by simple experimentation using a trusted and accurate existing device. Therefore, a digital micrometre measurement test method was performed using the calibrated system. This micrometre measurement test was designed to investigate the error between the dial reading and the calculated distance using the stereo-vision system.

Two target marks were set to two points on the micrometre, one target at a fixed position on the left end next to the anvil which remains stationery, while the second target was fixed to the spindle and moves laterally with any change in distance on the micrometre. The dial was set to zero and a reference image pair was taken. The dial was then moved along an interval by a spindle turn and the next image pair was taken (Figure 5-8). This process was repeated four-to-five times. The world coordinates for the centres of each target were computed using the methods in section 5.2.4. The distance between two targets at each interval was then calculated using basic 3D geometrics. The change in distance from the distance between the two points at reference, and the distance at

each interval based on the photogrammetric approach was calculated and compared with micrometre gauge readings to verify the measurement accuracy of the calibrated system.

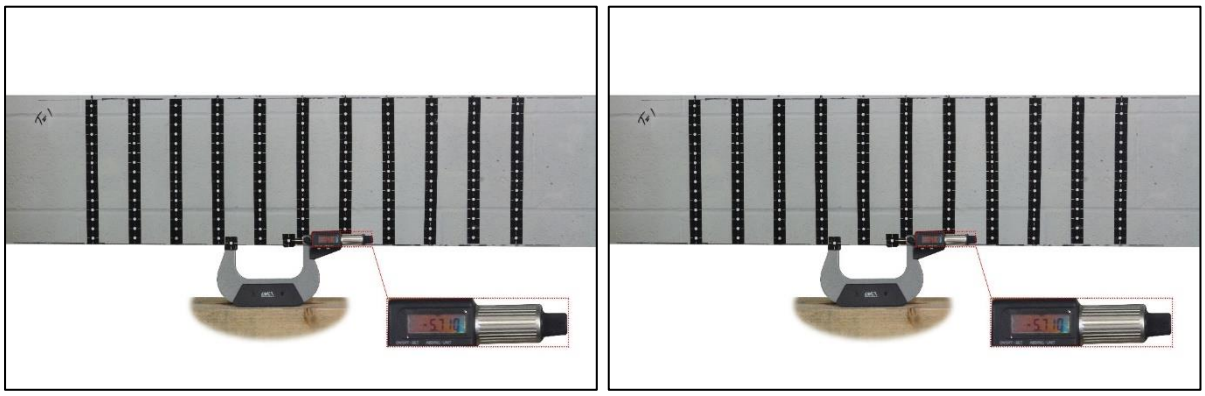

Figure 5-8: Micrometre test at zero (left) and interval (right) – left image taken from camera positioned horizontally apart from right camera image.

5.3.2 Torsion Test

As there is yet to be evidence of any standardised torsion test procedure for structural glass beams, this torsion test method has been developed by accounting for the material characteristics and behaviour of glass and laminated glass slender rectangular beams, and previous beam torsion experiments on other beam types such as timber [92, 98, 99, 102, 121].

Initial parameters such as the cross-sectional dimensions of the beam and the load-rate were set, which was to the machines default of 4° per minute. The temperature in the test facility is kept constant at ~ 20°c which was checked by thermometer. Firstly, each test sample was preloaded to a ~ 5° angle, as generally when clamping the beam some residual compressive stresses can build up at points of fixation and have some effect on the accuracy of results. Additionally, there may be a small amount of 'jump' in the rotation mechanism at the point of initiation. Concluding the preload, the test was paused, the torque angle and force were reset to zero (while the sample remains in its preloaded position) and a reference image pair is taken.

The torsion test (Figure 5-9) was then performed at the specified load-rate and stereo-image pairs were taken at consistent intervals. The third linked camera also simultaneously captured the image of the Test Navigator display on the control PC to relate the angle of twist and torsional force data to each stereo-image pair. The intervals for each sample were varied as laminated samples, particularly SGP, have higher torsional stiffness so are more resistant to torsional force, therefore larger intervals will result in a low number of data intervals. The tests were performed close to the machines output capacity of 1 kN-m. To conclude each test, the loading was ceased, and the final images were taken before returning the machine to zero degrees.

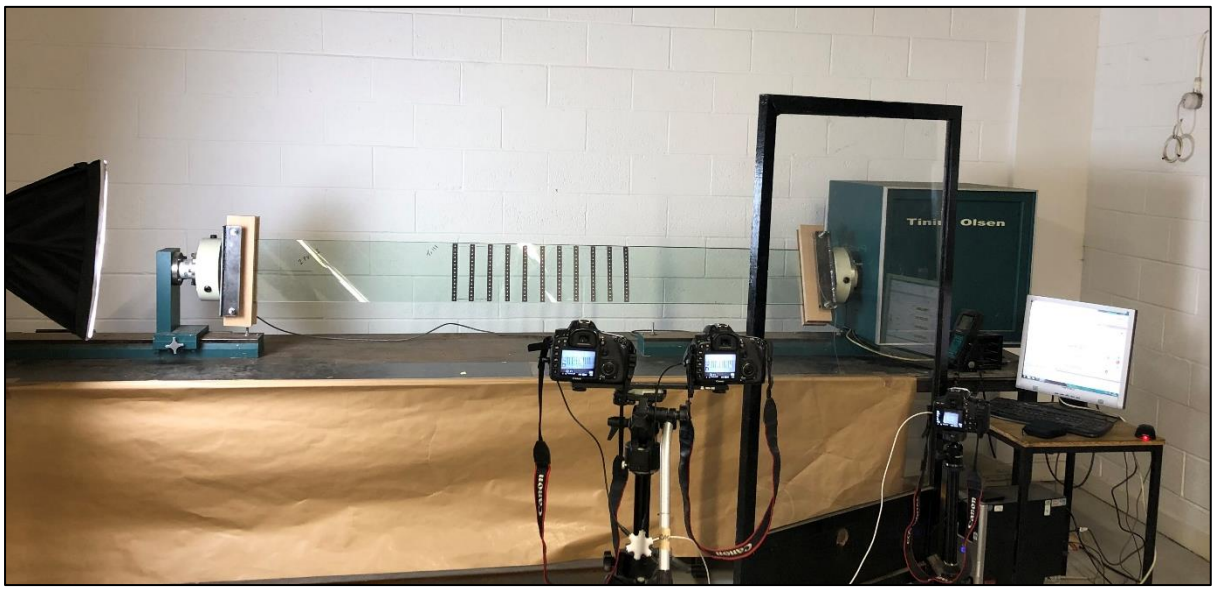

Figure 5-9: Active torsion test.

5.4 Equivalent-Sectional Shear Modulus (ESSM) Method

Saint-Venant's theory for the torsion of slender rectangular cross-sectioned elements was applied to determine the value of ESSM of the rectangular sections of the specimen tested in this study. Each rectangular section has been designated as the section between two target columns, referred to as C_i (any column) and C_{i+1} (adjacent column). The following equations based on Saint-Venants

theory are applied to determine G_{ESSM}. Firstly, the angular rotation per unit length, θ, is calculated by [31]:

$$\theta = \frac{T}{GJ} \tag{5.5}$$

Where T is the torque applied, and the Saint-Venant's torsional constant, J, is [31]:

$$J = \frac{1}{3}ht^3\left[1-\frac{192}{\pi^5}\left(\frac{t}{h}\right)\sum_{n=1,3,5,\ldots}^{\infty}\frac{1}{n^5}\tanh\frac{n\pi h}{2t}\right]. \tag{5.6}$$

Considering the dimensional properties of beam samples in Table 5-1, for the considered glass beam samples, equation (5.5) provides [31]:

$$\begin{aligned} J &= 0.3246\,ht^3 && \text{for monolithic glass beams} \\ J &= 0.3145\,h\left(t_1+t_2+t_{\text{int}}\right)^3 && \text{for laminated glass beams} \end{aligned} \tag{5.7}$$

where t_1, t_2 are thicknesses of their respective glass layers, and t_{int} is the thickness of the interlayer. Although the thickness of the sample laminated glass beams is of the order of 10-20 mm, while the width of the structural panes (beams and fins) is usually higher than 200 mm, the classical approximate solution for the elastic torsion of thin prisms with narrow rectangular section [33] can be used, according to which equation (5.5) can be approximated as:

$$J = \frac{1}{3}ht^3. \tag{5.8}$$

It is worthy to mention that caution should be taken as a perceptible difference can be noticed if this approximation is adopted. Therefore, to determine G_{ESSM}, equation (5.5) can be extended to:

$$G_{ESSM} = \frac{T}{J\theta} \tag{5.9}$$

By applying fundamental 3D geometry to the coordinates of target columns C_i and C_{i+1}, their spatial relationship to each other was determined and thus the angular rotation θ per section. In standard mathematics a plane in 3D space, which is determined by the coordinates of all targets and represents the flat target area at reference 0° of twist, can be expressed from three points by:

$$a_1x+b_1y+c_1z+d_1=0. \tag{5.10}$$

The method of least squares, a standard approach, was employed to fit the 3D plane from the coordinates of the 165 target points at initial status after pre-load. The parameters of equation (5.10) ; a_1, b_1, c_1 and d_1 were obtained from this step.

Each line of target columns in 3D space, which are determined by the coordinates of each target column, are described by:

$$\frac{x-x_0}{a_2}=\frac{y-y_0}{b_2}=\frac{z-z_0}{c_2} \tag{5.11}$$

Again, the method of least squares was employed to fit the 3D representative line of each target column at different loading stages, from which the parameters of x_0, y_0, z_0, a_2, b_2 and c_2 were obtained. Consider the above two steps are all standard approaches in linear algebra, and for the sake of brevity, the definitions of the parameters are not specified one by one.

The angle θC_i between the i^{th} target column line C_i and the reference plane (Figure 5-10) can be determined by applying the following equation:

$$\sin\left(\theta C_i\right)=\frac{a_1a_2+b_1b_2+c_1c_2}{\sqrt{\left(a_1^2+b_1^2+c_1^2\right)\left(a_2^2+b_2^2+c_2^2\right)}}. \tag{5.12}$$

The twist rate β_i of the i^{th} target column line to the neighbouring target column lines $(i+1)^{th}$ can be obtained from:

$$\beta_i = \frac{\theta C_{i+1} - \theta C_i}{l} \tag{5.13}$$

where l is the distance between the i^{th} and $(i+1)^{th}$ target column lines. The average twist rate of the target region $\bar{\beta}$ can be computed from:

$$\bar{\beta} = \frac{\sum \beta_i}{n}. \tag{5.14}$$

The average ESSM are calculated using the average twist rate of the target region.

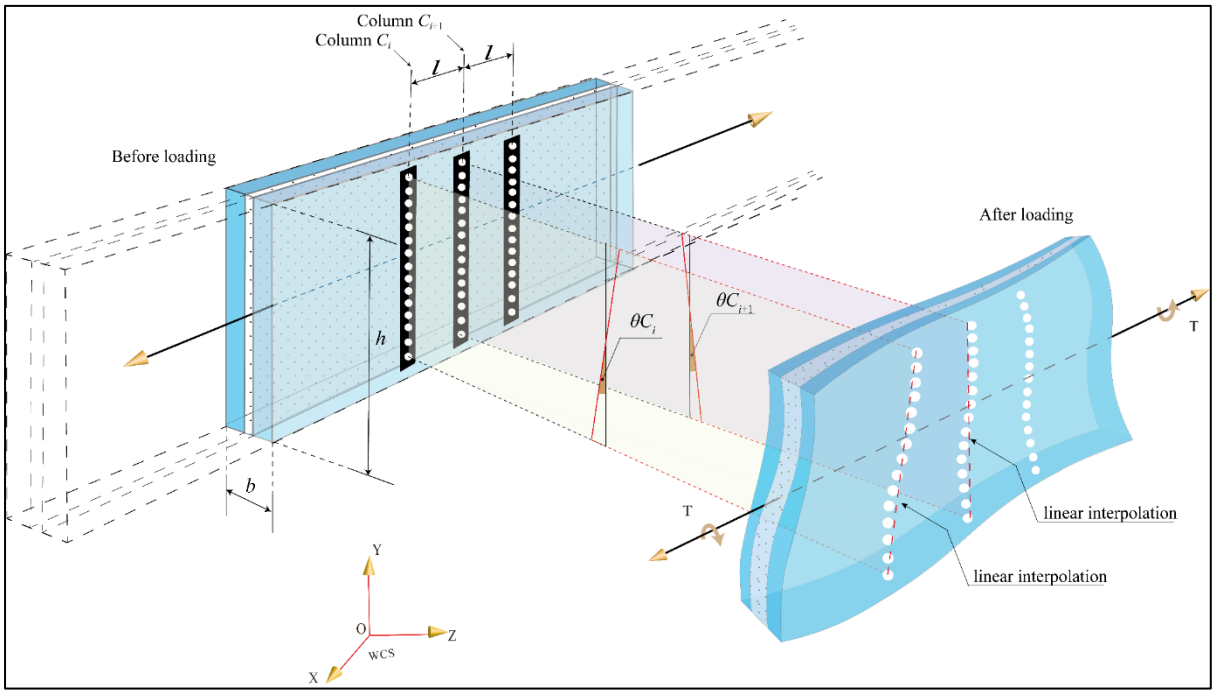

Figure 5-10: 2-layer laminated glass beam with target columns before and after torsion.

5.5 Results and Discussion

5.5.1 Validation of Photogrammetry and Torsion Test Method

Accuracy validation was performed in two stages. Firstly, at the instrumentation level, the measuring accuracy of the calibrated photogrammetric stereo-vision system was evaluated against an alternative reliable measuring device – the digital micrometre. This test proves the calibration process as shown in Figure 5-11 has been conducted properly and the photogrammetry setup at that moment provided the required accuracy for measuring the displacements of the target points attached on the surface of the glass beams. Once the calibration and the micrometre validation as shown in Figure 5-12 have been performed, the two cameras should be kept untouched until all tests completed. Once the cameras have been moved, the test setup must re-calibrate, and the micrometre validation should be conducted again to confirm the accuracy. A typical test result for the micrometre validations are displayed in Table 5-3. The displacement of target points on the micrometre ranged from around 3mm to 10mm - the typical displacement range of target points on the glass beam under torsion. A very high accuracy against micrometre dial readings was observed, with only 0.02% - 0.33% error between the two measuring systems. Therefore, a properly calibrated binocular stereo-vision system was confirmed and, furthermore, the use of small circular targets was found to be an accurate and reliable means to perform the displacement track-and-measure task.

Table 5-3: Results of photogrammetry accuracy validation.

Micrometre measurement (mm)	Photogrammetry method (mm)	Error (%)
-3.181	-3.173	0.26
-5.710	-5.712	0.03
-8.894	-8.924	0.33
-10.179	-10.155	0.24

Secondly, at structural member level, the monolithic soda-lime silica glass beam sample was used to examine the viability of the test design. As glass is an isotropic material, the theoretical

shear modulus can be calculated from its Young's modulus and the Poisson's ratio detailed in Table 5-2, i.e., $G = \frac{E}{2(1+\nu)}$, so that $G = 28.455\,\text{GPa}$. The theoretical value was then compared with the ESSM value that was computed from the torque-displacement results measured using the proposed photogrammetry method. The test results are shown in Figure 5-13, from which the ESSM value can be determined. $G_{ESSM} = \frac{T}{J\theta}$, so therefore $G_{ESSM} = 28.187\,\text{GPa}$. The ESSM value agreed well with the theoretical shear modulus. This proved that the proposed torsion test and photogrammetry method was an accurate method for measuring the shear modulus of the monolithic or laminated glass beam structures in the next step.

After these two stage validations, the PVB and SGP laminated glass beam samples were then tested with the torsion test method detailed in the Section 5.3.2. The ESSM values were calculated from the torque-rotation relationships captured by the proposed photogrammetry method detailed in this paper. The ESSM results were compared with results calculated by an analytical approach proposed by Amadio and Bedon [74], and the Enhanced Effective Thickness method for torsion proposed by Galuppi and Royer-Carfagni [79], the details of which are presented in the following section.

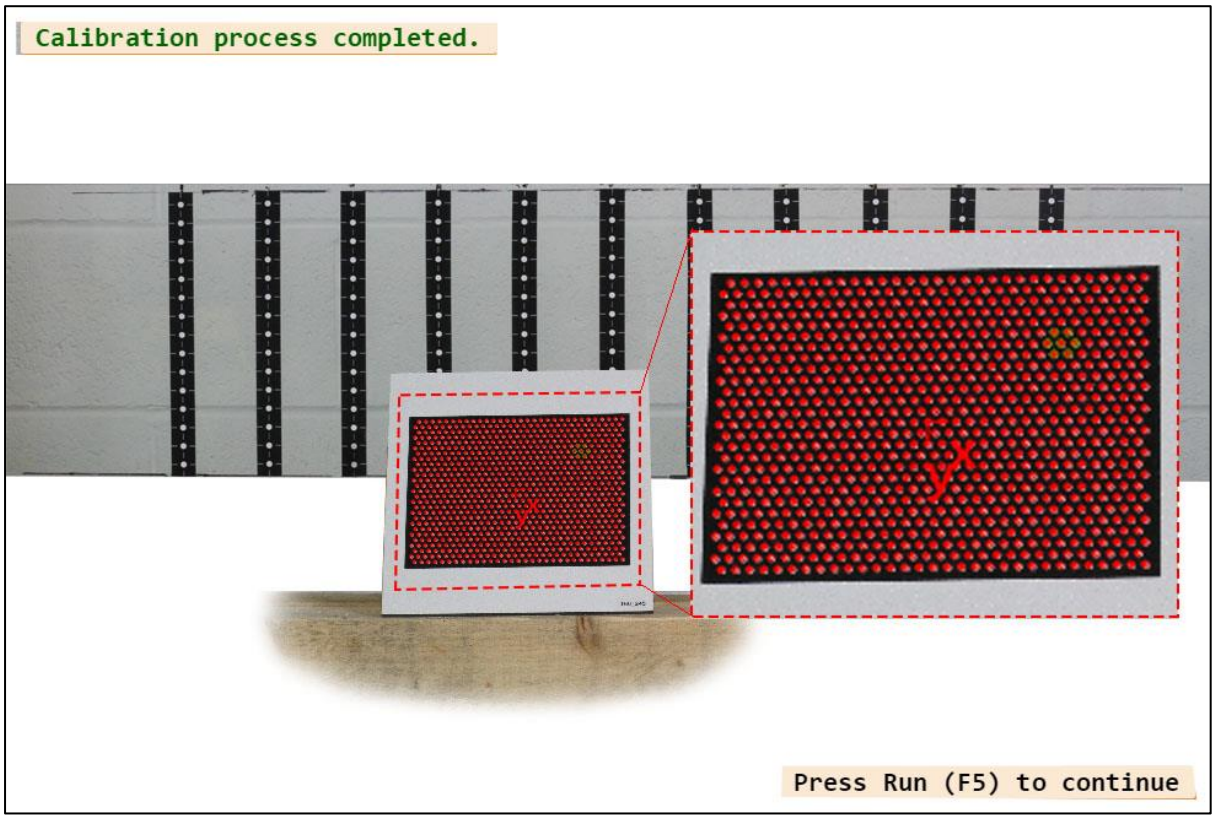

Figure 5-11: Calibration in HALCON software.

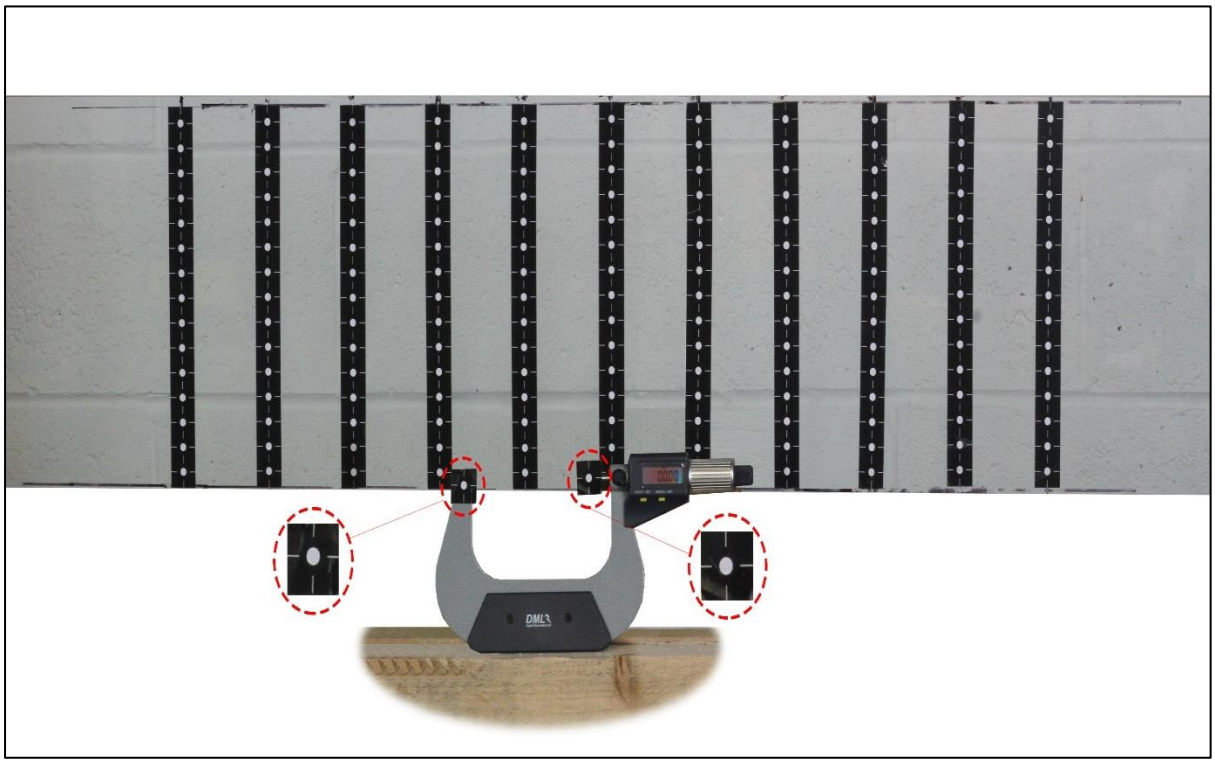

Figure 5-12: Recognition of micrometre targets.

5.5.2 Shear Modulus of Laminated Glass Beams

Three different approaches are suggested by the literature for the analytical evaluation of the *effective torsional stiffness* of laminated glass beams. The first approach is proposed by Feldmann and Kasper [8], which applies to laminates composed of two or three glass plies, all with the same thickness.

Another approach was proposed by Amadio and Bedon [74] and validated by Luible and Crisinel [81], allows determination of the torsional stiffness of laminated glass beams composed of two glass plies only by using sandwich theory to account for the composite action between glass and interlayers.

Considering the equivalent torsional stiffness in the model [74]:

$$GJ_{eff;A-B} = G\left(J_{glass_1} + J_{glass_2} + J_{comp}\right), \tag{5.15}$$

where G is the shear modulus of glass, $J_{glass_i} = \frac{ht_i^3}{3}$ is the torsional constant of the $i-th$ glass layer, evaluated by means of equation (5.7)[2], and suffix $A-B$ refers to the Amadio-Bedon model [74]. The torsional constant due to composite action of the interlayer J_{comp} is given by [74]:

$$J_{comp} = J_s\left(1-\frac{\tanh\frac{\lambda h}{2}}{\frac{\lambda h}{2}}\right). \tag{5.16}$$

$$J_s = 4\left(\frac{t_1+t_2}{2}+t_{INT}\right)^2 \frac{t_1 t_2}{t_1+t_2}h; \qquad \lambda = \sqrt{\frac{G_{INT}}{G}\frac{t_1+t_2}{t_{INT}\,t_1 t_2}}. \tag{5.17}$$

The theoretical values for G_{INT} can be determined by calculation of the elastic property relationship, where the relevant E and ν values for PVB and SGP exist in the available data [64].

These can also been verified by the results of Belis et al [77] where experimental LTB studies were performed.

Once the torsional stiffness is calculated with equation (5.15), the equivalent shear modulus G_{ESSM}, i.e., the homogenised value across the entire section, may be evaluated by requiring that [74]:

$$GJ_{eff;A-B} = G_{ESSM}\, J_{\text{homog}}, \tag{5.18}$$

where J_{homog} is the torsional constant of the homogenised section, evaluated by means of Equation (5.6) (or (5.8)), by considering the laminated glass dimensions recorded in Table 5-1.

The third analytical model proposed by the literature is the Enhanced Effective Thickness (EET) for laminated glass beams and plates under torsion [79]. This is a very general method, allowing to evaluate the torsional response of laminated rectangular panes composed by an arbitrary number of glass plies of arbitrary thickness. According to this approach, the equivalent torsional stiffness may be evaluated as $G_g K_{eff;EET}$, where, with the same notation of equations (5.15) and (5.18) [79]:

$$\frac{1}{J_{eff;EET}} = \frac{\eta}{J_m} + \frac{1-\eta}{J_{glass_1} + J_{glass_2}}, \tag{5.19}$$

where $J_m = J_{glass_1} + J_{glass_2} + J_s$ with J_s given by equation (5.17) is the torsion constant of an ideal beam cross section composed by the glass parts properly spaced of the interlayer thickness, rather than a full-glass section [79].

The non-dimensional shear coupling parameter η tunes the behaviour from the so-called layered limit with frictionless sliding glass plies $(\eta = 0)$ to the monolithic limit $(\eta = 1)$, where the tangential stiffness of the polymer provides the complete shear-coupling of the glass plies. Notice that this depends not only on the beam width, but also on its length, because the EET model for

torsion covers both the 1D beam and the 2D plate-geometries. The shear coupling parameter may be calculated as [79]:

$$\eta = \frac{1}{1+12\dfrac{t_{INT}\,t_1 t_2}{t_1+t_2}\dfrac{J_{glass_1}+J_{glass_2}}{J_m}\dfrac{G}{G_{INT}}\dfrac{L^2+h^2}{L^2h^2}}. \tag{5.20}$$

Once the torsional stiffness is calculated with (5.19), the equivalent shear modulus G_{ESSM} may be evaluated with a formula analogue to (5.17).

5.5.3 Results of PVB Sample

A total of seven experiments were performed on the two-layer PVB laminate beam sample. Errors were identified in acquiring the coordinate data in the fourth test and in the calibration of the sixth test, so these were disregarded from the results. This may be due to the camera(s) being accidentally moved after the calibration. From the remaining test datum, the ESSM value for the two-layer PVB laminated glass beam was computed; $G_{ESSM} = 7.19\,\text{Gpa}$, with results again closely adhering to the mean with a linear regression of $R^2 = 0.9976$ (Figure 5-13).

Calculation was performed by the methods detailed in the previous section based on sandwich theory [74] and effective thickness approximation [79], respectively. The shear modulus of G_{INT} is a time-dependent mechanical property as described in Table 5-4 provided by the manufacturer of the interlayer. The total testing duration is around 10 minutes including the preload period. The G_{INT} can be calculated by interpolation using the data in Table 5-4, and it is equal to $1.518\ \text{Mpa}$ for *G_PVB*. For the shear modulus of glass, the theoretical value $G = 28.455\,\text{GPa}$ has been used.

- $G = 6.448\,\text{GPa}$ for the Amadio-Bedon (A-B) method (10.33% difference to ESSM test result: $7.19\,\text{Gpa}$).

- $G = 6.445\,\text{GPa}$ for the Enhanced Effective Thickness method (10.36% difference to ESSM test result: $7.19\,\text{Gpa}$).

These results are noticeably lower than that obtained experimentally. The discrepancy may be explained by considering that, to use the Amadio-Bedon and the EET methods, the approximation of narrow rectangular cross section, on which the methods are based, has been used to evaluate the torsion constant of the individual glass plies. This means that they have been calculated by using the simplified expression (5.8) instead of (5.7). Remarkably, it may be verified that the accuracy of the analytical results may be increased by using, instead, expressions (5.6) and (5.7), even if this is not rigorous in the framework of the A-B and the EET methods. In this case, the theoretical shear modulus are:

- $G = 6.674\,\text{Gpa}$ for the A-B method (7.18% difference to ESSM test result: $7.19\,\text{Gpa}$).

- $G = 6.672\,\text{Gpa}$ for the Enhanced Effective Thickness method (7.21% difference to ESSM test result: $7.19\,\text{GPa}$).

which agrees closely to the experimental results obtained in this paper. More detailed calculations are included in the Appendix. As observed in [79], the results obtained with the two approaches are very close on to each other for low values of the interlayer shear modulus.

Table 5-4: PVB Shear Modulus under various load durations [129].

G_{PVB} (MPa)	3s	1 min,	1 hour	1 day	1 month
20°C	8.06	1.64	0.84	0.508	0.372

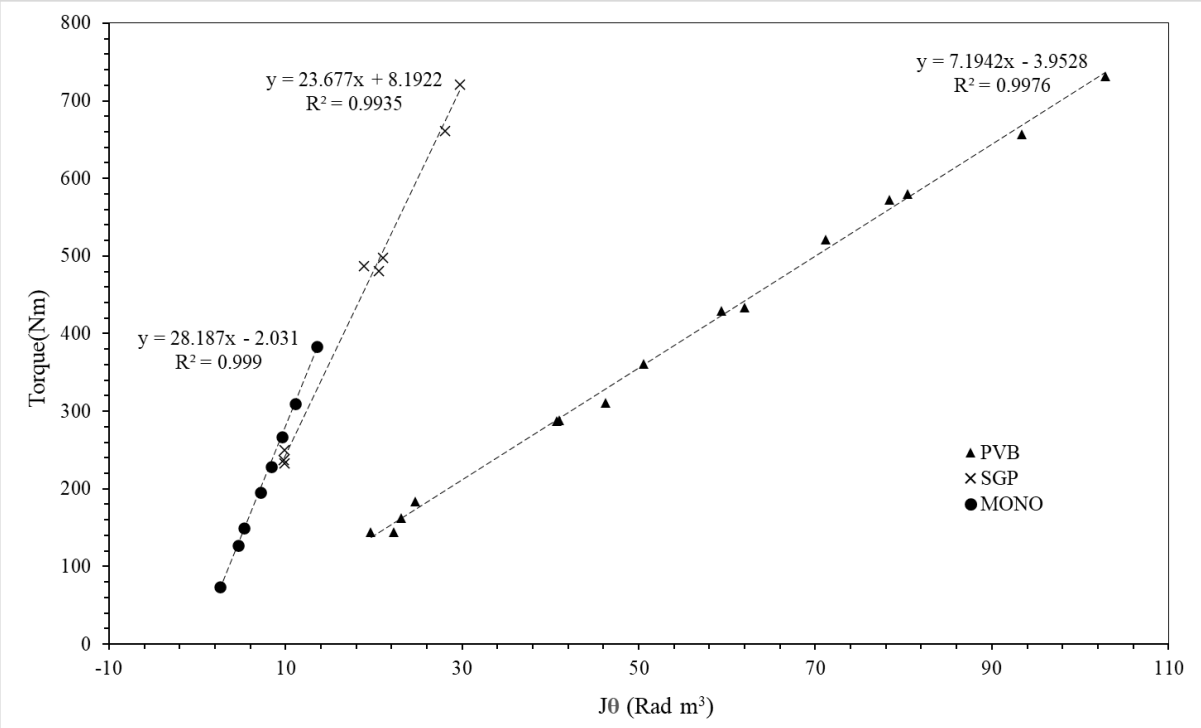

Figure 5-13: Shear modulus evaluation for monolithic and laminated glass beams.

5.5.4 Results of SGP Sample

A total of four experiments were performed on the two-layer SGP laminated glass beam sample. In the fourth test a mechanical failure occurred within the clamp inserts, so this experiment was disregarded. From the successful experiments, the calculation of the ESSM determined the value of $G_{ESSM} = 23.68\,\text{GPa}$ with linear regression adherence $R^2 = 0.9935$ (Figure 5-13). To calculate the shear modulus using the A-B and EET method, the G_{INT} for SGP can be calculated using the interpolation with the data listed in Table 5-5 provided by the manufacturer of the interlayer, i.e., $G_{INT} = 191.03\,\text{MPa}$ for *G_SGP*. Based on the method detailed in section 5.5.2, the shear modulus of

the two-layer SGP laminated glass beam has been calculated, by adopting the approximated expression (5.8) for the torsional constant of glass plies, as:

- $G = 22.081\text{GPa}$ for the A-B method (6.75% difference to ESSM test result: 23.68Gpa).
- $G = 24.071\text{GPa}$ for the EET method (1.65% difference to ESSM test result: 23.68Gpa).

By considering, instead, equation (5.6), the following results can be obtained:

- $G = 23.244\text{GPa}$ for the A-B method (1.84% difference to ESSM test result: 23.68Gpa).
- $G = 25.354\text{GPa}$ for the EET method (7.07% difference to ESSM test result: 23.68Gpa).

Notice that, in the former case the EET model is in better agreement with experimental results, while in the latter case the A-B model provides better results. This result revealed that the shear stiffness of the interlayer has a considerable impact to the overall composite effect of the laminated glass beam.

As observed in [79], for high values of the interlayer shear modulus, the torsional stiffness obtained with the EET approach is in general overestimated with respect to the A-B model. This study also revealed that measuring the structural torsional response and computing against the applied torque was a direct, effective, and accurate method of evaluating the composite shear/torsional stiffness of laminated glass beams. The shear modulus is an important mechanical property that directly affects the critical load estimated by various analytical model including lateral torsional buckling. The ESSM method provided not only a reliable way for validating the existing

or new analytical models for estimating the overall shear/torsional stiffness from the component mechanical properties but also a set of target data for the other researchers to fine tune their models.

Table 5-5: SGP Shear Modulus under various load durations [129].

G_{SGP} **(MPa)**	**3s**	**1 min,**	**1 hour**	**1 day**	**1 month**
20°C	211	195	169	146	112

5.6 Summary and Conclusions

- A novel concept was proposed the first time for quantifying the torsional stiffness of the laminated glass beams experimentally by introducing equivalent-sectional shear modulus (ESSM), which was directly measured from the torque and sectional-rotation correlation using the developed torsion test and tailor-maid photogrammetry technique.

- Accuracy of the instrumentation and the test setup was validated by a micrometre test. The test setup was proven to be highly accurate.

- The efficacy of the test design was examined by torsion tests on a monolithic structural glass beam, and the ESSM value calculated from experimental results agreed well with the theoretical shear modulus value.

- Seven PVB laminated glass beam torsion tests were performed, and the ESSM was determined. The test result of the PVB laminated glass beam has suggested a range of 7-10% difference from results calculated by the analytical model proposed in a previous study.

- Four SGP laminated glass beam torsion tests were performed, and the ESSM was determined. Experimental results had better agreement with results calculated by existing

analytical models. It suggested that the variation of interlayer shear stiffness had considerable impact on the overall composite shear/torsional stiffness.

- The proposed method is a direct, effective, and accurate method of evaluating the composite shear/torsional stiffness of laminated glass beams. It provides a reliable experimental approach to validate existing or new analytical models for estimating the overall shear stiffness of laminated glass beams from the component mechanical properties.

- Further development of the present work will possibly include the study of multi-layered (3 or more) laminated glass beams. Remarkably, the EET is the only analytical model that allows to evaluate the torsional stiffness for this general case.

- Another issue that will be interesting to experimentally investigate is the long-term response of laminated glass beams subject to constant torsional loading. Indeed, due to the viscoelastic properties of the polymer, a time-dependent relaxation is expected.

6. Extended ESSM Torsion Study on Multi-Layer Laminates

This chapter presents the extended torsion study performed on both two-layer and three-layer PVB and SGP laminated structural glass beams. Equipment and methods were further refined, optimised, and verified for this study. Torsion tests were performed on additional beam samples, including three-layer laminates that were not previously explored. Further investigation and validation of the experimental and ESSM approach were performed by employing dual-axis inclinometer sensors to measure displacements, evaluate their correlation to and further validate photogrammetric data. Furthermore, the experimental study was extended to evaluate the effect that lengthened torsional load-durations had on laminated glass beams. The ESSM was computed for each test and compared against the calculated shear modulus from existing analytical models.

6.1 Samples and Equipment

6.1.1 Test Samples and Preparation

Both monolithic and laminated structural glass beams were subjected to torsion experimentally in this study. The larger sample set was comprised of two monolithic beams, two 2-layer PVB laminated beams, two 2-layer SGP laminated beams, two 3-layer PVB beams and four 3-layer SGP beams. The glass of all beams were clear soda-lime silica glass, toughened (thermally), and were heat-soaked post-fabrication to minimise the risk of nickel-sulphide failure [26]. Dimensions of the monolithic beams were 2400 x 240 x 10 mm. All the 2-layer and 3-layer laminated glass beams were of the same 10:1 length-to-height ratio. The thickness was layered with the composition of 10 mm glass / 1.52 mm bonding / 10 mm glass for 2-layer samples, and 6 mm glass / 1.52 mm bonding / 10 mm glass / 1.52 mm bonding / 6 mm glass for the 3-layer samples (Table 6-1).

Test samples were prepared with a specialised setup of photogrammetric targets prior to experimentation. The aim was to prepare a target layout in a manner that would be easily readable from images using machine vision software and enable the extraction of torsional displacement data and their comparison to inclinometer sensors. The beams were set up with 5 mm diameter circular targets, as the centre points of circles can be accurately computed. These photogrammetric targets were arranged into 11 columns of 15 targets at an even horizontal distance apart of 70 mm, and with 15 mm vertical distancing between each target. These positions were also marked on all beam samples prior to experimentation (Figure 6-3).

To optimise the readability of these targets in images, a contrasting grey colour value between the targets and background is required. White targets with a black background were therefore selected. Each target was also designed with thin reticules to further optimise their readability. The targets were plotted to strips of non-reflective adhesive label and stuck in position to the beam face. An issue to consider is that each strip will behave as one unit, and as such the targets cease to move independently and their shape and position becomes distorted as angle of twist increases. To prevent this, each target was individually separated by cutting with a sharp blade, enabling each target to move with full independence.

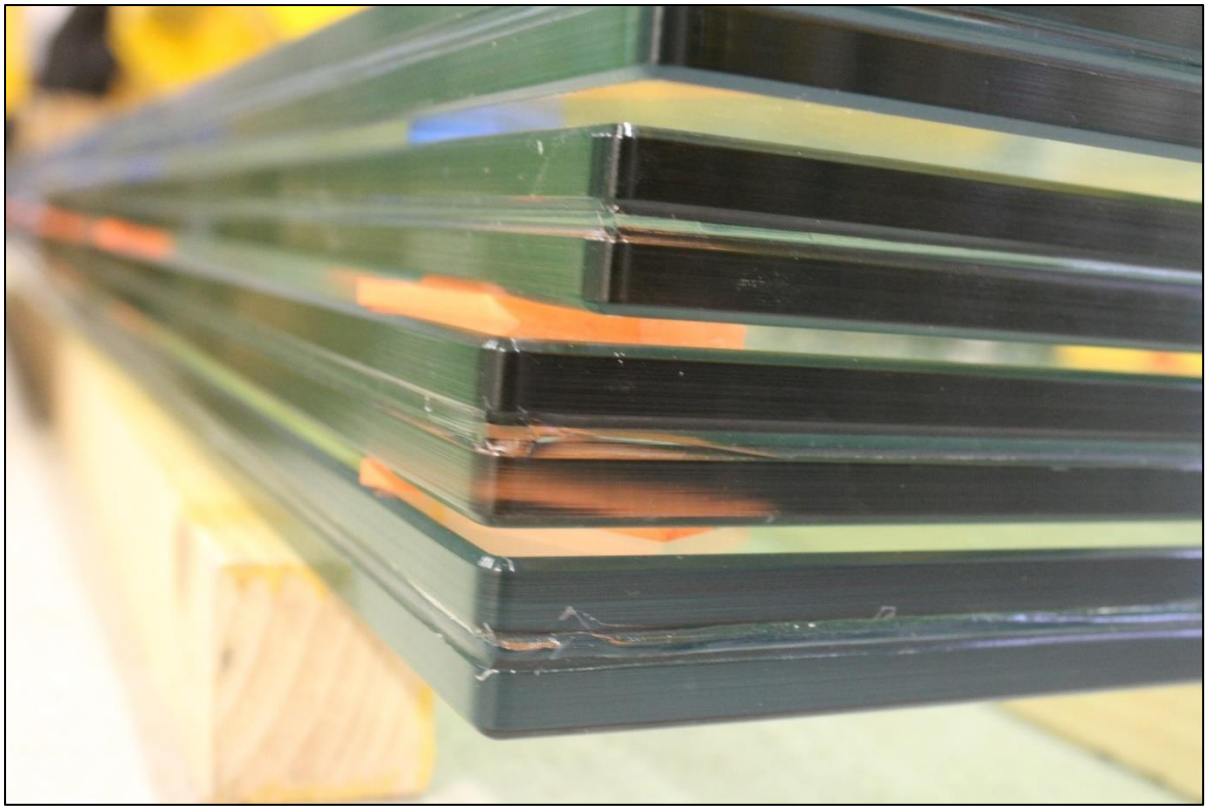

Figure 6-1: Two-layer lamination.

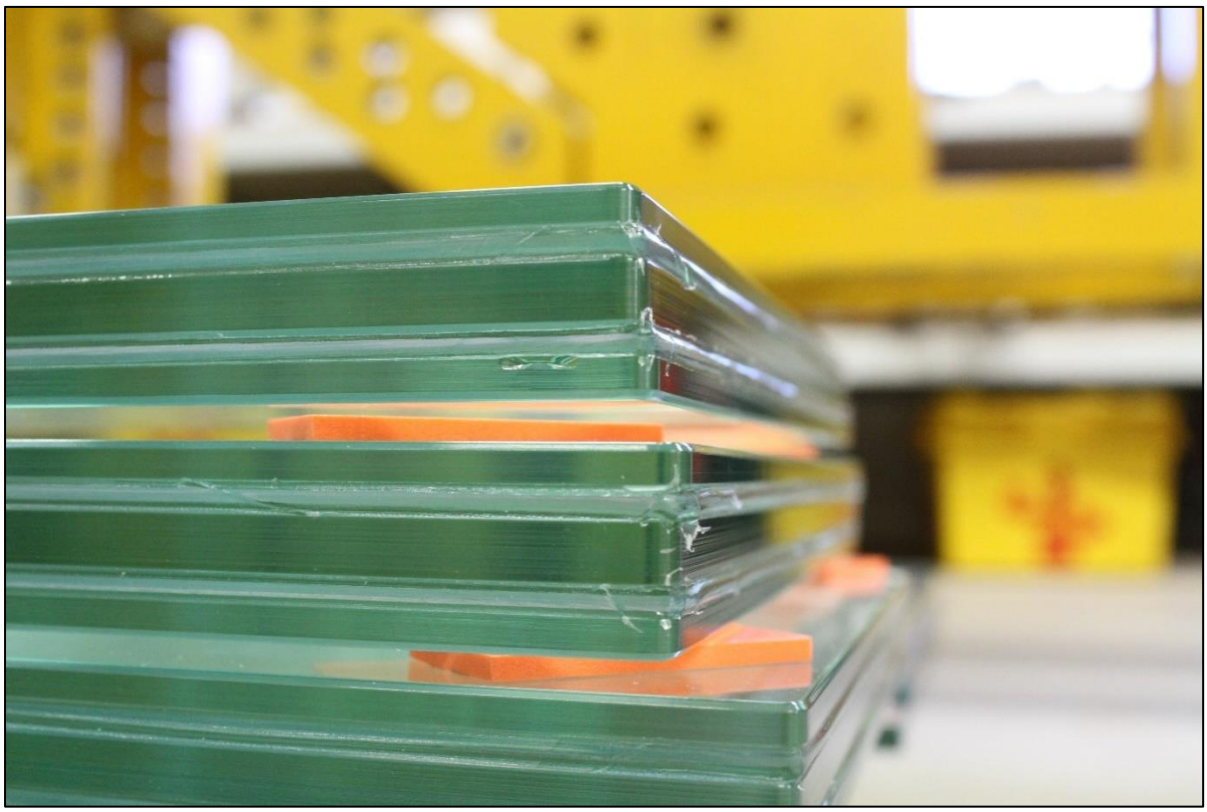

Figure 6-2: Three-layer lamination.

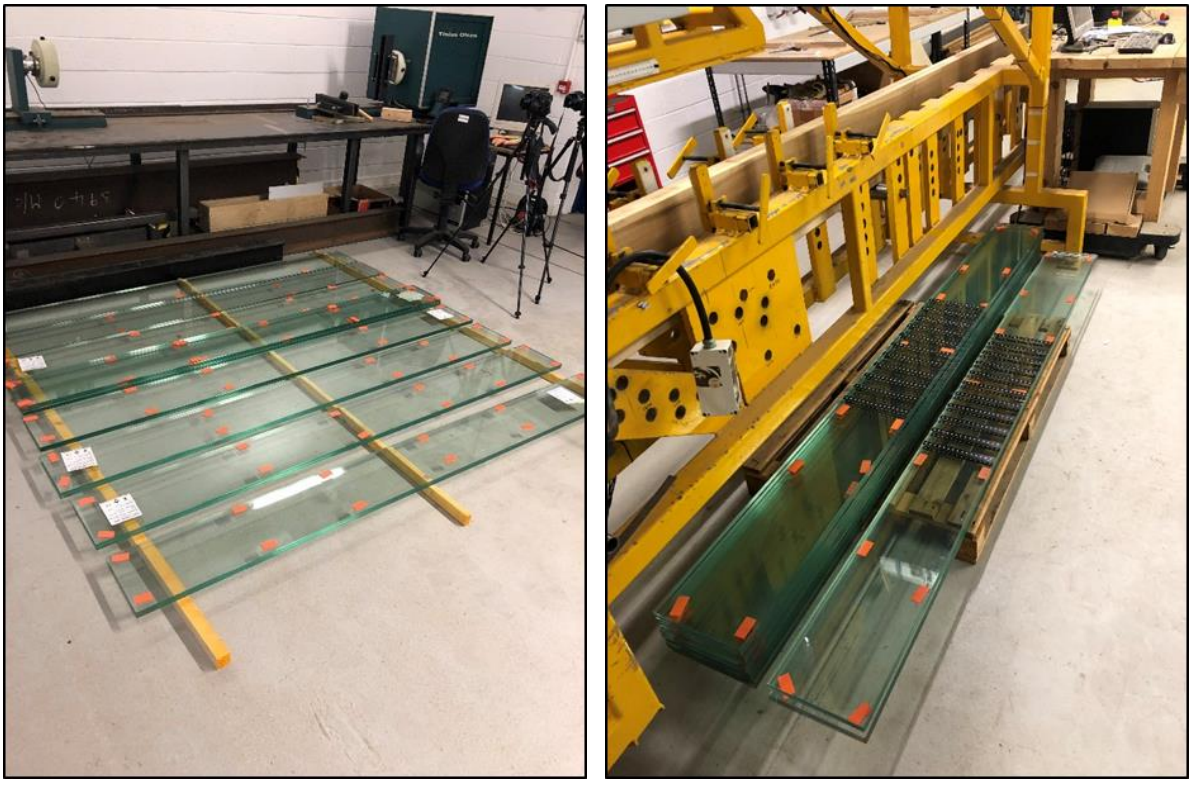

Figure 6-3: Beam samples as acquired (left) and post-marking and targeting (right).

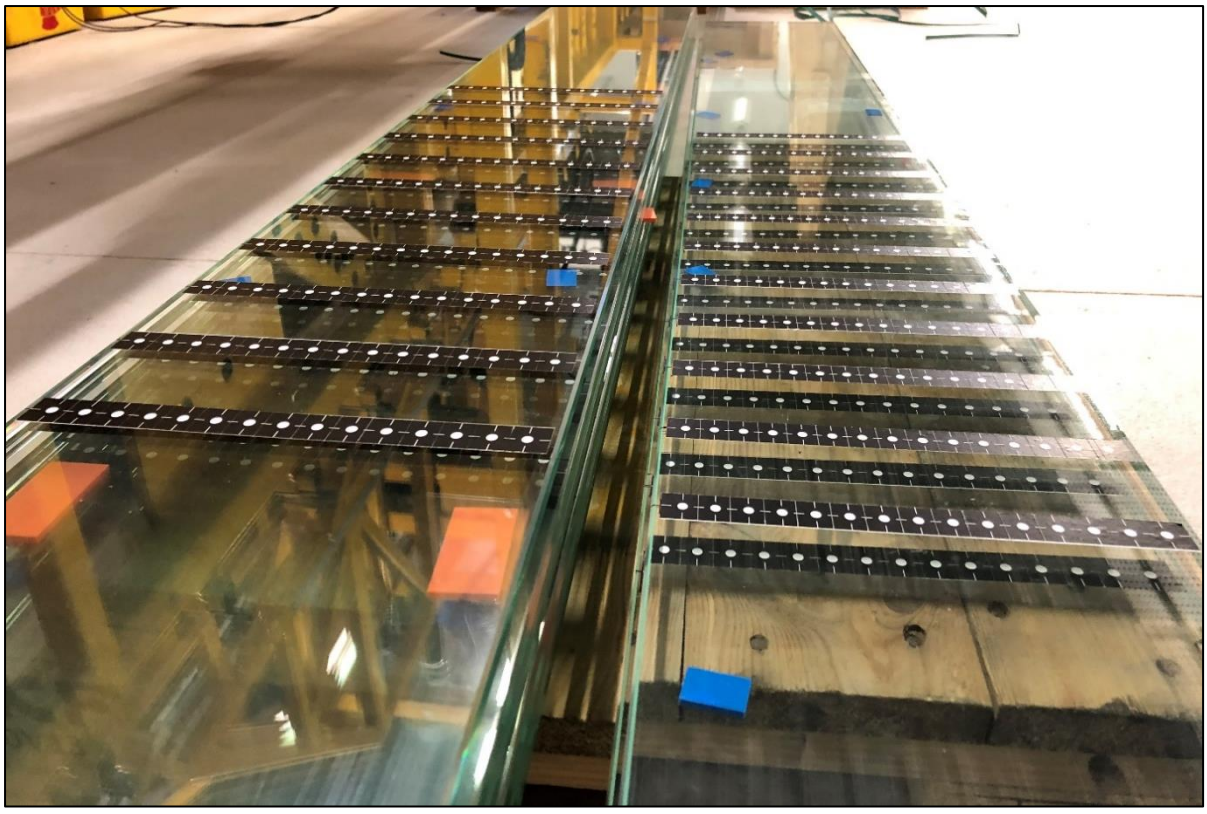

Figure 6-4: Beam targets post separation cutting.

Table 6-1: Test samples (* = toughened, ** = heat-soaked).

ABBREV	Length (mm)	Height (mm)	Thickness (mm)	Glass Type	No. Glass Plies	Composition (mm)
MONO2	2400	240	10	T*, HS**	1	10
MONO3	2400	240	10	T*, HS**	1	10
2PVB1	2400	240	21.52	T*, HS**	2	10 | 1.52 | 10
2PVB2	2400	240	21.52	T*, HS**	2	10 | 1.52 | 10
2SGP1	2400	240	21.52	T*, HS**	2	10 | 1.52 | 10
2SGP2	2400	240	21.52	T*, HS**	2	10 | 1.52 | 10
3PVB1	2400	240	25.04	T*, HS**	3	6 | 1.52 | 10 | 1.52 | 6
3PVB2	2400	240	25.04	T*, HS**	3	6 | 1.52 | 10 | 1.52 | 6
3SGP1	2400	240	25.04	T*, HS**	3	6 | 1.52 | 10 | 1.52 | 6
3SGP2	2400	240	25.04	T*, HS**	3	6 | 1.52 | 10 | 1.52 | 6
3SGP3	2400	240	25.04	T*, HS**	3	6 | 1.52 | 10 | 1.52 | 6
3SGP4	2400	240	25.04	T*, HS**	3	6 | 1.52 | 10 | 1.52 | 6

6.1.2 Torsion Machine

The same torsion machine was used in this study as in the previous chapter. For convenience, the information will be reiterated. The torsion testing machine was manufactured by Tinius Olsen, with a torsional force output capacity of roughly 1 kN-m. The torsion machine consists of one fixed end and one end allowing for free rotation. The chuck at the free end is marked with an angular deflection scale enabling the rotation at this end to be physically read by eye. The torsion rig itself is fixed to a 5.6 m in length, heavy steel bench, where the testing length between end supports is adjustable at the fixed end to account for various lengths of test specimen. Chuck jaws are situated at each end support, with open hexagonal connection points allowing clamps to be fixated. A control computer and monitor equipped with Test Navigator software are connected to the torsion machines sensory system, providing the outputs of angle of twist (°) at the machines rotating end, and torsional force in kN-m. The accuracies provided by the machine for both angle of twist and torsional force are about $\pm$ 0.05° and $\pm$ 0.5%, respectively.

6.1.3 Clamp System

Selecting the correct clamping mechanism is of great importance when it comes to mechanical experimentation on glass and laminated glass specimens. Extreme care must be taken to minimise direct steel-to-glass contact due to the brittle nature of glass – an aspect of considerably less risk when experimenting with other common structural materials such as steel, for example. The clamp system must also have great strength and rigidity, particularly in the case of laminated glass beams with rigid interlayers such as SGP, as a strong reactive torsional moment under large forces may cause part of the clamp system to fail before the test specimen, if a weaker material is used.

In the previous study in chapter 5 it was noted that such failure occurred during one experiment on the 2-layer SGP sample in the beech wood clamp inserts (supporting plates). Due to this, the clamp system was improved for this study. Due to these considerations and the unavailability of appropriately sized and shaped components at the time of this study, a tailor-made clamp system was developed and fabricated.

The clamp system (Figure 6-9) was comprised of several components. The main base of the system was comprised of a solid steel unit with a protruded hexagonal connector at the rear to allow fitment to the torsion machines rotating chuck end. Two steel side plates were welded to the base that span the bases entire length, each with circular clearance holes drilled at either end (two per plate). The holes were positioned at a sufficient distance apart to allow for a clearance space that is greater than the height of the test specimen, so it could be secured close to the base plate of the clamp.

Two clamp inserts which act as supporting plates were required in the clamp system to secure the test specimen in place. The plates must be made with a material of sufficient strength and rigidity, so they do not fail before the desired testing limits are reached. Solid steel plates at 10 mm thickness with a layer of rubber on the plates' face which points toward the test specimen were therefore designed and employed. When clamping glass specimens' careful consideration must be given to ensure that direct contact between steel-to-glass (or other materials with high hardness), as

well as localised stresses from bolting or point fixing, is minimised. Resultantly, two additional plates, which can be referred to as 'buffer plates', were included in the clamp system which situate between the glass specimen and main supporting plates. These are slimmer than the supporting plates at 6 mm thick and fabricated in polyvinyl chloride (PVC) plastic. Both supporting plates and buffer plates had holes drilled at matching size and alignment with those situated in the main clamp unit. Connection of the main clamp unit and plates was achieved using threaded rods, nuts, and washers above and below the test specimen.

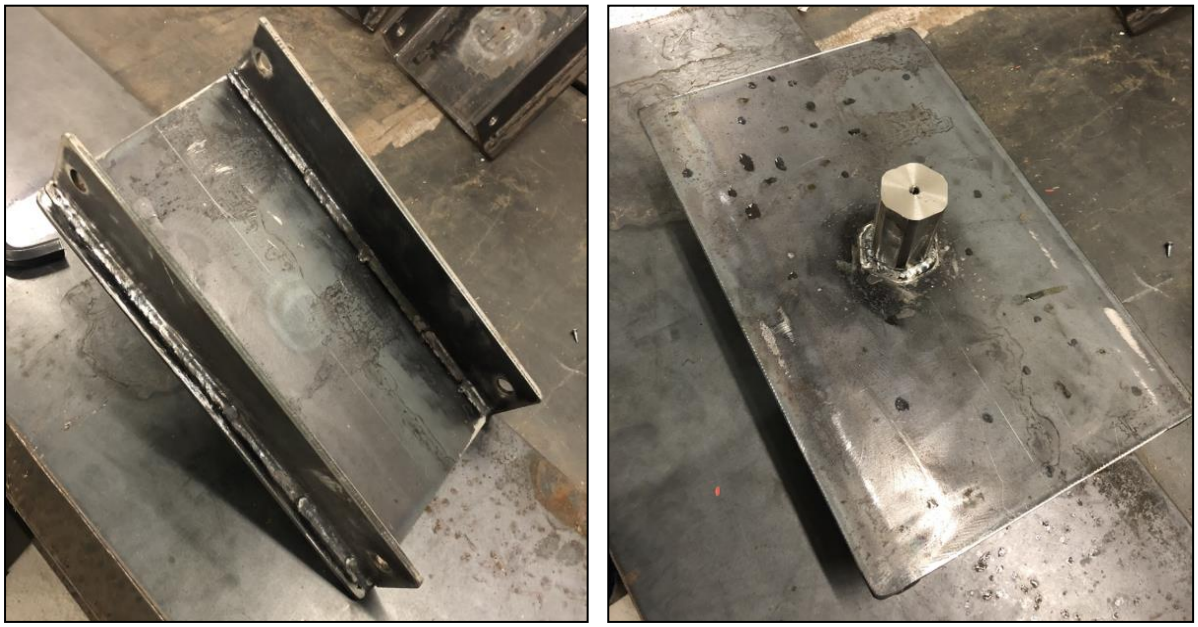

Figure 6-5: Steel clamp base unit; front (left), and rear (right) with hexagonal protruded fitment.

6.1.4 Alignment Marking

Inaccuracies when performing mechanical experiments may arise when a test sample is not clamped centrally or symmetrically prior to testing, as this may change the stress path and cause excessive stress at geometrically weak areas of the glass specimen. To improve the accuracy of installation, several markings were added to the clamp unit, torsion machine and bench. Firstly, to ensure that the clamp system is connected to the chucks at both ends centrally, the torsion machines

rotating end is set to zero and centrelines are marked on both chucks. Centrelines are also marked on the clamp unit both longitudinally and transversely to centrally install the test specimen, which is also centrally marked. Zero-centred ruler markings (Figure 6-9, Figure 6-14) have also been glued along both axes of the clamp units to aid in the process of beam and plate installation. Centrelines and boundary lines based on the target measurement area of the beam were marked on the torsion machines' bench in both longitudinal and transverse directions to aid in the upcoming position, orientation, and alignment of the binocular stereo-vision system, and to align the calibration object along the same longitudinal plane as the test specimen. Additionally, by implementing the use of a laser level (Figure 6-6) and centrelines on the torsion machine chucks, the rear wall behind the torsion rig was also marked in alignment as a reference point. This enables accurate re-centring of the chucks and beam installation via laser level between tests.

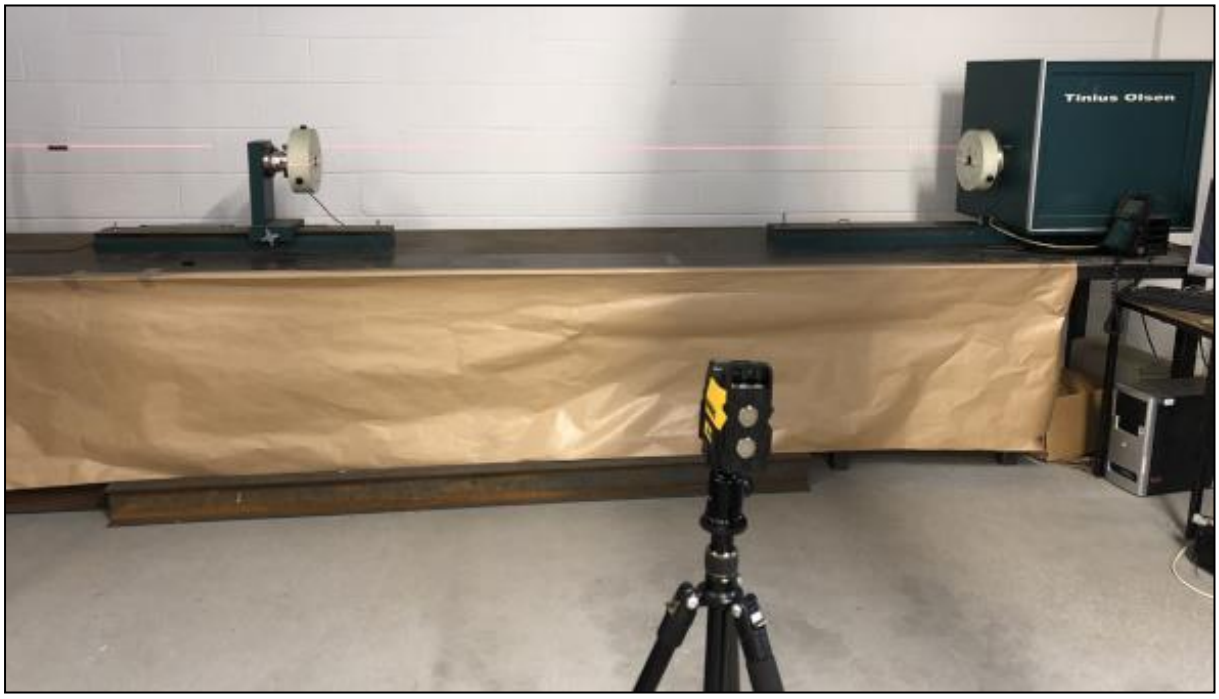

Figure 6-6: Alignment marking torsion machine chucks using laser level and wall reference marks prior to beam installation.

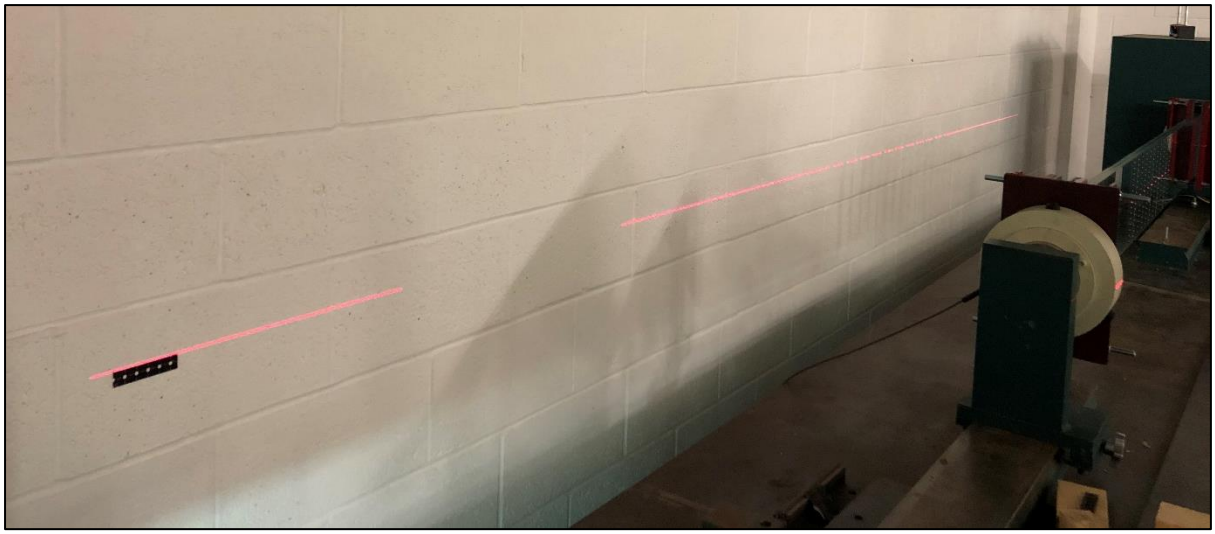

Figure 6-7: Installed beam with wall alignment – rear wall view.

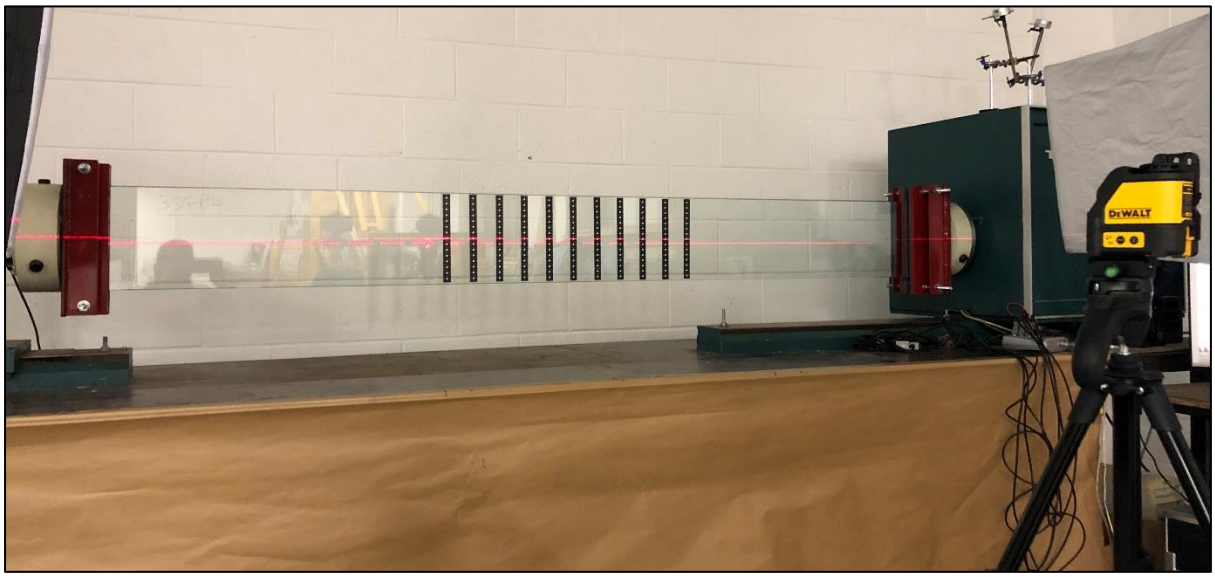

Figure 6-8: Centrally-aligned test installation using laser-level (front-view).

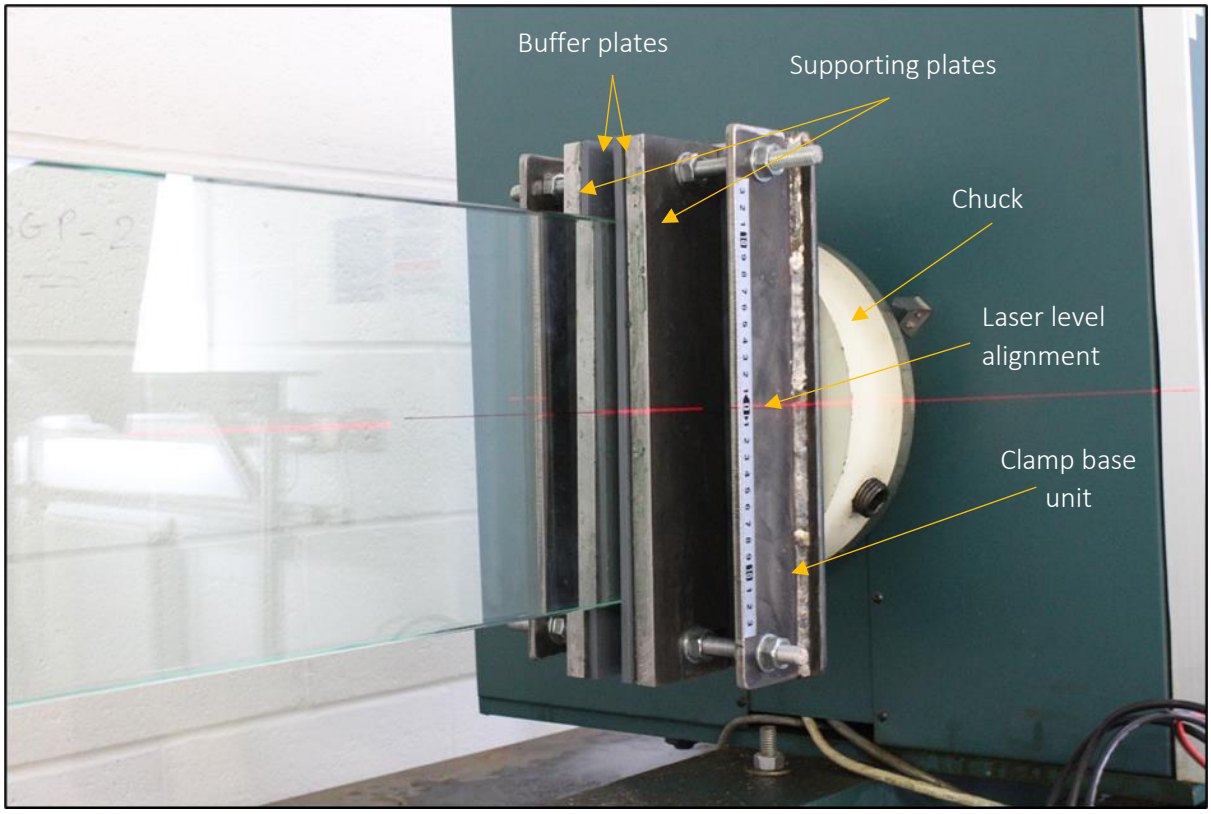

Figure 6-9: Tailor-made clamp system with steel supporting plates connecting torsion machine and test specimen.

6.2 Binocular Stereo-Vision System

6.2.1 Camera Setup

A photogrammetric approach was again employed in this study by applying binocular stereo-vision. The principles of binocular stereo-vision can be applied using many different methods and equipment types depending on the application, so long as the primary components – two interconnected cameras situated in a fixed position and their lenses – are present. The setup was made cost-effective due to the availability of affordable, modern, high-specification cameras, without the need for high-speed cameras which are used in other machine vision applications.

For the primary components of the stereo-vision system, two Canon EOS 7D digital single-lens reflect (DSLR) cameras with 50 mm Canon EF f/1.8 II fixed focal lenses were employed. It is vital that both cameras are fixed in place securely, as any slight movement to their position post-calibration will invalidate all prior coordinate data. A robust steel-based tripod was used as the

stand for the cameras. In combination with this, an adjustable aluminium-alloy horizontal extension arm was used to position the cameras apart from each other, left and right of the tripod respectively. This allowed further optimisation of the setup as a wider distance between left and right cameras can preferentially affect the accuracy of calibration and 3D coordinate generation. Despite a larger distance generally leading to more accurate triangulation [124, 125], the cameras' field of view must also be large enough for the area of interest to be fully visible. The cameras were spaced approximately 50 cm apart and approximately 280 cm from the central longitudinal plane of the torsion machine. Additionally, the rotation around the optical axis should be similar between the two cameras to give accurate calibration [124, 125], so this was accounted for in their positioning.

A third Canon EOS camera and tripod were set up to monitor the torsion machines data via the control PC monitor. All three cameras were linked using splitter, wires, and shutter to enable simultaneous images to be taken, which are all required at the same moment for 3D scene reconstruction and for parity with the torsion machines' rotation and torsional force data. All wiring was hazard taped to the ground and taped to the tripods to reduce the risk of accident during testing that could move and invalidate the calibrated stereo-camera system.

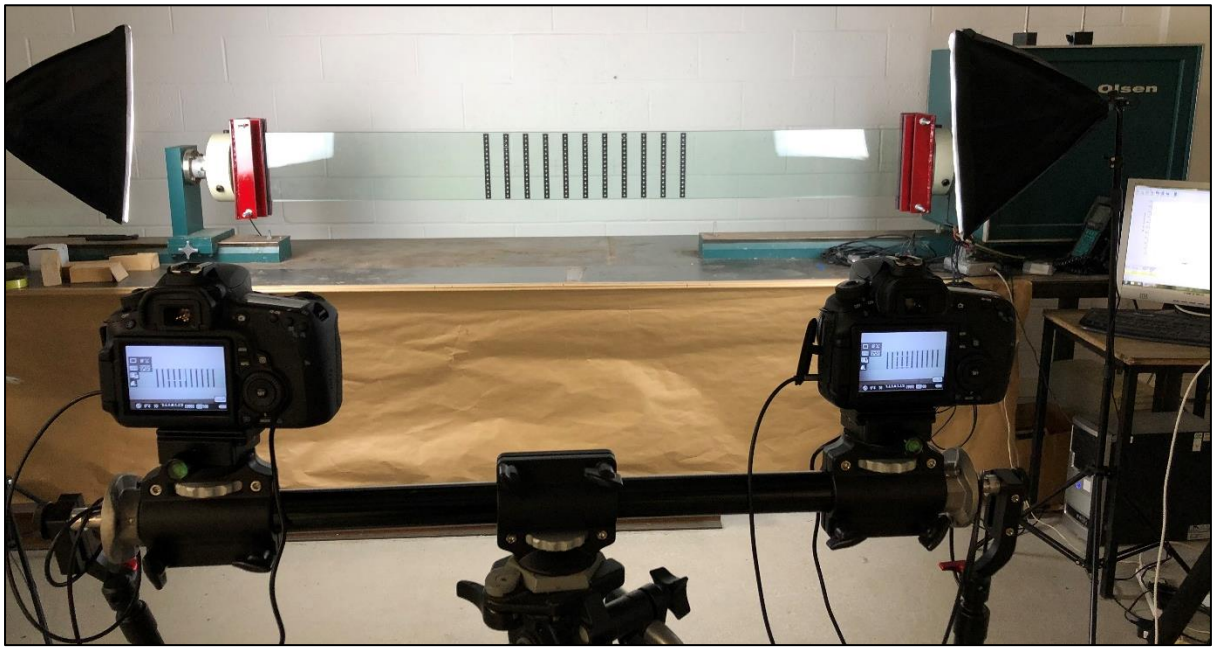

Figure 6-10: Target area fully visible in both cameras field of view.

6.2.2 Machine Vision Software

The binocular stereo-vision system in this study had to perform the following tasks:

- Stereo-camera calibration
- 3D scene reconstruction
- Image segmentation and point-of-interest identification
- 3D coordinate extraction of points of interest
- Translation of points of interest from camera coordinate system to a world coordinate system.

All the above procedures were required for many images and data points, which requires dynamic 3D displacement measuring algorithms with custom programmability in a convenient manner. HALCON software by MVTec was again selected as the software of choice for this study, due to its ease of use, visualisation abilities, programmable features, and integrated development environment.

6.2.3 Illumination

Illumination is a key consideration when preparing a photogrammetric setup, as points of interest must be visible and extractable by the HALCON program. Two Softbox lights with 800 W compact fluorescent lamps (CFLs) and reflective covers were set up to illuminate the test area and photogrammetric targets by transmitting continuous smoothed light streams. A level of glare was still observed from the glass beam samples. To suppress this undesired feature, both Softbox lights were set at a shallow angle to the test specimen (post installation) and the cameras were checked to ensure there was no severe reflectivity. Ceiling lights above the test area were also turned off to avoid glare when the test specimen is rotated. A further implementation that was employed in

accordance with the study in chapter 4 to ensure glare was not an issue was the fitting of polarising lens filters to the cameras, as this smoothed light from any unexpected reflection.

6.3 Calibration and Accuracy Validation

6.3.1 Calibration

In this study an optimised calibration process was employed in accordance with the results of chapter 4. A standard 160 x 120 mm calibration plate with multiple small circular target marks, along with its corresponding data file with all known properties provided by MVTec, were used in this study. The tailor-made calibration plate holder was employed for all calibrations described in this chapter. This allowed for optimal coverage of the entire measurement area of interest by allowing for multiple positional and orientation adjustments. Calibration images were to be taken along the same longitudinal axis as the front-facing plane of the beam samples were situated for greatest accuracy. Therefore, to align the calibration plate in this manner, the test bench was marked centrally using a laser level.

To perform the calibration procedure, multiple image pairs of the calibration plate were taken in various poses. As the experimental run presented in this chapter was performed on different days, the stereo-vision system was re-calibrated and verified at the beginning of each test day. The initial step of the calibration was to ensure that both cameras field-of-view was in alignment with the measurement area – that being the 700 x 240 mm photogrammetric target area. The measurement area was pre-marked on the test bench beforehand. The calibration plate was set inside the plate holder and the height was adjusted to mid-level. The plate was then positioned in the centre of the measurement area and both stereo cameras' field of view was adjusted so that the plate was in their centre, and the external boundaries of the measurement area were also visible. The calibration plate was then moved the left boundary of the measurement area, to begin the cycle through user defined poses from left to right.

The next stage involved taking multiple stereo image pairs of the calibration plate in positions and orientations that capture the full measurement area of interest, and to capture the range of displacements that occur in the physical torsion test. This is most efficiently performed with two people, one to control the cameras and one to adjust the calibration plates' pose. A range of 45-63 calibration image pairs were taken for the calibrations performed in this study. These included longitudinal positions covering the target area, 3 height levels, front facing, left/right tilted, left/right diagonal rotation, and forward and backward leaning positions, as were presented in chapter 4 (Figure 4-10). This larger set of calibration images overcompensates for cases where there is an issue in reading the calibration plate in some images in machine vision software, whilst still being efficient time-wise due to use of the calibration plate holder.

6.3.2 Accuracy Experiment

Once calibrated, the measuring accuracy of the stereo-vision system should be evaluated and verified for its use in the specific displacement measuring application. The tailor-made micrometre accuracy experiment developed in chapter 4 was therefore employed after each calibration for this study to validate the accuracy of each calibrated system specifically.

A DML 75 – 100 mm digital micrometre with external gauge and a measurement accuracy of $\pm$ 0.003 mm was again used for this study. For calibration runs, both two-target and four-target micrometre experiments were employed to validate the systems accuracy as the four-target method was developed later in the testing stage. Two (and four) circular target points were fixed to the micrometre apart from each other longitudinally. To achieve the greatest reproducibility, these targets were identical in size, shape, and colour to those set to the beam sample. The targets were again plotted to adhesive labels, cut, and stuck to squares of PVC plastic for firm backing to prevent any distortion. The first target was fixed to the stationery end at the left of the micrometre, while the second end was fixed to the spindle which moves laterally as it is rotated by the user, incurring change in distance. Targets were fixed to the micrometre using a hot glue gun. A

universal swivel clamp with magnetic base – which locks to the steel test bench – was used to hold the micrometre in place securely for the experimental process.

To set up the experiment, the micrometre was first clamped within the swivel clamp. Using the spindle, the micrometre was rotated to as close to the far end as possible with the target being forward facing. The moving target on the spindle was aligned to be forward facing to correspond with the static target by using a laser level along the target's longitudinal planes (Figure 6-11), as this alignment provides the best correspondence with micrometre gauge readings. Once aligned, the gauge was set to zero to begin the experimental process.

The micrometre was fixed to the test bench at the end-left boundary of the target area, and along the longitudinal measurement plane for best reproducibility to the forthcoming torsion test. With the gauge set to zero mm, the first reference stereo image pair was taken of the micrometre at this location. Subsequently, whilst keeping the micrometre distance to zero mm, the micrometre and swivel clamp were moved further along the longitudinal test plane, secured in place and another image pair was taken. This process was repeated for 5 locations along the test plane in total resulting in 5 reference image pairs. The micrometre was then returned to the first location and the distance was changed toward the far end of spindle rotation to create the measurement interval. Image pairs of this measurement interval were then captured at both this location and in the 4 other locations, resulting in 10 micrometre image pairs for each test.

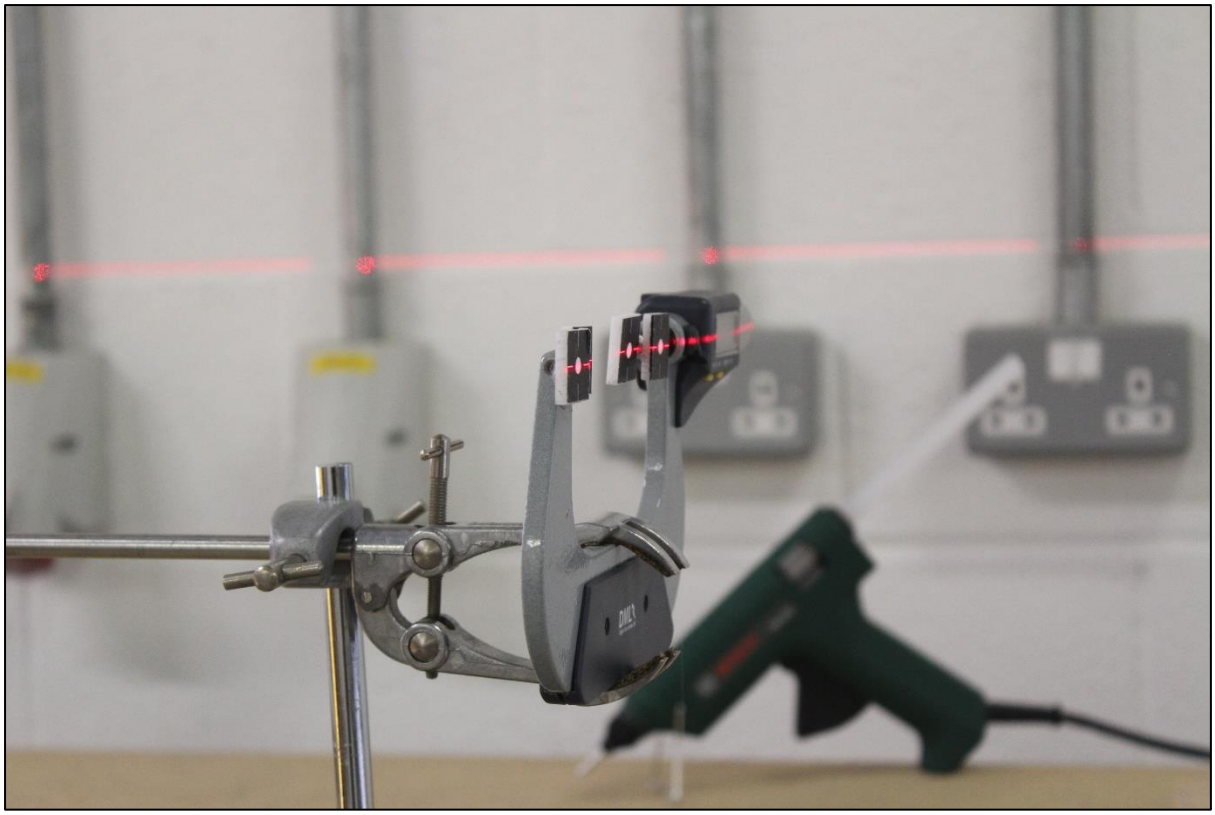

Figure 6-11: Micrometre target alignment using laser level.

Figure 6-12: Image pair of four-point micrometre during test.

6.4 Beam and Inclinometer Installation

6.4.1 Inclinometer Setup

Inclinometer sensors were employed in the experimental study for the main purpose of comparing displacement measurements with the photogrammetric target setup, in order to further validate its

efficacy. Inclinometers therefore had to be positioned in alignment with photogrammetric target columns for comparison. Inclinometer sensors were employed for experiments on the sample 2SGP2. Four inclinometer sensors were used for each test. As a relative rotation between two points on the beam sample is required, the inclinometer sensors were positioned in the point of theoretical best correspondence to the photogrammetric targets vertically and spread across the target area longitudinally. These were therefore setup in alignment with the centres of target column 10, between 7 and 8, between 4 and 5, and in alignment with 2. Inclinometer sensors were positioned on the rear (opposite from targets) beam face as presented in Figure 6-15.

The method of fixing inclinometers to the beam face must be considered. In the case of attaching to a glass sample, it is not possible to use screws or any such method that involves damage to the material structure. The use of a hot glue gun was therefore selected to fix inclinometer sensors to the beam face. Prior to physically installing the inclinometers to the beam and setting up their related software, the beam was installed to the torsion machine for convenience.

Figure 6-13: Hot glue gun.

6.4.2 Beam Installation

Efficient installation of structural-sized laminated glass beam samples ideally require around four people due to their length and weight to reduce the risk of inadvertent damage, and to ensure the centrally-aligned installation by using the employed implementations such as laser level and ruled marking on the clamps. Prior to installation, the laser level was set up to project central alignment in the longitudinal direction across the chucks, clamps, and reference wall markings. Pre-cut timber blocks were placed along the test bench to rest the test sample on during the clamping process at the required height, and the non-rotating end of the torsion machine was widened to allow efficient space to install the test sample.

The beam was first manually moved into the clamp system at the torsion machines rotating end with about 10 mm spacing to contact with the clamp. It was then positioned in central alignment and tightened securely in both longitudinal and transverse axes by aligning between centre markings on the test sample with laser level, and with ruled markings on the clamp, respectively. The other end of the torsion machine was then moved inward until about 10 mm spacing between the test sample and clamp was observed, then the same alignment and clamping process was performed. As noted, the inclinometers were installed after the beam was clamped for efficiency.

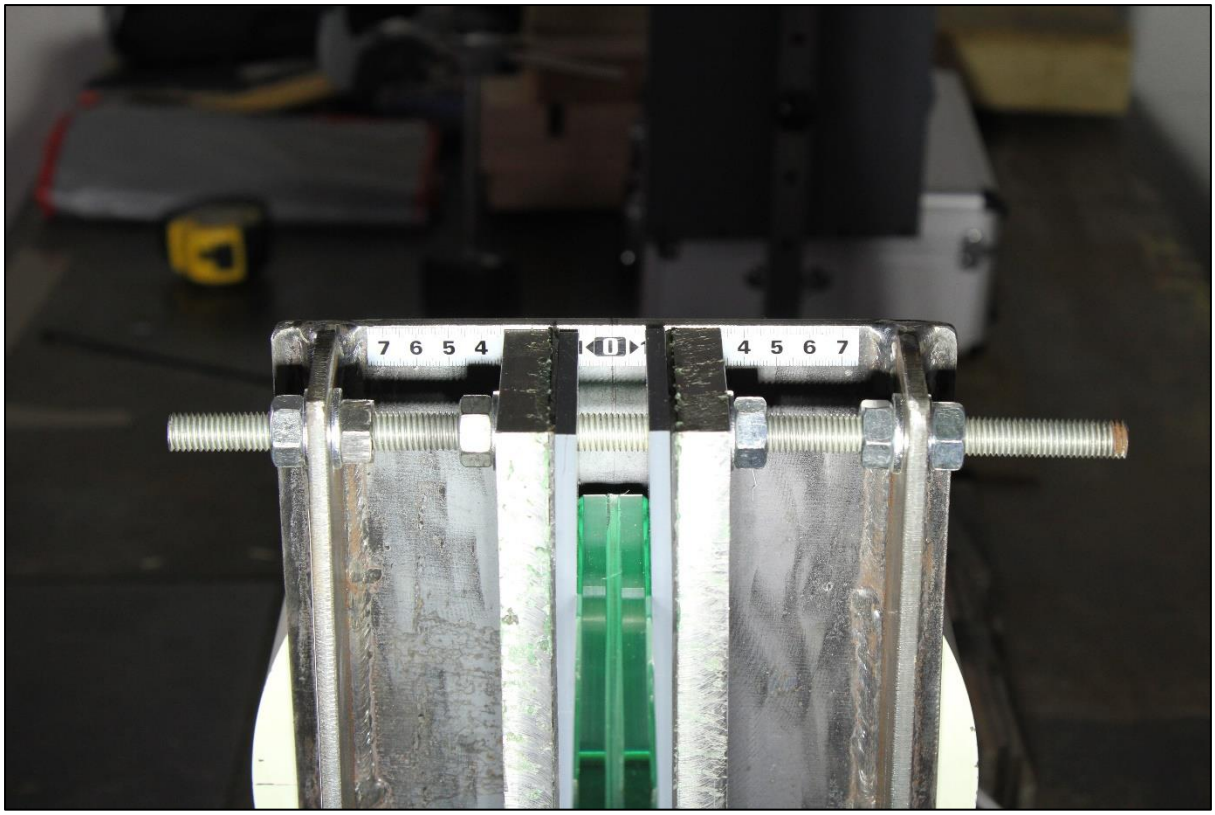

Figure 6-14: Beam clamped centrally with ruled markings.

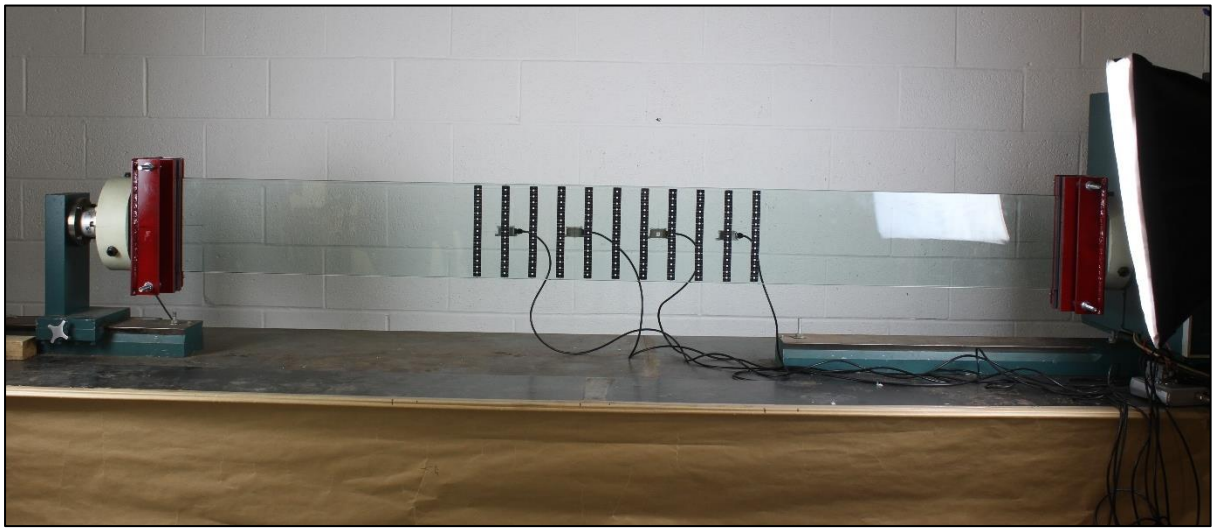

Figure 6-15: Fully installed experimental setup with inclinometers centrally aligned with target columns.

6.5 Torsion Test

A broader experimental study with additional test samples and additional torsion tests was conducted. Initially, the monolithic samples, MONO2 and MONO3, were tested twice each under torsion to determine the G_{ESSM} and compare with known theoretical shear modulus values for glass, which provides high confidence in experimental results for laminated samples. A total of 12 torsion experiments were performed on 2PVB2, which included tests of the inclinometer setup, and 2 experiments were performed on 2PVB1 further to those from chapter 5. A total of 6 and 8 torsion tests were performed on 2SGP1 and 2SGP2, respectively, with the 2SGP2 test set also including inclinometer employment. This study was also expanded into the experimentation of 3-layer laminated glass beam samples under torsion for the first time. The PVB 3-layer samples, 3PVB1 and 3PVB2, were tested 4 times each. The initial 3-layer SGP samples, 3SGP1 and 3SGP2, were tested 7 and 9 times, respectively. Furthermore, two additional SGP samples, denoted 3SGP3 and 3SGP4, were also acquired to further examine the torsional-mechanical behaviours of this modern interlayer material in the more complex form of a 3-layered composite. These were tested 3 and 4 times each, respectively.

Initial parameters such as the cross-sectional dimensions of the test sample and the load-rate were entered into the Test Navigator software. Both the Inclinometer displacement readings from their Datalog software (in tests where inclinometers were used), and the torsion machines force and rotation readings were set to zero prior to initiating each test. To synchronise inclinometer and Test Navigator data, these live data displays were split on the control PC's display so they could be captured in correspondence by the third linked camera. The temperature in the test facility was kept constant at ~ 20° C and was checked by thermometer. The load rate was set to 4° per minute as recommended per the timber code for torsion testing [91] for all the tests initially. In subsequent tests for the multi-layered SGP samples the load-rate was modified to extend the load-duration, which aimed to study if there was any effect of longer-term loading on this modern and high-specification interlayers' torsional rigidity.

Each torsion test was initiated by the researcher controlling the Test Navigator software via control PC. Considerations when initiating the test are that some residual compressive stress may be present in the sample from clamping, and there may also be a small amount of 'jump' in the torsion machines rotation mechanism. To account for this, either pre-loading can be performed, or the initial affected data can simply be disregarded. The degree of rotation for each test depended on the strength of the sample, the torsion machines output limitations, and achievable non-destructive displacement.

Monolithic samples were torqued to 24° of rotation at the torsion machines rotating end, which was considerably below the torsion machines output capacity but ensured no rupture to the beams. 2-layer PVB samples were torqued to 20° - 24° of rotation which reached around 85% of the torsion machines force limitations. 3-layer PVB samples were limited to around 10° of twist by the machines output capacity. 2-layer and 3-layer SGP samples had greater resistance to torsional force and were generally torqued to around 13-14° for 2-layer, and around 9° for 3-layer samples. The rotation during a torsion test is visualised in Figure 6-17.

Images were taken by a second researcher controlling the stereo-camera system at set intervals to capture displacements of the photogrammetric targets and torsion machines force and rotation outputs simultaneously. Image pairs were taken every 2° interval for monolithic and 2-layer PVB beams. For all the SGP samples and 3-layer PVB samples images were taken at 1° intervals to acquire sufficient data points from the lower twist angles. Each image set included a stereo-image pair of the photogrammetric targets and an image of the control PC monitor from the third linked camera, which displayed both the torsion machines force and rotation angle outputs and inclinometer displacement and time data for tests including inclinometers. To conclude each test, the torsion machine was stopped, the final image set was taken, the machine was returned to zero and all torsion machine and inclinometer readings were reset to zero.

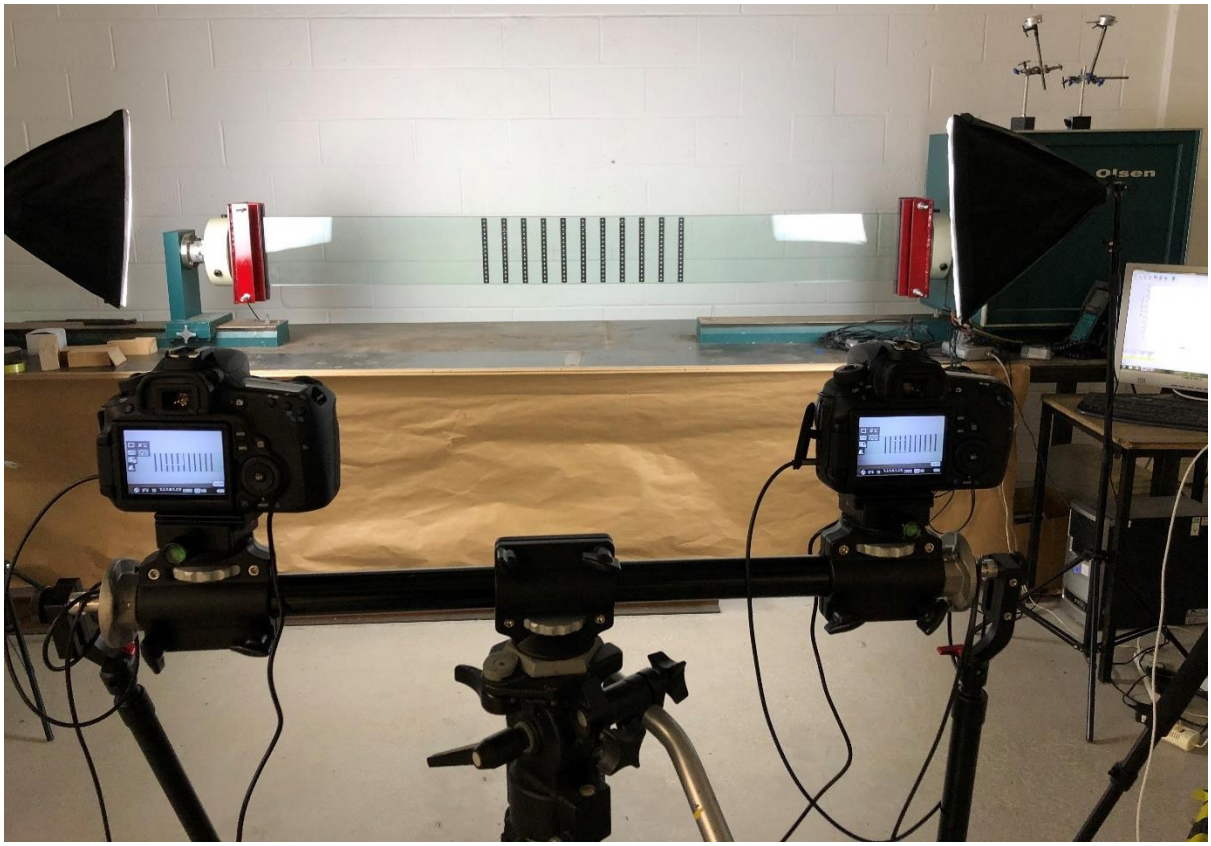

Figure 6-16: Torsion test and data monitoring.

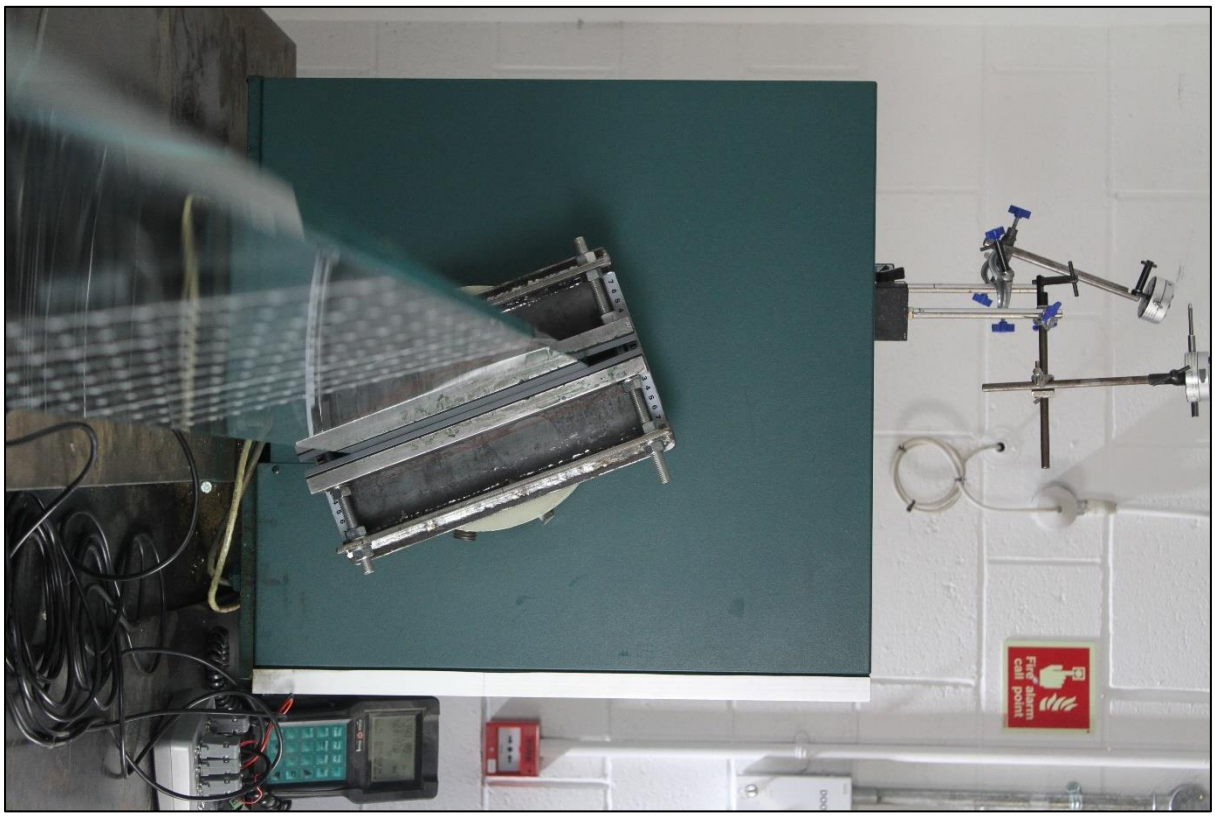

Figure 6-17: Torsional deformation during test.

6.6 Results and Discussion

6.6.1 Experimental Equipment and Setup

Torsion experiments were performed on monolithic, 2-layer, and 3-layer laminated glass beams using an optimised torsion test and photogrammetric method. Several tailor-made methods and equipment were implemented in this study; therefore, trial torsion experiments were first conducted to ensure the viability of these.

Regarding the preparation of beam samples, they each were prepared with a setup of photogrammetric targets that matched the layout in the previous chapters study. For the two tests on 2SGP2 inclinometer sensors were also employed. The method of attaching inclinometer sensors had to consider the physical properties of glass. In previous studies where inclinometers have been attached to timber beam samples [98, 99], these could be screwed or drilled on, whereas glass is more suited to an adhesive connection method. This study therefore employed the use of a hot glue gun (Figure 6-13) to attach inclinometer sensors, which were arranged in correspondence with photogrammetric target columns, but on the rear-face of beam samples.

The clamp system was also improved for this study. In the previous chapter, it was noted that failure occurred in one of the beech wood clamp inserts during one experiment on the 2-layer SGP sample. The latest optimised clamp system therefore employed solid steel inserts, which were layered with rubber. Additionally, to make installation of the beam centrally aligned, the clamps were also equipped with centre-ruled markings (Figure 6-14, Figure 6-9) along both longitudinal and transverse axes. Additionally, the chuck jaws were centrally marked, as was the rear wall behind the test area (Figure 6-6) to allow accurate re-centring and installation of the beams and clamp.

To evaluate the equipment and methods several trial torsion tests were performed. Firstly, a trial torsion test was performed on one of the theoretically strongest samples, 3SGP1, as if the clamp system does not fail due to this sample it can be safely assumed for use with all other beam samples. Other trial torsion experiments were performed on a combination of monolithic and 2-layer laminated glass beams to check that the inclinometer sensors would stay attached at higher

twist angles and deformation, and to check that their sensory data and Datalog software was working correctly. In the 3-layer trial, the beam sample was torqued to almost 10 degrees expending the maximum force output of the torsion machine. In the monolithic trial, the beam was torqued to 24°. The clamp system was proven to be effective as no failure or damage was induced to any of its components. In addition, the use of alignment markings was found to be an effective means to ensure that beam samples were centrally secured for each test and improved the efficiency of sample installation each time.

6.6.2 Validation of Photogrammetry System and ESSM Method

Once the stereo-vision system was calibrated for each test run and the pixel error was checked, validation of the photogrammetric methods' measurement accuracy was achieved by performing micrometre accuracy experiments in accordance with the methods developed in chapter 4. The calibration errors from each calibration performed were 0.0423, 0.0692, 0.0502, 0.0694, 0.0569 and 0.0331 pixels, which were all well within the recommended range of ≤ 0.1 [124, 125] indicating highly accurate and effective calibrations. Additionally, the calibration plate marks were identified and extracted successfully by the HALCON program in every image pair for each calibration, further indicating that the cameras focus, and lighting setup were optimal for photogrammetric application.

Subsequently, to quantify the actual displacement measurement accuracy of the specific target-based photogrammetric application of each calibrated system, a combination of two- and four- target approaches to the micrometre experiment were employed, using targets of identical size, shape, and colour to those on the glass beam samples. The results, as presented in Table 6-2 and Table 6-3, proved that compared with the micrometres gauge readings, the accuracy of the system was within the mean error range of 0.01% to 0.68% across 6 calibrated stereo camera systems. Therefore, this confirmed that both the system was properly calibrated, and was highly accurate for measuring displacements in this specific application.

Furthermore, to validate that the ESSM method (5.4) could be accurately employed in this study to determine the shear modulus, two torsion experiments each were performed on the monolithic glass beam samples, MONO2 and MONO3. From the results, the G_{ESSM} was calculated and this was again compared to the theoretical shear modulus for soda-lime silica glass from its relationship of elastic moduli, resulting in $G = 28.455\,\text{GPa}$. The calculated values using the ESSM method for MONO2 were $G_{ESSM} = 29.19\,\text{GPa}$ and $G_{ESSM} = 29.28\,\text{GPa}$. For MONO3, the calculated values were $G_{ESSM} = 29.24\,\text{GPa}$ and $G_{ESSM} = 29.32\,\text{GPa}$. The ESSM values therefore agreed well with the theoretical value for shear modulus, with the tested beam samples having just slightly higher torsional rigidity. A further note from these results was that compared with the monolithic beam tested in the previous chapter (5.5.1), where the $G_{ESSM} = 28.187\,\text{GPa}$, there was a modest variance in properties between identical glass samples as per manufacturer specification, which is also consistent with the literature [3].

Table 6-2: Two-target micrometre test results (* ***Test1*** *distance and error results averaged at each interval from 105 data points).*

Interval	Dial Reading (mm)	Photogrammetric Distance (mm) *	Distance Between Target and Zero (mm) *	Error (%) *
Test1				
Reference	0.00	86.674	-	-
1-1	5.728	92.419	5.745	0.382
1-2	10.17	96.875	10.201	0.461
1-3	13.981	100.656	13.982	0.549
1-4	4.457	91.100	4.426	0.695
Test2				
Reference	0.00	86.035	-	-
2-1	12.067	98.092	12.051	0.134
2-2	12.067	98.096	12.048	0.154
2-3	12.067	98.090	12.057	0.078
2-4	12.067	98.120	12.097	0.248
2-5	12.067	98.094	12.066	0.010

Table 6-3: Four-target micrometre test results (* ***Test1*** *distance and error results averaged at each interval from 105 data points).*

Interval	Dial Reading (mm)	Int. Target Dist. (mm) *	Ext. Target Dist. (mm) *	Dist. Target-Zero Int. (mm) *	Dist. Target-Zero Ext. (mm) *	Error Int. (%) *	Error Ext. (%) *
Test 1							
Reference	0.00	49.496	91.777	-	-	-	-
1-1	2.546	52.025	94.341	2.527	2.561	0.729	0.619
1-2	5.089	54.574	96.880	5.078	5.103	0.269	0.335
1-3	7.626	57.107	99.411	7.611	7.634	0.228	0.113
1-4	2.548	52.039	94.339	2.543	2.562	0.411	0.715
Test 2							
Reference	0.00	52.015	94.296	-	-	-	-
1-1	10.161	62.195	104.454	10.169	10.144	0.077	0.171
1-2	10.161	62.179	104.467	10.161	10.175	0.004	0.138
1-3	10.161	62.208	104.445	10.216	10.150	0.538	0.104
1-4	10.161	62.196	104.533	10.179	10.225	0.179	0.629
1-5	10.161	62.187	104.464	10.167	10.190	0.061	0.288
Test 3							
Reference	0.00	49.431	91.796	-	-	-	-
1-1	4.448	53.900	96.146	4.403	4.503	1.008	1.231
1-2	4.448	53.956	96.261	4.478	4.498	0.674	1.141
1-3	4.448	53.926	96.294	4.485	4.485	0.850	0.850
2-1	10.175	59.575	101.898	10.155	10.177	0.194	0.0273
2-2	10.175	59.653	101.981	10.197	10.196	0.222	0.208
2-3	10.175	59.675	102.014	10.205	10.237	0.304	0.612
Test 4							
Reference	0.00	49.448	91.738	-	-	-	-
1-1	4.452	53.905	96.234	4.473	4.475	0.469	0.520
1-2	4.452	53.891	96.178	4.426	4.455	0.580	0.075
1-3	4.452	53.910	96.204	4.463	4.473	0.241	0.478
2-1	11.447	60.933	103.201	11.501	11.441	0.475	0.045
2-2	11.447	60.297	103.209	11.462	11.486	0.132	0.339
2-3	11.447	60.892	103.195	11.444	11.464	0.020	0.150

6.6.3 Results of Two-Layer Beams

A total of 27 torsion experiments were performed on the set of two-layer laminated glass beam samples. This was comprised of two experiments on the samples 2PVB1, twelve experiments on 2PVB2, six experiments on 2SGP1, and seven experiments on 2SGP2. The ESSM was determined as per the method described in the previous chapter.

For the first two-layer PVB sample 2PVB1, the $G_{ESSM} = 7.54\,\text{GPa}$ and $7.66\,\text{GPa}$ in the first and second experiments, respectively, resulting in the average $G_{ESSM} = 7.6\,\text{GPa}$. For the next PVB sample, 2PVB2, in the first run of 8 experiments, the average $G_{ESSM} = 7.04\,\text{GPa}$ with results ranging from $6.87 - 7.49\text{GPa}$. Four more experiments were performed on 2PVB2 on a separate day. These resulted in a $G_{ESSM} = 7.23\,\text{GPa}$, therefore the overall average $G_{ESSM} = 7.10\,\text{GPa}$ for 2PVB1.

The Amadio-Bedon (A-B) and Enhanced Effective Thickness (EET) analytical methods were used for comparative calculation in the same manner as chapter 5.5 and Appendix A, with the same interpolation for G_{INT} values. By comparing these results with the two existing analytical models the following results were drawn:

- $G = 6.448\,\text{GPa}$ for the A-B method (16.4% difference to the ESSM test result for 2PVB1: $G_{ESSM} = 7.6\,\text{GPa}$; and 9.63% difference to the ESSM test result for 2PVB2: $G_{ESSM} = 7.10\,\text{GPa}$.
- $G = 6.445\,\text{GPa}$ for the EET method (16.45% difference to the ESSM test result for 2PVB1: $G_{ESSM} = 7.6\,\text{GPa}$; and 9.67% difference to the ESSM test result for 2PVB2: $G_{ESSM} = 7.10\,\text{GPa}$.

And if, as proposed in the previous chapter (5.5.3), use of expressions (5.6) and (5.7) are applied to A-B and EET methods, the difference in shear modulus values improve. For the A-B method, they improve to 12.97% for 2PVB1 and 6.18% for 2PVB2. For the EET method, they improve to 13% for 2PVB1, 6.21% for 2PVB2, and 6.22% for the additional inclinometer tests.

For the first 2-layer SGP sample, 2SGP1, on the first experimental run, $G_{ESSM} = 24.5\,\text{GPa}$ and $24.57\,\text{GPa}$ in the first and second experiments, respectively, resulting in the average

$G_{ESSM} = 24.54\,\text{GPa}$. A further three experiments were performed on another test day at the same load-rate of 4° per minute, resulting in an average $G_{ESSM} = 24.99\,\text{GPa}$, resulting in the overall average $G_{ESSM} = 24.81\text{GPa}$. By comparing these results with the theoretical results from A-B and EET methods, the results were:

- $G = 22.081\text{GPa}$ for the A-B method (11.64% difference to the ESSM test result for 2SGP1: $G_{ESSM} = 24.81\text{GPa}$.
- $G = 24.071\text{GPa}$ for the EET method (3.02% difference to the ESSM test result for 2SGP1: $G_{ESSM} = 24.81\text{GPa}$.

And again, by considering equations (5.6) and (5.7), the following results differed significantly. For the A-B method, the results improve to a 6.52% difference for 2SGP1. For the EET method, the results became slightly more accurate with this alteration, and still exhibited strong correlation to the experimental results and ESSM method with 2.17% difference. Overall, in both cases, the EET model exhibited better agreement to experimental and ESSM results for the first SGP sample, whereas in the previous study presented in chapter 5 for the 2-layer SGP beam, the A-B method showed better agreement for the latter case. For both 2-layer PVB samples, both the A-B and EET method had very similar agreements to experimental ESSM results.

6.6.4 Unexpected Results from Sample 2SGP2

Remarkable and somewhat peculiar results were obtained from the experimental run on the second 2-layer SGP sample. The same general level of torsional force and rotation at the machines chuck-end was reached as the first 2-layer SGP sample in all experiments. When computing the world

coordinate data and ESSM, however, the results were considerably higher than what should be theoretically possible based on the mechanical properties of glass and the SGP interlayer in this composition.

From the first four torsion tests performed, the experimental results returned the values of $G_{ESSM} = 76.92\,\text{GPa}, 82.73\,\text{GPa}, 79.39\,\text{GPa}$, and $G_{ESSM} = 78.63\,\text{GPa}$, resulting in an average of $G_{ESSM} = 79.42\,\text{GPa}$. In comparison with the theoretical results based on the analytical models of A-B and EET, and using equations (5.6) and (5.7) which previously proved to be more accurate, the following comparisons were obtained:

- $G = 23.244\,\text{GPa}$ for the A-B method (109.44% difference to the ESSM test result for 2SGP1: $G_{ESSM} = 79.42\,\text{GPa}$.
- $G = 25.354\,\text{GPa}$ for the EET method (103.55% difference to the ESSM test result for 2SGP1: $G_{ESSM} = 79.42\,\text{GPa}$; in relative terms for both cases the experimental results were roughly triple that of the theoretical values.
- When comparing the average ESSM experimental results between both two-layer SGP samples, there was a 104.79% difference between 2SGP2 ($G_{ESSM} = 79.42\,\text{GPa}$) and 2SGP1 ($G_{ESSM} = 24.81\,\text{GPa}$).

Due to these results having such a great degree of variance from what was expected, further experimental investigations were required to either validate, or invalidate said results. If these results were erroneous, some of the initial thoughts on the reasoning behind this were:

(1) The photogrammetric target columns were not properly read in the HALCON program, resulting in incorrect world coordinate data being generated.

(2) The calibrated stereo-camera system may have been nudged for these particular tests, invalidating the calibration from this point.

(3) There may have been several times during the test that 'jump' was present in the torsion machines rotational movement, at the moments that image pairs were taken, potentially skewing results.

Further experimental studies incorporating inclinometer sensors as additional measurement devices, and modifications to the load-duration were subsequently performed to answer these questions, which are detailed in forthcoming sections.

6.6.5 Inclinometer Validation Study

To further investigate the experimental results derived from the ESSM method for the 2SGP2 sample, two torsion tests with both inclinometer sensors and photogrammetric targets were performed. The aim was to validate or invalidate these results and to better understand the unpredictability of glass laminates with viscoelastic interlayers under torsion. This allowed both the reliability of the sensors to be evaluated, and correspondence to the photogrammetric target displacement to be evaluated by comparing the relative twist rate from both methods.

Four inclinometer sensors were fixed in central alignment with the longitudinal axis of the beam and spaced out along the target area. This positioning was for two reasons:

(1) The centre of the beam face should theoretically best represent the best fit regression line through a photogrammetric target column.

(2) Only four inclinometer sensors were available, which were most effectively applied by being spread across the entire distance of the target area.

The sensors were positioned on the 10th target column, between the 7th and 8th columns, between the 4th and 5th columns, and on the 2nd column (Figure 6-15). The torsion tests were both performed to 14° at the machines rotating end. Before both tests, the beam was re-installed as a fresh test all fitments were checked over to ensure they were fully secured, and all inclinometer sensors and the torsion machine were set to zero.

The results were analysed by determining the relative twist rate from the inclinometer sensors between the widest points available (r4 to r1) to give the most accurate representation of the torque-to-relative rotation relationship. The same was done for the corresponding photogrammetric targets, which were column 10 and column 2. By examining the results in Figure 6-18 and Figure 6-19, the relative twist rate from the sensors found good agreement with the photogrammetric relative twist rate. Therefore, it can be concluded that:

- These results give strong indication that the unexpected results of 2SGP2 ($G_{ESSM} = 79.42\,\text{GPa}$) were accurate and reliable, and represented the real physical torsional behaviour of this beam during these experiments.
- The photogrammetric approach was further proven in its efficacy, with a more smooth and consistent twist rate than inclinometer sensors.
- Further exploration into the complex and unpredictable behaviours of SGP laminated glass beams are required to better understand this viscoelastic interlayer material.

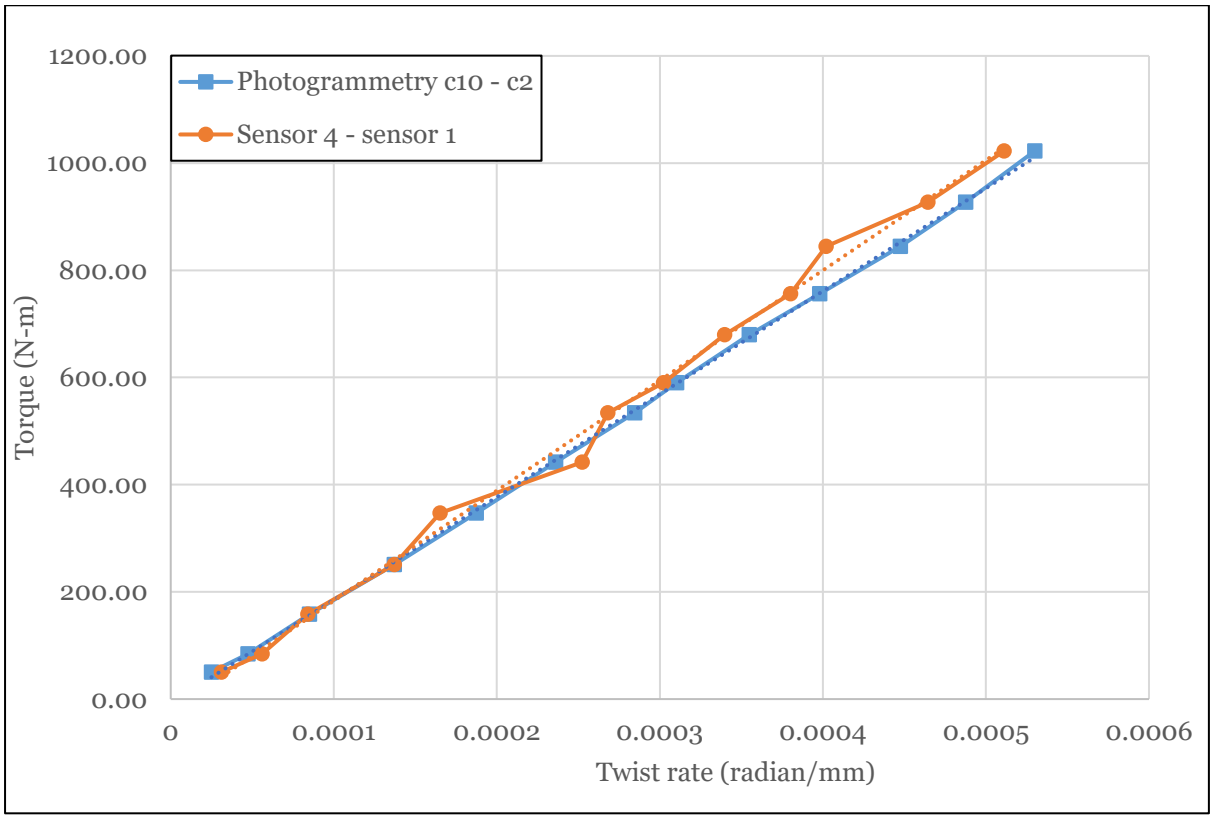

Figure 6-18: Test 1 2SGP2 relative twist-rate to relative torque relationship.

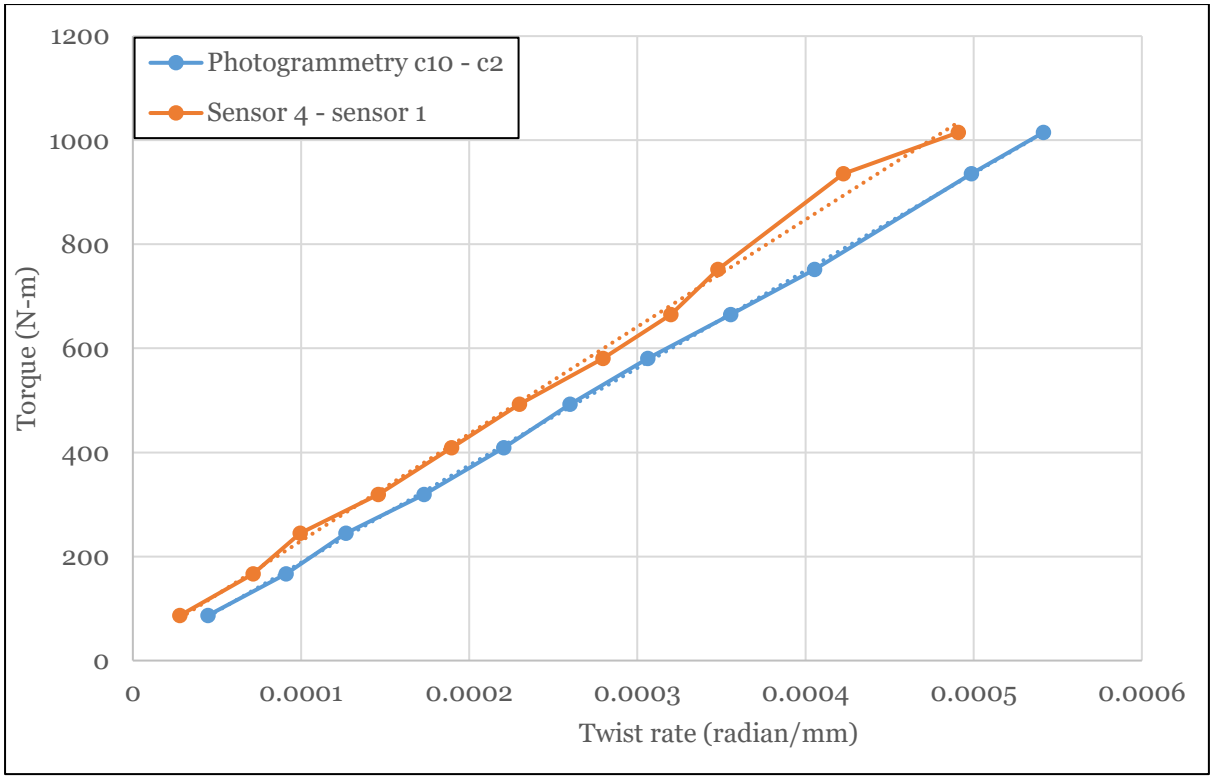

Figure 6-19: Test 2 2SGP2 relative twist-rate to relative torque relationship.

6.6.6 Analytical Model for Three-Layer Laminates

This experimental study was extended to include 3-layer laminated glass beam samples for the first time. The only analytical model to the authors' knowledge at present that allows the evaluation of torsional stiffness of slender, rectangular, three-layered glass beam elements with varying layer thicknesses is the general case of the Enhanced Effective Thickness (EET) model by Galuppi and Royer-Carfagni [79], so theoretical approximations using this method were performed for comparison with experimental results using the ESSM method.

First considering the ESSM method, in the case of a beam with an additional glass layer bonded by an additional interlayer, the additional layers must be accounted for in the torsional constant due to composite action from section 5.5.2. A laminated beam element of length L and width a comprised of an arbitrary number N of glass plies of thickness h_i, $i=1...N$, bonded by $N-1$ thin polymeric interlayers of thickness t_i, $i=1...N-1$ is used to model the three-layered

composite element. The equivalent torsional stiffness may be evaluated as $G_g J_{eff;EET} / J_{\text{homog}}$, where [79]:

$$J_{eff;EET} = \frac{1}{\frac{\eta}{J_{t,M}} + \frac{1-\eta}{J_{t,L}}}, \tag{6.1}$$

and where [79]:

$$J_{t,M} = \frac{1}{3} a \tilde{h}_{eq,M}^3, \qquad \tilde{h}_{eq,M} = \sqrt[3]{\sum_{i=1}^{N} h_i^3 + 12 \sum_{i=1}^{N} \bar{y}_i^2 h_i}, \tag{6.2}$$

$$J_{t,L} = \frac{1}{3} a \tilde{h}_{eq,L}^3, \qquad h_{eq,L} = \sqrt[3]{\sum_{i=1}^{N} h_i^3}. \tag{6.3}$$

The values for $H_i, \bar{y}$ describe the distance between centroids of each glass ply, and the distance between the centroid of each glass ply and the centroid of the entire structure, respectively. The geometrics of these parameters are presented in Figure 6-20.

The shear coupling coefficient for multi-laminates, η, can then be calculated by [79]:

$$\eta = \frac{1}{1 + 12 \frac{J_{t,L}}{J_{t,M}} \frac{\sum_{i=1}^{N} \bar{y}_i^2 h_i}{\sum_{i=1}^{N-1} H_i^2 / t_i} \frac{G_g}{G_{INT}} \frac{L^2 + a^2}{L^2 a^2}} \tag{6.4}$$

where G_g is the glass shear modulus and G_{INT} is the interlayer Shear Modulus. And where [79]:

$$J_{\text{homog}} = 0.3145 a \left(h_1 + h_2 + h_3 + t_1 + t_2 \right)^3 \tag{6.5}$$

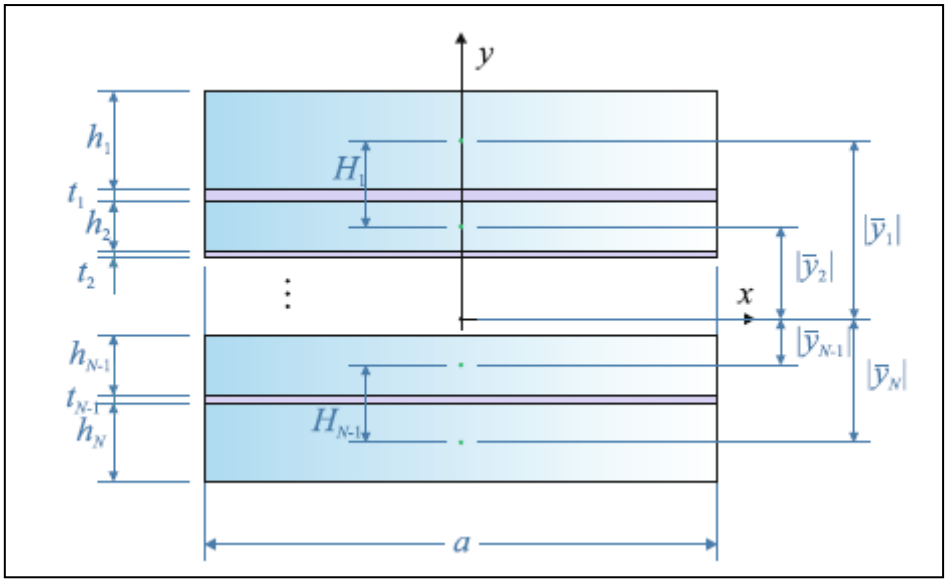

Figure 6-20: laminated glass beam composed of N glass plies of arbitrary thickness, bonded by $N-1$ polymeric interlayers [79].

6.6.7 Results for Three-Layer Beams

A total of 31 tests were performed across 6 test samples, which comprised of two beams with PVB interlayers, and four beams with SGP interlayers. This was comprised of four tests each on samples 3PVB1 and 3PVB2, seven and nine tests each on 3SGP1 and 3SGP2, respectively, which included tests with increased load-duration. 3SGP3 and 3SGP4 were tested three and four times each, respectively, which also included tests with lengthened load-durations. The experiments with modified load-duration are reserved for the next section. According to the theoretical EET model proposed by Galuppi and Royer-Carfagni [79] for three-layered PVB glass beams, the $G_{ESSM} = 21.15\,\text{GPa}$. For three-layered SGP laminates, the $G_{ESSM} = 79.83\,\text{GPa}$. A detailed calculation for both can be found in the appendices.

For the first PVB sample, 3PVB1, the experimental results using the ESSM method were $G_{ESSM} = 21.52\,\text{GPa},\ 21.46\,\text{GPa},\ 21.43\,\text{GPa},$ and $21.15\,\text{GPa}$. For the second sample, 3PVB2, the experimental results were $G_{ESSM} = 20.75\,\text{GPa},\ 21.55\,\text{GPa},\ 22.27\,\text{GPa},$ and $20.97\,\text{GPa}$. By averaging these results and comparing these to the EET model, the following comparisons were made:

- For the three-layer PVB samples ESSM test results; $G_{ESSM} = 21.39\,\text{GPa}$ for 3PVB1 and $G_{ESSM} = 21.39\,\text{GPa}$ for 3PVB2, which represents a 1.23% difference to the EET model (where $G_{ESSM} = 21.15\,\text{GPa}$).

Therefore, a very strong agreement was found between the experimental results using the developed ESSM method, and the EET model. The results indicate that both approaches are highly effective for determining the torsional rigidity in three-layered PVB laminated glass beams. Also, considering the general unpredictability of such composite structures due to several factors outlined throughout this Thesis, the experimental results had relatively little variance, in particular for 3PVB1.

For the first SGP sample, 3SGP1, the experimental results using the ESSM method were $G_{ESSM} = 45.82\,\text{GPa},\ 46.33\,\text{GPa},\ 47.89\,\text{GPa},$ and $47.04\,\text{GPa}$. For the second sample, 3SGP2, the experimental results using the ESSM method were $G_{ESSM} = 25.37\,\text{GPa},\ 25.47\,\text{GPa},\ 25.05\,\text{GPa},$ and $25.43\,\text{GPa}$. Again, by averaging these results and comparing to the EET model, the following comparisons were made:

- For the three-layer SGP samples ESSM test results; $G_{ESSM} = 46.77\,\text{GPa}$ for 3SGP1, and $G_{ESSM} = 25.33\,\text{GPa}$ for 3SGP2, which represent a 52.22% and a 103.65% difference to the EET model, respectively, (where $G_{ESSM} = 79.83\,\text{GPa}$).
- The experimental results of 3SGP1 and 3SGP2 returned a 59.47% difference from one another, despite both samples being identical in terms of specification and tested using the same method.

The experimental results therefore had a strong disagreement with the theoretical results of the EET model, and with the results from each other, despite being identical samples on paper. Interestingly, all the experimental results so far that yielded conflicting values for the shear modulus came from SGP laminated beam samples, whereas all the PVB laminated samples for both two- and three-layered composites returned values which maintained consistent and very close agreement to theoretical models. Some hypotheses were drawn as to the possible reasoning for these results.

(1) There may be some unexplained behaviours of the SGP interlayer under torsion, as this is the first time these elements have been studied experimentally, such as a time-dependent strain being induced through the composite beam element at a non-linear rate resulting in non-homogeneity in relation to the composite torsional resistance.

(2) The SGP material rigidity properties may vary greatly from sample-to-sample, and possibly under certain conditions (perhaps the material relaxes more than expected under longer-duration loading, which may have been induced from previous trial experiments or at the manufacturing stage without prior knowledge).

(3) There may be a simple error made in the experimental setup or calibration for these particular tests by chance, however this is unlikely as other beam samples were tested on the same days which yielded consistent results close to theoretical models. Furthermore, despite deviating greatly from theoretical models and each other, the shear modulus results of both samples were in a consistent range across all tests (45.82 GPa – 47.89 GPa for 3SGP1, 25.05 GPa – 25.47 GPa for 3SGP2).

By iterating the EET model in terms of the SGP interlayer based on experimental results, the shear modulus of the interlayer that was actually exhibited for each beam sample could be deduced as 67

MPa for 3SGP1 and 11 MPa for 3SGP2, compared to the quoted 191.03 MPa. Interestingly, the theoretical results from the EET model for three-layered SGP laminates agreed well with the experimental results of 2SGP2, which on the other hand significantly exceeded its theoretical value. Of course, due to these deviations, these results had to be investigated further. Consequently, the next two three-layered SGP samples, 3SGP3 and 3SGP4 were acquired from an alternative supplier. Also, due to the relaxation effects of viscoelastic interlayers under longer load-durations, all four three-layered SGP samples and both two-layered SGP samples were subjected to further torsion tests with modified load-rates in this regard.

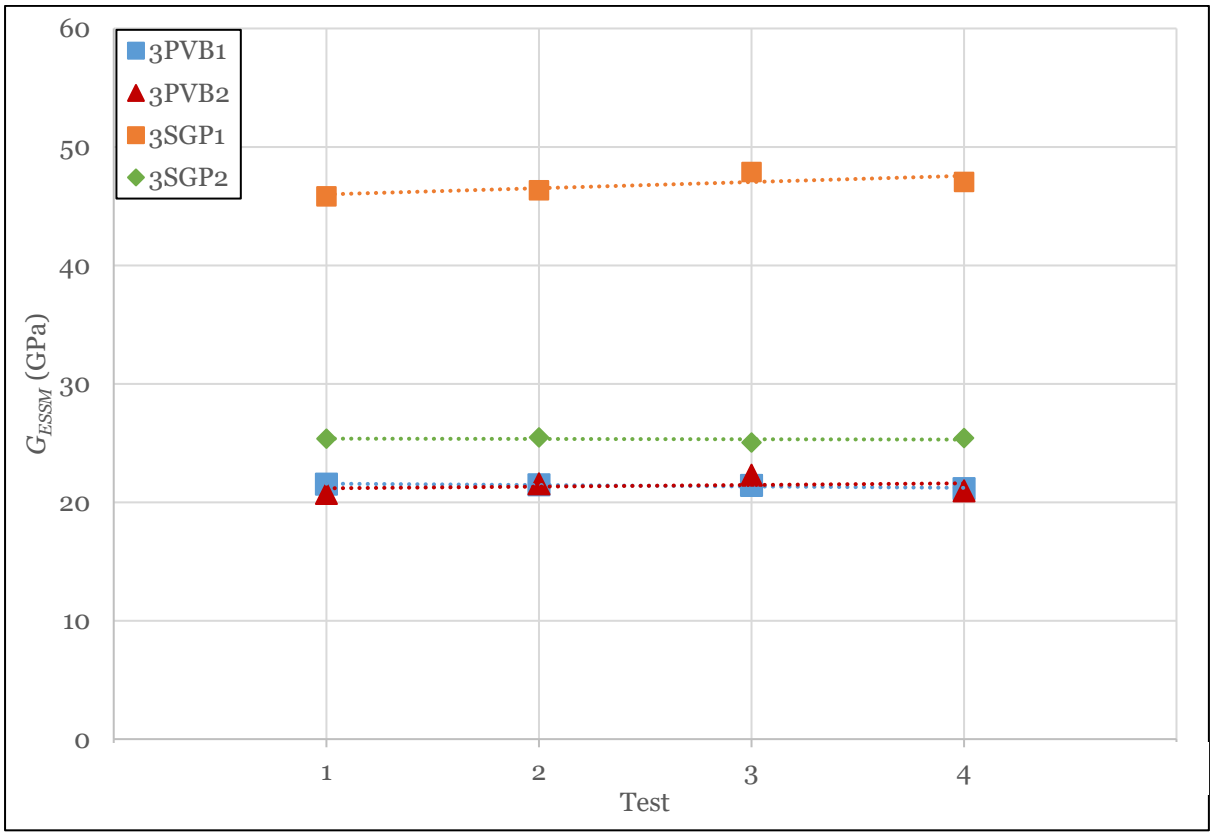

Figure 6-21: Experimental results for three-layered samples at 4° per min load-rate.

6.6.8 Increased Load-Duration on SGP Beams

One of the primary factors that effects viscoelastic interlayer materials such as PVB and SGP is the effect of load-duration. Generally, longer-term loading induces a relaxation effect on the interlayer

which should theoretically lower its shear modulus – an effect which is also quoted in the specifications for PVB and SGP [129] (Table 5-4,Table 5-5). The other primary factor that has an effect on the interlayer stiffness is temperature, which was kept constant at 20° in the testing facility throughout all tests described in this thesis.

All two- and three-layered samples containing SGP interlayers samples were tested with modified load-durations. The extended load-duration was induced by modifying the torsion machines load-rate from 4° per minute which was employed in all previous tests, to 2° per minute and 1° per minute. Additionally, an extra test on 3SGP4 was performed at 0.5° per minute. The resultant load durations were 2.75min, 5.5min and 11min for two-layer samples at 4°, 2°, 1°, respectively, and 2.25min, 4.5min, 9min, 18min for three-layer beams at 4°, 2°, 1°, 0.5°, respectively. One test each was performed for each load-rate, and the ESSM results are presented in Table 6-4.

Table 6-4: ESSM results under different load durations.

Sample	4° per min (GPa)	2° per min (GPa)	1° per min (GPa)	.5° per min (GPa)
2SGP1	25.454	24.985	24.289	-
2SGP2	84.739	80.945	72.756	-
3SGP1	32.379	32.914	32.826	-
3SGP2	32.484	33.189	33.725	-
3SGP3	33.499	33.583	34.233	-
3SGP4	23.851	23.208	26.445	24.254

Overall, the results were not conclusive to give evidence that the effect of lengthening load-durations in the short-to-medium term range were having any substantial effect on the SGP interlayer. However, this was exhibited in the two-layered samples, modestly in 2SGP1 and very clearly in 2SGP2. There was no clear trend observed across the four three-layered SGP samples, with 3SGP1 showing no significant difference, 3SGP2 and 3SGP3 showing a slight increase in stiffness which is contradictory, and no clear trend in 3SGP4 which was also tested under the

longer load-duration of 18 minutes and actually exhibited higher stiffness at this duration than at 2.25 and 4.5 minutes.

This was also the first time samples 3SGP3 and 3SGP4 were tested and had their ESSM determined. By evaluating the results at the same load-rate of 4° per minute against the theoretical EET model, the following was drawn:

- $G_{ESSM} = 33.49\,\text{GPa}$ for 3SGP3 and $G_{ESSM} = 23.85\,\text{GPa}$ for 3SGP4, which represented an 81.79% and a 107.97% difference to the EET model, respectively (where $G_{ESSM} = 79.83\,\text{GPa}$).
- When compared with each other, the results for 3SGP1, 3SGP2 and 3SGP3 were consistent, whereas 3SGP4 exhibited significantly lowered torsional rigidity.

The results from this study combined with the other findings presented in this chapter have given an indication that the complex behaviour of the SGP interlayer in a composite glass beam element may vary greatly between different samples for reasons that could not be firmly deduced at this time. This unpredictability also extends to analytical approximations for SGP laminated glass beams, which were found to be consistently accurate for modelling PVB beams.

6.7 Summary and Conclusions

- The novel concept of the equivalent-sectional shear modulus (ESSM) was further extended to study the torsional stiffness of additional two-layer, and for the first time three-layer laminated glass beams experimentally.

- Experimental equipment and test setup was further optimised by several implementations, improving the reliability and efficiency of the overall approach.

- Accuracy of the measurement system and photogrammetric approach was validated by optimised micrometre experiments, which proved to be highly accurate. The ESSM value for two monolithic beam samples was calculated from torsion experiments, which agreed well with theoretical shear modulus values, validating the approach.

- 27 torsion tests were performed on two samples each of PVB and SGP two-layered laminated glass beams. The ESSM results for both PVB samples and the first SGP sample found good agreement with analytical models, however the other SGP sample exhibited surprisingly high torsional stiffness.

- A further experimental investigation was performed on this sample to prove or disprove the results by employing inclinometer sensors on the beam in correspondence with photogrammetric targets. The sensor results agreed well with the photogrammetric targets in terms of relative torsional displacement, and the ESSM was again calculated to the same range. Therefore, it was concluded that this beam did really exhibit exceptionally high torsional stiffness.

- 31 torsion tests were performed on two samples each of PVB and SGP three-layered laminated glass beams. The ESSM results for both PVB beams agreed very well with the analytical model, however both SGP beams disagreed to a great degree from this, and also deviated significantly from each other in terms of torsion stiffness.

- A further experimental study was performed to investigate the effect of lengthened load-durations on two- and three-layered SGP beams, including two additional three-layered SGP samples. Results from 19 tests in the range of 2.25-18 minutes did not show any consistent effect of load-duration on the decreasing or increasing of torsional stiffness.

- The developed method was found to be direct, effective, and accurate when extended to three-layer laminated glass beams for evaluating the composite torsional stiffness. The optimisations made to the equipment and methods improved the reliability and efficiency of the setup and could be recommended for any further torsion tests.

- The SGP ionomer was found to exhibit great unpredictability in its torsional stiffness behaviour from sample to sample in the context of multi-layered glass beams. This therefore effects analytical models for the shear modulus which were found to be accurate and effective for all the PVB laminates tested. A few theories for this behaviour were given but nothing conclusive could be drawn.

- Further experimental work in the study of multi-layered SGP laminated glass beams under torsion is required to investigate the complex mechanical behaviours of this interesting ionomer, particularly to better understand why such unpredictability is present from sample to sample in order to improve existing analytical solutions.

7. Eccentric Torsion Study

This chapter presents the first experimental investigation into the effects of eccentric torque on the torsional stiffness of monolithic and laminated structural glass beams by inducing an eccentricated torsional load-path through a modified experimental setup. Torsion experiments were performed on monolithic, 2-layer and 3-layer laminated glass beams which were clamped at set intervals off from their centreline. The ESSM approach was employed to determine the torsional stiffness, and the results were compared to torsion tests on centrally-loaded beam specimens.

7.1 Purpose, Samples and Equipment

7.1.1 Purpose

In the previous study in chapter 6, the accurate central alignment of glass beam specimen clamping was optimised by the implementation of ruled markings and laser-levelling. This ensured that a symmetric torsional load path was induced, and the experimental results replicated existing analytical models and practical application. Without such considerations taking place, it may be difficult to ensure precise central alignment in the experimental process, and thus theoretically an eccentricated torsional load path may be induced which may influence the overall torsional rigidity of the beam specimen or have other potentially detrimental effects on experimental reliability. This phenomenon has not yet been studied in the context of experimental torsion for monolithic nor laminated structural glass beams, nor to the authors knowledge has it been study for structural glass beam elements under any experimental state or theoretically. Engineers, however, do need to think about eccentric loading in various forms in reality as opposed to simplified loads through the centroid of a member, as this may influence its overall limit state. This study therefore aimed to provide a first insight into the effects of eccentric torsion on the torsional rigidity of monolithic,

two-layer, and three-layer laminated structural glass beams by performing torsion experiments on these specimens with an enforced eccentricated load path at both clamped ends. The objective was for the results to give a basic initial insight into the magnitude of the effects of eccentric torque on the overall torsional rigidity of these members (if any) and provide some basis for further experimental work which may lead to the future development of analytical models in this regard.

7.1.2 Test Samples and Equipment

Monolithic, two-layer, and three-layer PVB and SGP laminated glass beams were tested under both centrally-aligned (C-A) and vertically-eccentricated torsion (VET) in this study. The same beam specimens were tested for this study as were used in the previous two chapters 5 and 6, as presented in Table 7-1. All beams were also prepared with the same layout of photogrammetric targets. The Tinius Olsen torsion testing machine was again used for this study. The optimised clamp system with ruled markings along both longitudinal and transverse axes from chapter 6 was again employed to fix beam specimens securely to the torsion machine. This, in combination with a laser level, allowed for eccentric fixation to be applied and quantified for eccentric torsion tests.

The binocular stereo-vision system was also the same as was employed in the previous chapter – incorporating two Canon EOS 7D DSLR cameras with 50 mm EF f/1.8 II fixed focal lenses fixed to a solid tripod and extension arm. Illumination was achieved by two softbox lighting units which were positioned at a shallow angle to the torsion machines bench to negate any glare from glass specimens. A third Canon camera was fixed to a tripod, linked to the other two cameras via splitter cables and positioned to capture the torsion machines output data from the control PC monitor.

Table 7-1: Glass beam test samples used in eccentric torsion study.

ABBREV	Length (mm)	Height (mm)	Thickness (mm)	Glass Type	No. Glass Plies	Composition (mm)
MONO1	2400	240	10	T*, HS**	1	10
MONO2	2400	240	10	T*, HS**	1	10
2PVB1	2400	240	21.52	T*, HS**	2	10 | 1.52 | 10
2PVB2	2400	240	21.52	T*, HS**	2	10 | 1.52 | 10
2SGP1	2400	240	21.52	T*, HS**	2	10 | 1.52 | 10
2SGP2	2400	240	21.52	T*, HS**	2	10 | 1.52 | 10
3PVB1	2400	240	25.04	T*, HS**	3	6 | 1.52 | 10 | 1.52 | 6
3PVB2	2400	240	25.04	T*, HS**	3	6 | 1.52 | 10 | 1.52 | 6
3SGP1	2400	240	25.04	T*, HS**	3	6 | 1.52 | 10 | 1.52 | 6
3SGP2	2400	240	25.04	T*, HS**	3	6 | 1.52 | 10 | 1.52 | 6

7.2 Experimental Methods

7.2.1 Calibration and Validation of Stereo-Vision System

The experimental runs for this study were performed on three different test days, therefore calibrations for the binocular stereo-vision system were performed and validated for their accuracy each time. Calibrations were again performed in accordance with the optimised methods detailed in chapter 4, and each were validated by micrometre accuracy experiments.

The calibration pixel errors were found to be well within the range of ≤ 0.1 for all the calibrations, with the results being 0.0502, 0.0478, and 0.0312 pixels, indicating a highly accurate and effective calibration. Furthermore, micrometre accuracy experiments were performed in accordance with the methods developed in chapter 4. The results for the all the micrometre accuracy experiments proved to be very high, with errors of 0.0688% / 0.0490% (internal / external targets) for the first test, 0.0530% / 0.0467% for the second test, and 0.0259% for the third test which was a two-target setup. These were all considerably better than the 1% error range that was aimed for, proving the calibrated stereo-vision system and photogrammetric target application was highly accurate and reliable.

7.2.2 Preparation and Setup

Monolithic, two-layer, and three-layer PVB and SGP beams were marked with columns of photogrammetric targets prior to the experimental run in the same layout of eleven columns of fifteen targets at 70 mm distance apart from each other, with targets being 5 mm in diameter with 15 mm vertical spacing between each target.

The process of clamping beam samples had to be modified to induce the eccentric torsional load-path. The use of a laser-level in combination with ruled and central-alignment markings were therefore employed during the clamping process before each test. All the test samples were clamped with a vertical distance of 10 mm off-centre at both ends. This distance was decided for this early investigation into eccentric torque-effects as it is a modest but fairly substantial, and also a realistic error that may be encountered during such types of experimental setup in absence of a carefully planned and executed setup. Furthermore, if an inadvertent slippage of a test specimen from its clamped location were to occur due to the clamp not being fully tightened for example, it would likely occur downward in the vertical direction due to gravity. Therefore, this investigation focused on a vertical eccentricity.

The clamping process was performed by first centrally securing the beam using the laser level and pre-cut blocks, then measuring a 10 mm change from the centre and adjusting the beam at each end to this level, before fully tightening the clamps. In between every test, the beam was removed and re-clamped in this manner to relieve any residual compressive stress that may have built up at the clamped ends from the prior test. A period of roughly ten to fifteen minutes was also allowed in between tests to allow the interlayer materials to ‘reset’ in case there were any relaxation effects due to the previous load-duration. To prepare for C-A torsion experiments which were performed for comparison with VET tests, laser-levelling and ruled markings were used to ensure an accurate centrally-clamped test specimen, the same as per the previous chapter.

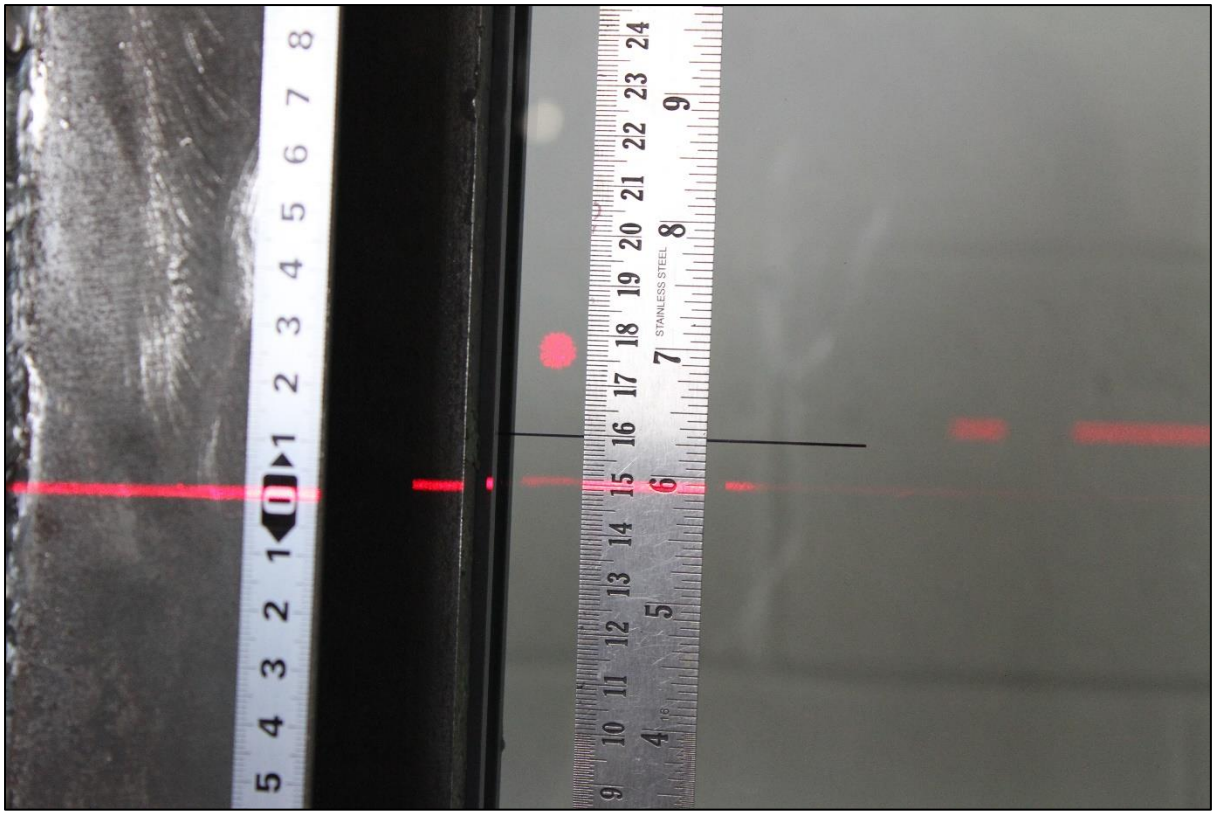

Figure 7-1: 10 mm off-centre clamped beam to induce eccentric load-path (fixed end).

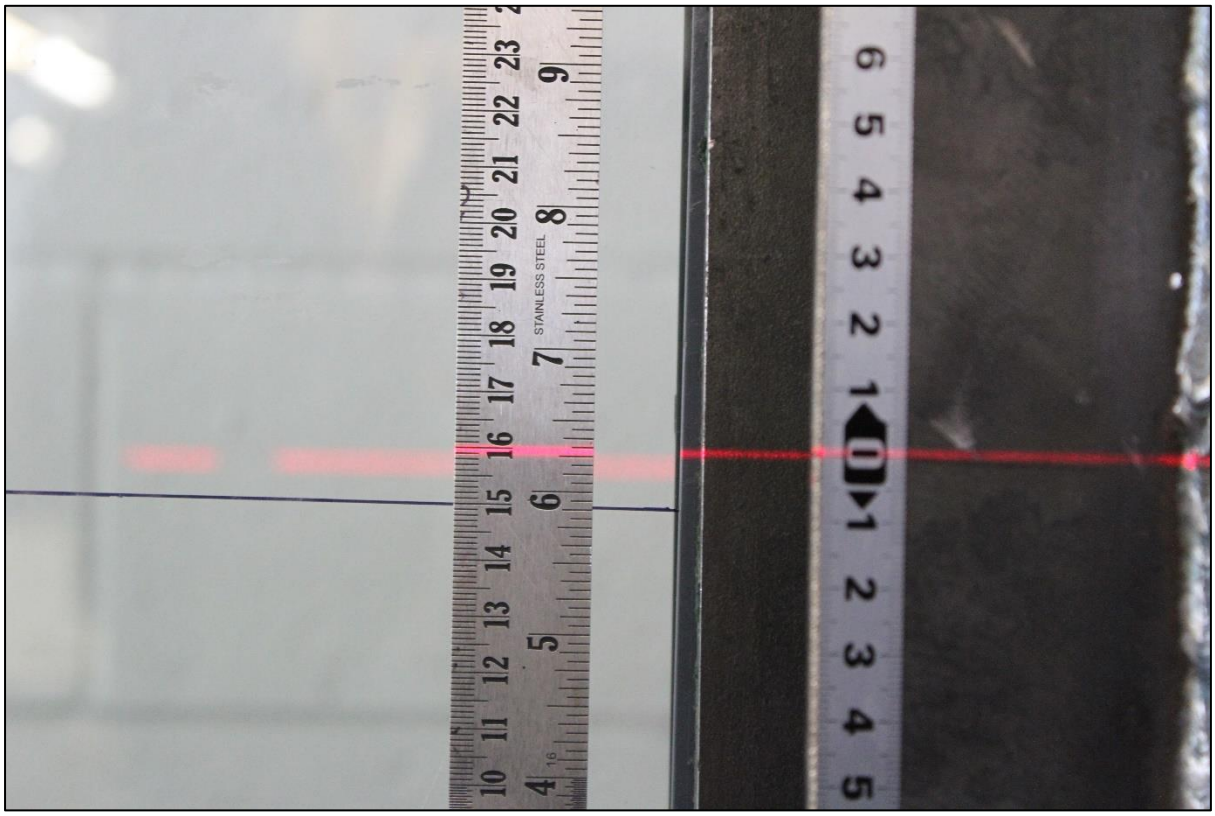

Figure 7-2: 10 mm off-centre clamped beam to induce eccentric load-path (rotating end).

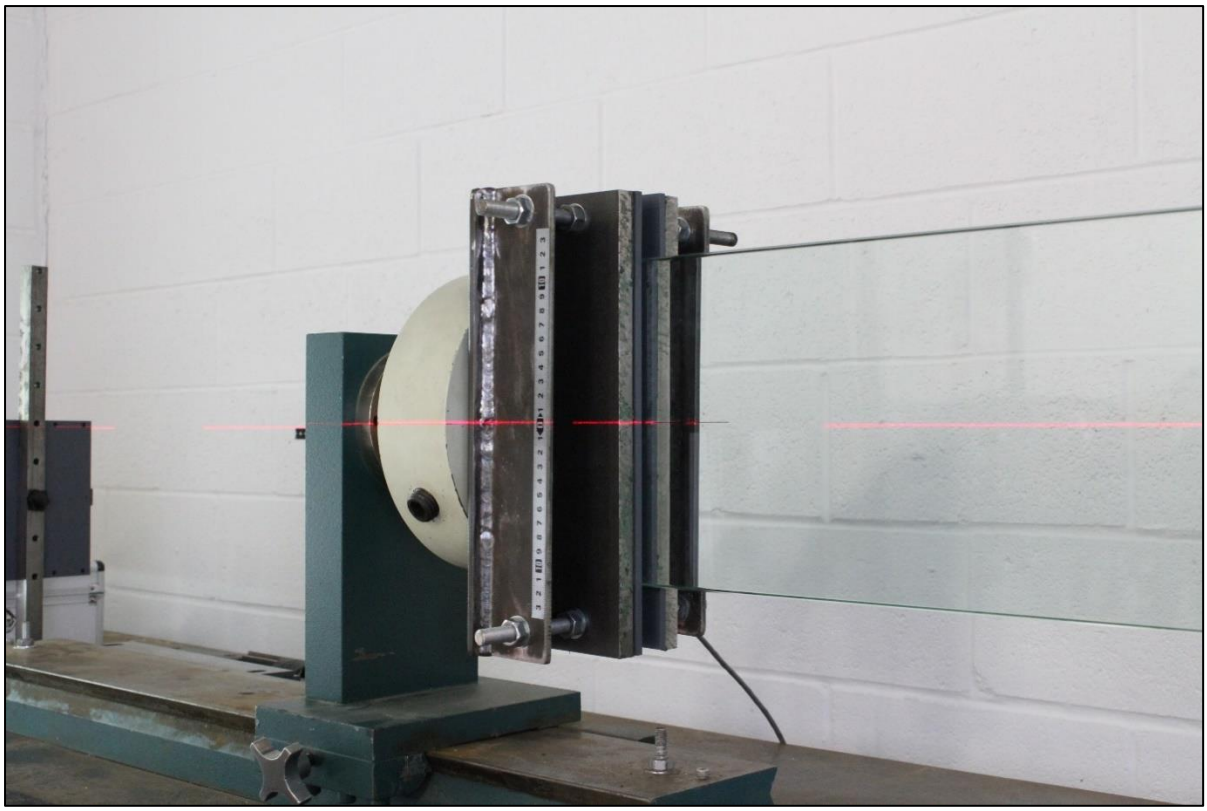

Figure 7-3: Vertically-centred test specimen.

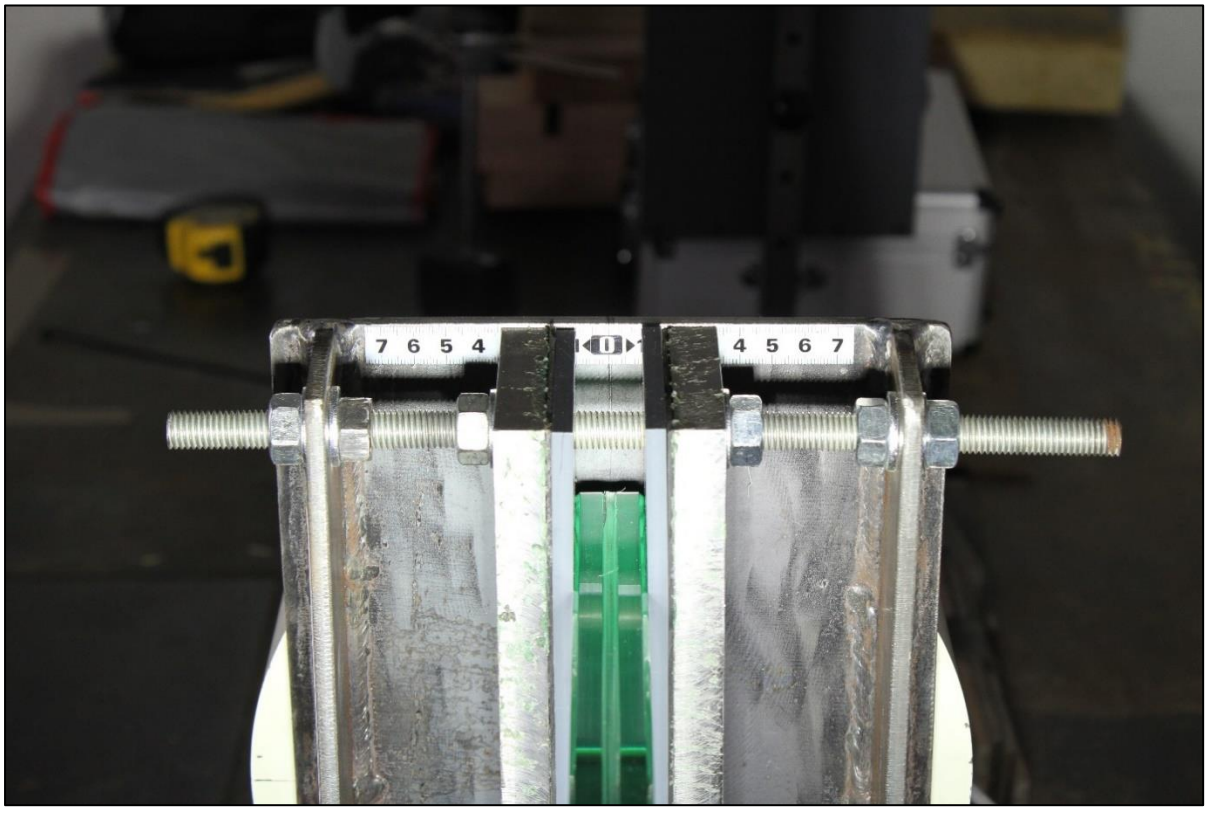

Figure 7-4: Horizontally-centred test specimen.

7.2.3 Torsion Tests

A total of twenty VET experiments were performed for the initial investigation on the sample set of monolithic, two-layer, and three-layer laminated glass beams. This was comprised of two experiments per each beam at the interval of 10 mm vertically-eccentricated fixation. Before initiating each test, the torsion machines rotating chuck was checked to confirm it was aligned to zero, then the torque and rotation were set to zero to take the first reference image using the calibrated stereo-vision system.

The VET experiments on monolithic beam samples, MONO1 and MONO2, were both torqued to 24°. The two-layered PVB samples, 2PVB1 and 2PVB2, were also both torqued to 24°, which required more than twice the torsional force as the monolithic samples. The two-layered SGP samples, 2SGP1 and 2SGP2, were torqued to 12° at the machines rotating end, which required the full capacity and slightly exceeded the machines 1 kN-m. The three layered PVB samples, 3PVB1 and 3PVB2, were both torqued to 10° expending the torsion machines full capacity. The three-layered SGP samples, 3SGP1 and 3SGP2, were also torqued to 10° each, also expending the torsion machines quoted output capacity. All torsion tests were performed at 4° per minute load-rate. The torque-rotation relationship based on the torsion machines output data is presented in Figure 7-5 for each 10 mm eccentric torsion test.

Stereo-image pairs were taken from the interconnected three-camera system – that being two from the binocular stereo-vision system and a third observing the torsion machines output data - at set intervals to capture the photogrammetric target displacements. For all monolithic and two-layered beam samples images were taken at every 2° intervals. For all three-layered samples, images were taken at every 1° interval. Once each experiment was concluded, the torsion machine was returned to zero degrees, the beam was removed and re-clamped with the same eccentricated alignment for the next test.

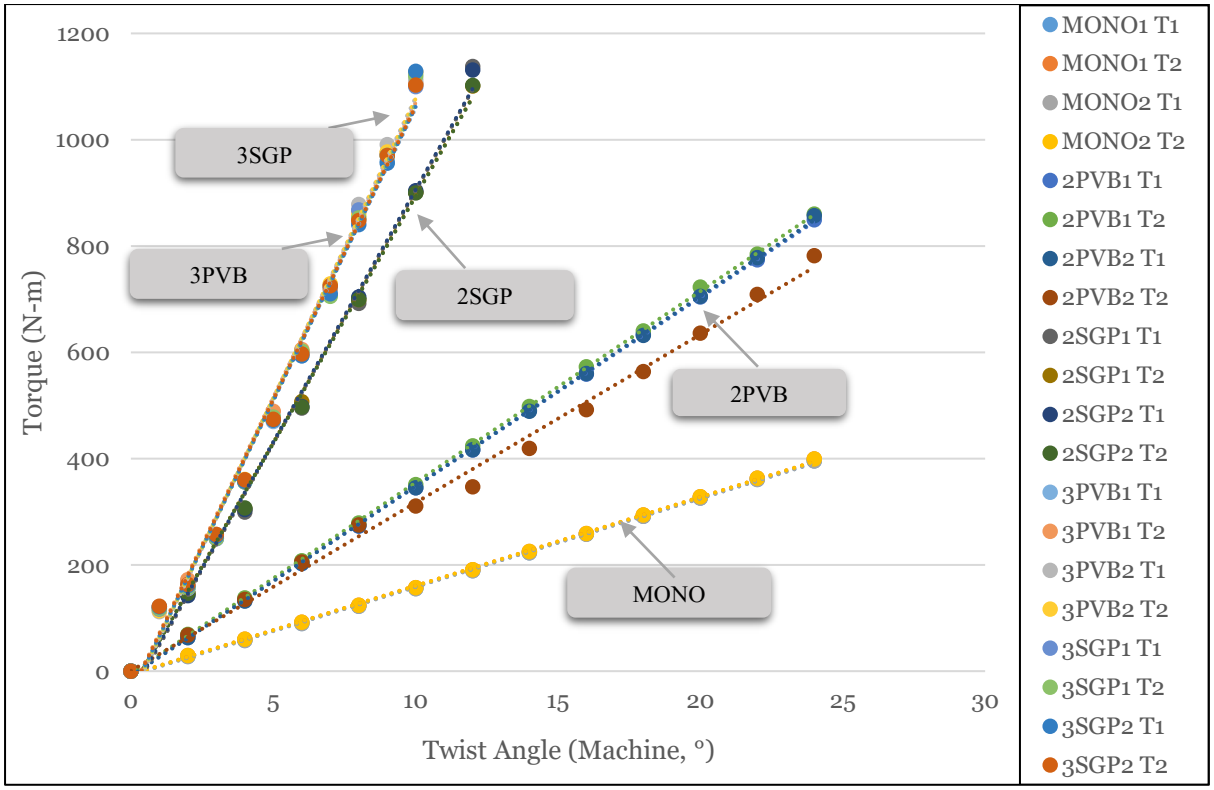

Figure 7-5: Torque-rotation relationship for 10 mm eccentric torsion tests.

7.3 Results and Discussion

7.3.1 Results for Monolithic Beams

Two torsion tests each were performed on the two monolithic beam samples, MONO1 and MONO2, with a vertical induced 10 mm eccentricity at both clamped ends, with a 10 mm lowering at the rotating end and 10 mm heightened at the fixed end. The ESSM was calculated from the experimental results and compared with the results from C-A torsion tests on the same beam samples.

For the first sample, MONO1, the $G_{ESSM} = 28.32\,\text{GPa}$ and $28.38\,\text{GPa}$ in the first and second VET experiments, respectively, providing an average value of $G_{ESSM} = 28.35\,\text{GPa}$. For the second monolithic sample, MONO2, the $G_{ESSM} = 29.73\,\text{GPa}$ and $29.75\,\text{GPa}$ in the first and second VET experiments, respectively, providing an average $G_{ESSM} = 29.74\,\text{GPa}$. As there are currently no analytical solutions available to model the effect of VET on beam elements, a comparison with C-A

experimental results was made. Compared with experimental results for C-A torsion tests on the same samples using the ESSM method, the following can be drawn:

- $G_{ESSM} = 27.84\,\text{GPa}$ for the C-A torsion test on MONO1, which meant the torsional stiffness from VET ESSM experimental results increased by 2.62% in comparison to C-A experiments.
- $G_{ESSM} = 29.23\,\text{GPa}$ for the C-A torsion test on MONO2, which meant the torsional stiffness from VET ESSM experimental results increased by 1.73% in comparison to C-A experiments.

The results for monolithic beam samples showed a slight increase in torsional stiffness when a 10 mm vertical eccentricity is induced to the torsional load path. This may have only a minor or insignificant impact on the reliability of experimental results for monolithic structural glass beams, as it is common for the level of variance observed to occur from test to test. Further investigations were therefore performed into two-layer and three-layer laminated glass beams, as the effects may be compounded by the viscoelastic nature of the interlayer.

7.3.2 Results for Two-Layer Beams

Two torsion experiments each were performed on the two-layer laminated glass beam samples - 2PVB1, 2PVB2, 2SGP1 and 2SGP2, making eight VET experiments in total for two-layered samples.

For the first two-layer PVB sample, 2PVB1, the $G_{ESSM} = 7.06\,\text{GPa}$ in the first VET experiment, and $G_{ESSM} = 7.14\,\text{GPa}$ in the second VET experiment, resulting in the average

$G_{ESSM} = 7.10\,\text{GPa}$. For the next PVB sample, 2PVB2, the $G_{ESSM} = 6.98\,\text{GPa}$ in the first VET experiment, and $G_{ESSM} = 6.21\,\text{GPa}$ in the second VET test, resulting in the average $G_{ESSM} = 6.59\,\text{GPa}$. Two C-A torsion tests were also performed on each sample. By comparing the VET results with the C-A torsion test results on the same samples using the ESSM method, the following observations were made:

- $G_{ESSM} = 7.6\,\text{GPa}$ for the C-A torsion tests on 2PVB1, therefore the VET ESSM experimental results showed a percentage *decrease* in the torsional stiffness of 13.29% in comparison to C-A experimental results using the ESSM method.
- $G_{ESSM} = 7.11\,\text{GPa}$ for the C-A torsion tests on 2PVB2, therefore the VET ESSM experimental results showed a percentage *decrease* in the torsional stiffness of 7.31% in comparison to C-A experimental results using the ESSM method.

For the first two-layer SGP sample, 2SGP1, the $G_{ESSM} = 24.63\,\text{GPa}$ in the first VET experiment, and $G_{ESSM} = 24.57\,\text{GPa}$ in the second VET experiment, resulting in the average $G_{ESSM} = 24.60\,\text{GPa}$. For the second two-layer SGP sample, which was the exceptionally rigid 2SGP2, the $G_{ESSM} = 79.39\,\text{GPa}$ in the first VET experiment, and $G_{ESSM} = 78.63\,\text{GPa}$ in the second VET experiment, resulting in the average $G_{ESSM} = 79.01\,\text{GPa}$. Two C-A torsion tests were again performed on each sample. By comparing the VET results with the C-A torsion test results on the same samples using the ESSM method, the following observations were made:

- $G_{ESSM} = 24.54\,\text{GPa}$ for the C-A torsion tests on 2SGP1, therefore the VET ESSM experimental results showed a percentage *increase* in the torsional stiffness of 0.24% in comparison to C-A experimental results using the ESSM method.

- $G_{ESSM} = 79.39\,\text{GPa}$ for the C-A torsion tests on 2SGP2, therefore the VET ESSM experimental results showed a percentage *decrease* in the torsional stiffness of 0.47% in comparison to C-A experimental results using the ESSM method.

In both cases of two-layered PVB and SGP laminated glass beams, the influence of a 10 mm VET induced by fixing the beam specimen off-centre at both clamped ends was assessed. For both the SGP samples there was no measurable difference in the torsional stiffness from this effect, with sub-percentage differences between both experiments. In the case of both PVB laminates, however, there was a quite significant decrease in torsional stiffness observed when the 10 mm vertical eccentricity was enforced for these torsion tests, when compared with C-A tests. The increases of 6.8% and 7.59% could have some significance in analytical models based on the shear modulus derived from torsion test data. Therefore, in the case of two-layer PVB laminated glass beams in particular, care should be taken in the setup to ensure accurate centrally-aligned fixation of the test sample at both ends.

7.3.3 Results for Three-Layer Beams

Three-layered PVB and SGP laminated glass beams were also studied under eccentricated torsion. Again, two torsion experiments each were performed on the three-layer laminated glass beam samples - 3PVB1, 3PVB2, 3SGP1 and 3SGP2, making eight VET experiments in total.

For the first three-layer PVB sample, 3PVB1, the $G_{ESSM} = 20.99\,\text{GPa}$ in the first VET experiment, and $G_{ESSM} = 21.19\,\text{GPa}$ in the second VET experiment, resulting in the average $G_{ESSM} = 21.09\,\text{GPa}$. For the second three-layer PVB sample, 3PVB2, the $G_{ESSM} = 21.19\,\text{GPa}$ in the first

VET experiment, and $G_{ESSM} = 21.46\,\text{GPa}$ in the second VET experiment, resulting in the average $G_{ESSM} = 21.33\,\text{GPa}$. Two C-A torsion tests were additionally performed on each sample. By comparing the VET results with the C-A torsion test results on the same samples using the ESSM method, the following observations were made:

- $G_{ESSM} = 21.29\,\text{GPa}$ for the C-A torsion tests on 3PVB1, therefore the VET ESSM experimental results showed a percentage *decrease* in the torsional stiffness of 0.94% in comparison to C-A experimental results using the ESSM method.
- $G_{ESSM} = 21.63\,\text{GPa}$ for the C-A torsion tests on 3PVB2, therefore the VET ESSM experimental results showed a percentage *decrease* in the torsional stiffness of 1.4% in comparison to C-A experimental results using the ESSM method.

For the first three-layer SGP sample, 3SGP1, the $G_{ESSM} = 47.27\,\text{GPa}$ in the first VET experiment, and $G_{ESSM} = 46.65\,\text{GPa}$ in the second VET experiment, resulting in the average $G_{ESSM} = 46.96\,\text{GPa}$. For the second three-layer SGP sample, 3SGP2, the $G_{ESSM} = 26.62\,\text{GPa}$ in the first VET experiment, and $G_{ESSM} = 25.06\,\text{GPa}$ in the second VET experiment, resulting in the average $G_{ESSM} = 25.85\,\text{GPa}$. Similarly, to the previous experiments, two C-A torsion tests were additionally performed on each sample. By comparing the VET results with the C-A torsion test results on the same samples using the ESSM method, the following observations were made:

- $G_{ESSM} = 47.47\,\text{GPa}$ for the C-A torsion tests on 3SGP1, therefore the VET ESSM experimental results showed a percentage *decrease* in the torsional stiffness of 1.08% in comparison to C-A experimental results using the ESSM method.

- $G_{ESSM} = 24.58\,\text{GPa}$ for the C-A torsion tests on 3SGP2, therefore the VET ESSM experimental results showed a percentage *increase* in the torsional stiffness of 5.17% in comparison to C-A experimental results using the ESSM method.

The results of the three-layered PVB samples, 3PVB1 and 3PVB2, were first considered. Overall, there was no significant difference observed in the torsional stiffness of these beams between centrally-aligned torsional loading and an eccentricated torsional load-path of 10 mm off-centre at each clamped end. The percentage differences of 0.94% for 3PVB1 and 1.4% for 3PVB2 were within a close variational range which was observed for many C-A torsion tests on glass beams from the earlier studies in this work. The direction of the torsional stiffness change was consistent between both beam samples, as both beams exhibited a slight decrease in torsional stiffness, measured by the ESSM method.

Considering the three-layered SGP samples, 3SGP1 and 3SGP2, there were more contrasting results. The first sample, 3SGP1, which was the more rigid beam of the two overall as confirmed by both previous and current C-A torsion tests, exhibited only a slight decrease in torsional stiffness of 1.08% by induced the VET of 10 mm at each end, compared to C-A tests. For the second sample, 3SGP2, however, a larger variance between C-A torsion tests and 10 mm VET tests was observed of 5.04%. Moreover, this was observed as a percentage increase in torsional stiffness caused by the eccentricity. This was contrary to the direction of the previous two samples which likewise displayed a greater variance from C-A experiments - two-layer laminates 2PVB1 and 2PVB2 – which displayed decreases in torsional stiffness when eccentricity was induced.

Variations of over 5% which were observed in a few samples may serve as point of caution to the experimenter (depending on the accuracy required), to apply some accuracy-improving implementations when setting up and performing glass beam torsion experiments. It was also interesting to observe that three-layered PVB and SGP samples both had very similar torque-to-machine twist angle relationships, however more significantly differing ESSM values. This

indicates that the torsional behaviours of these complex composite elements cannot be predicted using the end rotation data even in like-for-like specimens, and there may be even more non-linearity than previously thought.

Simple but effective strategies such as the use of laser levels, ruled markings on clamps and central markings which have been employed throughout this work can eliminate these uncertainties. Overall, there was no clear indication universally across monolithic, PVB or SGP two- or three-layer laminate glass beams that there would be a decrease or increase in the torsional stiffness resulting from 10 mm of vertically eccentric torsional loading, in comparison with a verified centrally-aligned experiment.

7.4 Summary and Conclusions

- The effects of an eccentric torsional load were studied on monolithic, two-layer and three-layer laminated structural glass beams for the first time experimentally.

- The experimental setup employed the use of laser-levelling, ruled markings and alignment markings to precisely prepare a 10 mm vertically-eccentricated fixation of glass beams to the torsion machine, and precisely enforce an eccentric torsional load-path experimentally.

- The photogrammetric approach developed earlier in this work was employed to measure torsional displacements. The measurement accuracy of the system was proven to be extremely high by way of micrometre experiments.

- A total of twenty VET experiments were performed, comprised of two each per beam sample. In addition, two C-A torsion tests were also performed for each beam to compare torsional stiffness effects. The novel ESSM method was employed to determine the values of torsional stiffness.

- In most glass beam samples there was no significant difference in torsional stiffness observed between eccentric and C-A torsion experiments. However, in both two-layer PVB samples and one three-layer SGP sample, there was a larger difference when VET was introduced which may have moderate influence on analytical models and design assumptions.

- The use of accuracy-boosting measures in the preparation of glass beam torsion tests, such as laser-levelling, ruled markings, and validating the accuracy of a calibrated stereo-vision system through micrometre experiments are again recommended to ensure reliability of experimental results.

- Further interesting research could be to study horizontal and combined horizontal and vertical eccentrically loaded laminated glass beams. In the future, further work in this area could lay the foundations to build analytical models which can improve clarity and efficiency in the design of laminated glass structures.

8. Conclusions and Further Work

This chapter summarises the main objectives, methods, and findings presented throughout this Thesis and provides the main conclusions resulting from both the individual studies and the entire work as a whole. Recommendations for further research are then provided to conclude the chapter.

8.1 Summarisation

The overall background and direction of the work is summarised in the abstract, and in the organisation of the Thesis section in chapter 1.4. A further summarisation of the work detailed in each individual chapter is provided in the summary and conclusions section of their respective chapters, except in the Introduction (1), and Structural Glass Fundamentals (2) chapter which gives some basic background information.

8.2 Objectives and Achievement

The initial primary objectives of this work and their backgrounds, the methods developed and utilised to meet them, and related accomplishments were as follows:

(1) Develop and optimise a non-destructive, structural-sized torsion test experimental approach for laminated glass beams to enable their torsional mechanical behaviours to be better studied.

- A structural-sized torsion test method was developed for the first time for laminated structural glass beams and optimised for the unique nature of glass and laminated glass.

(2) Develop, test, validate, and employ a precise, efficient, and fully verifiable approach to measure the crucial torsional displacement data during experimentation that is required for determining the shear modulus and other crucial mechanical properties.

- A tailor-made, non-contact, displacement measurement system was developed based on the principles of binocular stereo-vision. Furthermore, a target-based photogrammetric approach was employed for highly accurate and effective measurements during experimentation.

- A tailor-made micrometre accuracy experiment was developed to quantify the measurement accuracy of the system for the specific target-based application.

(3) Determine the torsional rigidity and related behaviours of laminated structural glass beams under physical experimentation using the developed methods and compare these to existing analytical models.

- The novel concept of the 'equivalent-sectional shear modulus' was developed which enabled the measurement of the actual shear modulus in torsion from two- and three-layer laminated structural glass beams experimentally, in a quantifiable way.

- Validation of the experimental equivalent-sectional shear modulus approach was achieved for monolithic beams by comparing the shear modulus value to the theoretical shear modulus for glass. For two-layer and three-layer laminates, the ESSM method was further validated by comparing the results to existing analytical models. Additional validation for a remarkable case of results was achieved through a tailor-made experimental method combining inclinometer sensors in combination with the photogrammetric targets.

(4) Determine the effects of eccentric-torsion on the shear modulus (*extended study not included in original objectives)*

- The effects of eccentric-loading on the shear modulus under torsion were found by a basic experimental investigation and analysis which employed the ESSM method with a modified setup which enforced an eccentricated torsional load-path.

8.3 Primary Conclusions

The primary focus of this Thesis was to study the torsional mechanical behaviour of laminated structural glass beams experimentally. Several key findings were obtained during the course of this work related to this. These can be summarised as follows:

(1) Glass beam experimental displacement measurement system:

- Great efficiency and reliability of results can be achieved by performing stereo-camera calibration with the developed calibration plate holder, and a larger set of stereo image pairs than is recommended by the literature and technical recommendations, as this helps to cover for any potential erroneous images and enables a large measurement area to be effectively calibrated for.

- The developed micrometre accuracy experiment found the measurement accuracy of the system to be extremely high, with the error for all experimental results being below 1% compared with micrometre dial readings. There was also no noticeable difference between measurements taken from different planes with respect to the *z*-axis (depth), indicating that the system was highly effective for measurements in three-dimensions.

- This system and procedure was then used to validate all subsequent torsion tests, which proved that they all had great and reliable measurement accuracy. It can be concluded

that the system as a whole is highly effective for measuring torsional displacements in glass beam experiments.

(2) Torsion test equipment, instrumentation, and setup:

- The use of steel clamp inserts were found to be much more effective at securing highly rigid SGP and three-layered laminated glass beam samples for torsion tests.
- The use of laser levelling and alignment markings were an important optimisation technique for setting up torsion tests, as this ensures central-alignment of test specimens to the clamps and ensures the torsion machines rotating end is reset to parallel for each test.
- Effective methods were found to minimise glare and optimise illumination for glass beams during experimentation, which affects the reading of photogrammetric displacement targets. These were the employment of softbox lights with reflective covers, which must be set at a shallow angle to the targeted face of the beam. Polarising camera lens filters also helped to eliminate any further unwanted glare.

(3) The equivalent-sectional shear modulus (ESSM) method:

- The novel ESSM method developed, which was directly measured from the torque and sectional-rotation correlation using the developed torsion test and tailor-maid photogrammetry technique, was validated, and proven to be reliable.
- The initial study applying the ESSM method to laminated glass beams was done to two two-layer samples of PVB and SGP for seven and four experiments, respectively. By comparing the results to two existing analytical models for the shear modulus, the

ESSM method was found to agree quite well with PVB, with a 7-10% difference, and agree more highly with SGP with a 1-7% difference.

- From the extended ESSM torsion study which applied the fully optimised experimental setup and additional test samples including three-layered laminates, some interesting results were obtained. While all the monolithic and PVB beams agreed well with theoretical values, some SGP samples deviated significantly from theoretical values.

(4) Observations on the general torsional behaviour of PVB and SGP laminates:

- Overall, PVB laminated glass beams were found to behave very consistently in terms of torsional rigidity from sample to sample, and in both two- and three-layered specimens.

- Expectedly, SGP samples all contained higher torsional rigidity than PVB laminates. What was unexpected, however, was the great deal of variation in the torsional rigidity observed through experimentation between different SGP samples.

- The deformed torsional shape of laminated glass beams may not be linearly correspondent to the end rotation in all cases. An example of this was present in Figure 7-5, where the three-layered PVB and SGP beams both had almost the same torque-to-machine twist angle, however when the ESSM/shear modulus was calculated experimentally, the SGP samples displayed higher values. This indicates that there may be more complex composite behaviours due to these interlayers than previously thought, and they may exhibit some time-dependent stiffening/loosening in a non-linear, non-homogenised manner, and possibly under certain conditions which could not be conclusively proven within the constraints of this work.

(5) Unexpected results and verification:

- The first and most prominent unexpected result was that of the two-layered SGP beam, 2SGP2, which exhibited in relative terms almost triple the torsional rigidity than theoretical values, and its counterpart sample, 2SGP1. Three-layered SGP samples ESSM all deviated from theoretical shear modulus values, and some also showed variance from each other. This of course had to be retested and further verified.

- The addition of inclinometer sensors was employed for two further tests on this beam to check their displacement-correlation to photogrammetric targets. If good agreement was found between the relative torque-to-twist rate from both methods, then great confidence in the reliability of displacements measured could be insured and thus the ESSM/shear modulus value was also reliable. In both tests a good agreement was found between inclinometer and photogrammetry measurements, and the ESSM was again calculated in the same range for these tests. Therefore, it was concluded that this exceptionally high torsional rigidity was legitimately displayed.

- After acquiring two additional three-layered SGP from an alternative supplier and determining their ESSM, three of the four samples had good agreement with one another with closely correlating values, however the fourth beam had quite significant variance from the others. All samples also varied significantly from theoretical values. As the reliability of the system and ESSM method was proven in several ways, this further proves that great variance may be observed in these composite elements under torsion or certain conditions that were not presently identified.

(6) Effect of torsional load-duration on the shear modulus:

- Overall, the results were not conclusive to give evidence that the effect of lengthening load-durations in the short-to-medium term range were having any substantial effect on the

composite torsional rigidity. However, this was exhibited in the two-layered samples, modestly in 2SGP1 and very clearly in 2SGP2. There was no clear trend observed across the four three-layered SGP samples, with 3SGP1 showing no significant difference, 3SGP2 and 3SGP3 showing a slight increase in stiffness which is contradictory, and no clear trend in 3SGP4 which was also tested under a longer load-duration and actually exhibited higher stiffness at this duration than at shorter durations.

(7) The effect of eccentricity on the shear modulus under torsion:

- Optimising the precision of the torsion test experimental setup opened up the question: 'what the effect would be if such precision was not present?'. This was then explored through the eccentric-torsion study, where an off-centre fixing of monolithic and laminated glass beams was used to induce and vertically-eccentricated torsional load path during experimentation.

- In most glass beam samples there was no significant difference in torsional stiffness observed between eccentric and centrally-aligned torsion experiments. However, in both two-layer PVB samples and one three-layer SGP sample, there was a larger difference when vertically-eccentricated torque was introduced which may have moderate influence on analytical models and design assumptions.

- Although no firm conclusions can be drawn on the direction and magnitude of effect on the shear modulus under torsion from 10 mm of eccentricated torsion, due to the changes in some samples, this further reinforces the use accuracy-optimising experimental preparation methods developed in this work. Also, horizontal, and combined horizontal/vertical eccentric torque effects were not able to be studied within the constraints of this work, which might have a more substantial effect.

8.4 Further Work

Based on the findings presented in this Thesis, several suggestions for further research can be proposed:

(1) Torsional rigidity of SGP laminated structural glass beams

- The SGP ionomer in the composite setting studied was found to exhibit great unpredictability in its torsional stiffness behaviour from sample to sample in the context of multi-layered glass beams. This affects analytical models for the shear modulus which were found to be accurate and effective for all the PVB laminates tested. Further experimental work in the study of multi-layered SGP laminates under torsion is required to investigate the complex mechanical behaviours of this material, with a focus on understanding why such unpredictability is present. This may help to fine tune analytical models and experimental techniques.

(2) Long-term response of laminated structural glass beams under torsional loading

- Due to the viscoelastic properties of PVB and SGP interlayers, an experimental investigation into the long-term effects of constant torsional loading would be an interesting avenue to explore. A level of time-dependent relaxation is expected in these materials, which plays a key role in the overall evaluation and design of laminated glass structures. An initial experimental investigation into these effects on short-to-midterm loading was performed, however a longer-duration study would be interesting to explore extending this to about 24 hours. By iterating based on existing analytical models used and the shear modulus of PVB and SGP at this load duration, the overall composite effects on G could range from 2% to 14% reduction.

(3) Effect of eccentric-torsion

- A basic initial investigation into the effects of a vertically-eccentricated torsional load were studied on monolithic, two-layer, and three-layer laminated glass beams for the first time experimentally. As the results were mixed, with some samples exhibiting a difference in torsional stiffness due to this eccentricity, and others not exhibiting any clear difference, a further experimental investigation would be an interesting avenue to explore. This could be extended to horizontally-eccentricated torsional load effects and combined vertical and horizontal eccentricity.

- Furthermore, as this was the first attempt at studying the effect of eccentric-torque on structural glass beams, the derivation of analytical models would be an avenue for future research once a broader scope of experimental results becomes available.

References

1. Achintha, M., *Sustainability of glass in construction*, in *Sustainability of Construction Materials*. 2016.
2. Le Bourhis, E., *Glass : mechanics and technology*. 2nd ed. 2014, Weinheim: Wiley-VCH.
3. O'Regan, C., *Structural use of glass in buildings*. 2nd ed. 2015, London: Institution of Structural Engineers.
4. Uusitalo, O., *Float glass innovation in the flat glass industry*, in *SpringerBriefs in Applied Science and Technology*, A. Öchsner, Editor. 2014, Springer.
5. Haldimann, M., *Fracture Strength of Structural Glass Elements - Analytical and Numerical Modelling, Testing and Design*. 2006, École Polytechnique Fédérale de Lausanne: Lausanne.
6. Haldimann, M., A. Luible, and M. Overend, *Structural use of glass*. Vol. 10. 2008: Iabse.
7. Ashby, M., *Materials Selection in Mechanical Design*. 3rd ed. 2005, Oxford: Butterworth-Heinemann.
8. Feldmann, M. and R. Kasper, *Guidance for European Structural Design of Glass Components - Support to the implementation, harmonization and further development of the Eurocodes*, in *JRC Scientific Policy Reports*. 2014: Luxembourg.
9. Orowan, E., *Fracture and strength of solids.* Reports on Progress in Physics, 1949. **12**(185).
10. Inglis, C.E., *Stresses in a Plate Due to the Presence of Cracks and Sharp Corners.* SPIE Milestone Series, 1913. **137**: p. 3-17.
11. Griffith, A.A., *The Phenomena of Rupture and Flow in Solids.* Philosophical Transactions, 1920. **221**: p. 163-198.
12. Drass, M., et al., *Adhesive connections in glass structures—part I: experiments and analytics on thin structural silicone.* Glass Structures & Engineering, 2017. **3**(1): p. 39-54.
13. Drass, M., et al., *Adhesive connections in glass structures—part II: material parameter identification on thin structural silicone.* Glass Structures & Engineering, 2017. **3**(1): p. 55-74.
14. Dias, V., et al., *Development of a constitutive hyperelastic material law for numerical simulations of adhesive steel–glass connections using structural silicone.* International Journal of Adhesion and Adhesives, 2014. **48**: p. 194-209.
15. Machalická, K. and M. Eliášová, *Environmental Conditions Effect for Adhesive Connections in Glass Structures.* Applied Mechanics and Materials, 2016. **827**: p. 19-22.
16. Santarsiero, M., C. Louter, and A. Nussbaumer, *Laminated connections for structural glass applications under shear loading at different temperatures and strain rates.* Construction and Building Materials, 2016. **128**: p. 214-237.
17. Bedon, C. and M. Santarsiero, *Laminated glass beams with thick embedded connections – Numerical analysis of full-scale specimens during cracking regime.* Composite Structures, 2018. **195**: p. 308-324.
18. Santarsiero, M., C. Bedon, and C. Louter, *Experimental and numerical analysis of thick embedded laminated glass connections.* Composite Structures, 2018. **188**: p. 242-256.
19. Zangenberg, J., et al., *Embedded adhesive connection for laminated glass plates.* International Journal of Adhesion and Adhesives, 2012. **34**: p. 68-79.

20. Zdrazilova, M., Z. Sokol, and M. Eliasova, *Tensile tests of embedded laminated glass connections*, in *IOP Conference Series: Materials Science and Engineering*. 2019, IOP Publishing: Prague.
21. BSI, *BS EN 1863-2:2004*, in *Glass in building - Heat strengthened soda lime silicate glass*. 2004: London.
22. BSI, *BS EN 1863-1:2011*, in *Glass in Building - Heat strengthened soda lime silicate glass*. 2011: London.
23. BSI, *BS EN 12150-1:2015*, in *Glass in building - Thermally toughened soda lime silicate safety glass*. 2015: London.
24. ASTM, *ASTM C1048-18 Standard Specification for Heat-Strengthened and Fully Tempered Flat Glass*. 2018: West Conshohocken, PA.
25. Ai, F.Q., et al., *On the Test Method for Determining Residual Stress on the Surface of Tempered Glass.* Key Engineering Materials, 2018. **768**: p. 19-23.
26. Veer, F.A., T. Bristogianni, and G. Baardolf, *A case study of apparently spontaneous fracture.* Glass Structures & Engineering, 2017. **3**(1): p. 109-117.
27. Gravit, M., et al., *Fire technical properties of intumescent and ablative fire resistant glass*, in *IOP Conference Series: Materials Science and Engineering*. 2019, IOP Publishing.
28. Belis, J., et al., *Failure mechanisms and residual capacity of annealed glass/SGP laminated beams at room temperature.* Engineering Failure Analysis, 2009. **16**(6): p. 1866-1875.
29. Bennison, S.J., et al., *Structural Performance of Laminated Glass Made with a Stiff Interlayer*, V. Block, Editor. 2002, ASTM International: West Conshohocken, PA. p. 57-65.
30. BASystems, *Comparing the 2 main glass interlayers: PVB v SGP*. p. https://www.basystems.co.uk/blog/2019/07/comparing-glass-interlayers/.
31. Boresi, A.P., *Advanced Mechanics of Materials* 6th ed. 2003, Hoboken, NJ: John Wiley & Sons, Inc.
32. Musgraves, D.J., J. Hu, and L. Calvez, *Springer Handbook of Glass*. 2019: Springer.
33. Hooke, R., *Lectures de Potentia Restitutiva, Or of Spring Explaining the Power of Springing Bodies*. 1678: John Martyn.
34. Morse, P.M., *Diatomic Molecules According to the Wave Mechanics. II. Vibrational Levels.* Phys. Rev, 1929. **34**: p. 57-64.
35. Gupta, P. and C. Kurkjian, *Intrinsic failure and non-linear elastic behaviour of glasses.* Journal of Non-Crystalline Solids, 2005. **351**(27-29): p. 2324-2328.
36. Mallinder, F.P. and B.A. Proctor, *Elastic constraints of fused silica as a function of large tensile strain.* Phys. Chem. Glasses, 1964. **5**: p. 91-103.
37. ASTM, *ASTM E8/E8M-21 Standard Test Methods for Tension Testing of Metallic Materials*. 2021: West Conshohocken, PA.
38. BSI, B.S.I., *BS EN ISO 6892-1:2019*, in *Metallic materials. Tensile testing. Method of test at room temperature*. 2019: London.
39. ASTM, *ASTM D1002-10(2019) Standard Test Method for Apparent Shear Strength of Single-Lap-Joint Adhesively Bonded Metal Specimens by Tension Loading (Metal-to-Metal)*. 2019: West Conshohocken, PA.
40. BSI, *BS EN ISO 9018:2015*, in *Destructive tests on welds in metallic materials. Tensile test on cruciform and lapped joints*. 2015: London.
41. BSI, *BS EN ISO 5178:2019*, in *Longitudinal tensile test on weld metal in fusion welded joints*. 2019: London.
42. BSI, *BS EN ISO 4136*, in *Destructive tests on welds in metallic materials. Transverse tensile test*. 2020: London.

43. ASTM, *ASTM D412 - 16(2021) Standard Test Methods for Vulcanized Rubber and Thermoplastic Elastomers—Tension*. 2021: West Conshohocken, PA.
44. ASTM, *ASTM C565-15(2021) Standard Test Methods for Tension Testing of Carbon and Graphite Mechanical Materials*. 2021: West Conshohocken, PA.
45. ISO, *ISO 527-1:2019*, in *Plastics — Determination of tensile properties — Part 1: General principles*. 2019.
46. ASTM, *ASTM D3039/D3039M-17 Standard Test Method for Tensile Properties of Polymer Matrix Composite Materials*. 2017: West Conshohocken, PA.
47. ASTM, *ASTM D1623-17 Standard Test Method for Tensile and Tensile Adhesion Properties of Rigid Cellular Plastics*. 2017: West Conshohocken, PA.
48. ASTM, *ASTM D882-18 Standard Test Method for Tensile Properties of Thin Plastic Sheeting*. 2018: West Conshohocken, PA.
49. ASTM, *ASTM D638-14 Standard Test Method for Tensile Properties of Plastics*. 2014: West Conshohocken, PA.
50. ISO, *ISO 11003-2:2019* in *Adhesives. Determination of shear behaviour of structural adhseives. Tensile test method using thick adherents.* . 2019: London.
51. Sun, H.C., et al., *In-situ tensile testing of ZrCu-based metallic glass composites.* Sci Rep, 2018. **8**(1): p. 4651.
52. Wang, Y.S., et al., *Fracture Morphology and Local Deformation Characteristics in the Metallic Glass Matrix Composite Under Tension.* Metallurgical and Materials Transactions A, 2015. **48**(4): p. 1545-1550.
53. Zhai, H., et al., *Strain rate sensitivity and deformation behavior in a Ti-based bulk metallic glass composite.* Journal of Non-Crystalline Solids, 2017. **471**: p. 128-136.
54. Stanciu, M.D., H.T. Draghicescu, and I.C. Rosca, *Mechanical Properties of GFRPs Exposed to Tensile, Compression and Tensile-Tensile Cyclic Tests.* Polymers (Basel), 2021. **13**(6).
55. Khan, Q., M. Sheikh, and M. Hadi, *Tensile Testing of Carbon FRP (CFRP) and Glass FRP (GFRP) Bars: An Experimental Study.* Journal of Evaluation and Testing 2021. **49**(3).
56. Alarcón, O.E., R.E. medrano, and P.P. Gillis, *Fracture of glass in tensile and bending tests.* Metallurgical and Materials Transactions A, 1994. **25(**5): p. 961-968.
57. ASTM, *ASTM D905-08(2021) - Standard Test Method for Strength Properties of Adhesive Bonds in Shear by Compression Loading*. 2021: West Conshohocken, PA.
58. ASTM, *ASTM D6641/D6641M-16e2 - Standard Test Method for Compressive Properties of Polymer Matrix Composite Materials Using a Combined Loading Compression (CLC) Test Fixture*. 2021: West Conshohocken, PA.
59. ASTM, *ASTM E9-19 Standard Test Methods of Compression Testing of Metallic Materials at Room Temperature*. 2019: West Conshohocken, PA.
60. ASTM, *ASTM E2954-15 - Standard Test Method for Axial Compression Test of Reinforced Plastic and Polymer Matrix Composite Vertical Members*. 2015: West Conshohocken, PA.
61. Angel, R.J., et al., *Elasticity measurements on minerals: a review.* European Journal of Mineralogy, 2009. **21**(3): p. 525-550.
62. Vedrtnam, A. and S.J. Pawar, *Experimental and simulation studies on flexural strength of laminated glass using ring-on-ring and three-point bending test.* Proceedings of the Institution of Mechanical Engineers, Part C: Journal of Mechanical Engineering Science, 2017. **232(**21): p. 3930-3941.
63. ASTM, *ASTM C598-93(2019) - Standard Test Method for Annealing Point and Strain Point of Glass by Beam Bending* 2019: West Conshohocken, PA.

64. Timoshenko, S., *History of Strength of Materials: With a Brief Account of the History of Theory of Elasticity and Theory of Structures*. 1953, Chelmsford: Courier Corporation.
65. Gaafar, M.S., H.A. Afifi, and M.M. Mekawy, *Structural studies of some phospho-borate glasses using ultrasonic pulse–echo technique, DSC and IR spectroscopy.* Physica B: Condensed Matter, 2009. **404**(12-13): p. 1668-1673.
66. Saddeek, Y.B., *Elastic properties of Gd3+-doped tellurovanadate glasses using pulse-echo technique.* Materials Chemistry and Physics, 2005. **91**(1): p. 146-153.
67. Zhang, J., F.-Z. Xuan, and F. Yang, *Effect of surface scratches on the characteristics of nonlinear Rayleigh surface waves in glass.* Journal of Non-Crystalline Solids, 2013. **378**: p. 101-105.
68. wróbel, G. and S. Pawlak, *A comparison study of the pulse-echo and through-transmission ultrasonics in glass/epoxy composites.* Journal of Achievements of Materials and Manufacturing Engineering, 2007. **22**(2).
69. ASTM, *ASTM C623-21 - Standard Test Method for Young's Modulus, Shear Modulus, and Poisson's Ratio for Glass and Glass-Ceramics by Resonance*. 2021: West Conshohocken, PA.
70. Duan, R.G., et al., *Microstructure research of glasses by impulse excitation technique (IET).* Journal of Non-Crystalline Solids, 2001. **281**: p. 213-220.
71. ASTM, *ASTM E1875-13 Standard Test Method For Dynamic Young's Modulus, Shear Modulus, And Poisson's Ratio By Sonic Resonance*. West Conshohocken, PA.
72. Song, W., Y. Zhong, and J. Xiang, *Mechanical parameters identification for laminated composites based on the impulse excitation technique.* Composite Structures, 2017. **162**: p. 255-260.
73. Otani, L.B. and A.H.A. Pereira, *Elastic Moduli characterization of composites using Impulse Excitation Technique.* ATCP Physical Engineering, 2014.
74. Amadio, C. and C. Bedon, *Buckling of laminated glass elements in out-of-plane bending.* Engineering Structures, 2010. **32**(11): p. 3780-3788.
75. Bedon, C., J. Belis, and C. Amadio, *Structural assessment and lateral–torsional buckling design of glass beams restrained by continuous sealant joints.* Engineering Structures, 2015. **102**: p. 214-229.
76. Bedon, C., J. Belis, and A. Luible, *Assessment of existing analytical models for the lateral torsional buckling analysis of PVB and SG laminated glass beams via viscoelastic simulations and experiments.* Engineering Structures, 2014. **60**: p. 52-67.
77. Belis, J., et al., *Experimental and analytical assessment of lateral torsional buckling of laminated glass beams.* Engineering Structures, 2013. **51**: p. 295-305.
78. Galuppi, L. and G. Royer-Carfagni, *Buckling of three-layered composite beams with viscoelastic interaction.* Composite Structures, 2014. **107**: p. 512-521.
79. Galuppi, L. and G. Royer-Carfagni, *Enhanced Effective Thickness for laminated glass beams and plates under torsion.* Engineering Structures, 2020. **206**.
80. Galuppi, L. and G.F. Royer-Carfagni, *Effective thickness of laminated glass beams: New expression via a variational approach.* Engineering Structures, 2012. **38**: p. 53-67.
81. Luible, A. and M. Crisinel, *Design of Glass Beams Subjected to Lateral Torsional Buckling*, in *IABSE Symposium, Budapest 2006: Responding to Tomorrow's Challenges in Structural Engineering*. 2006. p. 45-52.
82. Luible, A. and D. Schärer, *Lateral torsional buckling of glass beams with continuous lateral support.* Glass Structures & Engineering, 2016. **1**(1): p. 153-171.
83. Pešek, O. and J. Melcher, *Lateral-Torsional Buckling of Laminated Structural Glass Beams. Experimental Study.* Procedia Engineering, 2017. **190**: p. 70-77.

84. Schuler, C., et al., *Time and Temperature Dependent Mechanical Behaviour and Durability of Laminated Safety Glass.* Structural Engineering International, 2018. **14**(2): p. 80-83.
85. Sonck, D. and J. Belis, *Elastic lateral-torsional buckling of glass beams with continuous lateral restraints.* Glass Structures & Engineering, 2016. **1**(1): p. 173-194.
86. Valarinho, L., et al., *Lateral-torsional buckling behaviour of long-span laminated glass beams: Analytical, experimental and numerical study.* Materials & Design, 2016. **102**: p. 264-275.
87. Australia, S., *Glass in Building - Selection and Installation*. 2006: Sydney.
88. Newmark, N.M., *Test and analysis of composite beams with incomplete interaction.* Proceedings of Society for Experimental Stress Analysis, 1951. **9**(1): p. 75-92.
89. Wölfel, E., *Nachgiebiger Verbund – Eine Näherungslösung und deren Anwendungsmöglichkeiten.* Stahlbau, 1987. **6**: p. 173-180.
90. Bennison, S.J.E.I.D.d.N.C.I., et al., *Structural Performance of Laminated Glass Made with a Stiff Interlayer*. 2002, ASTM International: West Conshohocken, PA. p. 57-65.
91. BSI, *BS EN 408:2010+A1:2012 - Timber structures. Structural timber and glued laminated timber. Determination of some physical and mechanical properties.* 2010: London.
92. Gharavi, N. and H. Zhang, *Evaluation of the end effect impact on the torsion test for determining the shear modulus of a timber beam through a photogrammetry approach.* World Acad Sci Eng Technol Int J Mech Mechatron Eng, 2017. **11**(3): p. 677-680.
93. Gharavi, N. and H. Zhang, *Study on the impact of size and position of the shear field in determining the shear modulus of glulam beam using photogrammetry approach.* World Acad Sci Eng Technol Int J Struct Constr Eng, 2018. **12**(3): p. 218-222.
94. Gupta, R., L.R. Heck, and T.H. Miller, *Experimental Evaluation of the Torsion Test for Determining Shear Strength of Structural Lumber.* Journal of Testing and Evaluation, 2002. **30**(4): p. 283-290.
95. Gupta, R. and T. Siller, *Shear Strength of Structural Composite Lumber Using Torsion Tests.* Journal of Testing and Evaluation, 2005. **33**(2): p. 110-117.
96. Hindman, D., H. Manbeck, and J. Janowiak, *Torsional rigidity of rectangular wood composite materials.* Wood Fiber Sci, 2005. **37**(2): p. 283-291.
97. Khokhar, A., H. Zhang, and D. Ridley-Ellis. *The shear strength, and failure modes, of timber joists obtained from the torsion test method.* in *Proceedings of the 11th World Conference of Timber Engineering*. 2010. Riva del Garda, Italy.
98. Mohamed, A., et al., *Photogrammetric evaluation of shear modulus of glulam timber using torsion test method and dual stereo vision system.* European Journal of Wood and Wood Products, 2021. **79**(5): p. 1209-1223.
99. Mohamed, A., et al., *Applicability of the torsion test and photogrammetric approach on structural timber beams.* International Wood Products Journal, 2021. **12**(3): p. 206-217.
100. Zhang, H., et al. *Evaluation of shear constant of timber glulam composite with photogrammetric approach*. in *Proceedings of the fourteenth international conference on computing in civil and building engineering.* 2012. Moscow.
101. Zhang, H., A. Mohamed, and Z. Xiao, *Evaluation of the Shear Constant of a Timber Beam using a Photogrammetric Approach*. 2011.
102. Gharavi, N., et al., *End effect on determining shear modulus of timber beams in torsion tests.* Construction and Building Materials, 2018. **164**: p. 442-450.

103. Mohamed, A., et al., *Photogrammetric Evaluation of Glulam Timber Shear Modulus Using Torsion Test Method and Dual Stereo Vision System.* European Journal of Wood and Wood Products, 2021.
104. Yoder, N.C. and D.E. Adams, *Commonly used sensors for civil infrastructures and their associated algorithms*, in *Sensor Technologies for Civil Infrastructures*. 2014. p. 57-85.
105. Joshi, S. and S.M. Harle, *Linear variable differential transducer (LVDT) & its applications in civil engineering.* International Journal of Transportation Engineering and Technology, 2017. **3**(4): p. 62-66.
106. McDonald, P.C. and C. Iosifescu, *Use of a LVDT displacement transducer in measurements at low temperatures.* Measurement Science and Technology, 1998. **9**(4): p. 563-569.
107. Peddle, J., et al., *Bridge displacement measurement through digital image correlation.* Bridge Structures, 2011. **7**: p. 165-173.
108. Lord, J.D. and R.M. Morrell, *Elastic modulus measurement—obtaining reliable data from the tensile test.* Metrologia, 2010. **47**(2): p. S41-S49.
109. Tabin, J. and M. Prącik, *Methods for identifying dynamic parameters of clip-on extensometer–specimen structure in tensile tests.* Measurement, 2015. **63**: p. 176-186.
110. Granshaw, S.I., *Laussedat bicentenary: origins of photogrammetry.* The Photogrammetric Record, 2019. **34**(166): p. 128-147.
111. Aber, J.S., et al., *Principles of Photogrammetry*, in *Small-Format Aerial Photography and UAS Imagery*. 2019. p. 19-38.
112. Baqersad, J., et al., *Photogrammetry and optical methods in structural dynamics – A review.* Mechanical Systems and Signal Processing, 2017. **86**: p. 17-34.
113. Peters, W.H. and W.F. Ranson, *Digital imaging techniques in experimental stress analysis.* Optical Engineering, 1982. **21**(3).
114. Sutton, M.A., et al., *Determination of displacements using an improved digital correlation method.* Image and Vision Computing, 1983. **1**(3).
115. Hampel, U. and H. Maas, *Application of digital photogrammetry for measuring deformation and cracks during load tests in civil engineering material testing.* Optical 3-D, 2003.
116. Maas, H. and U. Hampel, *Photogrammetric techniques in civil engineering material testing and structure monitoring.* Photogrammetric Engineering & Remote Sensing, 2006. **72**(1): p. 39-45.
117. Mohamed, A., et al., *Performance study of photogrammetry method and displacement transducer in compression tests of timber plates.* Wood Material Science & Engineering, 2021 (Under Review).
118. Uheida, K., et al., *Determining equivalent-sectional shear modulus in torsion tests for laminated glass beams using photogrammetry method.* Composite Structures, 2021. **276**.
119. Zhang, H., et al., *Evaluation of the Shear Constant of a Timber Beam using a Photogrammetric Approach*, in *14th International Conference on Computing in Civil and Building Engineering* 2012: Moscow.
120. Zhang, H., et al., *Evaluation of shear constant of timber glulam composite with photogrammetric approach*, in *The 13th International Conference on Civil, Structural and Environmental Engineering Computing*. 2011: Crete, Greece.
121. Mohamed, A., et al., *A Low Cost Non-Contact and Non-Destructive Method for Evaluating the Variation of the Shear Modulus for Glued Laminated Timber Beams using a Photogrammetric Approach*, in *Proceedings of the Fifteenth International Conference on Civil, Structural and Environmental Engineering Computing*. 2015.

122. Zhang, H., A. Mohamed, and Z. Xiao, *Evaluation of the Shear Constant of a Timber Beam using a Photogrammetric Approach*, in *Proceedings of the Thirteenth International Conference on Civil, Structural and Environmental Engineering Computing*. 2011.
123. Gharavi, N. and H. Zhang, *Study on the Impact of Size and Position of the Shear Field in Determining the Shear Modulus of Glulam Beam Using Photogrammetry Approach.* International Journal of Structural and Construction Engineering, 2018. **12**: p. 218-222.
124. Steger, C., M. Ulrich, and C. Wiedemann, *Machine Vision Algorithms and Applications*. 2nd ed. 2018, Weinheim: Wiley-VCH.
125. GmbH, M.S., *Solution Guide III-C: 3D Vision.* 2020.
126. Wohler, C., *3D Computer Vision: Efficient Methods and Applications*. 2nd ed. 2013, London: Springer.
127. Hartley, R. and A. Zisserman, *Multiple view geometry in computer vision*. 2003: Cambridge University Press.
128. BSI, *BS EN 572-1-2012+A1-2016 Glass in building - Basic soda lime silicate glass products*, in *Part 1: Definitions and general physical and mechanical properties*. 2016, British Standards Institution BSI: London.
129. Kuraray, *Physical Properties of SentryGlas and Butacite*. 2014.

Appendices

Appendix A: Shear Modulus Calculations

Two-layer laminates

The equivalent sectional shear modulus for laminated glass beams with two glass layers is elucidated by applying sandwich theory, (A-B method) was used in this demonstration:

$$G_{ESSM} = \frac{G\left(J_{glass1} + J_{glass2} + J_{comp}\right)}{J_{homog}}$$

The shear modulus of single layer glass G is:

$$G = \frac{E}{2(1+\mu)} = \frac{7 \times 10^{10}}{2(1+0.23)} = \mathbf{28.455\ GPa}$$

The torsional constants for glass layers and laminated glass beams are:

$$J_{glass1} = J_{glass2} = 0.3246ht^3 = 0.3246 \times 240 \times 10^3 = 7.7904 \times 10^4\ mm^4$$

$$J_{homog} = 0.3145h(t_1 + t_{INT} + t_2)^3 = 0.3145 \times 240 \times (10 + 1.52 + 10)^3$$

$$= \mathbf{7.5224 \times 10^5\ mm^4}$$

The torsional constants due to composite action of interlayers are obtained as

$$J_s = 4\left(\frac{t_1 + t_2}{2} + t_{INT}\right)^2 \frac{t_1 t_2}{t_1 + t_2} b = 4 \times (\frac{10+10}{2} + 1.52)^2 \times \frac{10^2}{10+10} \times 240$$

$$= \mathbf{6.3701 \times 10^5\ mm^4}$$

The shear moduli with 10mins load duration and $20℃$ temperature of PVB and SGP may be calculated to be 1.52 and $191.03\ MPa$ by applying linear interpolation to the material properties data from DuPont. Hence, the analytical ESSM values for PVB and SGP laminated glass are respectively evaluated as follows:

$$\lambda = \sqrt{\frac{G_{PVB}}{G}\frac{t_1 + t_2}{t_{PVB}t_1t_2}} = \sqrt{\frac{1.52 \times 10^6}{28.455 \times 10^9}\frac{10 + 10}{1.52 \times 10^2}} = \mathbf{0.00265}\boldsymbol{mm^{-1}}$$

$$J_{comp} = J_s\left[1 - \frac{\tanh\frac{\lambda h}{2}}{\frac{\lambda h}{2}}\right] = 6.3701 \times 10^5\left[1 - \frac{\tanh\frac{0.00265 \times 240}{2}}{\frac{0.00265 \times 240}{2}}\right]$$

$$= \mathbf{2.0629 \times 10^4}\boldsymbol{mm^4}$$

$$G_{ESSM\_PVB} = \frac{G\left(J_{glass1} + J_{glass2} + J_{comp}\right)}{J_{homog}} = \frac{28.455 \times (7.7904 + 7.7904 + 2.0629) \times 10^4}{7.5224 \times 10^5}$$

$$= \mathbf{6.674}\boldsymbol{GPa}$$

$$\lambda = \sqrt{\frac{G_{SGP}}{G}\frac{t_1 + t_2}{t_{SGP}t_1t_2}} = \sqrt{\frac{191.03 \times 10^6}{28.455 \times 10^9}\frac{10 + 10}{1.52 \times 10^2}} = \mathbf{0.0297}\boldsymbol{mm^{-1}}$$

$$J_{comp} = J_s\left[1 - \frac{\tanh\frac{\lambda h}{2}}{\frac{\lambda h}{2}}\right] = 6.3701 \times 10^5\left[1 - \frac{\tanh\frac{0.0297 \times 240}{2}}{\frac{0.0297 \times 240}{2}}\right]$$

$$= \mathbf{4.5869 \times 10^5}\boldsymbol{mm^4}$$

$$G_{ESSM\_SGP} = \frac{G\left(J_{glass1} + J_{glass2} + J_{comp}\right)}{J_{homog}} = \frac{28.455 \times (7.7904 + 7.7904 + 45.869) \times 10^4}{7.5224 \times 10^5}$$

$$= \mathbf{23.244}\boldsymbol{GPa}$$

The ESSM values may also be evaluated by using EET model. Detailed determination of them is presented as follows:

$$J_m = J_{glass1} + J_{glass2} + J_s = 2 \times 7.7904 \times 10^4 + 6.3701 \times 10^5 = \mathbf{7.9282 \times 10^5}\boldsymbol{mm^4}$$

$$\eta = \frac{1}{1 + 12\ \frac{t_{INT}\ t_1t_2}{t_1 + t_2}\ \ \frac{J_{glass1} + J_{glass2}}{J_m}\ \ \frac{G}{G_{PVB}}\ \frac{L^2 + h^2}{L^2h^2}}$$

$$= \frac{1}{1 + 12\ \frac{1.52\ \times 10^2}{10 + 10}\ \ \frac{(7.7904 + 7.7904) \times 10^4}{7.9282 \times 10^5}\ \ \frac{28.455 \times 10^9}{1.52 \times 10^6}\ \frac{2400^2 + 240^2}{2400^2 \times 240^2}}$$

$$= \mathbf{0.1451}$$

$$J_{eff;EET} = \frac{1}{\frac{\eta}{J_m} + \frac{1-\eta}{J_{glass1} + J_{glass2}}} = \frac{1}{\frac{0.1451}{7.9282 \times 10^5} + \frac{1-0.1451}{(7.7904 + 7.7904) \times 10^4}}$$

$$= 1.7637 \times 10^5\ mm^4$$

$$G_{ESSM\_PVB} = \frac{G\, J_{eff;EET}}{J_{homog}} = \frac{28.455 \times 10^9 \times 1.7637 \times 10^5}{7.5224 \times 10^5} = \mathbf{6.674\ GPa}$$

$$\eta = \frac{1}{1 + 12\ \frac{t_{INT}\ t_1 t_2}{t_1 + t_2}\ \ \frac{J_{glass1} + J_{glass2}}{J_m}\ \ \frac{G}{G_{SGP}}\ \frac{L^2 + h^2}{L^2 h^2}}$$

$$= \frac{1}{1 + 12\ \frac{1.52\ \times 10^2}{10 + 10}\ \ \frac{(7.7904 + 7.7904) \times 10^4}{7.9282 \times 10^5}\ \ \frac{28.455 \times 10^9}{191.03 \times 10^6}\ \frac{2400^2 + 240^2}{2400^2 240^2}}$$

$$= \mathbf{0.9553}$$

$$J_{eff;EET} = \frac{1}{\frac{\eta}{J_m} + \frac{1-\eta}{J_{glass1} + J_{glass2}}} = \frac{1}{\frac{0.9553}{7.9282 \times 10^5} + \frac{1-0.9553}{(7.7904 + 7.7904) \times 10^4}}$$

$$= \mathbf{6.7032 \times 10^5 mm^4}$$

$$G_{ESSM\_SGP} = \frac{G\, J_{eff;EET}}{J_{homog}} = \frac{28.46 \times 10^9 \times 6.7032 \times 10^5}{7.5224 \times 10^5} = \mathbf{25.354\ GPa}$$

Three-layer laminates

The equivalent sectional shear modulus for laminated glass beams with three glass layers can only be determined using the EET model by Galuppi & Royer-Carfagni:

The equivalent torsional stiffness may be evaluated as $G_g J_{eff;EET} / J_{\text{homog}}$, where:

$$J_{\text{homog}} = 0.1345a\left(h_1 + h_2 + h_3 + t_1 + t_2\right) = 0.1345 * 240 * (6 + 10 + 6 + 1.52 + 1.52)$$
$$= \boldsymbol{11.85045 * 10^5\ mm^4}$$

$$J_{eff;EET} = \frac{1}{\frac{\eta}{J_{t,M}} + \frac{1-\eta}{J_{t,L}}},$$

and where:

$$J_{t,M} = \frac{1}{3} a \tilde{h}_{eq,M}^3, \qquad \tilde{h}_{eq,M} = \sqrt[3]{\sum_{i=1}^{N} h_i^3 + 12 \sum_{i=1}^{N} \bar{y}_i^2 h_i},$$

$$\tilde{h}_{eq,M} = \sqrt[3]{\left(h_1 + h_2 + h_3\right)^3 + 12\left(\left(\bar{y}_1 + \bar{y}_2\right)^2 \left(h_1 + h_2 + h_3\right)\right)} =$$

$$\sqrt[3]{\left(6+10+6\right)^3 + 12\left(\left(9.52+9.52\right)^2 \left(6+10+6\right)\right)} = 47.379$$

$$J_{t,M} = \frac{1}{3} a \tilde{h}_{eq,M}^3 = \frac{1}{3} * 240 * 47.379 = \boldsymbol{85.083 * 10^5\ mm^4}$$

Where $h_{eq,M}$ is the rotational-enhanced effective torsional thickness (EETT) and $J_{t,M}$ is the geometric torsional constant at the monolithic limits. Subsequently, $h_{eq,L}$ and $J_{t,L}$ are the rotational-EETT and geometric torsional constant at the layered limit:

$$J_{t,L} = \frac{1}{3} a \tilde{h}_{eq,L}^3, \qquad h_{eq,L} = \sqrt[3]{\sum_{i=1}^{N} h_i^3}.$$

$$h_{eq,L} = \sqrt[3]{\sum_{i=1}^{N} h_i^3} = \sqrt[3]{\left(h_1 + h_2 + h_3\right)^3} = \sqrt[3]{\left(6+10+6\right)^3} = 22$$

$$J_{t,L} = \frac{1}{3} a \tilde{h}_{eq,L}^3 = \frac{1}{3} * 240 * 22^3 = \boldsymbol{8.5184 * 10^5\ mm^4}$$

The values for $H_i, \bar{y}$ describe the distance between centroids of each glass ply, and the distance between the centroid of each glass ply and the centroid of the entire structure, respectively. The geometrics of these parameters are presented in Figure 6-20.

The shear coupling coefficient for multi-laminates, η, can then be calculated by:

$$\eta = \frac{1}{1+12\frac{J_{t,L}}{J_{t,M}}\frac{\sum_{i=1}^{N}\bar{y}_i^2 h_i}{\sum_{i=1}^{N-1}H_i^2/t_i}\frac{G_g}{G_{INT}}\frac{L^2+a^2}{L^2a^2}}$$

$$= \frac{1}{1+12\left(\frac{8.5184*10^5}{85.083*10^5}\right)\frac{\left((9.52+9.52)^2(6+10+6)\right)}{25.04^2/(1.52+1.52)}\frac{28.455*10^9}{1.52*10^6}\frac{2400^2+240^2}{2400^2*240^2}}$$

$$= \boldsymbol{0.036528 \quad .... \ for \ PVB}$$

$$= \frac{1}{1+12\left(\frac{8.5184*10^5}{85.083*10^5}\right)\frac{\left((9.52+9.52)^2(6+10+6)\right)}{25.04^2/(1.52+1.52)}\frac{28.455*10^9}{191.03*10^6}\frac{2400^2+240^2}{2400^2*240^2}}$$

$$= \boldsymbol{0.826534 \quad .... \ for \ SGP}$$

where G_g is the glass shear modulus and G_{INT} is the interlayer shear modulus. Now the effective torsional constant $J_{eff;EET}$ can be determined by:

$$J_{eff;EET} = \frac{1}{\frac{0.036528}{85.083*10^5}+\frac{1-0.036528}{8.5184*10^5}} = \boldsymbol{8.807925*10^5 \, mm^4 \ ... \ for \ PVB}$$

$$= \frac{1}{\frac{0.826534}{85.083*10^5}+\frac{1-0.826534}{8.5184*10^5}} = \boldsymbol{3324676.386*10^5 \, mm^4 \ ... \ for \ SGP}$$

Finally, the equivalent-sectional shear modulus according to the EET method can be calculated:

$$\frac{\left((28.455*10^9)*(8.8079254*10^5)\right)}{11.85045*10^5} = \boldsymbol{21.15GPa \ ... \ for \ PVB}$$

$$\frac{\left((28.455*10^9)*(3324676.386*10^5)\right)}{11.85045*10^5} = \boldsymbol{79.83GPa \ ... \ for \ SGP}$$

Appendix B: Interlayer Specification Tables

The following tables were provided by www.glasslaminatingsolutions.kuraray.com

Relaxation modulus G [N/mm²]	Product type	Load duration									
		3 sec	30 sec	1 min	5 min	30 min	1 hour	1 day	5 days	3 weeks	1 month	1 year
10°C Temperature	Trosifol® BG	-	-	-	-	-	-	-	-	-	-	-
	Trosifol® ES	699	603	573	502	420	388	234	157	95	80	19
	SentryGlas®	236	228	225	220	217	206	190	178	172	171	161
20°C Temperature	Trosifol® BG	8	-	1.6	-	-	0.8	0.5	-	-	0.4	0.3
	Trosifol® ES	342	230	196	122	55	37	5.3	2.8	2.0	1.9	1.6
	SentryGlas®	211	206	195	188	175	169	146	130	115	112	96.5
30°C Temperature	Trosifol® BG	1	-	0.8	-	-	0.4	0.3	-	-	0.1	0.1
	Trosifol® ES	58	14	9.2	4.0	2.3	2	1.6	1.6	1.5	1.5	1.5
	SentryGlas®	141	119	110	82.8	66.1	60	49.7	24.7	12.9	11.6	6.8
40°C Temperature	Trosifol® BG	0.6	-	0.5	-	-	0.2	0.2	-	-	0.1	0.1
	Trosifol® ES	3.4	1.9	1.8	1.6	1.6	1.6	1.5	1.5	-	1.5	-
	SentryGlas®	63	36.6	30.7	19.4	11.4	9.3	4.5	3.6	3.4	3.3	3.1
50°C Temperature	Trosifol® BG	0.4	-	0.3	-	-	0.1	0.1	-	-	0.1	0.1
	Trosifol® ES	1.7	1.6	1.6	1.5	1.5	-	-	-	-	-	-
	SentryGlas®	26.4	13.5	11.3	7.3	4.9	4.2	2.8	2.4	2.2	2.2	2.1
60°C Temperature	Trosifol® BG	-	-	-	-	-	-	-	-	-	-	-
	Trosifol® ES	1.6	1.5	1.5	-	-	-	-	-	-	-	-
	SentryGlas®	8.2	4.3	3.7	2.6	1.9	1.7	1.3	1.2	1.2	1.1	1.0
70°C Temperature	Trosifol® BG	-	-	-	-	-	-	-	-	-	-	-
	Trosifol® ES	-	-	-	-	-	-	-	-	-	-	-
	SentryGlas®	2.9	2.1	1.9	1.4	1.0	0.8	0.6	0.6	0.5	0.5	0.5
80°C Temperature	Trosifol® BG	-	-	-	-	-	-	-	-	-	-	-
	Trosifol® ES	-	-	-	-	-	-	-	-	-	-	-
	SentryGlas®	1.3	1.0	0.8	0.6	0.4	0.3	0.3	0.2	0.2	0.2	0.2

Figure B-1: PVB and SGP shear modulus under different conditions (Trosifol BG is the standard PVB product) (www.mornglass.com).

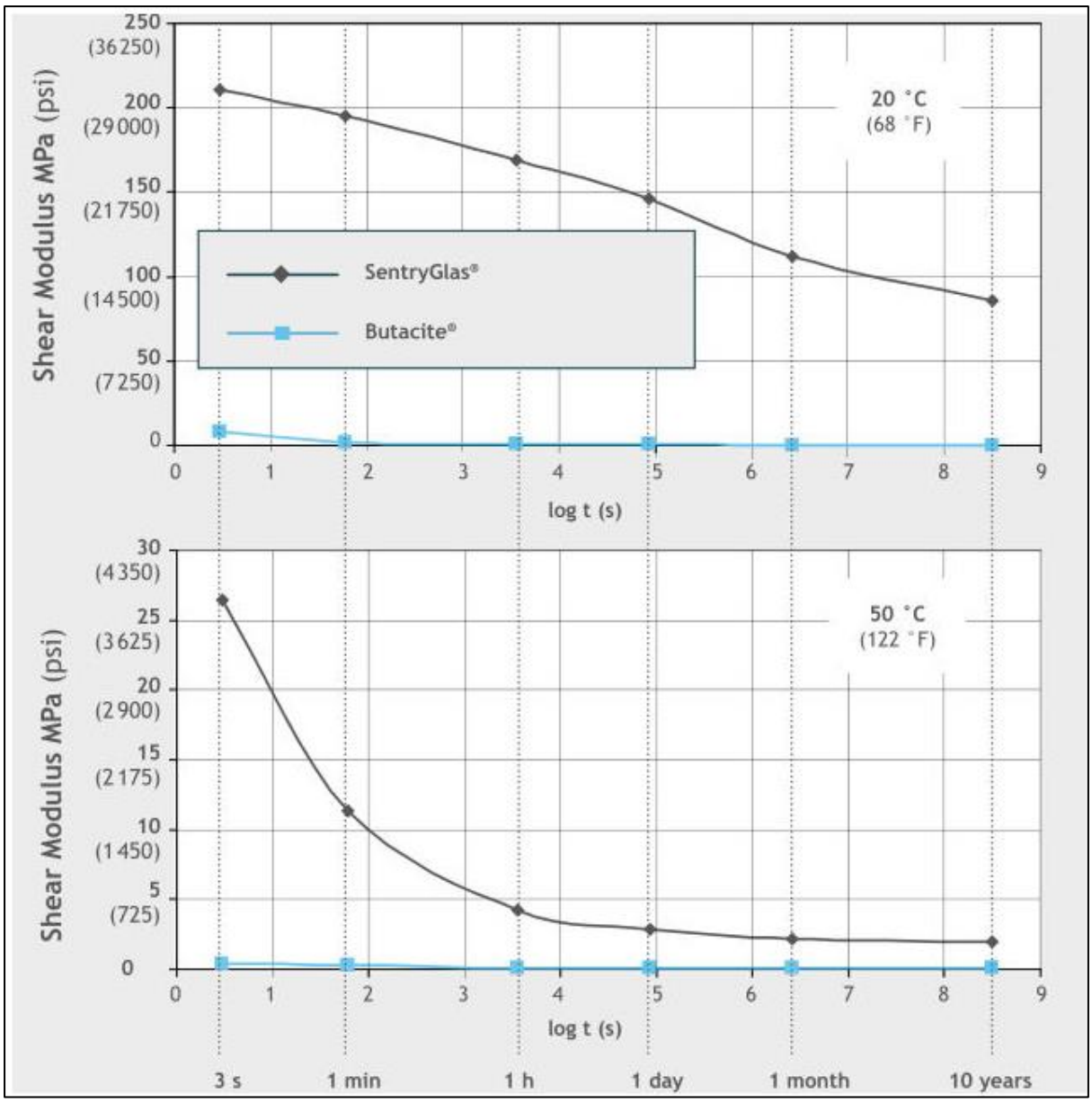

Figure B-2: PVB and SGP shear modulus under different conditions [129].

Appendix C: List of British and European Standards for Glass

British and European Standards (BS EN)

BS EN 356: Glass in building – Security glazing - Testing and classification of resistance against manual attack

BS EN 410: Glass in building - Determination of luminous and solar characteristics of glazing

BS EN 572: - Glass in building - Basic soda lime silicate glass products

- Part 1: Definitions and general physical and mechanical properties
- Part 2: Float glass
- Part 3: Polished wired glass
- Part 4: Drawn sheet glass
- Part 5: Patterned glass
- Part 6: Wired patterned glass
- Part 7: Wired or unwired channel shaped glass
- Part 8: Supplied and final cut sizes
- Part 9: Evaluation of conformity/Product standard

BS EN 673: Glass in building - Determination of thermal transmittance (U Value) - Calculation method

BS EN 674: Glass in building - Determination of thermal transmittance (U Value). Guarded hot plate method

BS EN 675: Glass in building - Determination of thermal transmittance (U Value) - Heat flow meter method

BS EN 1036: Glass in building - Mirrors from silver-coated float glass for internal use

- Part 1: Definitions, requirements and test methods
- Part 2: Evaluation of Conformity/Product standard

BS EN 1063: Glass in building - Security glazing – Testing and classification of resistance against bullet attack

BS EN 1096: Glass in building - Coated glass

- Part 1: Definitions and classification
- Part 2: Requirements and test methods for class A, B, and S coatings
- Part 3: Requirements and test methods for class C and D Coatings

- Part 4: Evaluation of conformity/Product standard
- Part 5: Test method and classification for the self-cleaning performances of coated glass surfaces

BS EN 1279: Glass in building – Insulating glass units

- Part 1: Generalities, dimensional tolerances and rules for the system description
- Part 2: Long term test method and requirements for moisture penetration
- Part 3: Long term test method and requirements for gas leakage rate and for gas concentration tolerances
- Part 4: Methods of test for the physical attributes of edge seals
- Part 5: Evaluation of conformity
- Part 6: Factory production control and periodic tests

BS EN 1288: Glass in building - Determination of bending strength of glass

- Part 1**:** Fundamentals of testing glass
- Part 2: Coaxial double ring test on flat specimens with large test surface areas
- Part 3: Test with specimen supported at two points (four-point bending)
- Part 4: Testing of channel shaped glass
- Part 5: Coaxial double ring test on flat specimens with small test surface areas

BS EN 1748: Glass in building – Special basic products

- Part 1-1: Borosilicate glasses - Definition and general physical and mechanical properties
- Part 1-2: Borosilicate glasses - Evaluation of conformity/Product standard
- Part 2-1: Glass ceramics - Definitions and general physical and mechanical properties
- Part 2-2: Glass ceramics - Evaluation of conformity/Product standard

BS EN 1863: Glass in building – Heat strengthened soda lime silicate glass

- Part 1: Definition and description
- Part 2: Evaluation of Conformity/Product standard

BS EN 12150: Glass in building – Thermally toughened soda lime silicate safety glass

- Part 1: Definition and description
- Part 2: Evaluation of conformity/Product standard

BS EN 12337: Glass in building – Chemically strengthened soda lime silicate glass

- Part 1: Definition and description
- Part 2: Evaluation of conformity/Product standard

BS EN 12488: Glass in building - Glazing recommendations

- Assembly principles for vertical and sloping glazing

BS EN ISO 12543:

Glass in building - Laminated glass and laminated safety glass

- Part 1: Definitions and description of component parts

- Part 2: Laminated safety glass
- Part 3: Laminated glass
- Part 4: Test methods for durability
- Part 5: Dimensions and edge finishing
- Part 6: Appearance

BS EN 14449: Glass in building - Laminated glass and laminated safety glass - Evaluation of conformity/Product standard

BS EN 12600: Glass in building – Pendulum test – Impact test method and classification for flat glass

BS EN 12758: Glass in building - Glazing and airborne sound insulation - Product descriptions and determination of properties

BS EN 12898: Glass in building - Determination of the emissivity

BS EN 13022: Glass in building - Structural sealant glazing

- Part 1: Glass products for structural sealant glazing systems supported and unsupported monolithic and multiple glazing
- Part 2: Assembly rules

BS EN 13024: Glass in building – Thermally toughened borosilicate safety glass

- Part 1: Definition and Description
- Part 2: Evaluation of conformity/Product standard

BS EN 13541: Glass in building - Security glazing - Testing and classification of resistance against explosion pressure

BS EN 14178: Glass in building – Basic alkaline earth silicate glass products

- Part 1: Float glass
- Part 2: Evaluation of conformity/Product standard

BS EN 14179: Glass in building - Heat soaked thermally toughened soda lime silicate safety glass

- Part 1: Definition and description
- Part 2: Evaluation of conformity/Product standard

BS EN 14321: Glass in building – Thermally toughened alkaline earth silicate safety glass

- Part 1: Definition and description
- Part 2: Evaluation of conformity/Product standard

BS EN 15434: Glass in building – Product standard for structural and/or ultraviolet resistant sealant (for use with structural sealant glazing and/or insulating glass units with exposed seals)

BS EN 15683: Glass in building – Thermally toughened alkaline earth silicate safety glass

- Part 1: Definition and description
- Part 2: Evaluation of conformity/Product standard

BS EN 15998: Glass in building - Safety in case of fire, fire resistance - Glass testing methodology for the purpose of classification

BS EN 16477: Glass in building – Painted glass for internal use

- Part 1: Requirements

British Standards (BS)

BS 476 Fire tests on building materials and structures

- Part 22: Methods for determination of the fire resistance of non-loadbearing elements of construction

BS 857: Specification for safety glass for land transport

BS 952: Glass for glazing

- Part 1: Classification
- Part 2: Terminology for work on glass

BS 3193: Specification for thermally toughened glass panels for use in domestic appliances

BS 3463: Specification for observation and gauge glasses for pressure vessels

BS 5357: Code of practice for installation of security glazing

BS 5516: Patent glazing and sloping glazing for buildings

- Part 1: Code of practice for design and installation of sloping and vertical patent glazing
- Part 2: Code of practice for sloping glazing

BS 5234: Partitions (including matching linings)

- Part 1: Code of practice for design and installation
- Part 2: Specification for performance requirements for strength and robustness including methods of test

BS 6180: Barriers in and about buildings - Code of practice

BS 6262: Glazing for buildings

- Part 1: General methodology for the selection of glazing
- Part 2: Code of practice for energy, light and sound
- Part 3: Code of practice for fire, security and wind loading
- Part 4: Code of practice for safety related to human impact
- Part 6: Code of practice for special applications
- Part 7: Code of practice for the provision of information

BS 8000: Workmanship on building sites

- Part 7: Code of practice for glazing

Appendix D: MATLAB Code for ESSM Calculation

```
clear all

DotInALine=15; %  15 points in a line.
TotalLine=11;  %  11 lines
HeightOfBeam=240; % glass beam height 240mm
ThicknessOfBeam=0; % Thickness to be read in

TargetLtoLDist=70; %line to line distance 70mm

TotalDots=DotInALine*TotalLine;

OutputExcel='*filepath*';

if isfile('*filepath*')
    delete '*filepath*';
end

excelapp = actxserver('Excel.Application');            %connect to excel
workbook = excelapp.Workbooks.Open('*filepath*');    %open workbook, specify
the full path

TotalTestNumber=workbook.Sheets.Count;



for t=1:TotalTestNumber

    NameofTheTest=workbook.Sheets.Item(t).Name;

    worksheet = workbook.Sheets.Item(t);                    %Test t

    NonZeroCell=2;
    while 1

curCellPosition=get(get(worksheet,'Cells',3,NonZeroCell),'Address');
        if isnan(worksheet.Range(curCellPosition).Value) %check if cell is
empty or not
            break;
        end
        NonZeroCell=NonZeroCell+1; %counting how many cells in third row is
non-zero
    end

    TotalPhotoPoint=(NonZeroCell-2)/3; %non-zero cell/3 = photo point taken
in one run

    Torque=zeros(1,TotalPhotoPoint);
    RelativeTorque=zeros(1,TotalPhotoPoint);

    x=zeros(TotalDots,TotalPhotoPoint);
    y=zeros(TotalDots,TotalPhotoPoint);
    z=zeros(TotalDots,TotalPhotoPoint);
```

```
    for pht=1:TotalPhotoPoint
        for i=1:TotalDots % 165 points
            for j=1:3 % x, y, z

                curCellPosition=get(get(worksheet,'Cells',2+i,1+(pht-
1)*3+j),'Address');

                switch j
                    case 1
                        x(i,pht)=worksheet.Range(curCellPosition).Value;
                    case 2
                        y(i,pht)=worksheet.Range(curCellPosition).Value;
                    case 3
                        z(i,pht)=worksheet.Range(curCellPosition).Value;
                end

            end
        end

        curCellPosition=get(get(worksheet,'Cells',170,2+(pht-
1)*3),'Address'); %reading torque at the moment of taking the image
        Torque(1,pht)=worksheet.Range(curCellPosition).Value*1000.0; %
also, convert the torque unit from N.m to N.mm

    end

    % read 165 points x photo point, x y z coordinates




    xp=x(:,1); % transpose, prepare for regression
    yp=y(:,1);
    zp=z(:,1);

    % to fit a plane equation z=C+Ax+By
    % use MATLAB, regress function to fit the plane:

    XP = [ones(size(xp)) xp yp];
    b = regress(zp,XP);

    % b=[C;A;B]; corresponding to the equation parameters above C A B for
    % plane zero

    Cp=b(1);
    Ap=b(2);
    Bp=b(3);

    %-----
    % Fit the 3D line



    ThetaAll=zeros(TotalLine,TotalPhotoPoint);
    RelativeThetaAll=zeros(TotalLine,TotalPhotoPoint);

    TwistRateCalx=zeros(TotalLine,1);
    TwistRateCaly=zeros(TotalLine,1);
    TwistRate=zeros(1,TotalPhotoPoint);
```

```
    TwistRatexJAccurate=zeros(1,TotalPhotoPoint);

    XL=zeros(DotInALine,3);


    for pht=2:TotalPhotoPoint

        for ln=1:TotalLine
            for pt=1:DotInALine

                XL(pt,1)=x((ln-1)*DotInALine+pt,pht);
                XL(pt,2)=y((ln-1)*DotInALine+pt,pht);
                XL(pt,3)=z((ln-1)*DotInALine+pt,pht);    % read in one line
"DotInALine" point coordinates

            end

            XL_ave=mean(XL,1);              % mean; line of best fit will
pass through this point
            dXL=bsxfun(@minus,XL,XL_ave);   % residuals
            C=(dXL'*dXL)/(DotInALine-1);           % variance-covariance
matrix of X
            [R,D]=svd(C,0);               % singular value decomposition of
C; C=R*D*R'

            % NOTES:
            % 1) Direction of best fit line corresponds to R(:,1)
            % 2) R(:,1) is the direction of maximum variances of dX
            % 3) D(1,1) is the variance of dX after projection on R(:,1)
            % 4) Parametric equation of best fit line:
L(t)=X_ave+t*R(:,1)', where t is a real number
            % 5) Total variance of X = trace(D)
            % Coefficient of determination; R^2 = (explained
variance)/(total variance)
            %D=diag(D);
            %R2=D(1)/sum(D);  % R2 value if required

            Al=R(1,1);
            Bl=R(2,1);
            Cl=R(3,1);


SinTheta=(Ap*Al+Bp*Bl+Cp*Cl)/sqrt((Ap^2+Bp^2+Cp^2)*(Al^2+Bl^2+Cl^2));
            Theta=asin(SinTheta);
%            Theta = Theta*180/pi; %convert to degrees
            ThetaAll(ln,pht)=Theta;

        end
    end

    xlswrite(OutputExcel,{'Torque Abs'},t,'A2');
    xlswrite(OutputExcel,Torque,t,'B2');
    xlswrite(OutputExcel,{'Angle Line-Plane'},t,'A4');
    xlswrite(OutputExcel,ThetaAll,t,'B4');

    curCellPosition=get(get(worksheet,'Cells',172,1),'Address'); % reading
the thickness of the beam
    ThicknessOfBeam=worksheet.Range(curCellPosition).Value;
```

```
    tmpJTerm2part=0.0;
    t_half=ThicknessOfBeam/2.0;
    h_half=HeightOfBeam/2.0;

    for n=1:2000:2

        tmpJTerm2part=tmpJTerm2part+1.0/(n^5)*tanh(n*pi*h_half/(2*t_half));

    end

    JAccurate=(2.0*t_half)^3*(2*h_half)/3.0*(1-
192.0/pi^5*(t_half/h_half)*tmpJTerm2part);

    for pht=3:TotalPhotoPoint

        RelativeTorque(1,pht)=Torque(1,pht)-Torque(1,2);

        for ln=1:TotalLine
            RelativeThetaAll(ln,pht)=ThetaAll(ln,pht)-ThetaAll(ln,2);

            TwistRateCalx(ln,1)=(ln-1)*TargetLtoLDist; % line to line
distance

            TwistRateCaly(ln,1)=RelativeThetaAll(ln,pht);
        end

        KtwistRateArray=polyfit(TwistRateCalx,TwistRateCaly,1);
        TwistRate(1,pht)=KtwistRateArray(1,1);

        TwistRatexJAccurate(1,pht)=KtwistRateArray(1,1)*JAccurate;

    end


GValueArray=polyfit(TwistRatexJAccurate(1,2:TotalPhotoPoint),RelativeTorque
(1,2:TotalPhotoPoint),1);


    xlswrite(OutputExcel,{'Relative Angle'},t,'A16');
    xlswrite(OutputExcel,RelativeThetaAll,t,'B16');

    xlswrite(OutputExcel,{'Twist Rate'},t,'A28');
    xlswrite(OutputExcel,TwistRate,t,'B28');

    xlswrite(OutputExcel,{'TwistRate x JAccurate'},t,'A30');
    xlswrite(OutputExcel,TwistRatexJAccurate,t,'B30');

    xlswrite(OutputExcel,{'Relative Torque'},t,'A32');
    xlswrite(OutputExcel,RelativeTorque,t,'B32');

    xlswrite(OutputExcel,{'Gphoto'},t,'A34');
    xlswrite(OutputExcel,{'N/mm2'},t,'C34');
    xlswrite(OutputExcel,GValueArray(1,1),t,'B34');

    workbookOut = excelapp.Workbooks.Open(OutputExcel);    % open workbook,
specify the full path
```

```
    workbookOut.Sheets.Item(t).Name=NameofTheTest; % set the worksheet name
    workbookOut.Save
    workbookOut.Close;
    %----


end

workbook.Close;                                          %close workbook when
done
excelapp.Quit;                                           %end excel
delete(excelapp);
```